

Boron Dye-PLA Materials for Oxygen Sensing

Christopher Arnett DeRosa
Frostburg, Maryland

B.S., Alderson-Broaddus College, 2012

A Dissertation presented to the Graduate Faculty
of the University of Virginia in Candidacy for the Degree of
Doctor of Philosophy

Department of Chemistry

University of Virginia
March, 2017

Abstract

Many applications benefit from the development of multicolor luminescent materials, such as bioimaging and displays. Optical bioimaging with fluorescent dyes can provide spatial and temporal information of important analytes, such as oxygen. Difluoroboron dibenzoylmethane–poly(lactic acid) (BF₂dbmPLA) exhibits both fluorescence (F) and oxygen sensitive room-temperature phosphorescence (RTP). This material has enabled ratiometric oxygen sensing. The fluorescence acts as an internal reference, and the phosphorescence changes intensity based on the oxygen concentration. While BF₂dbmPLA has blue fluorescence and green phosphorescence, non-ideal for biomedical applications, its simple structure is a powerful starting point. There are tremendous possibilities for chemically diverse derivatives to optimize the luminescence colors and oxygen sensitivities.

Synthesis of new dyes and polymers was conducted. First, halide substituents on the ligand scaffold proved to be an effective method to tailor the oxygen sensitivity of BF₂dbm(X)PLA (X = H, F, Cl, Br, or I). Second, for red-shifted optical properties, a combination of aromatic π -conjugation and polymer molecular weight was used to synthesize polymers of different luminescence colors. Exploration of different aromatic groups included phenyl, naphthyl, and thienyl substituents. Fluorescence colors range from ~400-550 nm, and phosphorescence colors span ~500-590 nm. Third, synthetic protocols were established to prepare BF₂bdk dye-poly(lactic acid)-poly(ethylene glycol) (BF₂bdk-PLA-PEG) block copolymers via a Mitsunobu reaction. Finally, polymers were fabricated as nanoparticles for oxygen sensing in cells, tumors and wounds. Synthesis and characterization are discussed.

Table of Contents

Abstract.....	ii
Table of Contents.....	iii
Acknowledgements.....	vii
Dedication	x
List of Tables	xi
List of Figures	xii

Chapter 1: Introduction to Polymers, Luminescence and Optical Bioimaging

1. Introduction.....	2
1.1. Macromolecular Chemistry	2
1.1.1. Polymer Synthesis & Characterization	3
1.1.2. Polymers & Nanoscience.....	8
1.2. Introduction to Luminescence	10
1.2.1. Molecular Luminescence	11
1.2.2. Optical Spectroscopy	12
1.3. Biological Luminescence Imaging	16
1.3.1. Fluorescence Imaging	17
1.3.2. Phosphorescence	19
1.3.3. Oxygen Sensing	21
1.4. Oxygen-Sensing Difluoroboron β-Diketonates	27
1.4.1. Discovery	27
1.4.2. Polymer Effects & Fabrication	28
1.4.3. Heavy-Atom Substitution & Imaging.....	31
1.5. Goals of this Research	33
1.6. References	35

Chapter 2: Tailoring Oxygen Sensitivity with Halide Substitution in Difluoroboron Dibenzoylethane Polylactide

2.1. Introduction	47
2.2. Results & Discussion	48

2.2.1. Synthesis.....	48
2.2.2. Optical Properties in Solution	50
2.2.3. Optical Properties of Films.....	52
2.2.4. Oxygen Sensitivity	57
2.2.5. Photostability	62
2.2.6. Conclusion.....	65
2.3. Experimental Section.....	67
2.3.1. Materials.....	67
2.3.2. Methods.....	67
2.4. Acknowledgements	72
2.5. References	72

Chapter 3: Difluoroboron Naphthyl Phenyl β -Diketonate-Polylactide Materials

3.1. Introduction.....	78
3.2. Results & Discussion.....	79
3.2.1. Synthesis.....	79
3.2.2. Optical Properties in Solution	81
3.2.3. Computational Studies	84
3.2.4. Optical Properties as Films.....	85
3.2.5. Iodide-Substituted BF ₂ nbm(I)PLA.....	89
3.2.6. Nanoparticles.....	91
3.2.7. Conclusion.....	94
3.3. Experimental Section	95
3.3.1. Materials.....	95
3.3.2. Methods	95
3.4. Acknowledgements.....	104
3.5. References	104

Chapter 4: Difluoroboron Dinaphthoymethane Polylactide

4.1. Introduction.....	108
4.2. Results & Discussion.....	109

4.2.1. Synthesis.....	109
4.2.2. Optical Properties in Solution	111
4.2.3. Optical Properties as Films.....	112
4.2.4. Nanoparticles.....	120
4.2.5. Conclusion.....	123
4.3. Experimental Section	124
4.3.1. Materials.....	124
4.3.2. Methods	124
4.4. Acknowledgements.....	130
4.5. References	131

Chapter 5: Difluoroboron Thienyl Phenyl β -Diketonate Polylactide

5.1. Introduction.....	134
5.2. Results & Discussion.....	135
5.2.1. Synthesis.....	135
5.2.2. Optical Properties in Solution	138
5.2.3. Optical Properties as Films.....	140
5.2.4. Nanoparticles.....	143
5.2.5. Conclusion.....	146
5.3. Experimental Section	147
5.3.1. Materials.....	147
5.3.2. Methods	147
5.4. Acknowledgements.....	153
5.5. References	153

Chapter 6: Difluoroboron β -Diketonate PLA-PEG Materials as Full-Color Luminescent Nanoparticles

6.1. Introduction.....	158
6.2. Results & Discussion.....	159
6.2.1. Synthesis.....	159
6.2.2. Nanoparticles.....	162

6.2.3. Fluorescence	163
6.2.4. Phosphorescence	164
6.2.5. Stability	169
6.2.6. Conclusion	171
6.3. Experimental Section	172
6.3.1. Materials	172
6.3.2. Methods	172
6.4. Acknowledgements	179
6.5. References	179

Chapter 7: Oxygen Sensing Capabilities and Performance of Difluoroboron β -Diketonate PLA Materials

7.1. Introduction	186
7.2. Results & Discussion	187
7.2.1. Photostability	187
7.2.2. Camera-Based Oxygen Sensing via Lifetime	189
7.2.3. RGB Camera Imaging	192
7.2.4. RGB Wound Hypoxia Imaging	195
7.2.5. Cell Imaging	198
7.2.6. Tumor Imaging	200
7.2.7. Conclusion	204
7.3. Experimental Section	204
7.3.1. Materials	204
7.3.2. Methods	204
7.4. Acknowledgements	207
7.5. References	208

Chapter 8: Future Directions

8.1. Introduction	212
8.2. Ongoing Research	212
8.2.1. Folate-Conjugated Nanoparticles	212

8.2.2. Optimization of Dyes for Camera Techniques.....	214
8.2.3. Biphenyl-Derived Dyes.....	217
8.2.4. Dyes with a Single Aromatic Unit	219
8.2.5. Calculations for Screening Red-Shifted Difluoroboron β -Diketonates	223
8.2.6. Dimethylamino-Substituted Dyes	226
8.3. Conclusion	228
8.4. Acknowledgements	229
8.5. References	229
Appendix A.....	232
Appendix B.....	236
Appendix C.....	242
Appendix D.....	248
Appendix E	254
Appendix F.....	267

Acknowledgements

Throughout my graduate career at the University of Virginia, I have had the support and guidance of many individuals. First of all, I need to thank my research advisor, Professor Cassandra L. Fraser. Her thoughtfulness for science and her “hawk-eye” attention of detail rarely fails. I’m thankful for the opportunity to learn and under her guidance, but also for the freedom to explore molecules of my own design. Also through grants, she has provided the lab with instrumentation and capitol to do high-quality science.

In these 5 years, I’ve had the opportunity to work with fantastic lab mates. My first mentor, Tiandong Liu, would answer all my annoying questions and look at my TLCs when I had no idea what was going on. His comment on everything was, “Just put it through a column,” which I quickly stopped doing, but I appreciate his help in my earlier years. Also, the biggest thanks to my fellow graduate students, Dr. William Morris and Tristan Butler. Our conversations over coffee every morning, or a celebratory beer, about boron dyes, science, politics or whatever else in life always provided the needed answers, distractions or stress relief. Big thanks to Alexander Mathew, who design the camera. I think it opened a lot of opportunities for our group at UVa. I want to thank the undergraduates, Ziyi, Caroline and Maggie, I’ve “mentored” through the years. I was lucky enough to get super smart, goal-driven students who contributed considerably. Ziyi’s inadvertent skill was helpful when things rarely worked, and her weird plum candies were tasty. Caroline is one of the hardest workers I know, and there is no doubt that she will go on to accomplish whatever she sets her mind to, and probably do some gymnastics flips while doing it. Maggie’s curiosity and appetite for science matches her ability to eat pasta (she eats pasta really quickly). There is no doubt that her ambition for good science will continue as she heads towards graduate career.

Big thanks to the collaborators throughout the years, Dr. Gregory Palamer at Duke, Dr. Carl. O. Trindle at UVa, and Dr. James N. Demas at UVa. Also to Dr. Shayn M. Peirce in Biomedical Engineering. Her willingness to commit students to do experiments will undoubtedly way the ground work for advancing our materials into new fields and applications. It has been exciting to see the other side of my work expand beyond the round-bottom flask.

Also, the staff in Chemistry Department have been really great. There was always a pile of old TLC plates on the floor of my bench, and I always meant to pick it up, but Joseph would always beat me to it, so thanks Joseph. Thanks to Dr. Jeff Elena for managing the NMR facility. Danny at the stockroom is incredible at his job, and Michael is always happy to help. Thanks to the building staff, Eddie, Jerry and Larry, for helping us relocate the lab. And thanks to the administrative staff, Susie and Cindy, for assisting with my silly questions and the undergraduate stuff.

I need to thank to thank my friends and family. Thanks to my roommate, Kim, for living with me, and for letting me take Deputy for runs. Last but not least, big thanks to my parents for supporting and loving me unconditionally. You guys have been the best. I promise I'll get that airbag recall for my car taken care of after the defense.

Dedication

This thesis is dedicated to my sister, Katie DeRosa.

“Why Do I Run?
The aches the pains,
The pouring rain,
Up at the crack of dawn,
The gasping breathes,
The Glory,
I run because I love it.”

-Katie DeRosa

Your life will inspire me forever.



(Katie, Greater Clarksburg 10K, 1998; 49:16)

List of Tables

Table 1.1. Optical Properties of Near-IR Emitting Organic Fluorophores in Water	19
Table 1.2. Optical Properties of Oxygen Sensitive Phosphors	27
Table 2.1. Polymer Molecular Weight Characterization.....	50
Table 2.2 Optical Properties of Boron Dye Initiators and Polymers in CH ₂ Cl ₂	51
Table 2.3. Optical Properties of Solution-Cast Films	52
Table 2.4. Lifetime Oxygen Sensitivity of BF ₂ dbm(X)PLA Films	59
Table 2.5. Ratiometric Oxygen Sensitivity of BF ₂ dbm(X)PLA Films	61
Table 3.1. Absorption and Emission Data for Boron Initiators and Representative Polymer Samples in CH ₂ Cl ₂	82
Table 3.2. Luminescence Data for Films made from Boron Polymers of Different Molecular Weights	86
Table 3.3. Optical Properties of Polymer Films.....	90
Table 3.4. Optical Properties of Nanoparticles	93
Table 4.1. Polymer Synthesis and Molecular Weight Characterization	111
Table 4.2. Optical Properties of Boron Initiators and Polymers in CH ₂ Cl ₂ Solution	112
Table 4.3. Optical Properties of Boron Polymer Films.....	113
Table 4.4. Nanoparticle Characterization.....	121
Table 5.1. Polymer Synthesis and Molecular Weight Characterization	138
Table 5.2. Optical Properties of Boron Initiators and Polymers in CH ₂ Cl ₂ Solution	140
Table 5.3. Optical Properties of Polymers as CH ₂ Cl ₂ Cast Films.....	141
Table 5.4. BF ₂ tbm(X)PLA Nanoparticle Properties	144
Table 6.1. Nanoparticle Properties.....	166
Table 7.1. Optical Properties of BF ₂ bdkPLA Nanoparticles.	166
Table 6.1. Nanoparticle Properties.....	187

List of Figures

Figure 1.1. Design of Metal-Centered Polymers (MCPs).....	3
Figure 1.2. Polymerization Mechanisms.....	4
Figure 1.3. Polymer Molecular Weight Characterization	6
Figure 1.4. Chemical Structures of Monomers (top) and their Associated Polymers (below).	7
Figure 1.5. Polymer Composition Versus Matrix Effects.....	8
Figure 1.6. Design Strategy for Polymeric Nanoparticles	9
Figure 1.7. Polyester-PEG Nanoparticles Used in Bioimaging and Drug Delivery	10
Figure 1.8. Jablonski Diagram of Luminescence Transitions.....	11
Figure 1.9. Chemical Structures of Xanthene Dyes with Oxygen and Bromide Heavy-Atom Modifications Influencing Optical Properties.....	12
Figure 1.10. Absorbance and Emission Spectra of Difluoroboron Dinaphthoylmethane in Methylene Chloride (1×10^{-5} M)	14
Figure 1.11. Lifetime Measurements	16
Figure 1.12. Multiplexed Fluorescence Imaging	17
Figure 1.13. Near-IR Emitting Molecules	19
Figure 1.14. Example of Phosphorescence Lifetime Imaging Microscopy (PLIM)	21
Figure 1.15. Compounds with Oxygen Sensitive Phosphorescence	23
Figure 1.16. Ratiometric O ₂ Sensing Nanoprobes	24
Figure 1.17. Discovery of Room-Temperature Phosphorescence from Difluoroboron Dibenzoylmethane-PLA	28
Figure 1.18. Polymer Molecular Weight Color Tuning of BF ₂ dbmPLA Materials	29
Figure 1.19. Nanoparticle Fabrication of BF ₂ dbmPLA (12kDa).....	30
Figure 1.20. Dual-emissive BF ₂ dbm(I)PLA Nanoparticles	31
Figure 1.21. Dye-Polymer Materials Design Strategy	32
Figure 1.22. Structure and Design of Difluoroboron β -Diketonate Materials	34
Figure 1.23. Method for Preparing and Optimizing Boron Dyes as Oxygen Sensing Materials..	35
Figure 2.1. Difluoroboron Dibenzoylmethane-Poly(lactic acid) and Halide-Substituted Derivatives	47

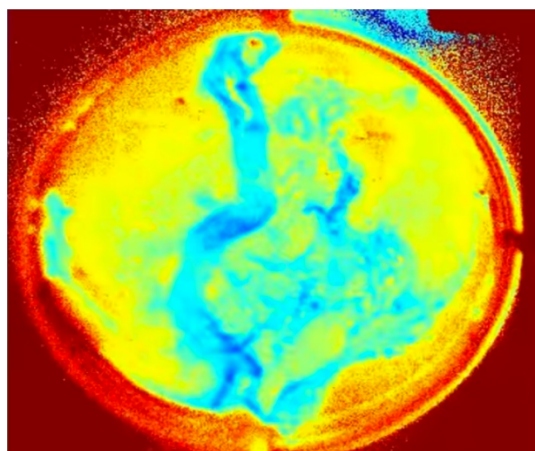
Figure 2.2. Molecular Weight and Fluorescence; Total Emission of BF ₂ dbm(F)PLA (12) and BF ₂ dbm(Br)PLA (14) in Air ($\lambda_{\text{ex}} = 369 \text{ nm}$)	53
Figure 2.3. Phosphorescence of High Molecular Weight BF ₂ dbm(X)PLA Polymer Films (11b-15b)	54
Figure 2.4. Images and Total Emission Spectra of Low Molecular Weight Polymer Films (11a-15a) Under Air and Nitrogen ($\lambda_{\text{ex}} = 369 \text{ nm}$)	56
Figure 2.5. Oxygen Sensitive BF ₂ dbm(X)PLA Polymers Suitable for Ratiometric Sensing	62
Figure 2.6. Influence of the Halide Substituent on the Photostability of BF ₂ dbm(X)PLA Spin-Cast Films	63
Figure 2.7. Total Emission of BF ₂ dbm(I)PLA Spin-Cast Films Under Air and Nitrogen Before (0h) and After 18 hour UV Exposure in Air (18h)	65
Figure 3.1. Design of Difluoroboron Naphthyl-Phenyl β -Diketonate Polymer Materials	78
Figure 3.2. Nomenclature and Numbering of Difluoroboron Naphthyl Phenyl β -Diketonate-Polylactide Materials with and Without Bromide	79
Figure 3.3. Absorption Spectra for Boron Initiators in Dilute CH ₂ Cl ₂ solutions (Abs < 0.1)	81
Figure 3.4. Boron Dye Initiators 5-8 in CH ₂ Cl ₂ Showing Emission Colors.....	82
Figure 3.5. Molecular Orbital Diagrams for Compounds 5-8	84
Figure 3.6. Heavy-Atom Placement and Oxygen-Sensing Response of Difluoroboron Naphthyl-Phenyl β -Diketonate PLA Polymers.....	88
Figure 3.7. Total Emission Spectra Showing Relative Fluorescence and Phosphorescence Intensities for Films of BF ₂ nbm(Br)PLA (10a-d) Under N ₂	89
Figure 3.8. Optical Properties of Polymer Films	91
Figure 3.9. I-NP Oxygen Calibration	94
Figure 4.1. Chemical Structure of Difluoroboron Dinaphthoylmethane Polylactide	108
Figure 4.2. Effects of Dye Loading on Fluorescence.	114
Figure 4.3. Temperature Dependent Delayed Emission of BF ₂ dnm(X)PLA	116
Figure 4.4. Images and Total Emission Spectra of Boron Polymers BF ₂ dnmPLA (7b), BF ₂ dnm(Br)PLA (8b), and BF ₂ dnm(I)PLA(9b) in Air and N ₂	118
Figure 4.5. Fluorescence to Phosphorescence Ratio Tuning for BF ₂ dnm(I)PLA/PLA Blends at Different Dye Loadings	120
Figure 4.6. Boron Nanoparticles.....	122
Figure 4.7. Boron Nanoparticle Oxygen Sensing.....	123

Figure 5.1. Chemical Structure of Difluoroboron Thienyl Phenyl β -Diketonate Poly lactides .	136
Figure 5.2. Calculated structure and HOMO/LUMO orbitals of BF ₂ tbm(I)OMe.....	141
Figure 5.3. Total Emission of BF ₂ tbm(X)PLA (7-9) Films in Air and N ₂	142
Figure 5.4. Total Emission of BF ₂ tbm(I)PLA (9) Blended with PLA (~1.0% dye) as Toluene-Cast Films in Air and N ₂	143
Figure 5.5. Optical Properties of Thienyl Boron Dye-polymers Fabricated as Nanoparticles ...	146
Figure 5.6. Oxygen Calibration of BF ₂ tbm(I)PLA/PLA (INP*) Nanoparticles.	147
Figure 6.1. Boron dyes for polymer initiation (initiators) or post polymerization modification (couplers)	160
Figure 6.2. Dye-Polymer Conjugation.....	162
Figure 6.3. Nanoparticle Fabrication	164
Figure 6.4. Images and total emission spectra of 1-4NP (solid lines) and 1-4scNP (dashed lines) in air	167
Figure 6.5. Images and total emission of 1-3NP	169
Figure 7.1. Structures and Photostability of BF ₂ bdkPLA Nanoparticles.....	189
Figure 7.2. Schematic of the System Setup (left) and Data Processing for Real-Time Rapid Lifetime Determination Imaging (right)	192
Figure 7.3. Lifetime Imaging with BF ₂ nbmPLA	193
Figure 7.4. RGB Camera Channels.....	194
Figure 7.5. Dual-Mode Oxygen Sensing with BF ₂ nbm(Br)PLA Nanoparticles.....	195
Figure 7.6. Optical Properties of BF ₂ nbm(I)PLA	197
Figure 7.7. In Vivo Camera Imaging with BF ₂ nbm(I)PLA Nanoparticles.....	197
Figure 7.8. Wound oxygenation and healing time course monitored by BF ₂ nbm(I)PLA Nanoparticles	198
Figure 7.9. Cellular Imaging with BF ₂ dnm(I)PLA Nanoparticles.....	200
Figure 7.10. Biodistribution of RED-NPs.....	202
Figure 7.11. IVIS Imaging of Harvested Organs	203
Figure 7.12. BF ₂ nbm(I)PLLA-PEG Nanoparticle Imaging and Radiation Therapy Efficacy in Mouse EO771	204
Figure 8.1. Fabrication and Optical Properties of Folate-Conjugated Nanoparticles.....	215
Figure 8.2. Design Strategy for Synthesizing Dye Candidates with Optimal RGB Properties. .	216

Figure 8.3. Examples of Dual-Emissive Dyes with Emission Peaks Optimal for RGB Imaging	217
Figure 8.4. Thermally-Activated Delayed Fluorescence Properties of BF ₂ dbpm.	219
Figure 8.5. Optical Properties of Difluoroboron β -Diketonates with a Single Aromatic Unit in PLA Blends (2% by weight).	222
Figure 8.6. Frontier Molecular Orbitals of Difluoroboron β -Diketonates with a Single Aromatic Unit. A) HOMO/LUMO diagrams and B) energy levels of participating orbitals.	223
Figure 8.7. Calculated Ground-State Geometries of Compounds 3 (A) and 4 (B).	223
Figure 8.8. Bandgap Engineering Strategy Involving Raising the HOMO Energy (left) or Lowering the LUMO Energy (right) versus the Unsubstituted DBM Dye (center).	225
Figure 8.9. Bandgap Screening of Dyes	226
Figure 8.10. Selected Dyes Identified in Computational Screening with Promising Features for Future Investigation	227
Figure 8.11. Dimethylamino-Substituted Dyes.	228
Figure 8.12. Environment-Sensitive Emission from Difluoroboron β -Diketonates.	229

Chapter 1:

Introduction to Polymers, Luminescence,
and Optical Bioimaging



1. Introduction

Advancing the design of functional oxygen-sensing biomaterials relies on many fields, including macromolecular chemistry, optical spectroscopy and fluorophore design. In a well-developed field such as oxygen sensing, awareness of current analytical practices commonly employed is required. This introductory chapter should sufficiently provide the needed background that this research is built upon.

1.1. Macromolecular Chemistry

Polymeric materials find wide application, from biomaterials and drug delivery,¹⁻⁶ to optoelectronic devices.⁷⁻¹⁰ In medicine, polymers have advantages over small molecules, as molecular size plays an important role of how drugs and materials interact with cells, tissues and other forms of biological matter. Molecules under the 1 kDa threshold are passively taken up by cells given their small size.¹¹ In contrast, larger molecules, well above this 1 kDa threshold (i.e. polymers), often interact with cells through active-uptake mechanisms. Polymers and macro-units greater than 1 kDa can be used in a plethora of ways as tailored materials for biological applications.¹²⁻¹⁵ For example, when Zheng and coworkers modified an Iridium complex with a water soluble poly(vinyl pyrrolidone) (PVP), cell-uptake of the Iridium complex was prevented, and the dye would passively accumulate in tumors via enhanced permeation and retention.¹⁶ When new interactions through side chains, end groups and main chain composition are introduced, properties such as increased solubility, tailored affinities, greater drug encapsulation, or slower polymer degradation can be achieved.^{17,18}

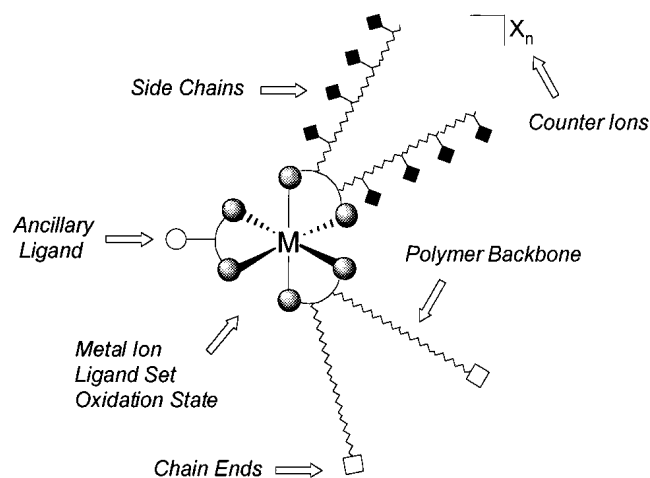


Figure 1.1. Design of Metal-Centered Polymers (MCPs). Image reproduced with permission from Corbin et al., *Biomacromolecules*, **2001**, 2, 223-232. Copyright American Chemical Society 2001.¹⁷

1.1.1. Polymer Synthesis & Characterization

Polymers are a sequence of repeating units.¹⁹ Preparation of polymers, known as polymerization, can be achieved by a chain-growth or step-growth mechanism. In chain-growth, monomers are added one at a time to an initiator.²⁰ For example, Kiessling and co-workers used a ring-opening metathesis polymerization (ROMP) to prepare polymers with an aliphatic backbone and succinimidyl side chains for later functionalization (i.e. fluorophore conjugation).²¹ In step-growth polymerizations, small monomers become shorter chains, and chains continuously merge together to form longer chains (i.e. $1 + 1 = 2$, then $2 + 2 = 4$, etc...). This is the common method to form semiconducting polymers with an aromatic backbone because it is compatible with Suzuki–Miyaura or Yamamoto cross-coupling reactions.^{22,23} For example, Chujo and coworkers recently prepared conjugated polymers with boron β -diiminate and fluorene moieties as multi-stimuli responsive materials for pH and aggregation.²⁴

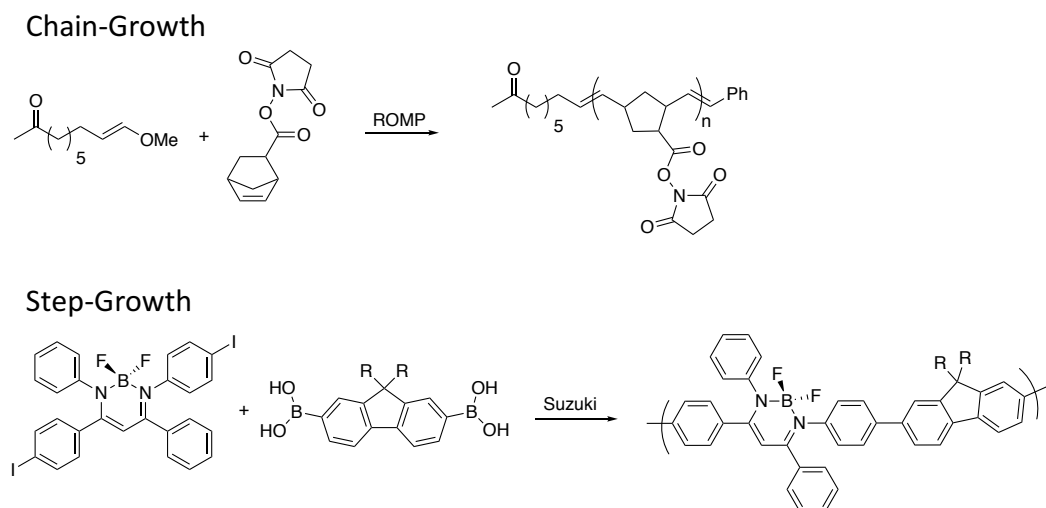


Figure 1.2. Polymerization Mechanisms. The chain-growth example is taken from Kiessling et al.,²¹ and step-growth polymerization is taken from Chujo et al.²⁴

To understand polymer synthesis, synthetic polymer features and properties are important. When polymers are synthesized a range of molecular weights are typically formed, given slow initiation versus propagation, termination and chain transfer side reactions. Rather than the laborious task of isolating a single molecular weight product, a range of molecular weights are collected. Polymer chemists use the average molecular weight (M_n) and the polydispersity (\mathcal{D}) to describe the final product population. Polymers are commonly characterized by gel-permeation chromatography (GPC). With GPC, important polymer characteristics, such as the number average molecular weight (M_n), weight average molecular weight (M_w) and polydispersity (\mathcal{D}), can be determined. In GPC, a polymer sample is separated by a gel column with porous beads that separate all the polymers in a sample by size. Small polymers get trapped in the beads more easily, and therefore take longer to traverse the column (Figure 1.2). This is demonstrated by the ring-opening polymerizations (ROP) of ϵ -caprolactone from BF_2dbmOH with different monomer loadings and reaction times to yield BF_2dbmPCL polymers with different molecular weights.²⁵ Larger polymers travel through the column more quickly, and have shorter elution times (i.e.

smaller elution volumes), and smaller polymers come after. A distribution of polymers can be visualized on a GPC trace, and each time slice of the trace refers to a specific molecular weight. Based on the elution time and detectors used, a molecular weight can be assigned to the slice. The concentration for each slice of the chromatogram is measured by the concentration detector (usually refractive index detector or UV detector). The molar masses based on elution volume (or time) can be inferred based on polymer standards, or alternatively, absolute molecular weights can be determined from the intensity of the scattered light (light-scattering detectors). The number average molecular weight (M_n) is calculated by taking the sum of all the polymers of a given molecular weight (M_i) over all molecular masses and dividing by the number (n_i) of polymers (Eq. 1.1). In the weighted average molecular weight (M_w), the M_i values are squared, preferentially giving a larger value to larger polymers (Eq. 1.2). From these two measurements, the polydispersity M_w/M_n can be determined (Eq. 1.3). Because M_w is always equal to (monodisperse sample) or greater value than M_n , the \bar{D} will always be greater than 1.

$$M_n = \frac{\sum n_i M_i}{\sum n_i} \quad \text{Eq. 1.1}$$

$$M_w = \frac{\sum n_i M_i^2}{\sum n_i M_i} \quad \text{Eq. 1.2}$$

$$\bar{D} = M_w/M_n \quad \text{Eq. 1.3}$$

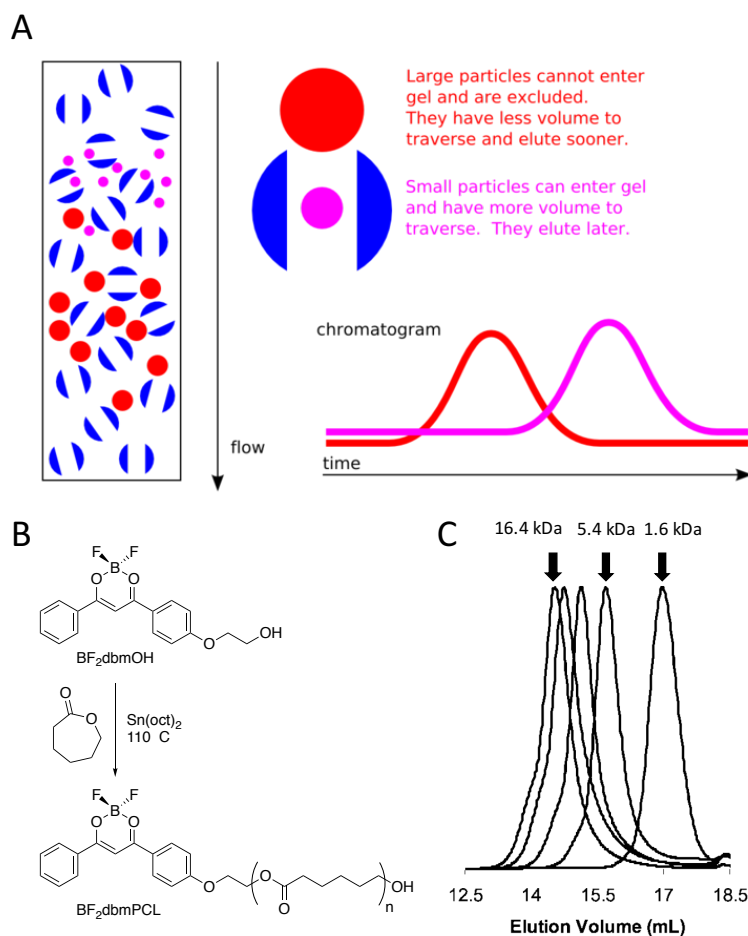


Figure 1.3. Polymer Molecular Weight Characterization. A) Schematic of gel-permeation chromatography (GPC) (Reproduced from Wyatt ©). B) Ring-opening polymerization of poly(ϵ -caprolactone) from BF₂dbmOH to yield BF₂dbmPCL. C) GPC differential refractive index (dRI) traces of BF₂dbmPCL polymers of variable MWs. Reproduced with permission from Zhang et al., *Macromolecules*, **2009**, 42, 3092–3097.²⁵ Copyright American Chemical Society.

These GPC techniques can be used in combination with proton nuclear magnetic resonance (¹H NMR) as a second form of molecular weight determination based on integrations and comparative end-group analysis, but ¹H NMR spectra cannot give information about polydispersity.

Polydispersity (\bar{D}) is a measurement of the polymer uniformity. Low \bar{D} (<1.3) is indicative of a controlled polymerization, as the weighted average is similar to the number average. This is most easily achieved via chain-growth polymerizations, as monomers are added to a chain one at a time. While some reports show good control over polydispersity in step-growth polymerizations,

it is generally considered a less-controlled reaction. Ideally, chains would grow at similar rates to achieve uniform molecular weights from the polymers, but chains of variable sized can recombine randomly (i.e. 1+4 or 5+9), and a large range on molecular weights is observed ($\bar{M}_w/\bar{M}_n > 1.3$). For reproducible and well-control products in situations where molecular weight is vital to material properties, step-growth polymerization is the preferred method. For biomedical applications, polyester biomaterials are often prepared by ring-opening polymerization of lactones, as shown in Figure 1.4.^{26–29} Examples of commonly used polymers are poly(ϵ -caprolactone) (PCL) and poly(lactic-acid) (PLA), synthesized from ϵ -caprolactone and DL-lactide, respectively. Polyesters are commonly used because they are bioderived, biodegradable, and biocompatible. Furthermore, desired properties, such as polymer degradability, can be controlled with polymer composition. Alternatively, cyclic ethers, such as ethylene oxide, can form polyethers such as poly(ethylene oxide) (PEO), also known as poly(ethylene glycol) (PEG), that introduce different properties (e.g. water solubility). However, polyethers do not degrade as readily as polyesters.

Polyesters are intensely investigated for biomedical applications because of their degradability.^{30–32} In the solid state, these polymers organize based on their molecular structure or thermal history.^{32,33} The polymer PCL is very crystalline, and organizes in dense crystal lattices (Figure 1.5). Between the dense lattices, there are large voids, referred to as free volume. In

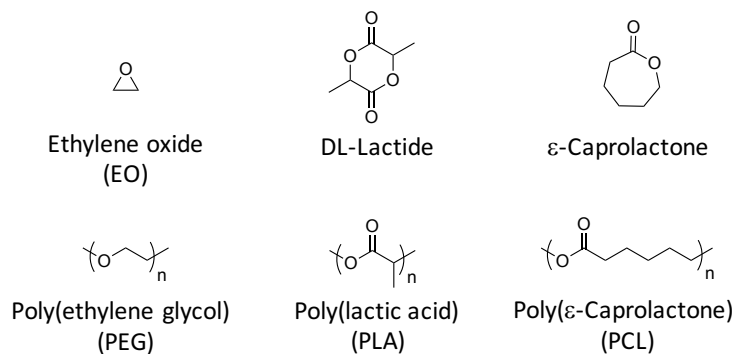


Figure 1.4. Chemical structures of monomers (top) and their associated polymers (below).

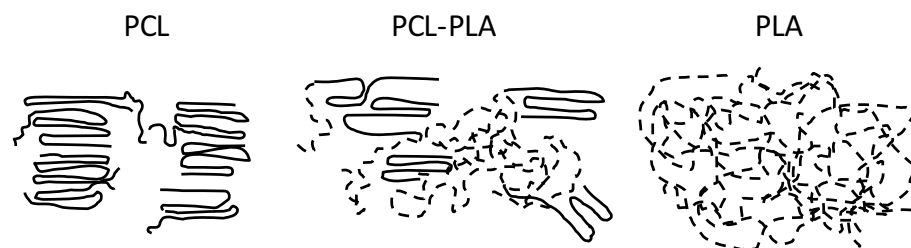


Figure 1.5. Polymer Composition Versus Matrix Effects (Crystalline = solid line; Amorphous = dashed lines). Adapted with permission from Zhang et al. *Macromolecules* **2009**, 42, 3162–3169.³⁴ Copyright the American Chemical Society 2009.

contrast, PLA is amorphous (no order), or sometimes semi-crystalline (some order) based on the thermal history. This means PLA lacks the high degree of organization of PCL, with a decrease in free volume in the polymer matrix. These traits define differences in stability in aqueous environments, as PLA degrades more quickly than PCL.²⁷ As a result, PLA polymers are used for applications that require shorter aqueous lifetimes, and PCL polymers are used for prolonged biomedical applications.

1.1.2. Polymers & Nanoscience

Nanoparticles (diameter = 20 - 250 nm) are well under the size ranges needed for enhanced permeation and retention (EPR) in tumors and for renal clearance.³⁵ The majority of polyester materials are completely insoluble in water, and therefore, fabrication of the materials as nanoparticles, or nanoaggregates, can be a means towards biomedical applications.^{36,37} Polymer nanoparticles often feature hydrophobic and hydrophilic components that self-assemble in water. Although purely hydrophobic polymers can also self-assemble in water, the hydrophobicity of these aggregates results in shorter circulation times.^{36,38} To address this, a water-soluble polymer, such as poly(ethylene glycol) (PEG), can be used for stealth properties (Figure 1.6).³⁹ The stealth

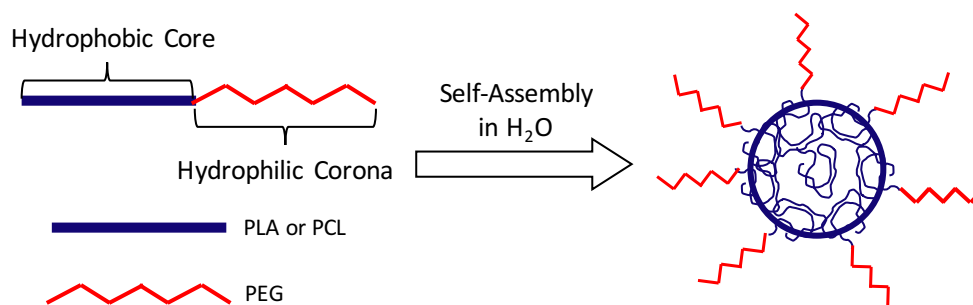


Figure 1.6. Design Strategy for Polymeric Nanoparticles.

properties rise from the nanoparticle avoiding the immune system and cell uptake, resulting in nanoparticle degradation. PEGylated materials have longer circulation times and passive tumor uptake by the enhanced permeation and retention (EPR) effect, given leaky vasculature and poor lymphatic drainage when the nanoparticles are injected intravenously.^{40–42}

Nanoparticle materials can be design for numerous applications, especially PLA-PEG and PCL-PEG block copolymer nanoparticles for drug delivery and imaging applications. For example, materials designed by Kwon et al., demonstrated the passive uptake of poly(ethylene glycol)-polyester assemblies in tumors.^{43–45} Poly(ethylene glycol)-poly(lactic acid) (PEG-PLA) micelles were used as drug nanocarriers for hydrophobic drugs (i.e. doxorubicin, curcumin), and similarly, more crystalline, and highly stable poly(ethylene glycol)-poly(ϵ -caprolactone) (PEG-PCL) micelles can be used as imaging agents when the lipophilic dye, 1,10-dioctadecyl tetramethyl indotricarbocyanine iodide is embedded in the polymer matrix.⁴⁶ Using these materials in succession (drug nanocarrier then imaging agent) allowed for controlled drug release and imaging.

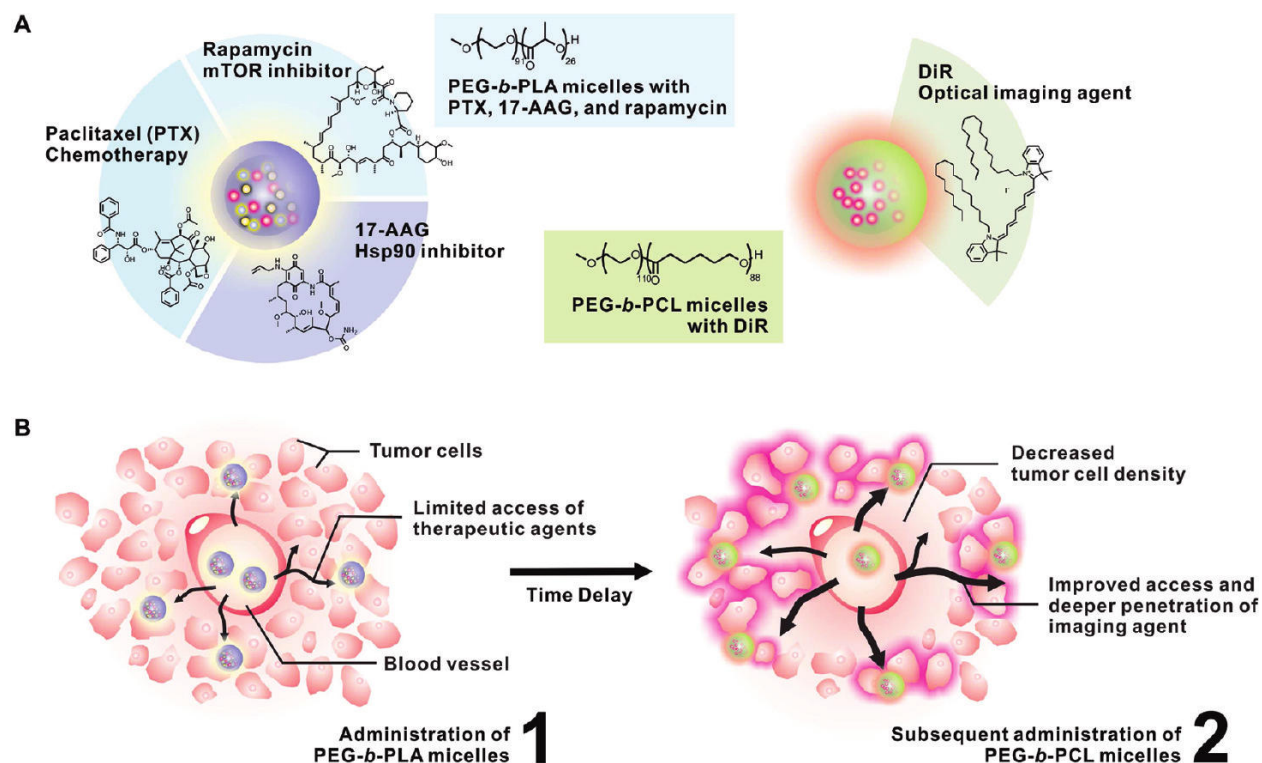


Figure 1.7. Polyester-PEG Nanoparticles Used in Bioimaging and Drug Delivery. A) The 3-in-1 PEG-*b*-PLA micelles containing PTX/17-AAG/RAPA and PEG-*b*-PCL micelles containing DiR-fluorophore. B) Schematic illustration of tumor-primed delivery of NIR optical imaging agent (DiR) by a tandem of PEG-*b*-PLA and PEG-*b*-PCL micelles. This figure was reproduced with permission from Kwon et al, *ACS Nano* **2011**, 5 (11), 8721–8729.⁴⁶ Copyright American Chemical Society 2011.

1.2. Introduction to Luminescence

Luminescence is broadly defined as energy emitted from a material or substance in the form of light. The development and optimization of luminescent materials can have broad implications. In a practical sense, luminescence technologies are essential for biological research and household electronic devices.⁴⁷ For example, 4',6-diamidino-2-phenylindole, or DAPI, is commonly used as a fluorescent contrast agent to tag DNA for cell imaging. Similarly, luminescent dyes have become used as the emitters in organic light emitting diodes (OLED) that activate upon electrical stimulation (electroluminescence). Therefore, new materials are desirable for brighter,

more efficient electronic displays or multifunctional, photoluminescent sensors for imaging technologies.^{6,48–52,7,53}

1.2.1. Molecular Luminescence

On a molecular level, luminescence originates from an electron relaxing from an excited state (S_n) to the ground state (S_0), resulting in the emission of a photon.⁴⁷ Luminescence can be further separated into two categories, fluorescence (F) and phosphorescence (P), and this depends on the nature of the excited state from which the electron originated (Figure 1.8.). In fluorescence, the electron in the excited state orbital is paired with a ground state electron (opposite spin).^{54,55} As a result, the relaxation to the ground state is spin allowed, occurring rapidly (nanoseconds). However, an excited state electron can undergo a process called intersystem crossing (ISC) to the triplet state, where the excited state electron “flips” to the same orientation of the ground state electron. Relaxation from this state is now spin forbidden, and therefore, much slower than fluorescence (microseconds or milliseconds).

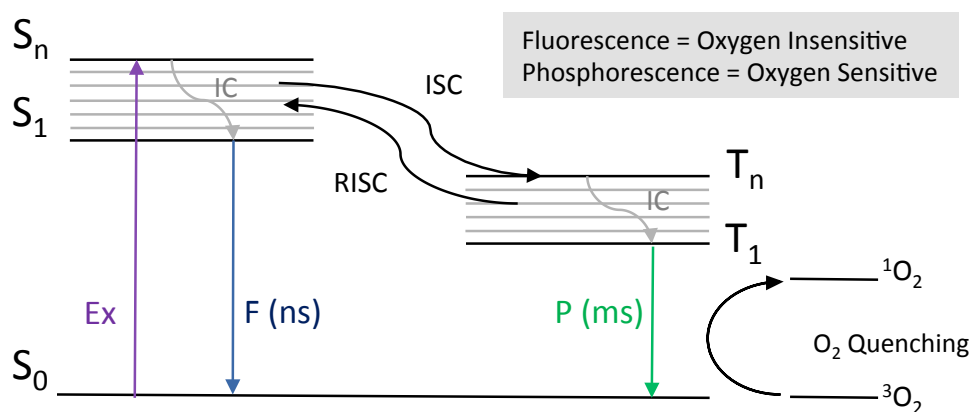


Figure 1.8. Jablonski Diagram of Luminescence Transitions.⁴⁷ S_0 = singlet ground state, S_n = singlet excited state, S_1 = lowest energy singlet excited state, Ex = excitation, IC = internal conversion, F = fluorescence, ISC = intersystem crossing, RISC = reverse intersystem crossing, T_n = triplet excited state, T_1 = lowest energy triplet excited state, P = phosphorescence.

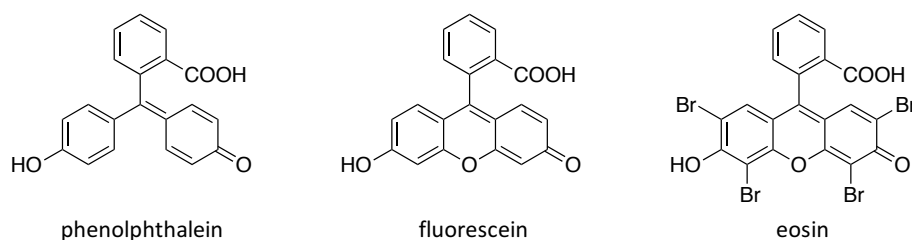


Figure 1.9. Chemical Structures of Xanthene Dyes with Oxygen and Bromide Heavy-Atom Modifications Influencing Optical Properties.

In some instances, electrons in the triplet excited state can back populate the singlet excited state, called reverse intersystem crossing (RISC). This is a thermally allowed process, and emission from this repopulated singlet state is called thermally activated delayed fluorescence (TADF).⁵⁶

To show how molecular structure influences these events, three xanthene dyes are shown for comparison (Figure 1.9).^{57,58} Phenolphthalein, a common pH indicator in general chemistry teaching labs, is completely non-fluorescent.^{59,60} However upon rigidifying the scaffold with a bridging oxygen atom, yielding fluorescein, bright green fluorescence is observed.⁵⁰ Fluorescein can be modified further with heavy atoms (bromide) to yield eosin, a common phosphorescent singlet oxygen generator. Heavy atoms, such as bromide, can be used to enhance the rate of ISC to increase the relative phosphorescence intensity, yielding new opportunities for photosensitization of oxygen to form reactive oxygen species (ROS) for targeted therapy.^{61–63} Differences in luminescence efficiency, defined as quantum yield (Φ_F), lifetimes (τ), and absorption and emission wavelengths (λ), are key components to the applications and limitations of fluorophores. Fortunately, techniques for studying luminescence materials are clearly defined.

1.2.2. Optical Spectroscopy

Two instruments are primarily used to analyze the optical properties of fluorescent compounds; a UV/Vis spectrophotometer and a fluorescence spectrophotometer. A UV/Vis spectrophotometer is used to analyze the absorption spectrum, indicative of the electronic

transitions of the optical material from the ground state to the excited state. This instrument is fairly simple. Light of all wavelengths is shined through a sample and the transmitted light from the sample is compared to a reference cell (no analyte present). The loss of transmitted light due to the sample is the absorbance. With this instrument, important properties can be determined, such as the molar extinction coefficient (ϵ) and the absorbance maxima (λ_{abs}). The Beer-Lambert Law can be used (Eq. 1.4) to determine ϵ , where “M” is the molar concentration, “l” is the path length of the cuvette being used, and “Abs” is the measured absorbance intensity at the peak wavelength.⁶⁴

$$\text{Abs} = \epsilon[\text{M}][\text{l}] \quad \text{Eq. 1.4}$$

The molar extinction coefficient is a valuable piece of information to describe fluorophores, and therefore, is always reported for new materials. The absorbing ability (ϵ) and wavelength (λ_{abs}) of novel dyes will determine pragmatic utility for later functions.

While UV/Vis spectra monitor all the ground state to excited state transitions molecules undergo, a spectrofluorometer instrument is used to monitor the relaxation; electrons from the excited to the ground state. A spectrofluorometer consists of an excitation source, typically a broadly emitting light source such as xenon lamp, which is filtered through a light monochromator (excitation monochromator) to form a single beam of light to excite the sample. The beam passes through the sample and through a second monochromator (emission monochromator) sweeping through all relevant wavelengths before detection by a photomultiplier tube. The data is then processed and displayed by a computer. In a fluorescence spectrum, the excitation monochromator is set to a constant wavelength, while the emission monochromator changes to monitor changes in the intensity as a function of wavelength. As shown in Figure 1.10, the emission spectrum mirrors the absorption spectrum. The difference between the peak absorbance (λ_{abs}) and fluorescence

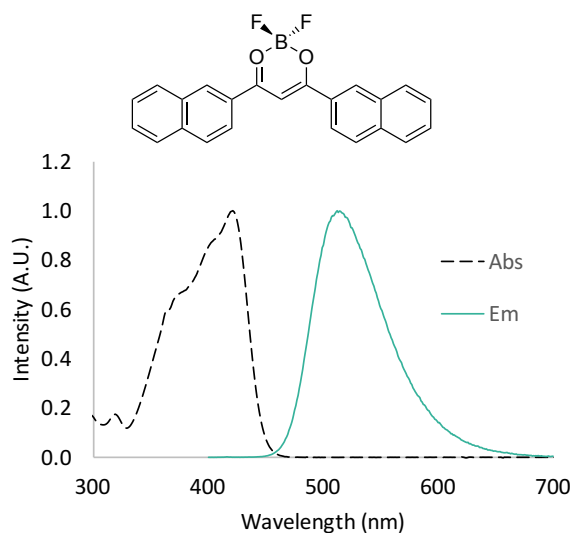


Figure 1.10. Absorbance and Emission Spectra of Difluoroboron Dinaphthoylemethane in Methylene Chloride (1×10^{-5} M).⁶⁵

emission (λ_f) is called the Stokes shift. If necessary, an excitation spectrum can be performed as well. In this case, the emission monochromator is set to a single wavelength and the excitation monochromatic sweeps through relevant wavelengths to detect changes in fluorescence intensity based on the excitation wavelength. This spectrum is analogous to a UV/Vis absorption spectra, however, the excitation spectra will only detect emissive species. In contrast, an absorbance spectrum using a UV/Vis detects all ground to excited state transitions, however, not all transitions are emissive. Therefore, an excitation spectrum can be used to detect the transitions responsible for the emission spectrum.⁶⁶

The absorbance and emission spectra of a compound can be used to determine the quantum yield (Φ).⁴⁷ The quantum yield is a measurement of the photon efficiency of a molecule. This is performed by comparing the number of photons absorbed versus the number of photons emitted, relative to a standard—a common dye with a well-known and highly trusted quantum yield (e.g. quinine sulfate, anthracene, or Rhodamine G6).⁶⁷ The quantum yield is determined using Equation

1.5, where the quantum yield of sample is “Q,” and “Q_R” is the quantum yield of the reference, “I” is the integrated intensity under the fluorescence curve, “OD” refers to the optical density or absorbance at the excitation wavelength, and “n” is the refractive index of the solvent medium (note: in all cases, subscript “R” refers to properties of the reference standard compound).⁶⁷

$$Q = Q_R \frac{I}{I_R} \frac{OD_R}{OD} \frac{n^2}{n_R^2} \quad \text{Eq. 1.5}$$

Luminescence measurements performed by a fluorescence spectrophotometer can be classified into two main categories; steady-state and time-resolved. Thus far, only steady-state measurements (i.e. fluorescence spectrum, quantum yield) have been discussed. In steady-state, the sample is continuously illuminated with a beam of light and the emission spectrum is recorded as just described. In time-resolved spectroscopy, the light emitted is monitored when the excitation source is turned off. Determination of emission lifetimes is a time-resolved technique. Fluorescence (τ_F) and phosphorescence lifetime (τ_P) are defined as the average amount of time an electron remains in the respective excited state after excitation. Fluorescence lifetimes can be measured using time-correlated single photon counting (TCSPC). The sample is continuously pulsed with a laser (e.g. a 369 nm LED) and photons generated between the pulses originated from the sample (note: a reference is also taken of the laser to cancel out the lifetime of the excitation source). After many pulses, an average of photons per start-stop time is collected and integrated into a histogram curve, as shown in Figure 1.11. Photons collected after the pulse can be fit to a multi-exponential decay to determine the lifetime of all emissive species.

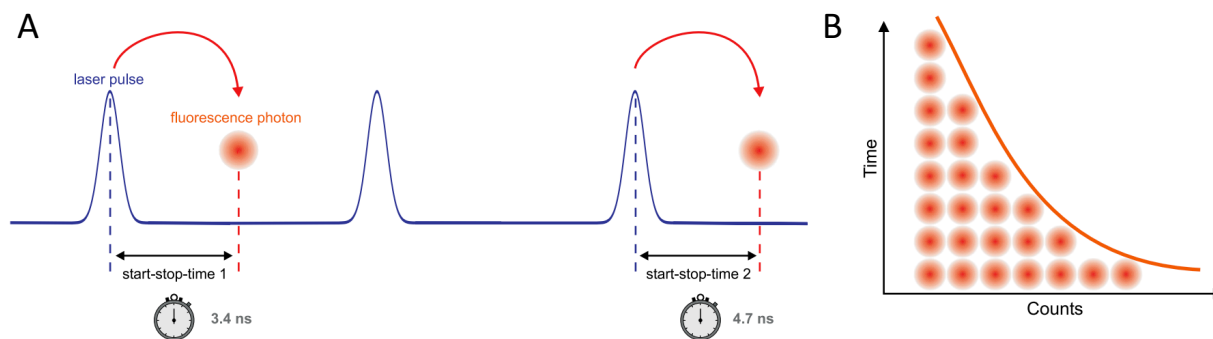


Figure 1.11. Lifetime Measurements. A) Measurement of start-stop times in time-resolved fluorescence measurements with TCSPC. B) Histogram of start-stop times in time-resolved fluorescence measurement with TCSPC. Images are reproduced from PicoQuant © Handbook of Fluorescence.⁶⁸

Phosphorescence can be observed via steady-state and time-resolved techniques. In steady-state (continuous illumination), the summation of the fluorescence and phosphorescence will be observed in the total emission spectra. By using a gated technique (time-resolved), the phosphorescence can be isolated. Because fluorescence is a short-lived phenomenon, by applying a gate longer than the time span of the fluorescence lifetime, the fluorescence can be filtered from the spectrum. In practice, the sample is illuminated with a flash lamp, and the emission intensity is recorded between the flashes as the emission monochromator changes the wavelength. All these measurements and properties are important considerations for designing novel materials, particularly for bioimaging.

1.3. Biological Luminescence Imaging

Many applications benefit from the development of multicolor luminescent materials, such as bioimaging and displays. Compared to other analytical techniques, such as multinuclear resonance imaging (MRI) and electrodes, fluorescence provides a cost-effective and non-invasive means to gather spatial and temporal information about biological systems.^{48,69,70}

1.3.1. Fluorescence Imaging

In cell imaging, fluorophores with distinct excitation and emission wavelengths can be used simultaneously, yet observed independently. This eliminates signal crosstalk, important for multiplexing in cell biology.^{71,72} For example, a DNA stain with blue fluorescence (4',6-diamidine-2'-phenylindole dihydrochloride; DAPI), an immunostain with green fluorescence (i.e. Alexa Fluor® 488), and an folate conjugated nanoparticle tag with red fluorescence (rhodamine B) were used to confirm cellular uptake and localization of the nanoparticles in folate receptor- α (FR α)-overexpressing ovarian cancer cells for *in vitro* imaging (Figure 1.12).⁷³ Bright luminescent dyes and materials provide excellent contrast against endogenous substances (e.g. fats). Furthermore, dyes can be designed to serve as bright tags, or as sensors for pH, O₂, polarity, viscosity, and other analytes and properties.

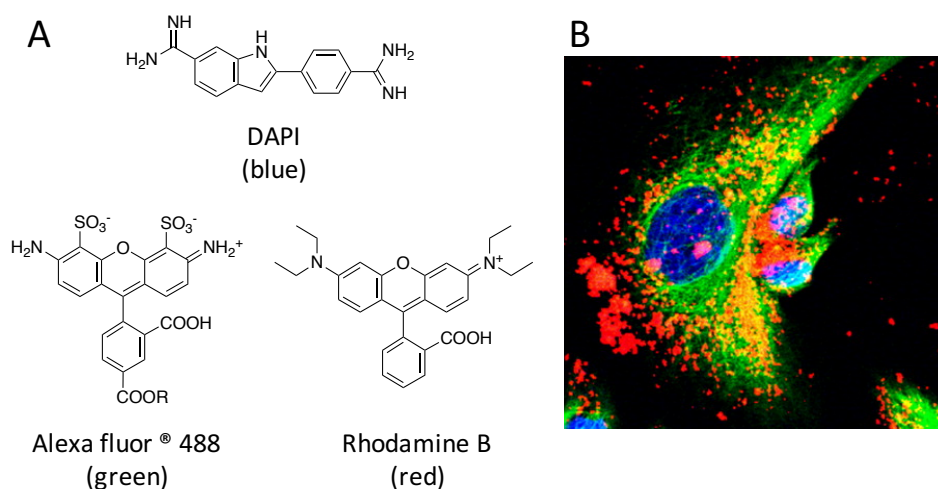


Figure 1.12. Multiplexed Fluorescence Imaging. A) Chemical structures of blue dye, 2-(4-Amidinophenyl)-1H-indole-6-carboxamide (DAPI), green dye, Alexa fluor® 488 (R = immune-tag reagent), and red dye, Rhodamine B. B) *In vitro* imaging of folate receptor- α (FR α)-overexpressing ovarian cancer cells; DAPI was used for nuclei staining, AlexaFlour 488 Goat Anti-Mouse IgG antibody (Molecular Probes) for staining α -tubulin, and Rhodamine B labeled folate conjugated nanoparticles were used to monitor cellular uptake of the nanoparticles. Images were reproduced with permission from the Singh et. al, *ACS Omega*, **2016**, *1*, 1114–1120.⁷⁴ Copyright. American Chemical Society 2016.

Cells, being transparent and non-fluorescent, are a simple model for imaging. For whole-body *in vivo* imaging, absorption and emission wavelength become more important due to many factors, such as light scattering, and autofluorescence.^{75,76} In particular, Rayleigh scattering by tissue and particles limits the wavelengths suitable for imaging, and the scope of fluorescence techniques altogether.⁷⁷⁻⁷⁹ The wavelength dependence of light scattering ($\sim\lambda^{-4}$) means that shorter wavelengths (i.e. blue fluorescence) are scattered more strongly than longer wavelengths (i.e. red fluorescence). Therefore, fluorophores with emission in the visible spectrum (400-700 nm) have compromised resolution and contrast with increasing tissue depths. Endogenous molecules with high absorptions within the visible range, such as oxy- and deoxy-hemoglobin in blood (HbO₂ and Hb; 400-600 nm), and water absorption in the infrared light region (900-1000 nm), limit useful wavelengths to a narrow range called the near-IR optical window (600-900 nm).⁸⁰ Molecules with emission within this window are very valuable as imaging agents. As shown in Figure 1.13 and Table 1.1, organic near-IR emitting fluorophores have been achieved, but have very low quantum yields, as seen with methylene blue (MB) and indocyanine green (ICG). Regardless of the quantum yield, these materials are still highly valuable for *in vivo* imaging, as wavelength is a high priority and emission, albeit dim, is still detectable.^{81,82} For example, a recently reported donor-acceptor compound, CH1055, with an astounding emission wavelength at 1055 nm could be visualized up to 4 mm deep and through the cranial bone to visualize fluorescence in the brain, even though the quantum yield is only 0.3% in H₂O. However, even these materials have limited utility. Fluorescence imaging is intrinsically limited due to light scattering and even near-IR emitting dyes can only visualize a maximum of 2 cm deep through tissue.^{76,83,84} Fluorescence imaging excels as a simple and inexpensive tool for surface applications, such as fluorescence guided surgery,^{85,86} and skin/wound care.^{87,88} High spatial resolution for full-body imaging, on the other hand, must

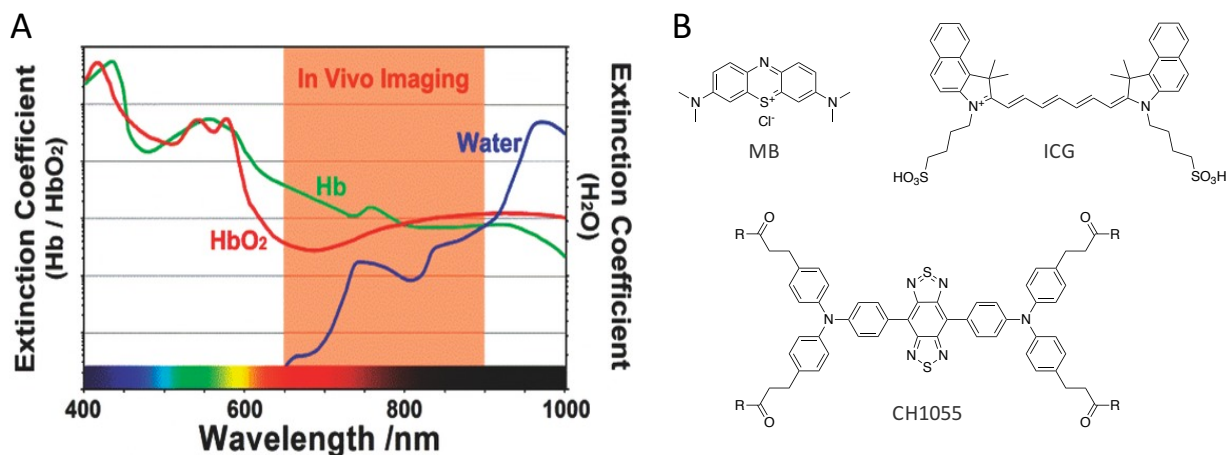


Figure 1.13. Near-IR Emitting Molecules. A) Optical Window for *in vivo* imaging. B) Examples of organic near-IR emitting fluorophores; Methylene blue (MB), Indocyanine green (ICG) and CH1055, where R = OH or poly(ethylene glycol) (PEG). Image in a was reproduced with permission from Shen et al., *Adv. Opt. Mater.* **2013**, *1*, 644-650.⁸⁹ Copyright Wiley 2013.

Table 1.1. Optical Properties of Near-IR Emitting Organic Fluorophores in Water

Sample	λ_{abs} (nm)	λ_{em} (nm)	Φ	Reference
MB ^a	665	686	0.093	81
ICG ^b	807	822	0.096	82
CH1055 ^c	808	1055	0.003	84

^aMethylene blue. ^bIndocyanine green. ^cStructure shown in Figure 1.13.

be accompanied by structural modalities such as magnetic resonance imaging (MRI), computed tomography with X-rays (CT) or ultrasound that bypass the light-scattering limitation.⁶⁹

1.3.2. Phosphorescence

Biological imaging using phosphorescent compounds has numerous advantages over conventional fluorescence techniques, and synthesis of phosphorescent compounds is well established. Conventional phosphors are lanthanide salts⁹⁰ or organometallic complexes^{55,76,91–95}. In organometallic complexes, phosphorescence is activated *via* a metal to ligand charge transfer (MLCT) mechanism, where d orbital electrons on the metal center populate a neighboring π^* orbital on the ligand upon excitation.⁹⁶ Therefore, electron rich metals, such as ruthenium (Ru),⁹⁷

iridium (Ir),⁹⁸ platinum (Pt),⁹⁹ palladium (Pd),¹⁰⁰ and europium (Eu)¹⁰¹ are combined with aromatic ligands with low-lying π^* states to facilitate efficient intersystem crossing (ISC).^{99,102} Furthermore, Lower et al. have explained phosphorescence enhancement via perturbation theory.⁵⁵

Shown in equation 1.6, where the perturbation factor (δ) describing singlet–triplet mixing by first-order spin–orbit coupling, can be enhanced via metal coordination (e.g. Ir, Pt, Eu, etc.). In Eq. 1.6, where Ψ^1 and Ψ^3 are the wavefunctions of singlet and triplet states, respectively, H_{so} is the spin–orbit Hamiltonian, and E_1 and E_3 are the energy levels for singlet and triplet states, the H_{so} is greater with heavier elements. Also, a smaller energy gap ($|E_1 - E_3|$ or ΔE_{ST}) corresponds to a larger δ ; that is, a high probability of electronic transition between singlet and triplet states.

$$\delta = \frac{\langle \psi^3 | H_{so} | \psi^1 \rangle}{|E_1 - E_3|} \quad \text{Eq. 1.6}$$

This method can also be applied to metal-free organic compounds. If the frontier molecular orbitals of an organic molecule are π - π^* character, similar to metal-ligand complexes that undergo intersystem crossing.¹⁰³ Because there is no heavy atom, the phosphorescence is typically very weak, but can be enhanced with a halide, such as bromide and iodide.⁹⁴ However, even with these requirements met (heavy atom and π^*), most organic molecules still have strict environmental requirements, such as low-temperature, rigid matrix and oxygen free environments to be observable.^{95,104,105,103,106,107} Therefore, it is rare that purely organic molecules exhibit room-temperature phosphorescence (RTP).^{108–110}

With well-defined and understood processes for preparing organometallic phosphors, much attention has been directed toward preparing alternatives to the conventional fluorophores for a variety of uses. Firstly, the relaxation from the triplet excited state to the singlet ground state must be accompanied by a spin flip of the electron.⁵⁴ As a result, phosphorescence lifetimes are magnitudes longer than fluorescence ($\tau_p = \mu\text{s}$ or ms , $\tau_f = \text{ns}$). Therefore, using time-resolved

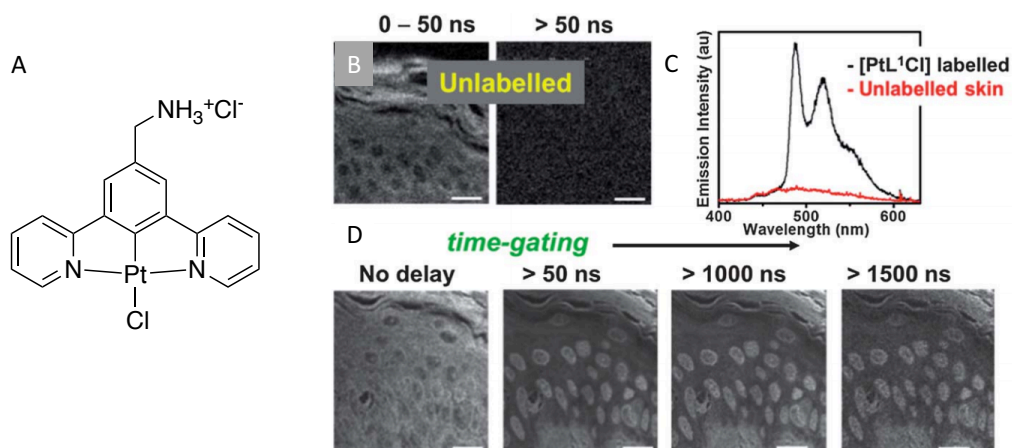


Figure 1.14. Example of Phosphorescence Lifetime Imaging Microscopy (PLIM). A) Chemical structure of long-lived metal complex; PtL^*Cl . B) Dye-labelled skin tissue section. Intensity image of unlabelled skin epidermis at early times (0–50 ns) and >50 ns. C) Total emission of unlabeled skin and the dye-labeled. D) intensity image of dye-labelled epidermis (rat) at progressively longer time delays. Images reproduced with permission from Baggaley et al., *Chem. Sci.*, **2014**, 5, 879–886.¹¹¹ Copyright. The Royal Society of Chemistry 2014.

techniques for biological imaging can remove autofluorescence emission altogether. This has been demonstrated by Baggaley et al., with a platinum organometallic complex, PtL_nCl , and a phosphorescence lifetime imaging (PLIM) technique, shown in Figure 1.14.¹¹¹ Autofluorescence of skin and tissues lasts only several nanoseconds, the same timescale of conventional fluorophores. Therefore, by using a probe with a microsecond long lifetime, a delay acquisition can be applied to remove the autofluorescence emission, and still observe emission from the probe.^{112–114} While this does not remove the effects of light scattering and the importance of wavelength, clearer images with higher spatial resolution can be achieved via time-resolved imaging with longer lived probes.

1.3.3. Oxygen Sensing

By far, the greatest application of phosphorescent dyes in imaging (Figure 1.15) is optical oxygen sensing.^{69,115} Oxygenation is a powerful indicator of health and healing, and the ability to quantify oxygen in a clinical setting would be an invaluable tool.^{69,116} Prof. Wolfbeis, a leading

academic, and entrepreneur (Presens ©) in the field of oxygen-sensing materials at the University of Regensburg, commented on the importance of oxygen, “[Humans] can survive about 1 month without food and 1 week without water supply, but usually not more than 10 minutes without air (O_2).”¹¹⁷ Deficits and excesses in oxygen levels are associated with medical conditions such as cancer, cardiac ischemia, and chronic wounds. Nevertheless, oxygen levels are rarely used for diagnosis in the clinical setting. For example, although it is well known that the oxygen level within wounds is directly related to healing potential, clinical monitoring of oxygen levels is not commonly practiced largely because the current tools are invasive, expensive, rely on indirect quantification of oxygenation, and do not provide oxygenation levels within the entire wound bed. Instead, clinical assessment of wound healing is largely qualitative and can be highly subjective.¹¹⁶ Therefore, phosphorescence imaging of oxygen may provide new and effective methods for imaging and diagnosis in the clinic.

Oxygen sensing is possible with phosphorescent materials because triplet oxygen exists naturally in the ground state, and upon collisional quenching with the excited-state triplet of the phosphor, the emission is quenched.¹¹⁸ Therefore, oxygen levels can be determined by comparing relative amounts of quenched phosphorescence. This is quantified using the Stern-Volmer equation for oxygen sensing (Eq. 1.7 and Eq. 1.8), where “ I_0 ” is the unquenched intensity, “ τ_0 ” is the unquenched lifetime, “ K_{SV} ” is the Stern-Volmer quenching constant, and “ O_2 ” is the concentration of oxygen (the quencher).¹¹⁵ The “ K_{SV} ” is defined as the initial unquenched lifetime of the phosphor (τ_0) times the diffusion rate constant of the quencher (O_2) through the dye impregnated matrix.⁴⁷

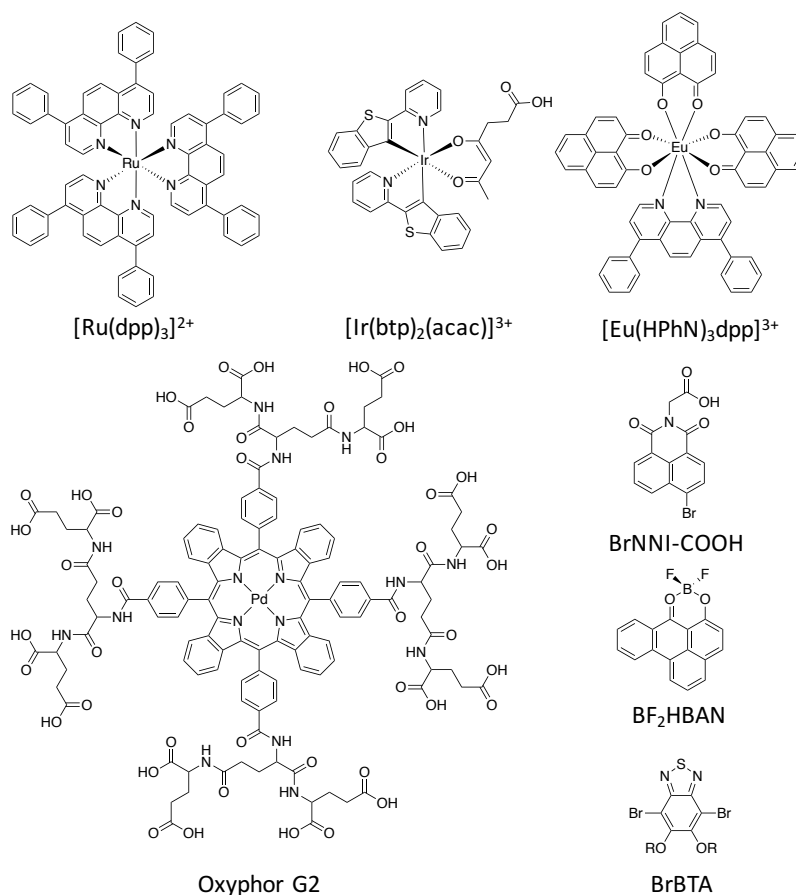


Figure. 1.15. Compounds with Oxygen Sensitive Phosphorescence. Compounds: [Ruthenium(II) tris(4, 7-diphenyl-1,10-phenanthroline)] dichloride; $[\text{Ru}(\text{dpp})_3]$,¹¹⁹ [Iridium (III) bis(2'-benzothienyl)-pyridinato-N,C) (acetylacetonate)] trichloride; $[\text{Ir}(\text{btp})_2(\text{acac})]$,¹²⁰ [Europium (III) tris-[9-(hydroxy-kO)-1H-phenaleno-1-onato-kO]-4,7-diphenyl-1,10-phenanthroline] trichloride; $\text{Eu}(\text{HPhN})_3\text{dpp}$, N- substituted carboxylate-bromo-naphthalene diimide; (BrNNI-COOH) ,¹²¹ Difluoroboron 6-hydroxybenz[de]anthracene-7-on; BF_2HBAN ,¹²² 4,7-dibromo-5,6-bis(tetradecyloxy) benzo[c] [1,2,5]thiadiazole ($\text{R} = -\text{C}_{14}\text{H}_{29}$); BrBTA .¹⁰⁹

$$\frac{I_0}{I} = \frac{\tau_0}{\tau} = 1 + K_{SV}[\text{O}_2] \quad \text{Eq. 1.7}$$

$$K_{SV} = k_q \tau_0 \quad \text{Eq. 1.8}$$

Quantifying oxygen via phosphorescence can be achieved by lifetime (time-resolved; τ) or intensity-based (steady-state; I) techniques. Lifetime sensing is often deemed more reliable because phosphorescence decay is independent of phosphor concentration, and the effects of light scattering and autofluorescence are minimized.^{77,123} Vinogradov and coworkers have developed

lifetime-based oxygen-sensing techniques with Oxyphor G2, a near-IR emitting O₂ sensor.^{100,123–125} Lifetime based imaging requires highly specialized imaging modalities. However, intensity-based measurements are more easily performed with common instrumentation (e.g. fluorescence microscopes or color cameras). Pure intensity based techniques are dependent on phosphor concentration. However, when phosphorescent dyes are combined with an O₂ non-sensitive fluorescent standard, ratiometric sensing can be achieved. The fluorescence intensity can be used to account for probe concentration (oxygen-insensitive), and the phosphorescence intensity is now indicative of the oxygen level. For example, Wolfbeis et al., developed cell permeable oxygen-sensing nanoprobe with Platinum(II) 5, 10, 15, 20-tetrakis(pentafluorophenyl)porphyrin (PtTFPP) as a phosphor and N-(5-carboxypentyl)-4-piperidino- 1,8-naphthalimide butyl ester as a fluorophore standard embedded into polystyrene beads (Figure 1.16). When the beads were functionalized with primary amine groups on the periphery, the nanoprobe is susceptible to cellular uptake and can monitor intracellular oxygen.

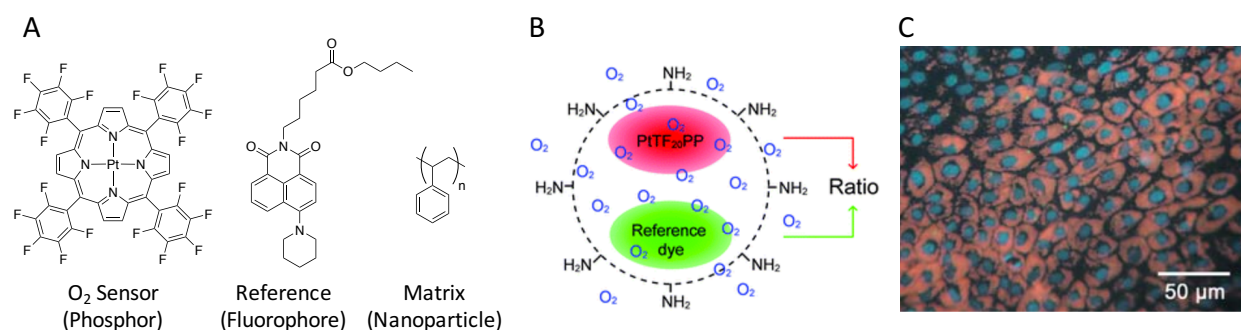


Figure 1.16. Ratiometric O₂ Sensing Nanoprobes. A) Materials in Nanoparobes including Platinum(II) 5, 10, 15, 20-tetrakis(pentafluorophenyl)porphyrin; (PtTFPP) (Phosphor), N-(5-carboxypentyl)-4-piperidino- 1,8-naphthalimide butyl ester (fluorophore), and the matrix is a polystyrene bead functionalized with amine groups to facilitate cell uptake. B) Schematic of the ratiometric nanoprobe. C) Optical oxygen sensing in normal rat kidney cells (NRK-52 E). Images were adapted from Wang et al., *Chem. Sci.* **2011**, 2, 901.¹²⁶ Copyright Royal Society of Chemistry 2011.

Though preparation of these multicomponent ratiometric O₂ sensor systems is facile, dye/media leaching, concentration heterogeneity, and differences in chemical photostabilities between the fluorophore and phosphor are major challenges. And the fact remains that optical oxygen sensing techniques have yet to become routine tools in the clinical setting to aid diagnosis to oxygen related conditions, such as cancer and wound treatment.^{127–130} Researchers have all but exhausted options using the prominent metal phosphors, including cyclometalated iridium, ruthenium bipyridines, and metal porphyrins (Figure 1.15), each with benefits and limitations. Iridium dyes are considered the brightest, with good oxygen sensitivity, but have poor photostability.⁹⁸ In contrast, ruthenium dyes are very photostable, but are less sensitive to oxygen (shorter τ_p), so the response to oxygen is less dynamic and often minimal.^{99,119} By far, the champions of oxygen sensitive metal phosphors are the platinum and palladium porphyrins, with NIR emission, good photostability, bright phosphorescence and good optical response to oxygen.¹¹⁵ The red-emitting PtTFPP derivative is the most commonly used commercial dye, and sells for \$1,210.00/g through Sigma Aldrich ® (Cas Number = 109781-47-7). Oxyphor G2, a commercial lifetime O₂ sensor is sold through Oxygen Enterprises, Ltd, a company founded by developers at the University of Pennsylvania, and sells for \$7,700.00/g. However, that price does not include the instrumentation needed to determine and read the dye lifetimes, and further investment is estimated to be ~\$20,000 or more. While these dyes are great options, more research is needed to bring down costs and usability for wide clinical utility. To enhance useability, Evans and coworkers at Harvard University are currently making progress with these materials via faster synthetic protocols, such as “clickable” side chains, or brighter dyes to reduce the amount of costly dye needed for imaging.¹³¹

Organic dyes are an alternative to metal phosphors, with red emitters of particular interest. Recently, Zhang and co-workers introduced bromide substituted naphthalene diimides, with blue fluorescence and red phosphorescence. These dyes can easily be conjugated with polymers such as PLA and proteins (BrNNI-COOH).¹²¹ Other notable organic phosphors include 4,7-dibromo-5,6-bis(tetradecyloxy) benzo[*c*] [1,2,5]thiadiazole (BrBTA)¹⁰⁹ and difluoroboron 6-hydroxybenz[*de*]anthracene-7-on (BF₂HBAN).¹²² However, as of now, these recently discovered dyes are far from reasonable alternatives to the metal phosphors. (Optical properties of all phosphors shown are summarized in Table 1.2). The red-emitting dyes, BrNNI-COOH and BrBTA, have the desirable wavelength advantage, but also have very low quantum yields in deoxygenated environments (5% and ~1% respectively). Furthermore, while the emission is very red, the absorption is extremely blue (<325 nm) which poses challenges for excitation. Difluoroboron dye alternatives have much redder absorption profiles, and multi-photon excitation abilities.¹³² Difluoroboron 6-hydroxybenz[*de*]anthracene-7-on (BF₂HBAN) is the most sensitive oxygen sensor to date, with an unprecedented 730 ms phosphorescence lifetime (note: BF₂HBAN is not, however, the first boron dye oxygen sensor discovered).¹²² But this boron dye presented by Lehner and coworkers showed poor stability due to the fused aromatic backbone.^{133,134} The ligand (9-hydroxyphenalenone) is more stable than the boron dye congener. Therefore, investigation of stable alternatives is important in designing new organic phosphorescent materials.

Table 1.2. Optical Properties of Oxygen Sensitive Phosphors

Sample	λ_{abs} (nm)	λ_{F} (nm)	λ_{P} (nm)	τ_{P} (μs)	Φ^a	References
[Ru(dpp) ₃] ^{2+b}	463	-	618	6.4	0.36	119,135
[Ir(btp) ₂ (acac)] ^{3+ c}	408	-	596	8.6	N.A. ^l	98,99,120
[Eu(HPhN) ₃ dpp] ^{3+d}	461	-	611	110.0	0.18	102
[PtTFPP] ^{2+ d}	538	-	710	60.0	0.08	136
Oxyphor G2 ^e	632	-	790	280.0	0.12	137
BrNNI-COOH ^f	N.A. ^l	420	611	5100.0	0.05	121
BrBTA ^g	325	-	643	3.4	0.005	109
BF ₂ HBAN ^h	459	495	565	730000.0	0.09	122
BF ₂ dbmPLA ⁱ	397	436	503	128000.0	0.85	138
BF ₂ dbm(I)PLA ^j	407	445	525	4500.0	0.67	139

^aTotal quantum yield (F + P)^b properties in EtOH-MeOH (4:1 v/v) ^c In CHCl₃. ^dIn a polystyrene film. ^eIn CH₂Cl₂ ^fIn water ^gIn CH₂Cl₂ ^hIn cyclohexane. ⁱIn a polystyrene film. ^j thin film. ^k thin film. ^lno data provided.

1.4. Oxygen-Sensing Difluoroboron β -Diketonates

1.4.1. Discovery

In 2007, Fraser and co-workers reported room-temperature phosphorescence upon polymerization of lactide from a hydroxyl-functionalized difluoroboron dibenzoylmethane (BF₂dbmOH) to yield difluoroboron dibenzoylmethane-poly(lactic acid) (BF₂dbmPLA). This material produced both intense fluorescence and long-lived phosphorescence upon single or multiphoton excitation (Figure 1.17).¹³⁸ This was the first report of a difluoroboron β -diketonate (BF₂bdk) exhibiting this phenomenon. This single component material is unique in that fluorescence and phosphorescence originate from the same dye, and the polymer matrix is covalently linked to the polymer matrix (PLA). Also, the presence of phosphorescence did not completely deteriorate the fluorescence properties (quantum yield = 85%), as in the cases of the other organic phosphors. This single-component material, with a polymer that is already widely used in biomedical applications,^{32,140} is simplified by comparison to multicomponent “cocktail”

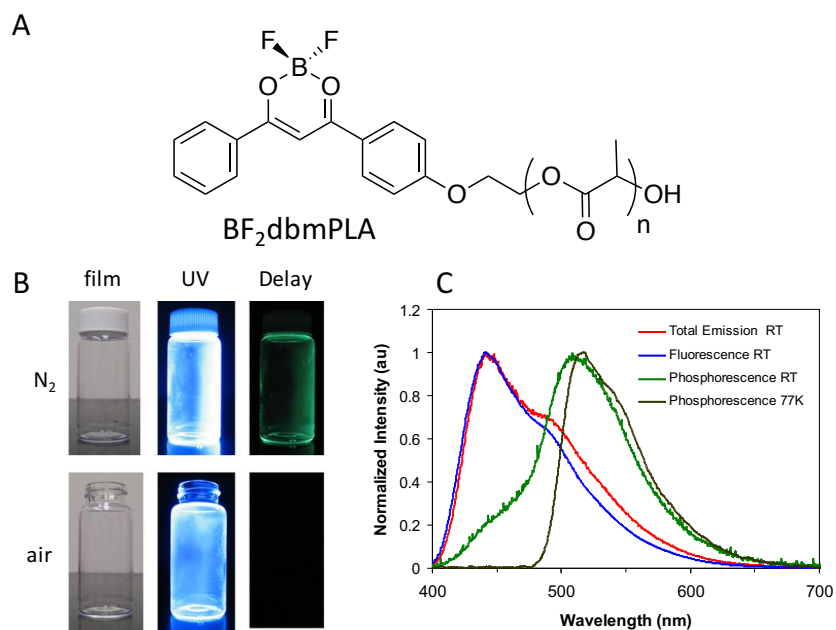


Figure 1.17. Discovery of Room-Temperature Phosphorescence from Difluoroboron Dibenzoylmethane-PLA. A) Chemical structure of BF₂dbmPLA. B) Thin solution-cast film on the inside of vial. C) Spectral properties at room-temperature (RT) and low temperature (liq. N₂; 77K).

formulations. Also, the ligand scaffold is prepared via a Claisen condensation between ketones and esters, meaning the dye can be further modified with different aromatic units and substituents such as halides or electron donating groups (i.e. -OR, or -NR₂) from a large source of commercially available and inexpensive starting materials. While this initial compound has blue fluorescence and green phosphorescence, non-ideal for biomedical applications, its simple structure was a powerful starting point. There are tremendous possibilities for chemically diverse derivatives to optimize the wavelengths towards to the redder end of the spectrum, and eventually tailor other properties.

1.4.2. Polymer Effects and Fabrication

In early experiments, it was found that polymer composition and molecular weight played important roles in the optical properties of the boron dye.^{25,34,141,142} Polymers can be prepared in solvent free lactide melts in the presence of stannous octoate (Sn(oct)₂), with good control of

molecular weight and polydispersity. Short ~ 4 kDa polymers of poly- (DL-lactic acid) (PLA), or poly- (ϵ -caprolactone) (PCL) result in green emission (~ 504 nm). Higher molecular weight polymers corresponded to a hypsochromic shift ($\lambda_F = \sim 443$ nm at 20 kDa) attributed to decreasing dye-dye interactions with increasing polymer molecular weight, as shown in Figure 1.18. Interestingly, BF₂dbmPCL polymers show no room-temperature phosphorescence (RTP), but when a BF₂dbm-PCL-PLA copolymer is synthesized, RTP is restored. This suggested that the polymer glass transition (T_g) may play a role in the phosphorescence; PCL ($T_g = -60^\circ\text{C}$) is a semi-crystalline polymer at room temperature, as opposed to PLA ($T_g = \sim 60^\circ\text{C}$) which is glassy at room temperature.³⁴ Therefore, for oxygen-sensing applications, PLA or other polymers with requisite properties for dual emission, are crucial components in the material design, and the molecular weight (i.e. dye loading) may assist in red-shifting the optical properties.

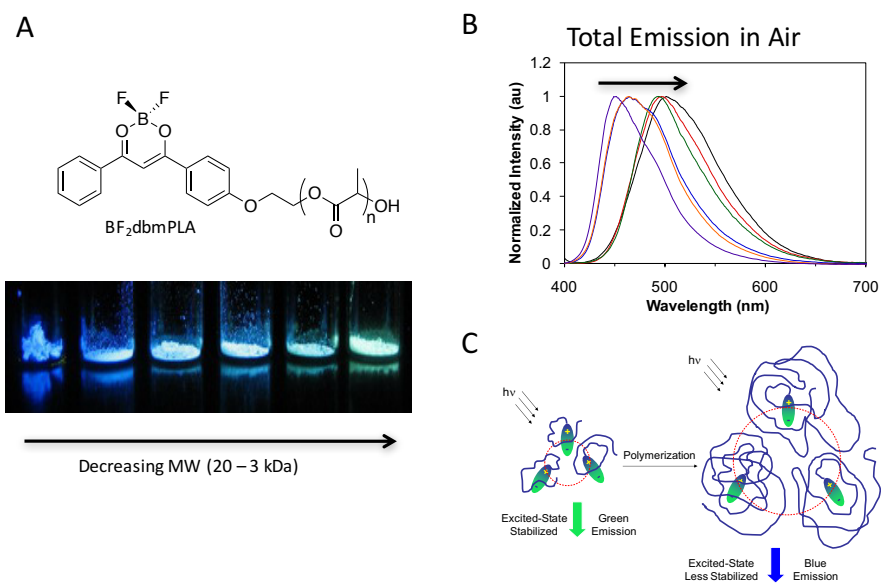


Figure 1.18. Polymer Molecular Weight Color Tuning of BF₂dbmPLA Materials. A) Structure of the BF₂dbmPLA and the images of polymers of variable molecular weights under UV illumination. B) Total emission spectra of the polymer powders. C) Mechanism of molecular control of dye-dye interactions to vary the fluorescence. Image adapted with permission from Zhang et al., *Adv. Mater.* **2008**, 20, 2099–2104.¹⁴¹ Copyright 2008. Wiley.

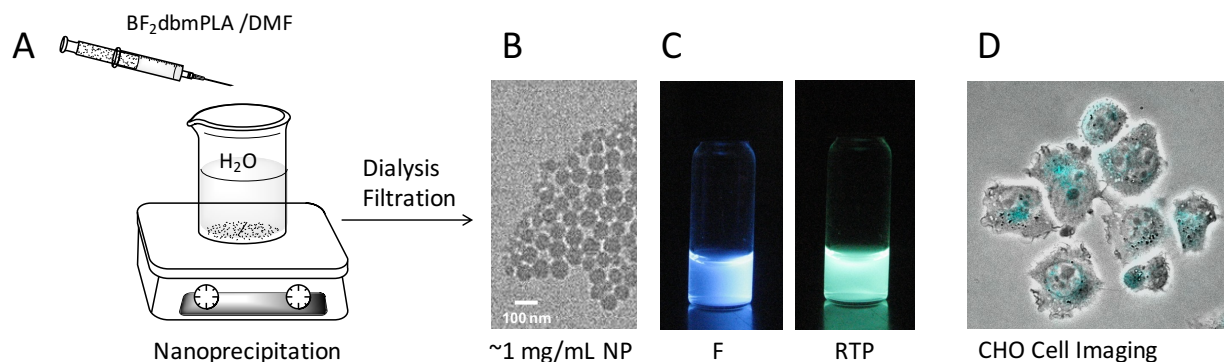


Figure 1.19. Nanoparticle Fabrication of BF₂dbmPLA (12kDa). A) Precipitation process of dropwise addition of the polymer dissolved in minimal DMF, and added dropwise to rapidly stirring water. DMF is removed via dialysis against DI water. B) TEM image of dried nanoparticles on a glass coverslip. C) Images of the nanoparticles in air under UV illumination (F) and afterglow emission under N₂ with the UV lamp turned off. D) Cellular imaging of Chinese hamster ovary (CHO) cells with after nanoparticles uptake. Images were adapted with permission from Pfister et al. *ACS Nano* **2008**, 2 (6), 1252–1258.¹⁴³ Copyright American Chemical Society 2008.

Nanoparticles can be prepared from BF₂dbmPLA polymers via nanoprecipitation.¹⁴³ The polymer is dissolved in a water miscible solvent (i.e. dimethylformamide; DMF), and added dropwise to rapidly stirring water (Figure 1.19). The DMF is removed by dialysis against deionized (DI) water, and the solution is filtered through a 200 nm filter (Whatman). The nanoparticle fabrication is very important for biological applications for a number of reasons:

- 1) the oxygen sensitive phosphorescence is only present in the solid state, not in solution
- 2) the difluoroboron moiety is susceptible to hydrolysis in aqueous environments (e.g. cells), particularly basic ones, with nucleophiles present, and the PLA polymer protects the dye from the immediate aqueous environment
- 3) the nanoparticles are small enough for cell uptake, but large enough to avoid renal clearance¹⁴⁴

1.4.3. Heavy-Atom Substitution & Imaging

The first-generation material (BF₂dbmPLA) showed oxygen-ultrasensitive phosphorescence in PLA (0-<1% O₂) as a result of a very long phosphorescence lifetime (τ_p = 128 ms). As shown in Eq. 1.7 and 1.8, very long lifetimes are indicative of a high quenching constant (K_{SV}), and thus high oxygen sensitivity.^{138,145} Oxygen levels are rarely low enough in a biological setting to even activate the phosphorescence of this dye. Therefore, except for anoxic environments, BF₂dbmPLA is not useful for biological oxygen sensing, but the polymer synthesis, material fabrication and cell imaging protocols developed brought meaningful advances. Altering the sensitivity towards a broader range of biologically relevant O₂ levels was achieved with the incorporation of halide substituents (e.g. iodide) to increase the rate of intersystem crossing via the heavy atom effect (Eq. 1.6).^{139,146}

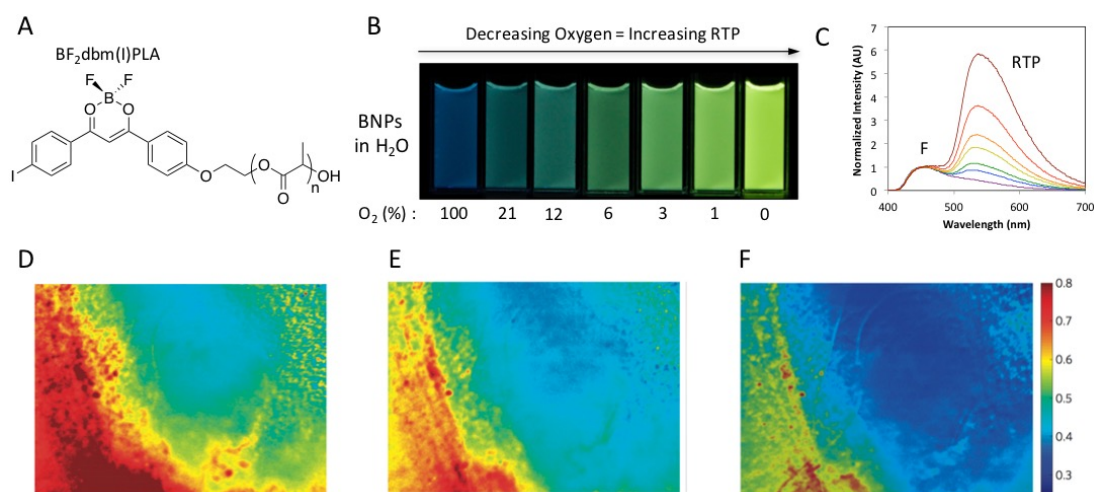


Figure 1.20. Dual-emissive BF₂dbm(I)PLA Nanoparticles. A) Chemical structure. B) Images under UV light of nanoparticles at varying oxygen concentration. C) Total emission spectra of nanoparticles at various oxygen concentrations. Images and spectra were generated in the Fraser Lab at the University of Virginia from previously reported materials and methods.¹³⁹ D-E) *In vivo* imaging of the breast cancer 4T1 mammary carcinoma tumor region in a mouse window chamber model in carbogen (D; 95% O₂), room air (E; 21% O₂) and nitrogen (F; 0% O₂). Emission intensity was averaged from 430 to 480 nm (fluorescence) and 530 to 600 nm (phosphorescence) then plotted ratios are shown. Images were adapted with permission from Zhang et al., *Nat. Mater.* **2009**, 8, 747–751.¹³⁹

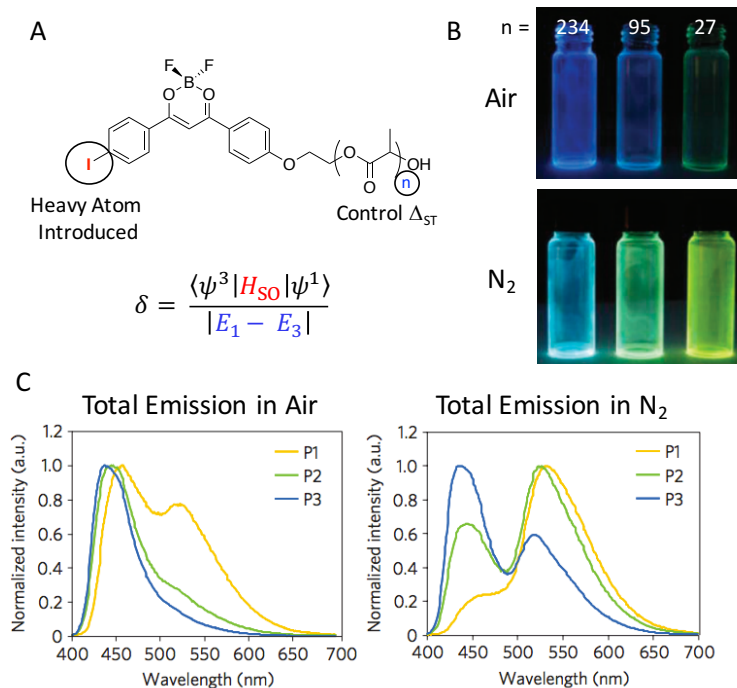


Figure 1.21. Dye-Polymer Materials Design Strategy. A) Chemical structure of iodide-substituted dye-polymer (BF₂dbm(I)PLA). The heavy atom enhances the phosphorescence, and degree of polymerization (n) controls the dye-dye interactions, and thus, the singlet-triplet energy gap (Δ_{ST}). Changes in fluorescence and phosphorescence intensities can be explained with perturbation theory. B) Images of polymers of BF₂dbm(I)PLA polymers of variable MWs in air and N₂. C) Total emission spectra of the polymers cast as films in air and N₂. Images were adapted with permission from Zhang et al., *Nat. Mater.* **2009**, 8, 747–751.¹³⁹

This was first demonstrated with iodide-substituted difluoroboron-dibenzoylmethane-poly(lactic acid) (BF₂dbm(I)PLA) which was used to determine oxygen levels in a mammary tumor model, shown in Figure 1.20. This was the first report of a single-component material enabling ratiometric imaging for biological oxygen sensing.

This polymer showed fluorescence in the range of 440–485 nm, and phosphorescence at about 525 nm. However, the interplay of polymer molecular weight and the singlet triplet energy gap had dramatic results on the phosphorescence intensities. Recall that short polymers have red-shifted emission, and therefore, a smaller gap between singlet-triplet state due to the invariant

triplet state (Figure 1.21). In heavy atom-substituted dyes, this siphoned the fluorescence intensity to the triplet state, boosting phosphorescence intensity and diminishing the relative fluorescence intensity. This introduced a new set of challenges, as tuning the ratio of fluorescence to phosphorescence (F/P ratio) was another key factor for designing useful materials.

1.5. Goals of this Research

The primary goal of this work was to optimize boron β -diketonate materials for oxygen sensing applications. Previous group members laid the ground work for tailoring the emission color by various methods, such as π -conjugation and donor-acceptor affects, as shown in Figure 1.22.¹⁴⁷ It remained for us to better understand how the optical properties and oxygen sensitivity could be conveniently controlled. Because the dye is covalently bound to the polymer matrix, all the properties are linked. Changing one variable, for example, substituting a phenyl for naphthyl group, can have a domino effect on all other optical properties. The dyes may aggregate differently in the polymer matrix, the polymer synthesis may not work the same way, and both fluorescence and phosphorescence can be affected. Changes in combinations of π -conjugation, polymer conjugation, polymer molecular weight and heavy atom placement and how they mutually affect each other all needed to be worked out and understood for these materials to be reasonable alternatives to and improvements upon the commonly used metal sensors.

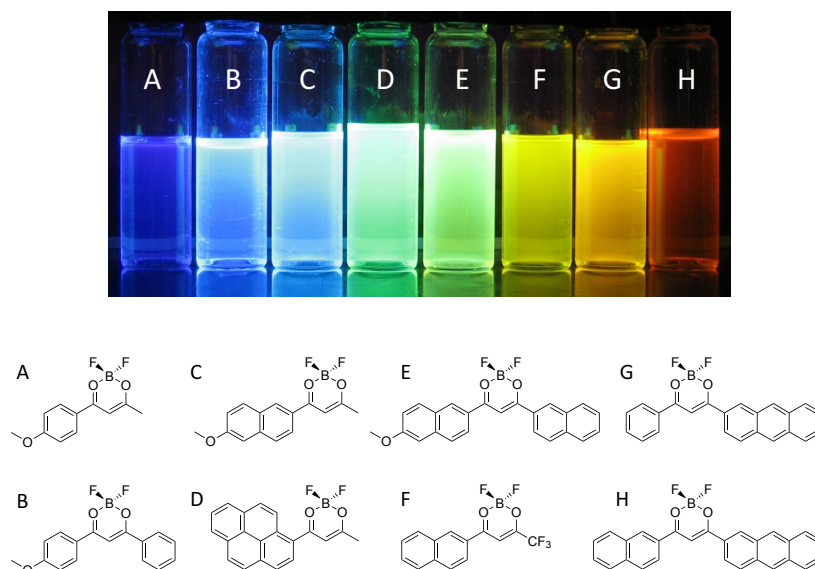


Figure 1.22. Structure and Design of Difluoroboron β -Diketonate Materials.¹⁴⁸

Through literature precedent and computational modelling, dyes were targeted to produce the reddest emission capable, without losing phosphorescence. For example, π -conjugation may have limitation, as anthracene derivatives of the fluorophore achieve red emission, but lack observable phosphorescence. Dyes and polymers were prepared and tested for optimized properties, and the best derivatives were used to explore new frontiers in optical oxygen sensing (Figure 1.23). This thesis demonstrates that through dye engineering, boron-PLA oxygen sensors can be tailored for a broad range of emission colors and oxygen sensitivities.

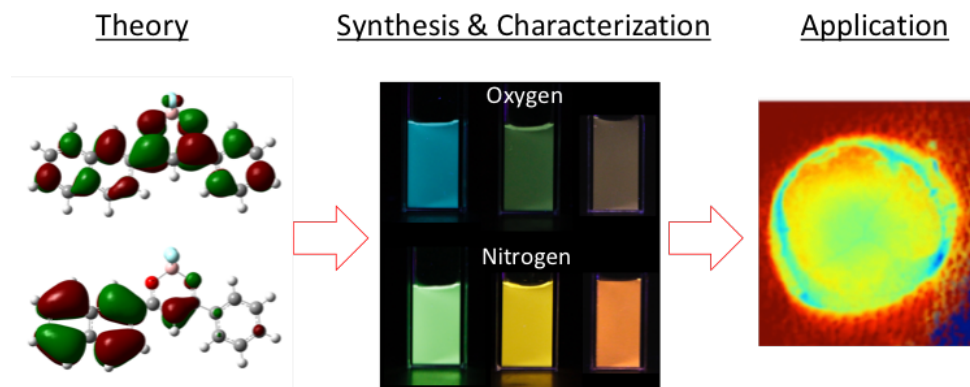


Figure 1.23. Method for Preparing and Optimizing Boron Dyes as Oxygen Sensing Materials.

Dye optimization is important, but developing new synthetic methods for different polymers with important functions is another goal. Particularly, incorporation of a poly(ethylene glycol) block improves the water solubility and in vivo lifetime of the nanoparticle material. Testing and screening new strategies for chemical conjugation and nanoparticle fabrication was another important goal. Ultimately, these materials may shed light on many medical conditions by helping to map relationships between O_2 and biological function with improved combined spatial and temporal resolution.

1.6. References

- (1) Bates, C. M.; Bates, F. S. *Macromolecules* **2017**, *50*, 3–22.
- (2) Hanlon, A. M.; Lyon, C. K.; Berda, E. B. *Macromolecules* **2016**, *49*, 2–14.
- (3) Schneiderman, D. K.; Hillmyer, M. A. *Macromolecules* **2016**, *49*, 2419–2428.
- (4) Carlini, A. S.; Adamiak, L.; Gianneschi, N. C. *Macromolecules* **2016**, *49*, 4379–4394.
- (5) Liu, J.; Liu, B. *J. Polym. Sci. Part A Polym. Chem.* **2017**, *55*, 519–532.
- (6) Reisch, A.; Klymchenko, A. S. *Small* **2016**, *12*, 1968–1992.
- (7) Ding, D.; Li, K.; Liu, B.; Tang, B. Z. *Acc. Chem. Res.* **2013**, *46*, 2441–2453.
- (8) Jenkins, R.; Burdette, M. K.; Foulger, S. H. *RSC Adv.* **2016**, *6*, 65459–65474.
- (9) Tokoro, Y.; Nagai, A.; Chujo, Y. *J. Polym. Sci. Part A Polym. Chem.* **2010**, *48*, 3693–

3701.

- (10) Matsumoto, T.; Tanaka, K.; Chujo, Y. *Macromolecules* **2015**, *48*, 1343–1351.
- (11) Xu, W.; Zeng, Z.; Jiang, J.-H.; Chang, Y.-T.; Yuan, L. *Angew. Chem. Int. Ed.* **2016**, *55*, 13658–13699.
- (12) Tanaka, K.; Chujo, Y. *Macromol. Rapid Commun.* **2012**, *33*, 1235–1255.
- (13) Wolfbeis, O. S. *Chem. Soc. Rev.* **2015**, *44*, 4743–4768.
- (14) Fernando, L. P.; Kandel, P. K.; Yu, J.; McNeill, J.; Ackroyd, P. C.; Christensen, K. A. *Biomacromolecules* **2010**, *11*, 2675–2682.
- (15) Le Meins, J.-F.; Schatz, C.; Lecommandoux, S.; Sandre, O. *Mater. Today* **2013**, *16*, 397–402.
- (16) Zheng, X.; Wang, X.; Mao, H.; Wu, W.; Liu, B.; Jiang, X. *Nat Commun* **2015**, *6*, 5834.
- (17) Corbin, P. S.; Webb, M. P.; McAlvin, J. E.; Fraser, C. L. *Biomacromolecules* **2001**, *2*, 223–232.
- (18) Bender, J. L.; Corbin, P. S.; Fraser, C. L.; Metcalf, D. H.; Richardson, F. S.; Thomas, E. L.; Urbas, A. M. *J. Am. Chem. Soc.* **2002**, *124*, 8526–8527.
- (19) Harris, F. W. *J. Chem. Educ.* **1981**, *58*, 837–843.
- (20) Dove, A. P. *ACS Macro Lett.* **2012**, *1*, 1409–1412.
- (21) Mangold, S. L.; Carpenter, R. T.; Kiessling, L. L. *Org. Lett.* **2008**, *10*, 2997–3000.
- (22) Yu, J.; Rong, Y.; Kuo, C.-T.; Zhou, X.-H.; Chiu, D. T. *Anal. Chem.* **2017**, *89*, 42–56.
- (23) Yokozawa, T.; Ohta, Y. *Chem. Rev.* **2016**, *116*, 1950–1968.
- (24) Yoshii, R.; Hirose, A.; Tanaka, K.; Chujo, Y. *J. Am. Chem. Soc.* **2014**, *136*, 18131–18139.
- (25) Zhang, G.; St. Clair, T. L.; Fraser, C. L. *Macromolecules* **2009**, *42*, 3092–3097.
- (26) Hillmyer, M. A.; Tolman, W. B. *Acc. Chem. Res.* **2014**, *47*, 2390–2396.

- (27) Schneiderman, D. K.; Hillmyer, M. A. *Macromolecules* **2016**, *49*, 2419–2428.
- (28) Albertsson, A.-C.; Varma, I. K. *Biomacromolecules* **2003**, *4*, 1466–1486.
- (29) Olsén, P.; Undin, J.; Odelius, K.; Keul, H.; Albertsson, A.-C. *Biomacromolecules* **2016**, *17*, 3995–4002.
- (30) Madhavan Nampoothiri, K.; Nair, N. R.; John, R. P. *Bioresour. Technol.* **2010**, *101*, 8493–8501.
- (31) Sitia, L.; Ferrari, R.; Violatto, M. B.; Talamini, L.; Dragoni, L.; Colombo, C.; Colombo, L.; Lupi, M.; Ubezio, P.; D’Incalci, M.; Morbidelli, M.; Salmona, M.; Moscatelli, D.; Bigini, P. *Biomacromolecules* **2016**, *17*, 744–755.
- (32) Farah, S.; Anderson, D. G. *Adv. Drug Deliv. Rev.* **2016**, *107*, 367–392.
- (33) Dong, H.; Esser-Kahn, A. P.; Thakre, P. R.; Patrick, J. F.; Sottos, N. R.; White, S. R.; Moore, J. S. *ACS Appl. Mater. Interfaces* **2012**, *4*, 503–509.
- (34) Zhang, G.; Fiore, G. L.; Clair, T. L. S.; Fraser, C. L. *Macromolecules* **2009**, *42*, 3162–3169.
- (35) Aryal, S.; Hu, C.-M. J.; Zhang, L. *Mol. Pharm.* **2011**, *8*, 1401–1407.
- (36) Elsabahy, M.; Wooley, K. L. *Chem. Soc. Rev.* **2012**, *41*, 2545.
- (37) Brannon-Peppas, L.; Blanchette, J. O. *Adv. Drug Deliv. Rev.* **2012**, *64*, 206–212.
- (38) Alexis, F.; Pridgen, E.; Molnar, L. K.; Farokhzad, O. C. *Mol. Pharm.* **2008**, *5*, 505–515.
- (39) Knop, K.; Hoogenboom, R.; Fischer, D.; Schubert, U. S. *Angew. Chem. Int. Ed.* **2010**, *49*, 6288–6308.
- (40) Marusyk, A.; Almendro, V.; Polyak, K. *Nat. Rev. Cancer* **2012**, *12*, 323–334.
- (41) Junttila, M. R.; de Sauvage, F. J. *Nature* **2013**, *501*, 346–354.
- (42) Upreti, M.; Jyoti, A.; Sethi, P. *Transl. Cancer Res.* **2013**, *2*, 309–319.

- (43) Cho, H.; Indig, G. L.; Weichert, J.; Shin, H.-C.; Kwon, G. S. *Nanomedicine Nanotechnology, Biol. Med.* **2012**, 8, 228–236.
- (44) Cho, H.; Lai, T. C.; Kwon, G. S. *J. Control. Release* **2013**, 166, 1–9.
- (45) Cho, H.; Lai, T. C.; Tomoda, K.; Kwon, G. S. *AAPS PharmSciTech* **2015**, 16, 10–20.
- (46) Cho, H.; Kwon, G. S. *ACS Nano* **2011**, 5, 8721–8729.
- (47) Lakowicz, J. R. *Principles of Fluorescence Spectroscopy*; Springer US: New York, 2006.
- (48) Berezin, M. Y.; Achilefu, S. *Chem. Rev.* **2010**, 110, 2641–2684.
- (49) Sarder, P.; Maji, D.; Achilefu, S. *Bioconjug. Chem.* **2015**, 26, 963–974.
- (50) Lavis, L. D.; Raines, R. T. *ACS Chem. Biol.* **2008**, 3, 142–155.
- (51) Li, D.; Zhang, H.; Wang, Y. *Chem. Soc. Rev.* **2013**, 42, 8416–8433.
- (52) Kwon, J. E.; Park, S. Y. *Adv. Mater.* **2011**, 23, 3615–3642.
- (53) Mei, J.; Leung, N. L. C.; Kwok, R. T. K.; Lam, J. W. Y.; Tang, B. Z. *Chem. Rev.* **2015**, 115, 11718–11940.
- (54) Lewis, G. N.; Kasha, M. *J. Am. Chem. Soc.* **1944**, 66, 2100–2116.
- (55) Lower, S. K.; El-Sayed, M. A. *Chem. Rev.* **1966**, 66, 199–241.
- (56) Reineke, S. *Nat. Photonics* **2014**, 8, 269–270.
- (57) Lavis, L. D.; Raines, R. T. *ACS Chem. Biol.* **2014**, 9, 855–866.
- (58) Terai, T.; Nagano, T. *Curr. Opin. Chem. Biol.* **2008**, 12, 515–521.
- (59) Prall, B. R.; Jeannine Eddleton. *J. Chem. Educ.* **2008**, 85, 527.
- (60) Coleman, W. F. *J. Chem. Educ.* **2008**, 85, 1152.
- (61) Liu, G.; Hu, J.; Zhang, G.; Liu, S. *Bioconjug. Chem.* **2014**, 26, 1328–1338.
- (62) Zhao, J.; Wu, W.; Sun, J.; Guo, S. *Chem. Soc. Rev.* **2013**, 42, 5323–5351.
- (63) Garland, P. B.; Moore, C. H. *Biochem. J.* **1979**, 183.

- (64) Perkampus, H.-H. *UV-VIS Spectroscopy and Its Applications*; Springer Berlin Heidelberg: Berlin, Heidelberg, 1992.
- (65) Butler, T.; Morris, W. A.; Samonina-Kosicka, J.; Fraser, C. L. *ACS Appl. Mater. Interfaces* **2016**, 8, 1242–1251.
- (66) Morris, W. A.; Kolpaczynska, M.; Fraser, C. L. *J. Phys. Chem. C* **2016**, 120, 22539–22548.
- (67) Crosby, G. A.; Demas, J. N. *J. Phys. Chem.* **1971**, 75, 991–1024.
- (68) Wahl, M. *The Principle of Time-Correlated Single Photon Counting*; PicoQuant GmbH, Rudower Chaussee 29, 12489 Berlin, Germany, 2016.
- (69) Roussakis, E.; Li, Z.; Nichols, A. J.; Evans, C. L. *Angew. Chem. Int. Ed.* **2015**, 54, 8340–8362.
- (70) Kobayashi, H.; Ogawa, M.; Alford, R.; Choyke, P. L.; Urano, Y. *Chem. Rev.* **2010**, 110, 2620–2640.
- (71) Stack, E. C.; Wang, C.; Roman, K. A.; Hoyt, C. C. *Methods* **2014**, 70, 46–58.
- (72) Resch-Genger, U.; Grabolle, M.; Cavaliere-Jaricot, S.; Nitschke, R.; Nann, T. *Nat. Methods* **2008**, 5, 763–775.
- (73) Dmitriev, R. I.; Kondrashina, A. V.; Koren, K.; Klimant, I.; Zhdanov, A. V.; Pakan, J. M. P.; McDermott, K. W.; Papkovsky, D. B. *Biomater. Sci.* **2014**, 2, 853–866.
- (74) Singh, R.; Ho, D.; Lim, L. Y.; Iyer, K. S.; Smith, N. M. *ACS Omega* **2016**, 1, 1114–1120.
- (75) Monici, M. *Biotechnol. Annu. Rev.* **2005**, 11, 227–256.
- (76) Xiang, H.; Cheng, J.; Ma, X.; Zhou, X.; Chruma, J. J. *Chem. Soc. Rev.* **2013**, 42, 6128–6185.
- (77) Lemon, C. M.; Karnas, E.; Han, X.; Bruns, O. T.; Kempa, T. J.; Fukumura, D.; Bawendi,

- M. G.; Jain, R. K.; Duda, D. G.; Nocera, D. G. *J. Am. Chem. Soc.* **2015**, *137*, 9832–9842.
- (78) Chen, G.; Roy, I.; Yang, C.; Prasad, P. N. *Chem. Rev.* **2016**, *116*, 2826–2885.
- (79) Clarke, R. J.; Oprysa, A. *J. Chem. Educ.* **2004**, *81*, 705.
- (80) Weissleder, R. *Nat. Biotechnol.* **2001**, *19*, 316–317.
- (81) Matsui, A.; Tanaka, E.; Choi, H. S.; Winer, J. H.; Kianzad, V.; Gioux, S.; Laurence, R. G.; Frangioni, J. V. *Surgery* **2010**, *148*, 87–95.
- (82) Frangioni, J. V. *Curr. Opin. Chem. Biol.* **2003**, *7*, 626–634.
- (83) Hong, G.; Antaris, A. L.; Dai, H. *Nat. Biomed. Eng.* **2017**, *1*, 0010.
- (84) Antaris, A. L.; Chen, H.; Cheng, K.; Sun, Y.; Hong, G.; Qu, C.; Diao, S.; Deng, Z.; Hu, X.; Zhang, B.; Zhang, X.; Yaghi, O. K.; Alamparambil, Z. R.; Hong, X.; Cheng, Z.; Dai, H. *Nat. Mater.* **2015**, *15*, 235–242.
- (85) Hill, T. K.; Mohs, A. M. *Wiley Interdiscip Rev Nanomed Nanobiotechnol.* **2016**, *8*, 498–511.
- (86) Hill, T. K.; Abdulahad, A.; Kelkar, S. S.; Marini, F. C.; Long, T. E.; Provenzale, J. M.; Mohs, A. M. *Bioconjug. Chem.* **2015**, *26*, 294–303.
- (87) Li, Z.; Roussakis, E.; Koolen, P. G. L.; Ibrahim, A. M. S.; Kim, K.; Rose, L. F.; Wu, J.; Nichols, A. J.; Baek, Y.; Birngruber, R.; Apiou-Sbirlea, G.; Matyal, R.; Huang, T.; Chan, R.; Lin, S. J.; Evans, C. L. *Biomed. Opt. Express* **2014**, *5*, 3748–3764.
- (88) Bruce, A. C.; Cao, Y.; Henry, C.; Peirce, S. M.; Laughon, K. *J. Forensic Sci.* **2016**, *61*, 1493–1497.
- (89) Shen, J.; Chen, G.; Vu, A.-M.; Fan, W.; Bilsel, O. S.; Chang, C.-C.; Han, G. *Adv. Opt. Mater.* **2013**, *1*, 644–650.
- (90) Wilkinson, J. A. *J. Phys. Chem.* **1908**, *13*, 691–728.

- (91) You, Y.; Nam, W. *Chem. Soc. Rev.* **2012**, *41*, 7061–7084.
- (92) You, Y. *Curr. Opin. Chem. Biol.* **2013**, *17*, 699–707.
- (93) Zhao, Q.; Huang, C.; Li, F. *Chem. Soc. Rev.* **2011**, *40*, 2508–2524.
- (94) Mukherjee, S.; Thilagar, P. *Chem. Commun.* **2015**, *51*, 10988–11003.
- (95) Bolton, O.; Lee, K.; Kim, H.-J.; Lin, K. Y.; Kim, J. *Nat. Chem.* **2011**, *3*, 205–210.
- (96) Ho, C.-L.; Wong, W.-Y. *Coord. Chem. Rev.* **2011**, *255*, 2469–2502.
- (97) Payne, S. J.; Fiore, G. L.; Fraser, C. L.; Demas, J. N. *Anal. Chem.* **2010**, *82*, 917–921.
- (98) Tobita, S.; Yoshihara, T. *Curr. Opin. Chem. Biol.* **2016**, *33*, 39–45.
- (99) Quaranta, M.; Borisov, S. M.; Klimant, I. *Bioanal. Rev.* **2012**, *4*, 115–157.
- (100) Esipova, T. V.; Karagodov, A.; Miller, J.; Wilson, D. F.; Busch, T. M.; Vinogradov, S. A. *Anal. Chem.* **2011**, *83*, 8756–8765.
- (101) Moßhammer, M.; Strobl, M.; Kühn, M.; Klimant, I.; Borisov, S. M.; Koren, K. *ACS Sensors* **2016**, *1*, 681–687.
- (102) Borisov, S. M.; Fischer, R.; Saf, R.; Klimant, I. *Adv. Funct. Mater.* **2014**, *24*, 6548–6560.
- (103) Climent, C.; Alemany, P.; Lee, D.; Kim, J.; Casanova, D. *J. Phys. Chem. A* **2014**, *118*, 6914–6921.
- (104) Bolton, O.; Lee, D.; Jung, J.; Kim, J. *Chem. Mater.* **2014**, *26*, 6644–6649.
- (105) Kwon, M. S.; Lee, D.; Seo, S.; Jung, J.; Kim, J. *Angew. Chem. Int. Ed.* **2014**, *53*, 11177–11181.
- (106) Lee, D.; Bolton, O.; Kim, B. C.; Youk, J. H.; Takayama, S.; Kim, J. *J. Am. Chem. Soc.* **2013**, *135*, 6325–6329.
- (107) Kwon, M. S.; Jordahl, J. H.; Phillips, A. W.; Chung, K.; Lee, S.; Gierschner, J.; Lahann, J.; Kim, J. *Chem. Sci.* **2016**, *7*, 2359–2363.

- (108) Zhang, X.; Xie, T.; Cui, M.; Yang, L.; Sun, X.; Jiang, J.; Zhang, G. *ACS Appl. Mater. Interfaces* **2014**, *6*, 2279–2284.
- (109) Gutierrez, G. D.; Sazama, G. T.; Wu, T.; Baldo, M. A.; Swager, T. M. *J. Org. Chem.* **2016**, *81*, 4789–4796.
- (110) Cheng, X.; Wang, K.; Huang, S.; Zhang, H.; Zhang, H.; Wang, Y. *Angew. Chem. Int. Ed.* **2015**, *127*, 8489–8493.
- (111) Baggaley, E.; Botchway, S. W.; Haycock, J. W.; Morris, H.; Sazanovich, I. V.; Williams, J. A. G.; Weinstein, J. A. *Chem. Sci.* **2014**, *5*, 879–886.
- (112) Baggaley, E.; Sazanovich, I. V.; Williams, J. A. G.; Haycock, J. W.; Botchway, S. W.; Weinstein, J. A. *RSC Adv.* **2014**, *4*, 35003–35008.
- (113) Baggaley, E.; Gill, M. R.; Green, N. H.; Turton, D.; Sazanovich, I. V.; Botchway, S. W.; Smythe, C.; Haycock, J. W.; Weinstein, J. A.; Thomas, J. A. *Angew. Chem. Int. Ed.* **2014**, *53*, 3367–3371.
- (114) Baggaley, E.; Weinstein, J. A.; Williams, J. A. G. Springer Berlin Heidelberg, 2014; pp 205–256.
- (115) Wang, X.; Wolfbeis, O. S. *Chem. Soc. Rev.* **2014**, *43*, 3666–3761.
- (116) Schreml, S.; Szeimies, R. M.; Prantl, L.; Karrer, S.; Landthaler, M.; Babilas, P. *Br. J. Dermatol.* **2010**, *163*, 257–268.
- (117) Wolfbeis, O. S. *BioEssays* **2015**, *37*, 921–928.
- (118) Hasebe, N.; Suzuki, K.; Horiuchi, H.; Suzuki, H.; Yoshihara, T.; Okutsu, T.; Tobita, S. *Anal. Chem.* **2015**, *87*, 2360–2366.
- (119) Liu, J.; Liu, Y.; Bu, W.; Bu, J.; Sun, Y.; Du, J.; Shi, J. *J. Am. Chem. Soc.* **2014**, *136*, 9701–9709.

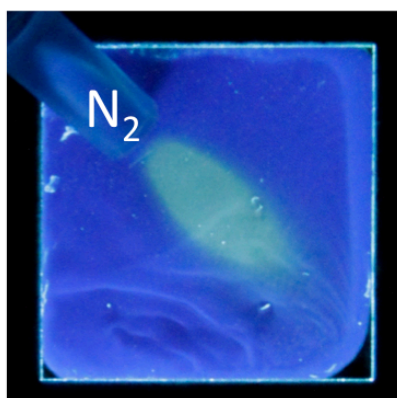
- (120) Yoshihara, T.; Yamaguchi, Y.; Hosaka, M.; Takeuchi, T.; Tobita, S. *Angew. Chem. Int. Ed.* **2012**, *124*, 4224–4227.
- (121) Chen, X.; Xu, C.; Wang, T.; Zhou, C.; Du, J.; Wang, Z.; Xu, H.; Xie, T.; Bi, G.; Jiang, J.; Zhang, X.; Demas, J. N.; Trindle, C. O.; Luo, Y.; Zhang, G. *Angew. Chem. Int. Ed.* **2016**, *55*, 9872–9876.
- (122) Lehner, P.; Staudinger, C.; Borisov, S. M.; Klimant, I. *Nat. Commun.* **2014**, *5*, 4460.
- (123) Sakadžić, S.; Roussakis, E.; Yaseen, M. A.; Mandeville, E. T.; Srinivasan, V. J.; Arai, K.; Ruvinskaya, S.; Devor, A.; Lo, E. H.; Vinogradov, S. A.; Boas, D. A. *Nat. Methods* **2010**, *7*, 755–759.
- (124) Lecoq, J.; Parpaleix, A.; Roussakis, E.; Ducros, M.; Houssen, Y. G.; Vinogradov, S. A.; Charpak, S. *Nat. Med.* **2011**, *17*, 893–898.
- (125) Finikova, O. S.; Lebedev, A. Y.; Aprelev, A.; Troxler, T.; Gao, F.; Garnacho, C.; Muro, S.; Hochstrasser, R. M.; Vinogradov, S. A. *ChemPhysChem* **2008**, *9*, 1673–1679.
- (126) Wang, X.; Gorris, H. H.; Stolwijk, J. A.; Meier, R. J.; Groegel, D. B. M.; Wegener, J.; Wolfbeis, O. S. *Chem. Sci.* **2011**, *2*, 901–906.
- (127) Sano, H.; Ichioka, S.; Sekiya, N. *PLoS One* **2012**, *7*, 1–7.
- (128) Tandara, A. A.; Mustoe, T. A. *World J. Surg.* **2004**, *28*, 294–300.
- (129) Harris, A. L. *Nat. Rev. Cancer* **2002**, *2*, 38–47.
- (130) Carreau, A.; Hafny-Rahbi, B. El; Matejuk, A.; Grillon, C.; Kieda, C. *J. Cell. Mol. Med.* **2011**, *15*, 1239–1253.
- (131) Roussakis, E.; Li, Z.; Nowell, N. H.; Nichols, A. J.; Evans, C. L. *Angew. Chem. Int. Ed.* **2015**, *54*, 14728–14731.
- (132) Cogné-Laage, E.; Allemand, J.-F.; Ruel, O.; Baudin, J.-B.; Croquette, V.; Blanchard-

- Desce, M.; Jullien, L. *Chem. Eur. J.* **2004**, *10*, 1445–1455.
- (133) Lehner, P.; Staudinger, C.; Borisov, S. M.; Regensburger, J.; Klimant, I. *Chem. Eur. J.* **2015**, *21*, 3978–3986.
- (134) D'Aléo, A.; Heresanu, V.; Giorgi, M.; Le Guennic, B.; Jacquemin, D.; Fages, F. *J. Phys. Chem. C* **2014**, *118*, 11906–11918.
- (135) Alford, P. C.; Cook, M. J.; Lewis, A. P.; McAuliffe, G. S. G.; Skarda, V.; Thomson, A. J.; Glasper, J. L.; Robbins, D. J. *J. Chem. Soc. Perkin Trans. 2* **1985**, *5*, 705–709.
- (136) Lee, S.-K.; Okura, I. *Anal. Commun.* **1997**, *34*, 185–188.
- (137) Dunphy, I.; Vinogradov, S. A.; Wilson, D. F. *Anal. Biochem.* **2002**, *310*, 191–198.
- (138) Zhang, G.; Chen, J.; Payne, S. J.; Kooi, S. E.; Demas, J. N.; Fraser, C. L. *J. Am. Chem. Soc.* **2007**, *129*, 8942–8943.
- (139) Zhang, G.; Palmer, G. M.; Dewhurst, M. W.; Fraser, C. L. *Nat. Mater.* **2009**, *8*, 747–751.
- (140) Xiao, R. Z.; Zeng, Z. W.; Zhou, G. L.; Wang, J. J.; Li, F. Z.; Wang, A. M. *Int. J. Nanomedicine* **2010**, *5*, 1057–1065.
- (141) Zhang, G.; Kooi, S. E.; Demas, J. N.; Fraser, C. L. *Adv. Mater.* **2008**, *20*, 2099–2104.
- (142) Zhang, G.; Evans, R. E.; Campbell, K. A.; Fraser, C. L. *Macromolecules* **2009**, *42*, 8627–8633.
- (143) Pfister, A.; Zhang, G.; Zareno, J.; Horwitz, A. F.; Fraser, C. L. *ACS Nano* **2008**, *2*, 1252–1258.
- (144) Liao, L.; Liu, J.; Dreaden, E. C.; Morton, S. W.; Shopsowitz, K. E.; Hammond, P. T.; Johnson, J. A. *J. Am. Chem. Soc.* **2014**, *136*, 5896–5899.
- (145) Payne, S. J.; Zhang, G.; Demas, J. N.; Fraser, C. L.; Degraff, B. A. *Appl. Spectrosc.* **2011**, *65*, 1321–1324.

- (146) DeRosa, C. A.; Kerr, C.; Fan, Z.; Kolpaczynska, M.; Mathew, A. S.; Evans, R. E.; Zhang, G.; Fraser, C. L. *ACS Appl. Mater. Interfaces* **2015**, 7, 23633–23643.
- (147) Xu, S.; Evans, R. E.; Liu, T.; Zhang, G.; Demas, J. N.; Trindle, C. O.; Fraser, C. L. *Inorg. Chem.* **2013**, 52, 3597–3610.
- (148) Fraser, C. L.; Zhang, G. Luminescent Diketonate Polymers. WO 2011011646, 2011.

Chapter 2:

Tailoring Oxygen Sensitivity with Halide Substitution in Difluoroboron Dibenzoylmethane Polylactide



2.1 Introduction

It is widely known that halide substituents can modulate structural and optical properties of materials.¹⁻³ Previously, Baranoff et al., showed that halide substitution of cyclometalled iridium complexes can alter the ligand geometry and bandgap properties.⁴ Additionally, Kim *et al.* recently presented benzaldehyde/dibromobenzene co-crystals with tunable phosphorescence by changing alkyl chain length and halide substitution.⁵ Mechanochromic luminescence (ML) and mechanochromic luminescence quenching (MLQ) have also been reported with halide substituted $\text{BF}_2\text{dbm}(\text{X})\text{C}_{12}\text{H}_{25}$ materials, where $\text{X} = \text{F}, \text{Cl}, \text{Br}, \text{I}$.⁶ Previously reported difluoroboron dibenzoylmethane polylactide (BF_2dbmPLA) materials (Figure 2.1, $\text{X} = \text{H}$) had phosphorescence lifetimes in the range of a hundred milliseconds (80-150 ms) depending on the polymer molecular weight,^{7,8} while the iodine substituted derivatives ($\text{BF}_2\text{dbm}(\text{I})\text{PLA}$) had phosphorescence lifetimes of only 4-5 ms.⁹ This change in heavy atom substitution drastically affected the oxygen sensitivity of these materials. The BF_2dbmPLA materials are highly sensitive in the hypoxic range (0-1% O_2), while $\text{BF}_2\text{dbm}(\text{I})\text{PLA}$ can effectively sense up to ambient conditions (0-21% O_2). Dyes with different oxygen sensitivities can be adapted for various biological applications. For example, probes with high sensitivities within 0.5-3.0% O_2 are well suited for tumor hypoxia imaging, 2-6% O_2 can monitor brain oxygenation in great detail, while less sensitive probes with sensitivities within the 5-15% O_2 range can effectively monitor blood oxygenation (veins versus arteries).¹⁰⁻¹²

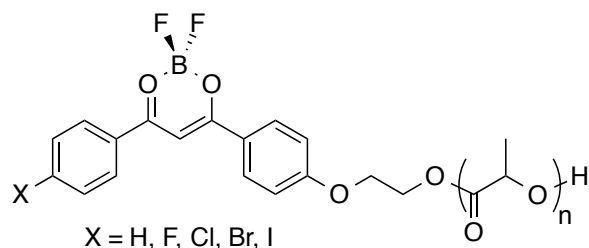


Figure 2.1. Difluoroboron Dibenzoylmethane-Poly(lactic acid) and Halide-Substituted Derivatives.

Here, a systematic study of the effects of halide substitution on BF₂dbmPLA optical and oxygen sensing properties is reported. A series of halide substituted BF₂dbm(X)PLA materials were synthesized, where X = H, F, Cl, Br, and I (Figure 2.1), to effectively tune the triplet emission of the materials *via* an internal electron withdrawing group and heavy atom effects. Dye-polymer conjugates can be fabricated into nanoparticles¹³ or nanofibers¹⁴ for biomedical imaging,^{15,16} minimizing phase separation, heterogeneity and dye leaching that can occur for comparable dye loadings in dye/PLA blends.^{17,18} The dyes and polymers are analyzed in dilute CH₂Cl₂ solutions and in solid-state films. In the solid state, phosphorescence lifetime, and thus oxygen sensitivity, can be controlled with the halide substituent and polymer molecular weight. The photostability of the polymers was studied over extended excitation times (~18 hours) with a handheld UV light source.

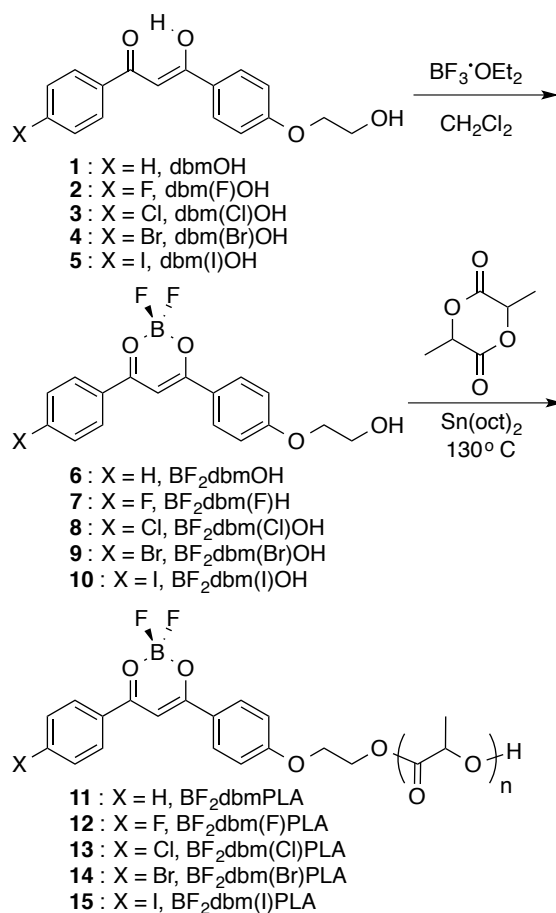
2.2. Results & Discussion

2.2.1 Synthesis

The β -diketones **1-5** (Scheme 1) were prepared as previously described.⁸ Namely, the aromatic ketone 1-(4-(2-((tetrahydro-2H-pyran-2-yl)oxy)ethoxy)phenyl)ethan-1-one was combined with the appropriate aromatic ester to generate the diketone via a Claisen condensation, followed by removal of the dihydropyran hydroxyl protecting group, to give compounds **1-5**. By varying the aromatic ester, ligands with different halide substituents were easily produced via the same synthetic methods. The diketones were purified by recrystallization in EtOAc and hexanes.

Boronation was performed by stirring boron trifluoride diethyletherate with the β -diketones, **1-5**, in anhydrous CH₂Cl₂ for 4-10 hours at room temperature. The parent compound, BF₂dbmOH (**6**), and the iodine substituted BF₂dbm(I)OH (**10**) were purified by recrystallization from acetone/hexanes to obtain yellow crystalline powders. The lighter halide derivatives (**7-9**)

Scheme 2.1 Synthesis of Dye-PLA Conjugates



had very similar solubility to the ligand analogues, and were instead purified by silica column chromatography (EtOAc/hexanes eluent) and were also obtained as yellow powders. Poly(lactic acid) (PLA) was grown from the primary alcohol sites of boron initiators **6-10** in lactide melts in the presence of a stannous octoate catalyst, as previously described.⁸ Initiators **6-10** readily in molten lactide, even with low equivalents of the monomer (i.e. 50 equivalents). To assess the effects of molecular weight (MW) on the luminescence properties of dye-PLA conjugates, two polymers were grown for each halide initiator—one with low MW (6.0-7.5 kDa) and one with higher MW (16.5-20.0 kDa) (Table 2.1). With 50 equivalents of lactide, polymerizations became viscous and were stopped after 1 hour by cooling to room temperature, and purification by

Table 2.1. Polymer Molecular Weight Characterization

Polymer	Loading ^a	M _n (NMR) ^b	M _n (GPC) ^c	M _w (GPC) ^c	PDI ^c
11a	50:1/40	6000	6600	6900	1.05
12a	50:1/40	6200	6100	6600	1.08
13a	50:1/40	7700	7500	8200	1.09
14a	50:1/40	5800	6400	7600	1.18
15a	50:1/40	6700	6600	7100	1.08
11b	200:1/40	24200	19100	20800	1.09
12b	200:1/40	20400	16500	18500	1.12
13b	200:1/40	23400	18700	20600	1.10
14b	200:1/40	18500	17100	18500	1.08
15b	200:1/40	24200	20300	23100	1.14

^a Molar ratio of monomer to Sn(oct)₂ catalyst per equiv. boron initiator. ^b Molecular weights determined by end group analysis (Dye-Ar-OCH₂CH₂- vs PLA-CH integration). ^c Polydispersity index (PDI) = M_w/M_n determined by GPC.

precipitation from CH₂Cl₂/MeOH (cold) then CH₂Cl₂/hexanes. Reactions with 200 equivalents of lactide were typically run for 3 hours. Reactions were stopped at ~60-80% conversion to ensure more controlled reaction conditions and polymers with low polydispersities (1.05-1.18). This minimizes thermal depolymerization¹⁹ or transesterification²⁰ side reactions to ensure reliable and reproducible polymer MWs.

2.2.2 Optical Properties in Solution

The dye initiators (**6-10**) and polymers (**11-15**) were analyzed in dilute CH₂Cl₂ solutions in air at room temperature, and the optical properties are summarized in Table 2.2. The dyes and polymers have near identical properties in CH₂Cl₂ and all absorb light in the UV to violet range (395-410 nm, Figure S2.1; Appendix A). As the halide substituent becomes heavier, the absorbance is red-shifted (i.e. BF₂dbmOH (**6**) λ_{abs} = 397 nm versus BF₂dbm(I)OH (**10**) λ_{abs} = 407 nm). The extinction coefficient increased slightly with heavier substituted halides as well (BF₂dbmOH (**6**) ε = 53000 M⁻¹ cm⁻¹ versus BF₂dbm(I)OH (**10**) ε = 58000 M⁻¹ cm⁻¹). As is commonly observed,⁷ extinction coefficient values decreased from dyes to polymers with the same halide substituent (i.e. BF₂dbm(F)OH (**7**): ε = 48000 M⁻¹ cm⁻¹ versus BF₂dbm(F)PLA (**12a**) ε =

45000 M⁻¹ cm⁻¹), perhaps due to minor dye degradation during the polymerization, purification processes, or inherent error in estimating dye content and ascribing an extinction coefficient to polydisperse samples.

The dyes emit blue fluorescence in CH₂Cl₂ solution, and the halide substituents have only minor influences on the color (BF₂dbmOH (**6**); λ_F = 433 nm, BF₂dbm(I)OH (**10**); λ_F = 441 nm). However, halide substitution does alter the fluorescence lifetime (τ_F) and quantum yield (Φ_F) of the boron dyes. Lighter halide dyes and polymers (X = H, F, Cl, and Br) have similar lifetimes of (~1.95 ns), and quantum yields near unity (~0.95). The iodine derivatives showed lower quantum yields and shorter fluorescence lifetimes as a result of the heavy atom effect.⁶ In solution, enhanced intersystem crossing via the heavy atom effect resulted in non-radiative decay pathways as a result of oxygen quenching or intramolecular motions.

Table 2.2 Optical Properties of Boron Dye Initiators and Polymers in CH₂Cl₂

Sample		λ_{abs}^a (nm)	ϵ^b (M ⁻¹ cm ⁻¹)	λ_{em}^c (nm)	τ_F^d (ns)	Φ_F^e
BF ₂ dbmOH	6	397	53 000	433	1.96 ^f	0.95 ^f
BF ₂ dbmPLA	11a	396	52 000	425	1.94	0.95
BF ₂ dbm(F)OH	7	397	48 000	430	3.27	0.99
BF ₂ dbm(F)PLA	12a	397	45 000	426	1.95	0.98
BF ₂ dbm(Cl)OH	8	401	56 000	438	3.43	0.99
BF ₂ dbm(Cl)PLA	13a	398	55 000	435	1.96	0.99
BF ₂ dbm(Br)OH	9	403	56 000	440	2.24	0.96
BF ₂ dbm(Br)PLA	14a	404	54 000	438	1.77	0.91
BF ₂ dbm(I)OH	10	407	58 000	441	1.03 ^g	0.55 ^g
BF ₂ dbm(I)PLA	15a	405	49 000	435	0.95	0.40

^aAbsorption maxima. ^bExtinction coefficients calculated at the absorption maxima. ^cFluorescence emission maxima excited at 369 nm. ^dFluorescence lifetime excited with a 369 nm light-emitting diode (LED) monitored at the emission maximum. All fluorescence lifetimes are fitted with single-exponential decay. ^eRelative quantum yield, versus anthracene in EtOH as a standard. ^fValues taken from Ref 8. ^gValues taken from Ref 9.

2.2.3 Optical Properties of Films.

Boron polymers were also studied as films in the solid state. Optical properties for polymers **11-15** with variable molecular weights are presented in Table 2.3. Fluorescence spectra and lifetime measurements were obtained under ambient conditions (e.g., air, ~21% oxygen). Phosphorescence measurements were conducted under N₂. Molecular weight is an effective way to tune the luminescence properties of boron dye-PLA materials.⁷ In previously reported BF₂dbmPLA polymer conjugates, low MW polymers (~4 kDa) showed green fluorescence (500 nm), high MW polymers (~20 kDa) showed blue fluorescence (425 nm), and peak emission could be modulated using the PLA MW or dye concentration in blends. This is attributed to a change in the dye-dye interactions within the PLA matrix; therefore, dye concentration plays an important role. Similarly, this concentration dependent emission can also be seen in other difluoroboron dyes. For example, Venkatesan *et al.* successfully generated β -ketoiminates that exhibited

Table 2.3. Optical Properties of Solution-Cast Films

Sample		M _n ^a (kDa)	Fluorescence		Phosphorescence	
			λ_{em} ^b (nm)	τ_{pw0} ^c (ns)	λ_{em} ^d (nm)	τ_{pw0} ^e (ms)
BF ₂ dbmPLA	11a	6.6	457	6.63	516	142.1
	11b	19.1	426	1.53	510	207.4
BF ₂ dbm(F)PLA	12a	6.1	502	45.47	512	122.8
	12b	16.5	428	2.53	508	195.9
BF ₂ dbm(Cl)PLA	13a	7.5	466	6.91	520	113.6
	13b	18.7	437	2.57	516	168.0
BF ₂ dbm(Br)PLA	14a	6.4	471	5.32	522	28.9
	14b	17.1	436	1.79	520	47.1
BF ₂ dbm(I)PLA	15a	6.6	455	3.46	528	5.6
	15b	20.3	437	0.90	522	5.8

^aNumber-average molecular weight (GPC) ^bSteady-state fluorescence spectra emission maximum under air. Excitation source: 369 nm xenon lamp. ^cFluorescence lifetime excited with a 369 nm light-emitting diode (LED) monitored at the emission maximum. All fluorescence lifetimes are fitted with triple-exponential decay. ^dDelayed emission spectra maxima under N₂. Excitation source: xenon flash lamp. ^ePre-exponential weighted RTP lifetime. Excitation source: xenon flash lamp; RTP lifetime fit to triple-exponential decay.

phosphorescence across the visible spectrum at different concentrations in CH_2Cl_2 and poly(methyl methacrylate) (PMMA) environments.²¹ In the solid-state, dye structure is critical in determining how dye-dye interactions influence material optical properties. Phenyl-phenyl systems (BF_2dbmPLA) reached a maximal blue-shifted fluorescence at a MW of ~ 20 kDa, which corresponded to about 1% dye by total mass; further dilution did not affect the fluorescence color significantly.⁷

Halide interactions play important roles in molecular assemblies and crystal engineering and serve as a way to modulate optical properties.²² In this study two polymers of each halide-substituted dye were prepared to analyze MW effects and dye-dye interactions on the optical properties. (See spectra of dye-polymer films in Figures S2-4; Appendix A). The expected trend in fluorescence lifetimes (τ_F) across the halide series is observed. As the halide becomes heavier, τ_F decreases (H = 6.6 ns, F = 45.4 ns, Cl = 6.9 ns, Br = 5.3 ns, I = 3.4 ns). The fluorescence color sensitivity to dye loading (i.e., M_n) also varied with different halide dyes. For instance, between $\text{BF}_2\text{dbm(F)PLA}$, **12a** (6.1 kDa; $\lambda_F = 502$ nm) and **12b** (16.5 kDa; $\lambda_F = 428$ nm), the emission wavelength shifted by 74 nm. In contrast, emission wavelengths for the bromide analogues $\text{BF}_2\text{dbm(Br)PLA}$, **14a** (6.0 kDa ; $\lambda_F = 471$ nm) and **14b** (17.1 kDa; $\lambda_F = 436$ nm), shifted

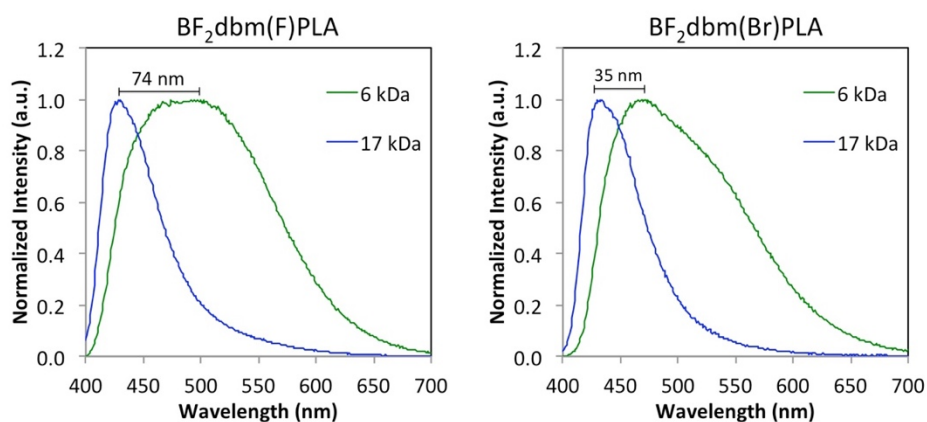


Figure 2.2 Molecular weight and fluorescence; total emission of $\text{BF}_2\text{dbm(F)PLA}$ (**12**) and $\text{BF}_2\text{dbm(Br)PLA}$ (**14**) in air ($\lambda_{\text{ex}} = 369$ nm).

only 35 nm with a comparable shift in molecular weight (Figure 2.2 and Table 2.3). The difference in emission maxima between low and high MW polymers decreases for heavier halides. When heavy atoms are present, there is enhanced intersystem crossing (ISC) to the triplet state, siphoning off redshifted fluorescence. The unsubstituted dye, BF₂dbmPLA, showed a smaller range than the chloro- and fluoro- adducts. This could be a result of increased inductive effects due to the electron withdrawing properties of the aromatic halides influencing the donor-acceptor scaffold of the dye.²³ Fluorescence properties can inspire designs for future dye scaffolds, controlling color ranges within the PLA matrix and by modulating the donor-acceptor structure of the boron dyes.

The phosphorescence properties of boron polymers were studied under a N₂ atmosphere at room temperature. All polymers showed delayed emission in the absence of oxygen. (Figures 2.3 and S2.5; Appendix A). Delayed emissions were green and the maxima ranged from 500 to 530 nm. Unlike the fluorescence maxima (λ_F), the phosphorescence maxima (λ_P) did not vary with polymer MW. For example, the

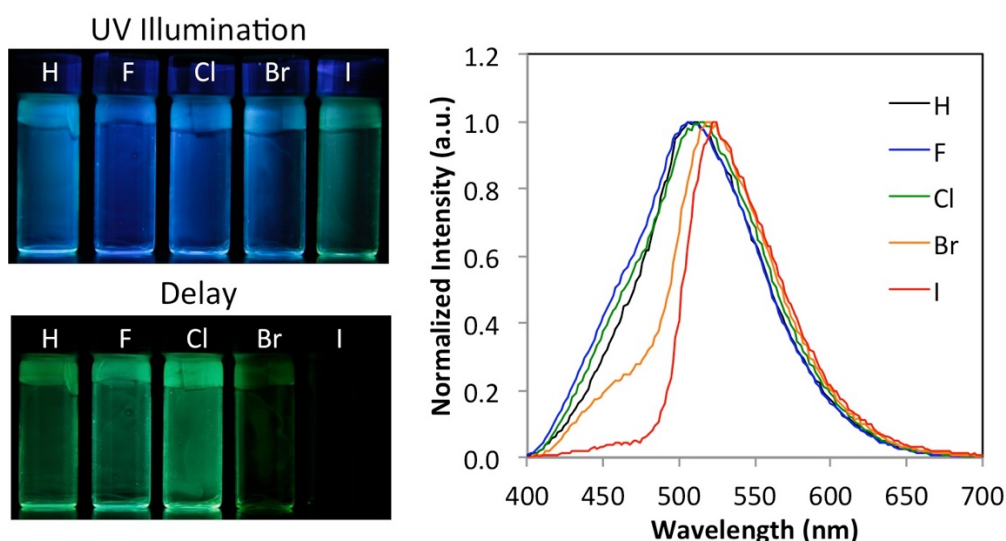


Figure 2.3. Phosphorescence of high molecular weight BF₂dbm(X)PLA polymer films (**11b-15b**). Left: Images of BF₂dbm(X)PLA films under N₂ with UV illumination and after the lamp is turned off (delay). Right: Delayed emission spectra of films (excitation = xenon flash lamp with 2 ms delay).

fluorescence of BF₂dbmPLA (**11**) blue-shifted from 457 nm (~6 kDa) to 426 nm (~19 kDa), while the phosphorescence changed only slightly, from 516 nm to 510 nm with increasing MW. Heavier halide substituents red-shifted the phosphorescence (**11a-15a**; λ_p : H = 516 nm, F = 512 nm, Cl = 520 nm, Br = 522 nm, I = 528 nm). The emission peak also sharpened with heavier halide substituents, along with a decrease in delayed fluorescence at shorter wavelengths, similar to previously described BF₂bdk-PLA conjugates.⁷ Because delayed fluorescence (DF) is temperature sensitive, it is important to suppress DF in ratiometric oxygen probes, as the fluorescence internal standard would otherwise respond to O₂ quenching and temperature.²⁴ The addition of heavier halides (Br and I) is an effective way to minimize the DF transitions.

The phosphorescence lifetime (τ_p) is highly dependent on both the molecular weight and the halide substituent. The phosphorescence emission maxima stayed at a constant wavelength with changing MW, while the fluorescence maxima blue-shifted. Increasing the molecular weight expanded the singlet-triplet gap, and decreased the rate of intersystem crossing and thermally activated delayed fluorescence, resulting in longer lifetimes (e.g. τ_p of BF₂dbmPLA: **11a** = 142 ms, **11b** = 207 ms). The halides influenced the τ_p differently. With increased atomic mass of the halide substituents, the phosphorescence intensity increased (Figure 2.4), at the expense of the fluorescence intensity. Lighter halide substituents (H **11a**, F **12a**, and Cl **13a**) had weak phosphorescence shoulders in their total emission under N₂ but long green afterglows (>100 ms lifetimes) (Figure 2.4). For heavier halide dyes (Br and I) with short polymers, the emission color of the material changed from blue-green (~470 nm) to yellow (~525 nm), as the phosphorescence dominated the total emission. These types of materials are well suited for ratiometric sensing, where the fluorescence serves as the internal standard, and the phosphorescence intensity relates

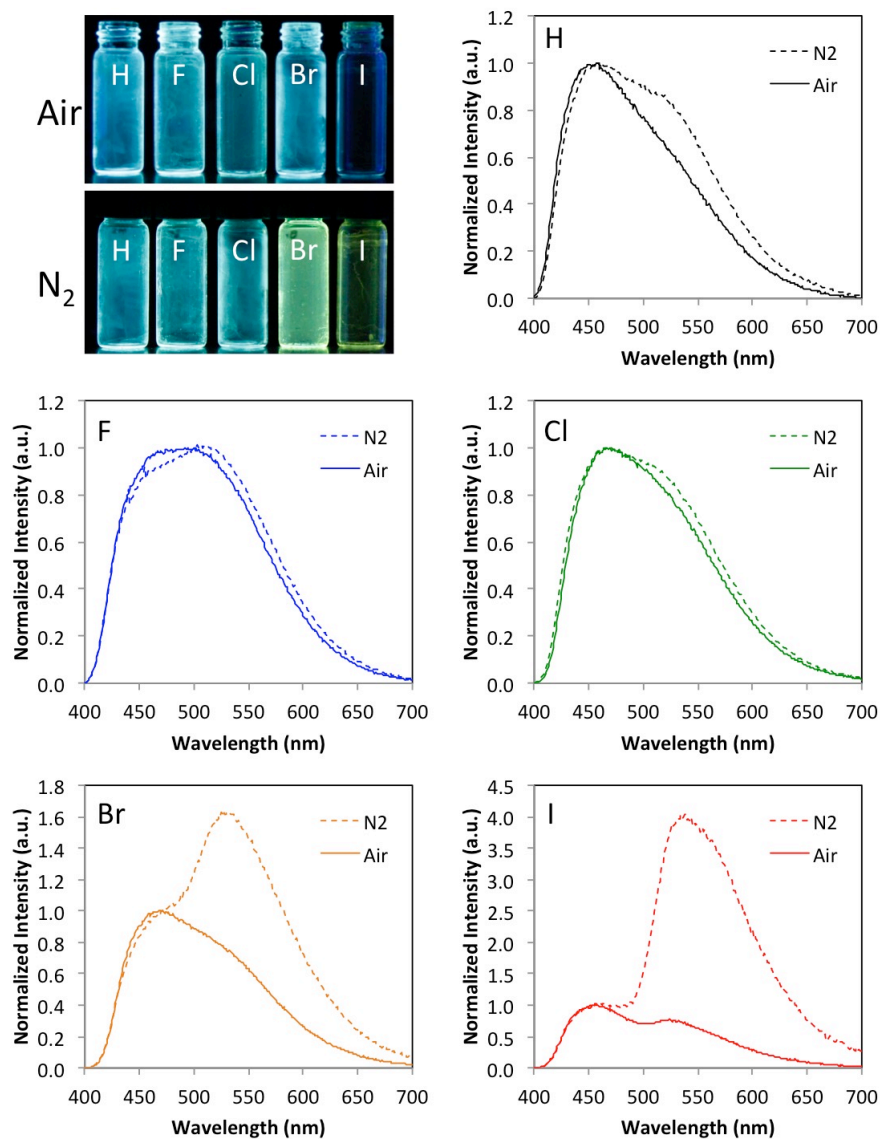


Figure 2.4. Images and total emission spectra of low molecular weight polymer films (**11a-15a**) under air and nitrogen ($\lambda_{\text{ex}} = 369 \text{ nm}$).

to the O₂ concentration. Lighter halide substituted dyes with long RTP lifetimes are well suited for lifetime methods for quantifying O₂ concentration.

The fluorescence to phosphorescence intensity ratio (F/P) can be controlled by polymer molecular weight.⁹ This is linked to the singlet-triplet energy gap; as the gap becomes larger, the rate of intersystem crossing decreases, lowering the phosphorescence intensity. For short polymers, Br **14a** and I **15a**, the fluorescence and phosphorescence peaks overlap (Figure 2.4).

Higher MW polymers can potentially resolve the two peaks to facilitate detection of the fluorescence and phosphorescence. This strategy has been demonstrated for previously for the BF₂dbm(I)PLA polymers to make them useful as ratiometric sensing materials. While it is important to have a large singlet-triplet gap for imaging, if the energy gap becomes too great, the rate of intersystem crossing may reduce to phosphorescence intensity, rendering the material impractical for sensing. In fact, this is what is observed for bromine substituted BF₂dbm(X)PLA derivatives in this study. The singlet-triplet gap in the 20 kDa polymer (**14a**) became so great that the phosphorescence no longer dominated the total emission under N₂ (Figure S2.6; Appendix A). The phosphorescence peak still resulted in a visible color change for BF₂dbm(I)PLA, but was much weaker than the fluorescence. Therefore, it is concluded that BF₂dbm(X)PLA (X = Br, I) materials are most useful at higher dye loadings for ratiometric sensing.

2.2.4. Oxygen Sensitivity.

The two most conventional ways for luminescence O₂ quantification are based on lifetime and intensity based phosphorescence measurements. Lifetime methods do not require internal standards to determine O₂ concentration.²⁵ In this method, spectrally isolated fluorescence and phosphorescence peaks, or intense phosphorescence, are not needed for O₂ quantification, as long as the lifetime is gated and does not include the fluorescence.²⁶ Lifetime is directly linked to oxygen sensitivity, as shown in Equations 1 and 2.²⁷ Therefore, materials with the longest unquenched phosphorescence lifetimes (τ_0) and fastest diffusion of oxygen through the matrix, will be the most sensitive. Klimant *et al.* recently developed ultrasensitive materials with aluminum or difluoroboron hydroxyphenalenone complexes within polystyrene, Teflon and Hyflon polymer matrices based on these concepts.²⁸ By combining complexes of variable unquenched lifetimes, with polymer matrices of high O₂ permeabilities (P), such as polystyrene

($P \approx 8.8 \times 10^{-16} \text{ mol m}^{-1} \text{ s}^{-1} \text{ Pa}^{-1}$), Hyflon ($P \approx 170 \times 10^{-16} \text{ mol m}^{-1} \text{ s}^{-1} \text{ Pa}^{-1}$), or Teflon ($P \approx 1200 \times 10^{-16} \text{ mol m}^{-1} \text{ s}^{-1} \text{ Pa}^{-1}$), the oxygen hypersensitivity could be tuned, and oxygen concentration could be detected in the parts per million range.²⁸ In contrast, purely organic crystals exhibited long-lived phosphorescence, insensitive to oxygen. When the phosphorescence is confined to a crystal, the oxygen barrier is too great, and the phosphorescence persists under ambient conditions.^{29,30}

$$\frac{\tau_0}{\tau} = 1 + K_{SV}[O_2] \quad \text{Eq. 2.1}$$

$$K_{SV} = \tau_0 * k_D \quad \text{Eq. 2.2}$$

This effect has yet to be studied for boron dyes in biodegradable polylactide. Polylactide exhibits permeabilities that are magnitudes lower than that of perfluorinated polymers and polystyrene (PLA: $P \approx 0.86 \times 10^{-16} \text{ mol m}^{-1} \text{ s}^{-1} \text{ Pa}^{-1}$) and can change dependent on material fabrication, film treatment (e.g. annealing), polymer microstructure (e.g. stereochemistry) and other factors affecting material microcrystallinity.³¹ At first this might seem like a drawback, but in fact, the lower permeability of oxygen in PLA is beneficial, given that it counterbalances the long-lived phosphorescence in BF₂bdkPLA materials. The net effect is biocompatible materials with dynamic ranges that are well matched to biological processes. Another advantage of the long phosphorescence lifetimes in BF₂dbm(X)PLA materials is that they enable detection by convenient and inexpensive imaging techniques, such as with portable high-speed cameras that can be useful in clinical and field contexts.³²

Given that phosphorescence lifetimes vary with halide substituent and polymer MW, samples **11-15** provide a convenient model to test O₂ sensitivity versus lifetime.

Table 2.4. Lifetime Oxygen Sensitivity of BF₂dbm(X)PLA Films

Sample		τ_0^a (ms)	τ_1^b (ms)	Sensitivity ^c
BF ₂ dbmPLA	11a	142.1	10.2	13.9
	11b	207.4	14.7	14.1
BF ₂ dbm(F)PLA	12a	122.8	9.1	13.5
	12b	195.9	10.2	19.2
BF ₂ dbm(Cl)PLA	13a	113.6	7.7	14.7
	13b	168.0	9.7	17.3
BF ₂ dbm(Br)PLA	14a	28.9	5.8	5.0
	14b	47.1	6.9	6.8
BF ₂ dbm(I)PLA	15a	6.6	3.2	2.1
	15b	7.4	3.1	2.4

^a Phosphorescence lifetime in N₂. ^b Phosphorescence lifetime in 1% O₂. ^c (τ_0/τ_1)²⁵

Previously, it was shown that the phosphorescence intensity of BF₂dbm(I)PLA varied linearly with oxygen concentrations between 0-1%.⁹ Highly sensitive dual-emitters within this O₂ range could assist in detecting tumors with severe hypoxia, and be used in monitoring tumor growth and proliferation during therapy.³³ To determine sensitivity within this range, the unquenched phosphorescence lifetime (τ_0) (i.e. 0% oxygen) was compared to the lifetime at 1% oxygen (τ_1) (Table 2.4). The sensitivity of each polymer was determined by the rate of the change between the two O₂ concentrations (τ_0/τ_1), as is routine within the field for comparison between oxygen probes.²⁵

Lighter halide substituted dye-polymer conjugates (H, F, and Cl) showed the most dynamic response to oxygen, as the phosphorescence lifetimes became ~14 times shorter at 1% oxygen. However, between these three samples, sensitivity changes are minimal (BF₂dbmPLA, **11a**, τ_0/τ_1 = 13.9; BF₂dbm(F)PLA, **12a**, τ_0/τ_1 = 13.5; BF₂dbm(Cl)PLA, **13a**, τ_0/τ_1 = 14.7). The sensitivities are too similar to conclude definitively that the lighter halides (F, Cl) are altering the oxygen sensitivity, as minor changes in polymer MW may be the defining factor for the observed changes (i.e. BF₂dbm(F)PLA: **12a** (6.1kDa) and BF₂dbm(Cl)PLA: **13a** (7.5 kDa)). At 1% oxygen, these dyes are approaching the upper limit of detection as well, defined as τ_1/τ_0 = 1% (e.g. BF₂dbmPLA:

11b, $\tau_1/\tau_0 = 7\%$).³⁴ Therefore, the detected phosphorescence at 1% oxygen may be the result of a different detectable solid-state species (i.e. aggregates or dimers) within the PLA matrix as BF₂dbm type fluorophores are well known to form in polymer matrices.^{18,35} Different phosphorescence quenching rates, or completely unquenchable species may also influence the sensitivity of these materials.⁶³ The mere presence of long-lived phosphorescence within the BF₂dbm(X)PLA samples, where X = H, F, and Cl, will indicate a highly deoxygenated environment, useful for numerous applications.³⁶

The less dynamically sensitive bromine (**14**) and iodine (**15**) polymers serve as better systems for analyzing trends in phosphorescence lifetimes. The lifetimes of the bromide **14a** and iodide **15a** polymers under nitrogen were 28.9 ms and 6.6 ms, respectively. The resultant change in oxygen sensitivity was dramatic (Br, **14a**, $\tau_0/\tau_1 = 5.0$; I, **15a**, $\tau_0/\tau_1 = 2.1$). In the higher MW polymers, **14b** and **15b**, the τ_0 became longer, and thus, the sensitivity changed (Br, **14b**, $\tau_0/\tau_1 = 6.8$; I, **15b**, $\tau_0/\tau_1 = 2.4$). This suggests that heavy atom substitution and polymer MW can effectively tune the oxygen sensitivity of these BF₂dbm(X)PLA materials, primarily through changes in the phosphorescence lifetimes.

Oxygen sensitive materials with the unique combination of millisecond long decays and intense phosphorescence are scarce.³⁷ Polymers with heavier halide substituted dyes, bromine (**14a**) and iodine (**15a-b**), meet these criteria (Table 2.5). The long phosphorescence lifetimes can be used to detect oxygen by phosphorescence lifetime imaging microscopy (PLIM), and the phosphorescence is strong enough for intensity-based ratiometric measurements.²⁵ When analyzing the fluorescence to phosphorescence ratios (F/P) of the low MW polymers, the bromide polymer (**14a**) experienced slightly higher sensitivity in the 0-1% O₂ range than the iodide polymers (BF₂dbm(Br)PLA: **14a**, $P_0/P_1 = 2.09$, BF₂dbm(I)PLA: **15a**, $P_0/P_1 = 1.61$) (Figure 2.5).

More pronounced than sensitivity is the change in range and limits of detection with heavy atom substitution. At 21% oxygen (air), the bromide polymer **14a** has a negligible difference in F/P compared to the ratio at 1% (BF₂dbm(Br)PLA: **14a**, P₀/P₁ = 2.09, P₀/P₂₁ = 2.35). In contrast, iodide polymers, **15a-b**, have more intense phosphorescence that can sense well beyond 1% oxygen. Iodide polymers of different MWs, have similar oxygen sensitivities, but the range of detection changes. The phosphorescence of high MW BF₂dbm(I)PLA (20 kDa) was fully quenched in air (21% O₂), whereas low MW BF₂dbm(I)PLA (6 kDa) exhibited phosphorescence under ambient conditions (i.e. air). This suggests that oxygen levels higher than 21% could be detected with this sensing material. These results demonstrate that the oxygen sensing capability of BF₂dbm(X)PLA-type fluorophore probes can be fine-tuned with halide substitution and polymer molecular weight for a variety of applications in biological and other contexts.

Table 2.5. Ratiometric Oxygen Sensitivity of BF₂dbm(X)PLA Films

Sample		F/P ₀ ^a	F/P ₁ ^b	F/P ₂₁ ^c	Sensitivity ^d (1% [O ₂])	Sensitivity ^e (21% [O ₂])
BF ₂ dbm(Br)PLA	14a	0.64	1.34	1.51	2.09	2.35
BF ₂ dbm(I)PLA	15a	0.28	0.45	1.15	1.61	4.10
	15b	1.43	2.48	6.43	1.73	4.50

^aFluorescence/phosphorescence in N₂. ^b Fluorescence/phosphorescence in 1% O₂.

^cFluorescence/phosphorescence in air (21% O₂). ^d F/P₁ ÷ F/P₀ = P₀/P₁. ^eP₀/P₂₁.

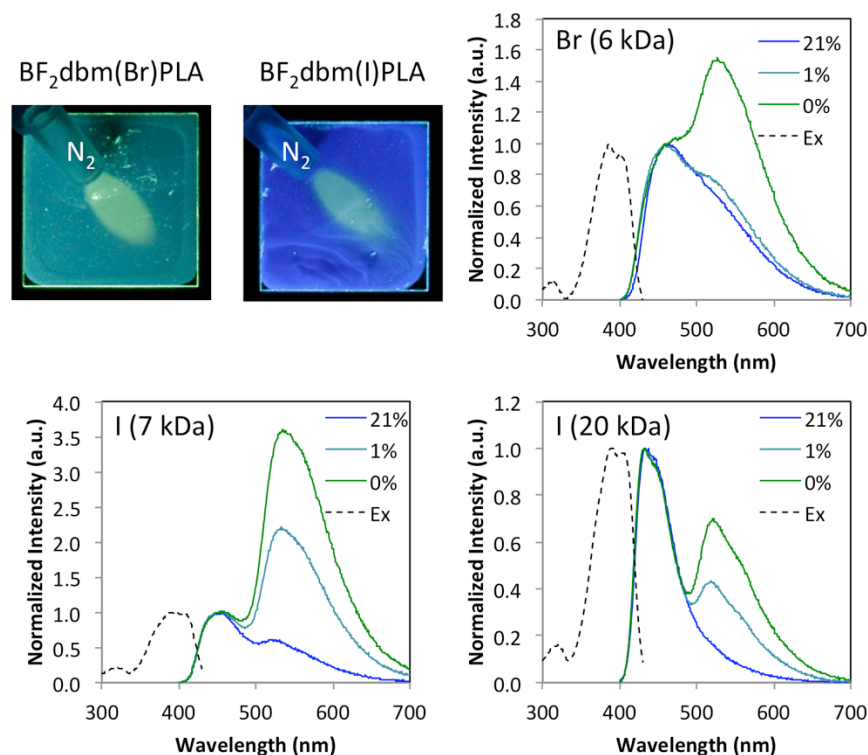


Figure 2.5. Oxygen sensitive $\text{BF}_2\text{dbm}(\text{X})\text{PLA}$ polymers suitable for ratiometric sensing. Images: $\text{BF}_2\text{dbm}(\text{Br})\text{PLA}$ (**14a**, 6 kDa) and $\text{BF}_2\text{dbm}(\text{I})\text{PLA}$ (**15b**, 20 kDa) spin cast films with a stream of nitrogen gas blown across the surface. Spectra: excitation monitored at peak fluorescence wavelength (Ex, dashed line) and total emission spectra under 0% O_2 (nitrogen), 1% O_2 and 21% O_2 (air) ($\lambda_{\text{ex}} = 369 \text{ nm}$).

2.2.5. Photostability.

It is well known that β -diketones can photobleach with UV exposure.^{38–40} For example, in sunscreens, the diketone, avobenzone, is commonly used to absorb short-wave UVA radiation and is known to photodegrade over time.^{41,42} Additionally, recent reports showed that halide substitution can create new degradation pathways for diketone compounds.⁴³ Furthermore, Zakharova and co-workers demonstrated that both boron detachment and singlet oxygen generation are relevant pathways for BF_2dbm degradation in organic solvents.⁴⁴ Thus, it is important to analyze the degradation and photobleaching of boron dye polymers to assess the material lifetime and accuracy for sensing.

Photostability studies were conducted by exposing spin-cast polymer films to UV light using a handheld 4 W UV lamp ($\lambda_{\text{ex}} = 369 \text{ nm}$) for 18 hours. A monochrome camera was used to monitor the total intensity while the dyes were excited. An image was captured every five minutes during the 18 hour period. This was a simple way to monitor multiple samples at once, and to eliminate environmental variations between samples. The resultant changes in intensity are shown in Figure 2.6. For lighter halide substituted $\text{BF}_2\text{dbm}(\text{X})\text{PLA}$ ($\text{X} = \text{H}, \text{F}, \text{and Cl}$, **11a-13a**), the total intensity decreased but only by $\sim 5\%$ over the 18 hour period, consistent with only modest dye degradation. Compared to many fluorescent probes commonly used in biology,^{45,46} these materials are intense and show excellent photostability. Furthermore, these findings confirm their suitability for lifetime oxygen sensing or as turn on sensors in oxygen-free or very low oxygen environments.

Low molecular weight polymers with bromide and iodide (**14a** and **15a**), in contrast, actually became 9-10% brighter after excitation for 18 hours (Figure 2.6). At first it might seem surprising that the overall intensity increased even though the number of fluorophores decreased upon photodegradation, but in fact, this is understandable given what is known about dye loading and intersystem crossing effects in BF_2bdkPLA materials.⁶ When dye concentration decreases

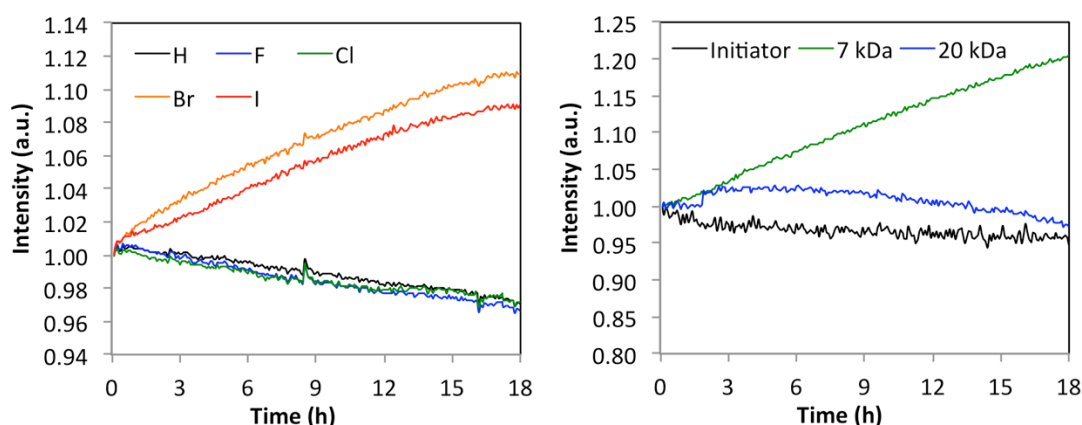


Figure 2.6. Influence of the halide substituent on the photostability of $\text{BF}_2\text{dbm}(\text{X})\text{PLA}$ spin cast films. Total intensity versus UV exposure time ($\lambda_{\text{ex}} = 369 \text{ nm}$; normalized to initial intensity). Left: Short polymers **11a-15a**. Right: Comparison of the photostability of **10** (Initiator) and iodide polymers **15a** (7 kDa) and **15b** (20 kDa).

in PLA the fluorescence blueshifts and the energy gap between fluorescence and phosphorescence maxima increases. This decreases the rate of intersystem crossing to the oxygen sensitive triplet state, which is quenched in air, and thus, results in more intense total emission. It is interesting to compare this process with mechanochromic luminescence quenching (MLQ) in solid BF₂dbk dye samples, wherein thermally annealed samples have a larger singlet-triplet gap and are bright until smearing narrows the singlet-triplet gap, thus facilitating intersystem crossing and quenching of the triplet state, causing total emission to decrease.⁶ Unlike the 7 kDa iodide polymer the 20 kDa sample **15b** showed little change in the fluorescence maximum or total intensity over time (Figure 2.6). Given that the dye is already primarily in the monomeric state in the high molecular weight polymer, it does not blueshift upon photodegradation and further dilution. Higher molecular weight samples show good photostability however some changes in the F/P intensity ratio are noted for phototreated 20kDa BF₂dbm(I)PLA analyzed under nitrogen (Figure 2.7, bottom right). It is possible that dye monomers and aggregates could degrade at different rates in PLA samples. To test this, a control was run with initiator BF₂dbm(I)OH (**10**) spin cast films. Results in Figure 2.6 (right) showed stable emission for this sample. In the solid state however, under air or nitrogen, no phosphorescence is observed for **10**. This suggests involvement of the triplet state for photodegradation pathways through singlet oxygen generation or radical formation in dye-PLA films where phosphorescence is present. In summary, these

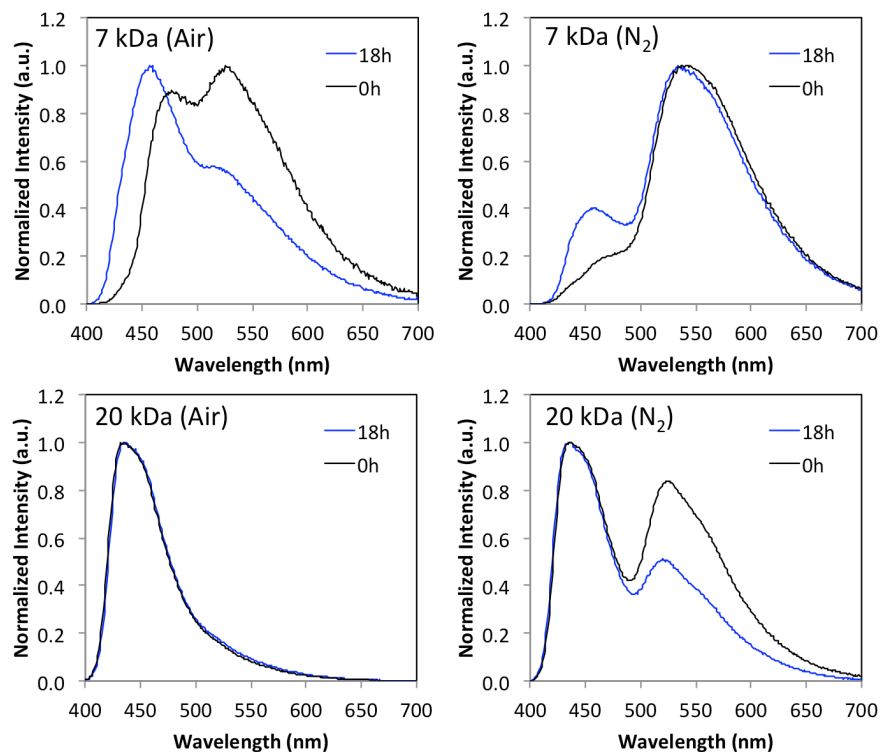


Figure 2.7. Total emission of BF₂dbm(I)PLA spin cast films under air and nitrogen before (0h) and after 18 hour UV exposure in air (18h) ($\lambda_{\text{ex}} = 369$ nm).

findings indicate that high molecular weight samples with long phosphorescent lifetimes (i.e. BF₂dbm(X)PLA where X = H, F, Cl) are best for lifetime imaging given greater photostability. But further improvements in dye design are required for reliable quantitative ratiometric sensing. Instead, heavy atom substituted dyes that exhibit strong phosphorescence at low dye loading are desirable.

2.2.6. Conclusion.

In summary, BF₂dbm(X)PLA materials were synthesized for X = H, F, Cl, Br, and I. The effects of changing the halide substituent as well as the length of the PLA on the optical properties of the polymers were studied in dilute CH₂Cl₂ solutions and solid state films. All samples show intense fluorescence suitable for use as probes. Several properties ideal for oxygen sensing were also observed, including fluorescence and intense phosphorescence for the short iodine and

bromine polymers suitable for ratiometric sensing, and long phosphorescence lifetimes for the lighter halide-dye polymers useful for lifetime sensing and convenient and cost effective camera imaging. The long lifetimes increased the sensitivity of the dye-polymers. The lifetimes of the iodine and bromine polymers were shorter due to the heavy atom effect. Varying the polymer MW affected the ratio of fluorescence to phosphorescence intensity under anoxic conditions. For the long bromine and iodine polymers, increasing the polymer molecular weight to ~20 kDa created a larger singlet-triplet gap but decreased the rate of intersystem crossing. The result is slightly improved fluorescence and phosphorescence peak resolution but with much weaker phosphorescence, demonstrating that low molecular weight BF₂dbm(X)PLA polymers are preferable for ratiometric oxygen sensing.

Comparing the phosphorescence lifetimes of films under nitrogen versus a 1% oxygen environment revealed the ability to tune the oxygen sensitivity by changing the halide substituent from bromine to iodine or by changing the polymer molecular weight. Finally, the photostability of the polymers was monitored over an 18 hour continuous UV light excitation period. The total intensity for the lighter halides decreased only 5% over time, indicating good photostability. Bromide and iodide derivatives, on the other hand, display an increase in fluorescence intensity, which counter intuitively, is also ascribed to dye degradation, and thus, lower dye loading. Dye dilution corresponds to a blueshift in fluorescence, an increase in the singlet triplet energy gap, and thus, decreased rates of intersystem crossing, analogous to the molecular weight effect commonly observed for this family of materials. The longer bromide and iodide substituted polymers did not show an increase in signal intensity upon extended exposure to UV light, given dyes existed in the maximally blueshifted monomeric state both before and after UV illumination. Results from this investigation point to dyes with long lifetimes for lifetime imaging modalities or

more conjugated heavy atom substituted dyes with intense, separated and readily detectable fluorescence and phosphorescence peaks for ratiometric sensing. And importantly, sensing materials should be made from high MW polymers (lower dye loading) to ensure photostability and reliable quantitative sensing with BF₂bdkPLA materials.

2.3 Experimental Section

2.3.1 Materials

3,6-Dimethyl-1,4-dioxane-2,5-dione (D,L-lactide, Sigma Aldrich) was recrystallized twice from ethyl acetate and stored under nitrogen. The ligand precursor 1-(4-(2-((tetrahydro-2H-pyran-2-yl)oxy)ethoxy)phenyl)ethan-1-one,⁴⁷ ligands dbmOH (**1**)⁴⁷ and dbm(I)OH (**5**),⁹ boron initiators BF₂dbmOH (**6**)⁸ and BF₂dbm(I)OH (**9**)⁹ and polymers **11-15**⁷ were prepared as previously described. Tin(II) 2-ethylhexanoate (Sn(oct)₂, Spectrum), boron trifluoride diethyl etherate (Aldrich, purified, redistilled), and all other reagents and solvents were used as received without further purification. Solvents CH₂Cl₂ and THF were dried and purified over 3 Å molecular sieves activated at 300 °C.⁴⁸ All other chemicals were reagent grade from Sigma-Aldrich and were used without further purification.

2.3.2 Methods

¹H NMR spectra were recorded on a Varian Unity Inova 300/51 (300 MHz) or a Varian VMRS/600 (600 MHz) instrument in CDCl₃. ¹H NMR peaks were referenced to the signals for the residual protiochloroform at 7.26 ppm. Coupling constants are given in hertz. Polymer molecular weights were determined by gel permeation chromatography (GPC) (THF, 25 °C, 1.0 mL/min, *dn/dc* = 0.050) using multiangle laser light scattering (SEC-MALS) (λ = 658 nm, 25 °C) and refractive index (RI) (λ = 658 nm, 25 °C) detection. Polymer Laboratories 5 μ m mixed-C columns (guard column plus two columns) along with Wyatt Technology (Optilab T-rEX interferometric

refractometer, miniDAWN TREOS multiangle static light scattering (MALS) detector, ASTRA 6.0 software) and Agilent Technologies instrumentation (series 1260 HPLC with diode array (DAD) detector, ChemStation) were used in GPC analysis. UV–vis spectra were recorded on a Hewlett-Packard 8452A diode-array spectrophotometer.

Luminescence Measurements. Steady-state fluorescence emission spectra were recorded on a Horiba Fluorolog-3 Model FL3-22 spectrofluorometer (double-grating excitation and double-grating emission monochromator). A 2 ms delay was used when recording the delayed emission spectra. Time-correlated single-photon counting (TCSPC) fluorescence lifetime measurements were performed with a NanoLED-370 ($\lambda_{\text{ex}} = 369$ nm) excitation source and a DataStation Hub as the SPC controller. Phosphorescence lifetimes were measured with a 1 ms multichannel scalar (MCS) excited with a flash xenon lamp ($\lambda_{\text{ex}} = 369$ nm; duration <1 ms). Lifetime data were analyzed with DataStation v2.4 software from Horiba Jobin Yvon. Fluorescence quantum yields (Φ_{F}) of initiator and polymer samples in CH_2Cl_2 were calculated against anthracene as a standard as previously described, using the following values: $\Phi_{\text{F}}(\text{anthracene}) = 0.27^{49}$ $n_{\text{D}}^{20}(\text{EtOH}) = 1.360$, $n_{\text{D}}^{20}(\text{CH}_2\text{Cl}_2) = 1.424$. Optically dilute CH_2Cl_2 solutions of the dyes, with absorbances <0.1 au, were prepared in 1 cm path length quartz cuvettes. Thin films were prepared on the inner wall of vials by dissolving polymers in CH_2Cl_2 (2 mg/mL) and evaporating the solvent by slowly rotating the vial under a low stream of nitrogen. The solution-cast films were then dried *in vacuo* for at least 15 min before measurements. Fluorescence spectra and lifetimes were obtained under ambient conditions (e.g., air, ~21% oxygen). Phosphorescence measurements were performed under a N_2 atmosphere. Phosphorescence measurements were taken under N_2 . The vials with the solution-cast films were purged and sealed with a Teflon cap and wrapped in parafilm in a glove box prior to measurements. The glove box was purged for 30 min prior to samples being sealed.

For oxygen sensitivity measurements, solution cast films in vials were fitted with a 12 mm PTFE/silicone/PTFE seal (Chromatography Research Supplies), connected by a screw cap. Vials were continuously purged with analytical grade N₂ (Praxair) or 1.0% O₂ (Praxair) during measurements. For 21% O₂ (i.e. air), measurements were taken under ambient conditions (open vial, no cap). Fluorescence and phosphorescence lifetimes were fit to double or triple exponential decays in solid-state films.

Photostability Measurements. Spin-cast films were prepared by dropwise addition of 1 mL of a ~1.0 mg/mg CH₂Cl₂ solution on 18 × 18 mm glass cover slides (Fisher Scientific) using a Laurel Technologies WS-650s spin-coater at 3000 rpm. Films were dried in vacuo for ~15 min prior to measurements. Films were placed on a black surface 10 cm below the camera and were irradiated with a 4 W UV lamp. A Watec 902H2 Ultimate monochrome CCD camera, equipped with a Fujinon DV5X3.6R4B-SA2L 3.6-18 mm F/1.8 lens and an Ion Video 2 PC analog to digital converter was used to monitor photostability. Linearity was ensured by a neutral density filter calibration (Tiffen, 58 mm Neutral Density = 0.9) and by disabling automatic gain and gamma control. A custom-made MATLAB program was implemented to record the pixel intensity of each sample every 5 min for 18 h.

1-(4-Fluorophenyl)-3-(4-(2-hydroxyethoxy)phenyl)propane-1,3-dione (dbm(F)OH) (**2**). The aromatic ketone, 1-(4-(2-(((tetrahydro-2H-pyran-2-yl)oxy)ethoxy)phenyl)ethan-1-one⁴⁷ (870 mg, 3.3 mmol), and ethyl 4-fluorobenzoate (674 mg, 3.9 mmol), were dissolved in anhydrous THF (50 mL). A suspension of NaH (120 mg, 5.0 mmol) in THF (10 mL) was transferred to the reaction via cannula. The reaction was refluxed at 60 °C under a nitrogen atmosphere, and monitored by TLC, until consumption of the aromatic ketone was complete (7 h). The reaction mixture was removed from the heat and allowed to cool to RT, before excess NaH was quenched with sat.

aqueous NaHCO_2 (20 mL), and the THF was removed via rotary evaporation. The crude reaction mixture was treated with 1M HCl to adjust the pH to ~ 5 . The resulting mixture was extracted with EtOAc (2×20 mL), then combined organic layers were washed with H_2O (2×20 mL). The organic solvent, EtOAc, was removed *via* rotary evaporation to yield a brown oil. The crude reaction mixture was dissolved in a THF (100 mL)/ H_2O (20 mL) solution, a catalytic amount of TsOH (20 mg, 0.12 mmol) was added, then the reaction mixture was refluxed at 60°C and monitored by TLC for the disappearance of protected diketone (2 h). The THF was removed by rotary evaporation, resulting in an aqueous suspension of the crude organic product. The organics were extracted with CH_2Cl_2 (2×20 mL) and washed with H_2O (2×20 mL), and brine (2×20 mL), and dried over anhydrous Na_2SO_4 . The mixture was filtered and the solvent was removed by rotary evaporation to yield a brown solid. The crude solid was purified by recrystallization (EtOAc/hexanes) to yield a white powder: 649 mg (65 %). ^1H NMR (600 MHz, CDCl_3): δ 17.10 (s, broad, 1H, -OH), 8.03 – 7.93 (m, broad, 4 H, 2', 6'-ArH, 2'', 6''-ArH), 7.20 – 7.10 (m, broad, 2H, 3', 5'-ArH), 6.99 (d, $J = 9$, 2H, 3'', 5''-ArH), 6.74 (s, 1H, -COCHCO), 4.17 (t, $J = 6$, 2H, Ar-OCH₂CH₂OH), 4.01 (t, $J = 6$, 2H, Ar-OCH₂CH₂OH), 1.65 (s, broad, 1H, Ar-OCH₂CH₂OH). HRMS (ESI, TOF) m/z calcd for $\text{C}_{17}\text{H}_{16}\text{O}_4\text{F}$, 303.1033 $[\text{M} + \text{H}]^+$; found 303.1031.

1-(4-Chlorophenyl)-3-(4-(2-hydroxyethoxy)phenyl)propane-1,3-dione (dbm(Cl)OH) (**3**). The chloro ligand (**3**) was prepared as described for **2**, but using methyl 4-chlorobenzoate as the aromatic ester in the Claisen condensation to yield a tan flaky solid: 210 mg (45%). ^1H NMR (300 MHz, CDCl_3): δ 16.91 (s, broad, 1H, -OH), 7.96 (d, $J = 9$, 2H, 2', 6'-ArH), 7.89 (d, $J = 8.4$, 2H, 2'', 6''-ArH), 7.44 (d, $J = 8.4$, 2H, 3', 5'-ArH), 7.00 (d, $J = 9$, 2H, 3'', 5''-ArH), 6.74 (s, 1H, -COCHCO-), 4.16 (t, $J = 4.2$, 2H, -ArOCH₂-), 4.00 (s, broad, 2H, -CH₂OH), 3.50 (s, broad, 1H, -CH₂OH). HRMS (ESI, TOF) m/z calcd for $\text{C}_{17}\text{H}_{16}\text{O}_4\text{Cl}$ 319.0728 $[\text{M} + \text{H}]^+$; found 319.0737.

1-(4-Bromophenyl)-3-(4-(2-hydroxyethoxy)phenyl)propane-1,3-dione (dbm(Br)OH) (**4**). The bromo ligand (**4**) was prepared as described for **2**, but using methyl 4-bromobenzoate as the aromatic ester in the Claisen condensation to yield a tan powder: 855 mg (63%). ¹H NMR (300 MHz, CDCl₃): δ 16.90 (s, broad, 1H, -OH), 7.97 (d, J = 9, 2H, 2', 6'-ArH), 7.83 (d, J = 8.4 2H, 2'', 6''-ArH), 7.62 (d, J = 8.4, 2H, 3', 5'-ArH), 7.00 (d, J = 9, 2H, 3'',5''-ArH), 6.75 (s, 1H, -COCHCO-), 3.89 (s, 3H, -ArOCH₃), 4.17 (t, J = 4.2, 2H, -ArOCH₂-), 4.02 (s, broad, 2H, -CH₂OH), 1.99 (s, broad, 1H, -CH₂OH). HRMS (ESI, TOF) m/z calcd for C₁₇H₁₆O₄Br 363.0232 [M + H]⁺; found 363.0237.

BF₂dbm(F)OH (**7**). The fluoro initiator **7** was prepared by dissolving dbm(F)OH (**2**) (200 mg, 0.66 mmol) in anhydrous CH₂Cl₂ (50 mL) in a dry 100 mL round bottom flask. Boron trifluoride diethyl etherate (122 μL, 0.99 mmol) was added *via* syringe, whereupon the solution turned light yellow. The reaction mixture was stirred at room temperature and monitored by TLC until the ligand substrate was consumed (4 h). Excess boron trifluoride diethyl etherate was quenched by addition of K₂CO_{3(s)} (100 mg, 0.72 mmol). After stirring for 15 min, the reaction mixture was filtered and the solvent was removed *via* rotary evaporation to yield a dark yellow powder. The product was purified by column chromatography (1:1 hexanes/EtOAc, then EtOAc) to yield a faint yellow powder: 151 mg (69%). ¹H NMR (600 MHz, CDCl₃): δ 8.17 - 8.14 (m, broad, 4H, 2', 6' -ArH, 2'', 6'' -ArH), 7.21 (d, J = 6, 2H, 3', 5'- ArH), 7.07 – 7.04 (m, 2H, 3'',5''-ArH), 6.97 (s, 1H, COCHCO), 4.99 (s, 1H, Ar-OCH₂CH₂OH), 4.21 (t, J = 6, 2H, Ar-OCH₂CH₂OH), 4.03 (t, J = 6, 2H, Ar-OCH₂CH₂OH). HRMS (ESI, TOF) m/z calcd for C₁₇H₁₄O₄BF₂ 331.0953 [M - F]⁺; found 331.0949.

BF₂dbm(Cl)OH (**8**). The chloro initiator **8** was prepared as described for **7** using dbm(Cl)OH (**3**) instead of dbm(F)OH (**2**). A yellow powder was obtained: 118 mg (76%). ¹H NMR (600 MHz, CDCl₃): δ 8.16 (d, J= 9, 2H, 2', 6'-ArH), 8.06 (d, J= 9, 2H, 2'', 6''-ArH), 7.52 (d, J=8.4, 2H, 3', 5'-ArH),

7.07 – 7.05 (m, 3H, 3'',5''-ArH, -COCHCO-), 4.21 (t, J = 3.9, 2H, -ArOCH₂-), 4.04 – 4.02 (m, 2H, -CH₂OH). HRMS (ESI, TOF) m/z calcd for C₁₇H₁₄O₄ClBF 347.0661 [M - F]⁺; found 347.0658.

BF₂dbm(Br)OH (**9**). The bromo initiator was prepared as previously described for **7** using dbm(Br)OH (**4**) instead of dbm(F)OH (**2**). A yellow powder was obtained: 110 mg (49%). ¹H NMR (600 MHz, CDCl₃): δ 8.16 (d, J= 9, 2H, 2', 6'-ArH), 7.97 (d, J= 9, 2H, 2'', 6''-ArH), 7.69 (d, J= 8.4, 2H, 3', 5'-ArH), 7.07 – 7.05 (m, 3H, 3'',5''-ArH, -COCHCO-), 4.21 (t, J = 3.9, 2H, -ArOCH₂-), 4.07 – 4.03 (m, 2H, -CH₂OH). HRMS (ESI, TOF) m/z calcd for C₁₇H₁₄O₄BrBF 391.0153 [M - F]⁺; found 391.0156.

2.4 Acknowledgements

This research was published in *ACS Applied Materials and Interfaces*.⁵⁰ I thank Prof. Guoqing Zhang and Ruffin Evans for designing and initiating the project when they were a part of the group, Caroline Kerr, Ziyi Fan, and Dr. Milena Kolpaczynska for helping in the synthesis and characterization of these BF₂dbm(X)PLA polymers, Alexander Mathew for developing and performing the photostability measurements, Prof. Fraser, Caroline, and Ziyi for assistance in the preparation of the manuscript, and the financial support of the National Cancer Institute of the National Institutes of Health (R01 CA167250).

2.5 References

- (1) Lukasiewicz, R. J.; Mousa, J. J.; Winefordner, J. D. *Anal. Chem.* **1972**, *44*, 963–966.
- (2) Sun, X.; Zhang, B.; Li, X.; Trindle, C. O.; Zhang, G. *J. Phys. Chem. A* **2016**, *120*, 5791–5797.
- (3) Thompson, L. G.; Webber, S. E. *J. Phys. Chem.* **1972**, *76*, 221–224.
- (4) Baranoff, E.; Curchod, B. F. E.; Monti, F.; Steimer, F.; Accorsi, G.; Tavernelli, I.;

- Rothlisberger, U.; Scopelliti, R.; Grätzel, M.; Nazeeruddin, M. K. *Inorg. Chem.* **2012**, *51*, 799–811.
- (5) Bolton, O.; Lee, D.; Jung, J.; Kim, J. *Chem. Mater.* **2014**, *26*, 6644–6649.
- (6) Morris, W. A.; Liu, T.; Fraser, C. L. *J. Mater. Chem. C* **2015**, *3*, 352–363.
- (7) Zhang, G.; Kooi, S. E.; Demas, J. N.; Fraser, C. L. *Adv. Mater.* **2008**, *20*, 2099–2104.
- (8) Zhang, G.; Chen, J.; Payne, S. J.; Kooi, S. E.; Demas, J. N.; Fraser, C. L. *J. Am. Chem. Soc.* **2007**, *129*, 8942–8943.
- (9) Zhang, G.; Palmer, G. M.; Dewhurst, M. W.; Fraser, C. L. *Nat. Mater.* **2009**, *8*, 747–751.
- (10) Roussakis, E.; Li, Z.; Nichols, A. J.; Evans, C. L. *Angew. Chem. Int. Ed.* **2015**, *54*, 8340–8362.
- (11) Kalani, M.; Brismar, K.; Fagrell, B.; Ostergren, J.; Jorneskog, G. *Diabetes Care* **1999**, *22*, 147–151.
- (12) Sakadžić, S.; Roussakis, E.; Yaseen, M. A.; Mandeville, E. T.; Srinivasan, V. J.; Arai, K.; Ruvinskaya, S.; Devor, A.; Lo, E. H.; Vinogradov, S. A.; Boas, D. A. *Nat. Methods* **2010**, *7*, 755–759.
- (13) Pfister, A.; Zhang, G.; Zareno, J.; Horwitz, A. F.; Fraser, C. L. *ACS Nano* **2008**, *2*, 1252–1258.
- (14) Bowers, D. T.; Tanes, M. L.; Das, A.; Lin, Y.; Keane, N. A.; Neal, R. A.; Ogle, M. E.; Brayman, K. L.; Fraser, C. L.; Botchwey, E. A. *ACS Nano* **2014**, *8*, 12080–12091.
- (15) Palmer, G. M.; Fontanella, A. N.; Shan, S.; Hanna, G.; Zhang, G.; Fraser, C. L.; Dewhurst, M. W. *Nat. Protoc.* **2011**, *6*, 1355–1366.
- (16) Palmer, G. M.; Fontanella, A. N.; Zhang, G.; Hanna, G.; Fraser, C. L.; Dewhurst, M. W. *J. Biomed. Opt.* **2010**, *15*, 066021–066021.

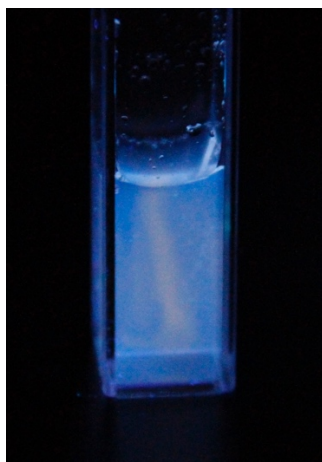
- (17) Xu, S.; Evans, R. E.; Liu, T.; Zhang, G.; Demas, J. N.; Trindle, C. O.; Fraser, C. L. *Inorg. Chem.* **2013**, *52*, 3597–3610.
- (18) Zhang, G.; Xu, S.; Zestos, A. G.; Evans, R. E.; Lu, J.; Fraser, C. L. *ACS Appl. Mater. Interfaces* **2010**, *2*, 3069–3074.
- (19) Dong, H.; Esser-Kahn, A. P.; Thakre, P. R.; Patrick, J. F.; Sottos, N. R.; White, S. R.; Moore, J. S. *ACS Appl. Mater. Interfaces* **2012**, *4*, 503–509.
- (20) Aluthge, D. C.; Xu, C.; Othman, N.; Noroozi, N.; Hatzikiriakos, S. G.; Mehrkhodavandi, P. *Macromolecules* **2013**, *46*, 3965–3974.
- (21) Koch, M.; Perumal, K.; Blacque, O.; Garg, J. A.; Saiganesh, R.; Kabilan, S.; Balasubramanian, K. K.; Venkatesan, K. *Angew. Chem. Int. Ed.* **2014**, *53*, 6378–6382.
- (22) Morris, W. A.; Sabat, M.; Butler, T.; DeRosa, C. A.; Fraser, C. L. *J. Phys. Chem. C* **2016**, *120*, 14289–14300.
- (23) Berger, G.; Soubhye, J.; Meyer, F. *Polym. Chem.* **2015**, *6*, 3559–3580.
- (24) Payne, S. J.; Zhang, G.; Demas, J. N.; Fraser, C. L.; Degraff, B. A. *Appl. Spectrosc.* **2011**, *65*, 1321–1324.
- (25) Wang, X.; Wolfbeis, O. S. *Chem. Soc. Rev.* **2014**, *43*, 3666–3761.
- (26) Baggaley, E.; Weinstein, J. A.; Williams, J. A. G. Springer Berlin Heidelberg, 2014; pp 205–256.
- (27) Lakowicz, J. R. *Principles of Fluorescence Spectroscopy*; Springer US: New York, 2006.
- (28) Lehner, P.; Staudinger, C.; Borisov, S. M.; Klimant, I. *Nat. Commun.* **2014**, *5*, 4460.
- (29) Bolton, O.; Lee, K.; Kim, H.-J.; Lin, K. Y.; Kim, J. *Nat. Chem.* **2011**, *3*, 205–210.
- (30) Zhang, X.; Xie, T.; Cui, M.; Yang, L.; Sun, X.; Jiang, J.; Zhang, G. *ACS Appl. Mater. Interfaces* **2014**, *6*, 2279–2284.

- (31) Colomines, G.; Ducruet, V.; Courgneau, C.; Guinault, A.; Domenek, S. *Polym. Int.* **2010**, *59*, 818–826.
- (32) Meier, R. J.; Fischer, L. H.; Wolfbeis, O. S.; Schäferling, M. *Sens. Actuat. B: Chem.* **2013**, *177*, 500–506.
- (33) Zheng, X.; Tang, H.; Xie, C.; Zhang, J.; Wu, W.; Jiang, X. *Angew. Chem. Int. Ed.* **2015**, *54*, 8094–8099..
- (34) Kochmann, S.; Baleizão, C.; Berberan-Santos, M. N.; Wolfbeis, O. S. *Anal. Chem.* **2013**, *85*, 1300–1304.
- (35) Sun, X.; Zhang, X.; Li, X.; Liu, S.; Zhang, G. *J. Mater. Chem.* **2012**, *22*, 17332–17339.
- (36) Lorusso, G.; Rüegg, C. *Histochem. Cell Biol.* **2008**, *130*, 1091–1103.
- (37) Quaranta, M.; Borisov, S. M.; Klimant, I. *Bioanal. Rev.* **2012**, *4*, 115–157.
- (38) Mayoral, M. J.; Ovejero, P.; Cano, M.; Orellana, G. *Dalton Trans.* **2011**, *40*, 377–383.
- (39) Huong, S. P.; Rocher, E.; Fourneron, J.-D.; Charles, L.; Monnier, V.; Bun, H.; Andrieu, V. *J. Photochem. Photobiol. A Chem.* **2008**, *196*, 106–112.
- (40) Zawadiak, J.; Mrzyczek, M. *Spectrochim. Acta Part A Mol. Biomol. Spectrosc.* **2010**, *75*, 925–929.
- (41) Sayre, R. M.; Dowdy, J. C.; Gerwig, A. J.; Shelds, W. J.; Lloyd, R. V. *Photochem. Photobiol.* **2007**, *81*, 452–456.
- (42) Chatelain, E.; Gabard, B. *Photochem. Photobiol.* **2001**, *74*, 401–406.
- (43) Yamaji, M.; Suwa, Y.; Shimokawa, R.; Paris, C.; Miranda, M. Á. *Photochem. Photobiol. Sci.* **2015**, *14*, 1673–1684.
- (44) Zakharova, G. V.; Chibisov, A. K.; Sazhnikov, V. A.; Kononevich, Y. N.; Muzafarov, A. M.; Alfimov, M. V. *High Energy Chem.* **2013**, *47*, 327–330.

- (45) Wang, X.; Gorris, H. H.; Stolwijk, J. A.; Meier, R. J.; Groegel, D. B. M.; Wegener, J.; Wolfbeis, O. S. *Chem. Sci.* **2011**, 2, 901–906.
- (46) Zhou, Y.; Chen, Y.-Z.; Cao, J.-H.; Yang, Q.-Z.; Wu, L.-Z.; Tung, C.-H.; Wu, D.-Y. *Dye. Pigment.* **2015**, 112, 162–169.
- (47) Bender, J. L.; Corbin, P. S.; Fraser, C. L.; Metcalf, D. H.; Richardson, F. S.; Thomas, E. L.; Urbas, A. M. *J. Am. Chem. Soc.* **2002**, 124, 8526–8527.
- (48) Williams, D. B. G.; Lawton, M. *J. Org. Chem.* **2010**, 75, 8351–8354.
- (49) Demas, J. N.; Crosby, G. A. *J. Phys. Chem.* **1971**, 75, 991–1024.
- (50) DeRosa, C. A.; Kerr, C.; Fan, Z.; Kolpaczynska, M.; Mathew, A. S.; Evans, R. E.; Zhang, G.; Fraser, C. L. *ACS Appl. Mater. Interfaces* **2015**, 7, 23633–23643.

Chapter 3:

Difluoroboron Naphthyl Phenyl β -Diketonate-Polylactide Materials



3.1. Introduction

In this chapter, a series of naphthyl-phenyl dye-polymer conjugates is presented.¹ Diketonate ligands, boron initiators, and associated polymers products were designed with the following fundamental and applied considerations in mind. First, extended conjugation afforded by the naphthyl ring in Np-Ph systems (versus Ph-Ph in dbm) can lead to more redshifted dyes in new color regimes for multiplexing applications.² Additionally, understanding ways that conjugation length correlates with emission wavelengths for BF₂bdk-PLA materials is important for generating redshifted materials for greater tissue penetration of light in biological contexts. Previous studies showed that overall conjugation length is not the only determinative factor for emission wavelength, given ICT effects.^{2,3}

Substituents and their placement influence electron density of the arene rings and thus, material optical properties. The challenge with naphthyl-phenyl dyes is the initial electron imbalance between the rings, so it is important to consider where a heavy atom or an alkoxy linkage for the polymer is placed (Figure 3.1.). Previous Fraser lab members studied modulation of triplet emission by heavy atom placement in Np-Ph dye/polymer blends.³ Here, we test whether this

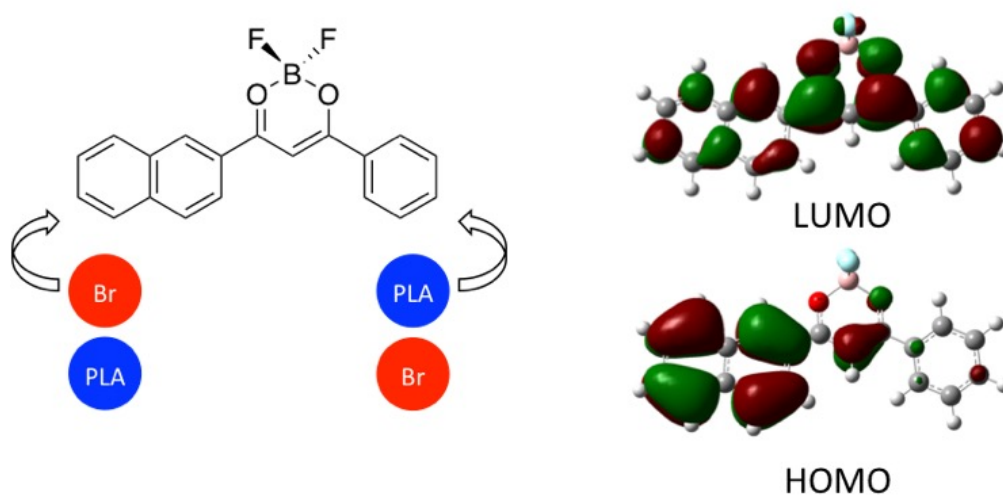


Figure 3.1. Design of Difluoroboron Naphthyl-Phenyl β-Diketonate Polymer Materials.

phenomenon extends to dye-polymer conjugates. In the present series, polymers are attached to dyes via electron donating alkoxy linkages that can perturb the donor strength of the two arene rings. Thus, polymer and bromide substituent attachment at either phenyl or naphthyl rings is compared. Once dye-scaffolds were shown to have promising properties, the investigation was extended to an iodide substituted derivative to tailor the oxygen sensitivity.^{4,5}

3.2. Results and Discussion

3.2.1. Synthesis

Boron-dye initiators and PLA polymer congeners were prepared using previous methods (Figure 3.2).⁵⁻⁷ A representative boron polymer synthesis via β -diketonate ligand **3** and boron complex initiator **7** is illustrated in Scheme 3.1 for BF_2bnmPLA (**11**). Ligands are prepared via Claisen condensation of appropriate ketone and ester building blocks. Primary alcohols are installed on the ketones to serve as sites for D,L-lactide polymerization. Commercially available 4-

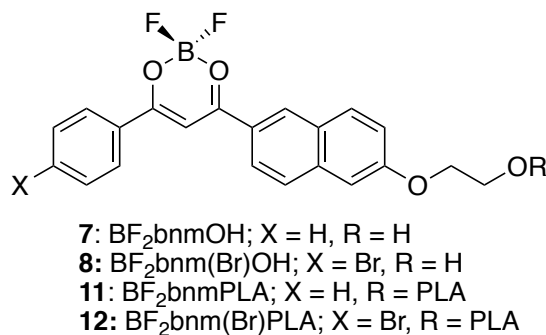
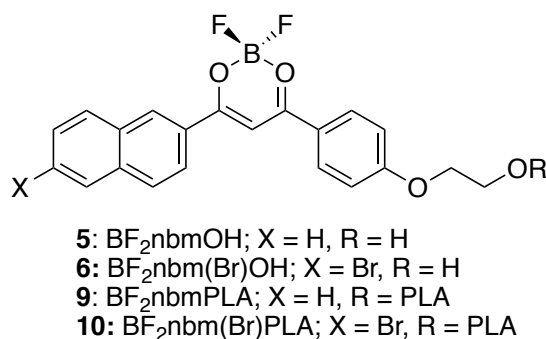
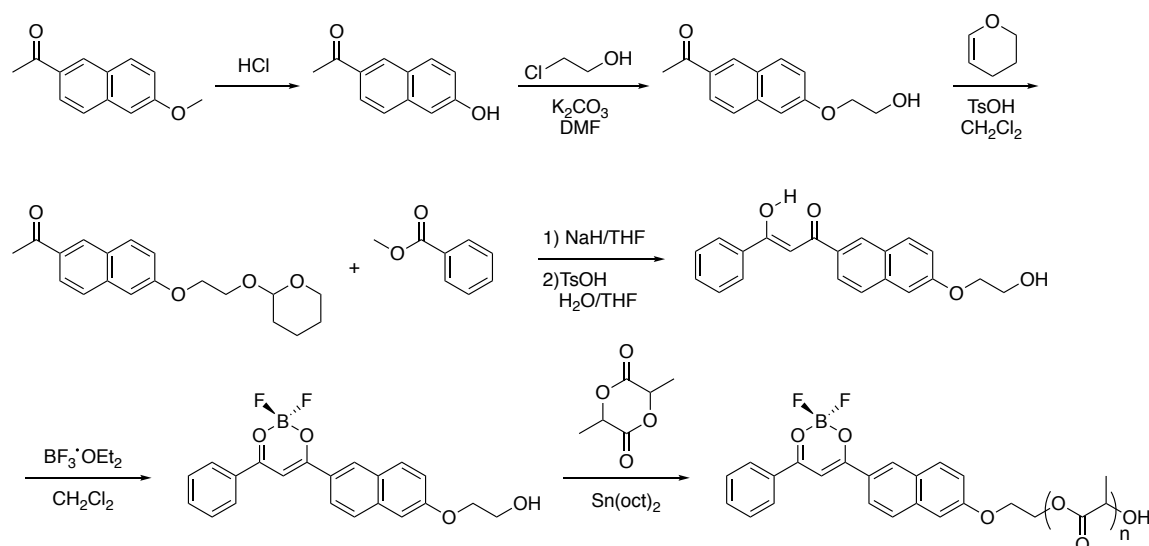


Figure 3.2. Nomenclature and Numbering of Difluoroboron Naphthyl Phenyl β -Diketonate-Polylactide Materials With and Without Bromide.

hydroxyacetophenone, or 6-hydroxy-2-acetonaphthone prepared by acid hydrolysis of 6-methoxy-2-acetonaphthone, are functionalized with $-OCH_2CH_2OH$ via Williamson ether synthesis, and protected with 1,2-dihydropyran for Claisen condensation in the presence of NaH. Following deprotection and purification by recrystallization. The β -diketonate ligands (**1-4**) were boronated with $BF_3 \cdot OEt_2$ to yield the initiators for lactide polymerization. Reactions were stirred until substrates were completely consumed, according to TLC. In many instances, products precipitated from the reaction mixture over time. After purification by recrystallization, powders **5-8** were obtained. The structure and purity of boron dye products were confirmed by MS and 1H NMR spectroscopy.

Hydroxyl-functionalized boron initiators **5-8** were used to produce dye-polymer conjugates **9-12** by solvent-free ring opening polymerization of D,L-lactide using a tin octoate catalyst at 130 °C. Samples were purified by precipitation from CH_2Cl_2 /hexane to remove the catalyst, and

Scheme 3.1. Representative Synthesis of β -Diketonate Ligand, Boron Initiator and Polymer Shown for bnmOH (**3**), BF_2 bnmOH (**7**) and BF_2 bnmPLA (**11**).



multiple times with CH_2Cl_2 /cold methanol until ^1H NMR spectroscopy confirmed all monomer was removed. Higher molecular weight polymers were achieved via higher monomer loadings and longer reaction times.

3.2.2. Optical Properties in Solution

Absorption spectra for boron initiators are compared in Figure 3.3. All complexes have high extinction coefficients ($48000\text{--}65000\text{ M}^{-1}\cdot\text{cm}^{-1}$) typical for $\pi\text{--}\pi^*$ transitions in this family of dyes and high-energy features on dominant peaks. For initiators **5** and **6**, the high-energy shoulders at 402 and 395 nm are more distinct. Introduction of the bromide heavy atom onto the Np site of BF_2nbmOH resulted in a slight bathochromic shift (3 nm) and increase in extinction coefficient; whereas, bromination of the Ph site of BF_2nbmOH showed a slightly greater redshift (7 nm) but a decrease in molar absorptivity. Representative UV/Vis spectral data for polymers ($\sim 8\text{ kDa}$ samples) are also provided in Table 3.1. Spectra are very similar to corresponding boron initiators with slightly decreased extinction coefficients, typical for these boron bdk PLA materials.

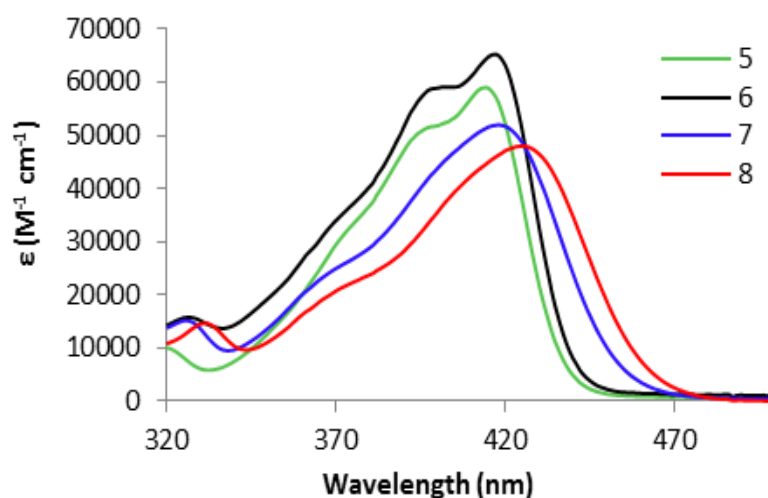


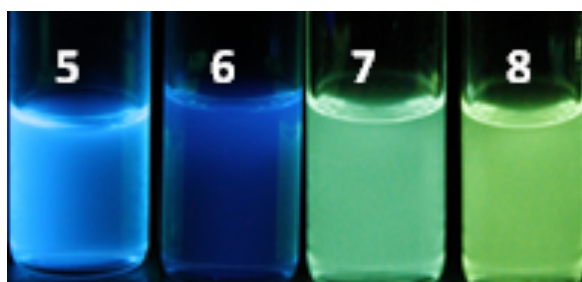
Figure 3.3. Absorption spectra for boron initiators in dilute CH_2Cl_2 solutions ($\text{Abs} < 0.1$).

Table 3.1. Absorption and Emission Data for Boron Initiators and Representative Polymer Samples in CH₂Cl₂.

		λ_{abs}^a (nm)	ϵ^b (M ⁻¹ cm ⁻¹)	λ_{em}^c (nm)	τ_F^d (ns)	Φ_F^e	τ_{rad}^f	Stokes shift (cm ⁻¹)
BF ₂ nbmOH	5	414	59 000	452	1.55	0.40	3.88	2031
BF ₂ nbmPLA	9b	414	54 000	458	1.75	0.38	4.61	2321
BF ₂ n(Br)bmOH	6	417	65 000	448	0.53	0.19	2.79	1659
BF ₂ n(Br)bmPLA	10b	416	50 000	448	0.52	0.18	2.89	1717
BF ₂ bnmOH	7	418	52 000	505	3.41	0.64	5.33	4121
BF ₂ bnmPLA	11b	418	43 000	501	3.32	0.71	4.68	3963
BF ₂ b(Br)nmOH	8	425	48 000	521	3.33	0.75	4.44	4336
BF ₂ b(Br)nmPLA	12a	425	25 000	514	3.27	0.72	4.54	4074

^aAbsorption maxima. ^bExtinction coefficients calculated at the absorption maxima. ^cFluorescence emission maxima. ^dFluorescence lifetime excited with a 369 nm light-emitting diode (LED) monitored at the emission maximum. All fluorescence lifetimes are fitted with single-exponential decay. ^eRelative quantum yield, with anthracene in EtOH as a standard. ^fRadiative lifetime, where $\tau_{\text{rad}} = \tau_F / \Phi_F$.

Luminescence data for initiators and representative polymers in solution are given in Table 3.1. All samples exhibit intense emission under UV excitation (Figure 3.4). Initiators **5** and **6** with alkoxy donors on the phenyl rings show intense blue emission at 452 nm and 448 nm, respectively, while fluorescence for **7** and **8** with –OR donors on the naphthyl rings are redshifted to 505 nm and 521 nm, respectively. Once PLA is grown from the initiators, the emission maxima slightly blue-shifted (4–7 nm), which may be attributed to a solvatochromic effect or enhanced solubility and thus, diminished tendency to dimerize (Table 3.1).⁸

**Figure 3.4.** Boron dye initiators **5–8** in CH₂Cl₂ showing emission colors.

Typically, increased conjugation results in redshifted emission.² Naphthyl-phenyl systems here are redshifted as predicted, compared to previously reported phenyl-phenyl (i.e. dbm) derivatives. For example, BF₂dbmPLA showed an absorption maximum, $\lambda_{\text{abs}} = 396$ nm and emission maximum, $\lambda_{\text{em}} = 426$ nm, which are more blue-shifted than these naphthyl dye samples, **9-12** (Table 3.1; e.g. **9b**: $\lambda_{\text{abs}} = 414$ nm, $\lambda_{\text{em}} = 458$ nm).⁶ Previous studies showed that a π -donating methoxy group red-shifts emission.² Fluorescence wavelengths for samples **5-12** with the –OCH₂CH₂OR initiator (R = H) and polymer (R = PLA) tails are consistent with this trend. Alkoxy placement also plays a role in emission maxima. For example, **5** (Np-Ph) with alkoxy substitution on the phenyl ring emits at 452 nm and displays a small Stokes shift (2031 cm⁻¹). In comparison, dye **7** (Ph-Np) with substitution on the naphthyl ring has further redshifted emission (i.e. 505 nm) and shows a larger Stokes shift (4121 cm⁻¹).

In addition to red-shifting absorbance, bromide heavy atom incorporation in dyes **6** and **8** also affects emission. It is well known that halide heavy atoms result in decreased luminescence lifetimes and quantum yields via enhanced intersystem crossing.⁹ Results for brominated and parent (i.e. H) compounds are consistent with this trend. For example, the presence of bromide in BF₂n(Br)bmOH **6** results in a decrease in fluorescence lifetime compared to BF₂nbmOH **5** (i.e. **5**: $\tau = 1.55$ ns (no heavy atom) vs **6**: $\tau = 0.53$ ns (heavy atom)) and a decrease in fluorescence quantum yield (**5**: $\Phi_F = 0.4$ vs **6**: $\Phi_F = 0.19$). A similar trend is noted in the corresponding polymers **9** and **10**. In samples **6** and **10**, heavy atom substitution is on the larger, more electron rich naphthyl donor, but in **8** and **12**, when the bromide is present on the smaller, less electron rich phenyl donor, the heavy atom effect is much less pronounced.⁹ Lifetimes and quantum yields for **8** and **12** are very similar (Table 3.1). These results with initiators and polymer conjugates are consistent with prior BF₂bdk model studies indicating moderate to strong ICT character for unsymmetrically

substituted difluoroboron diketonates.^{2,10} A greater disparity in π -electron-donating ability of the two arene rings results in stronger ICT character dominated by the more electron-rich aryl group.

3.2.3. Computational Studies

Previously, it was shown that the electronic transitions of BF₂bdks depend on their molecular symmetries. According to TD-SCF calculations,¹¹ the reddest and strongest transitions are the HOMO to the LUMO transitions. Stronger ICT is observed for complexes with unsymmetrical di-arene ligands, where there is a disparity in electron donor ability from one arene ring (e.g. anthracene) compared to another (e.g. phenyl). On the other hand, when the bdk arene rings are comparable (i.e. Ph-Ph in dbm), a delocalized π - π^* model is proposed.¹² Similar trends are noted here for initiator complexes, **5-8**, which were chosen as the subjects for computational modeling given their relative simplicity compared to the respective polymers. Molecular orbital diagrams for compounds **5**, **7** and **8** suggest intramolecular charge transfer (ICT) (Figure 3.5). Electron density is localized on the stronger naphthyl donor in the HOMOs for **5**, **7** and **8**; whereas, in the LUMOs it is distributed across the molecular structure. In contrast, for **6** the electron density is

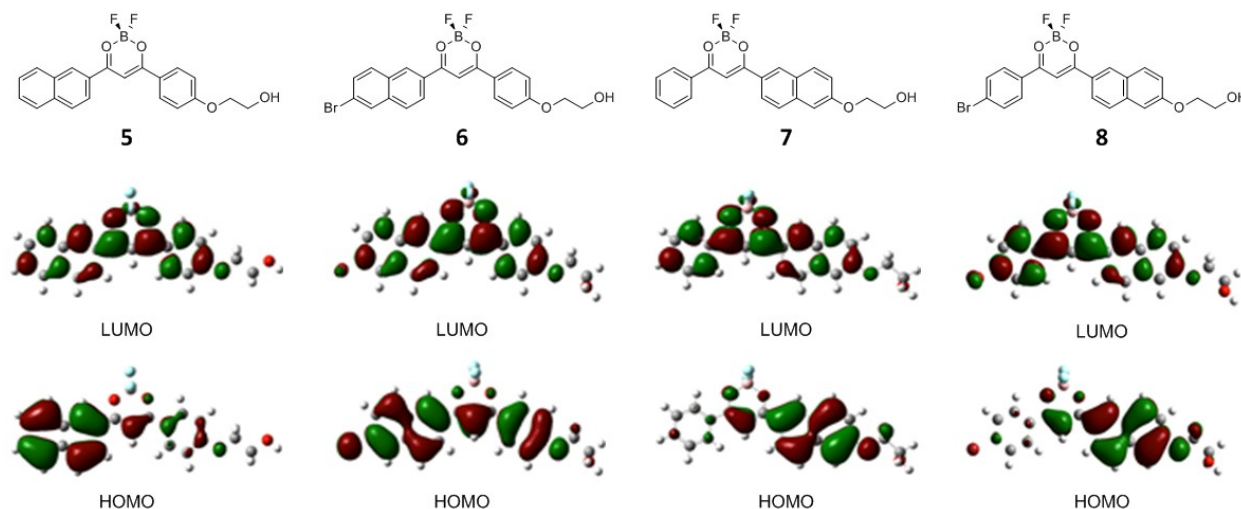


Figure 3.5. Molecular orbital diagrams for compounds **5-8** showing the highest occupied molecular orbitals (HOMO) and lowest unoccupied molecular orbitals (LUMO) in CH₂Cl₂.

more distributed through the molecular structure on both HOMO and LUMO and the π to π^* transition dominates (Figure 3.5). The electron withdrawing bromide substituent may diminish electron density on the naphthyl ring, making donor capacity of Br-Np and Ph-OR rings comparable. Experimental absorption and emission data lend credence to this claim. Radiative lifetimes (τ_{rad}) increase with increasing ICT character,² and this is a trend that is observed for samples **5**, **7** and **8** (3.88-5.33 ns) compared to **6** (2.89 ns), with **6** showing the shortest τ_{rad} . Additionally, both **7** and **8** have larger Stokes shifts compared to **5** and **6**. As in naphthyl model studies, these systems show no distinct ITC features in absorption or emission spectra.

3.2.4. Optical Properties as Films

Boron polymers were also studied in the solid state. Thin films were prepared in vials by slow evaporation of CH_2Cl_2 solutions, followed by drying *in vacuo*. Optical properties for polymers **9-12**, including different molecular weights, are presented in Table 3.2. Fluorescence spectra and lifetime measurements were obtained under ambient conditions (e.g. air, ~21% oxygen). Previous studies showed that BF_2bdk luminescence properties are dependent upon the molecular weight of polylactide,¹¹ or dye loading in dye/polymer blends.^{19,20} Shorter dye–dye distances corresponding to low dye-PLA molecular weight, resulted in lower energy green emission for BF_2dbmPLA ; whereas, longer polymer chains (small dye loadings) with diminished dye-dye interactions correlated with blueshifted emission.^{11,19} Polymers **9-12** also follow this trend, namely, wavelength

Table 3.2. Luminescence Data for Films made from Boron Polymers of Different Molecular Weights.

Sample			Fluorescence		RTP	
Polymer	ID	M_n^a (kDa)	λ_{em}^b (nm)	τ_{pw0}^c (ns)	λ_{em}^d (nm)	τ_{pw0}^e (ms)
BF ₂ nbmPLA	9a	5.4	526	12.85	558	69.76
	9b	7.7	496	8.84	555	102.7
	9c	16.1	461	2.57	552	130.9
BF ₂ nbm(Br)PLA	10a	6.8	491	3.69	568	10.50
	10b	8.8	483	1.71	565	11.61
	10c	11.7	467	1.02	566	14.36
	10d	26.2	460	0.76	565	14.64
BF ₂ bnmPLA	11a	5.2	533	13.39	550	20.26
	11b	7.5	512	9.10	540	61.94
	11c	9.5	505	7.74	545	91.14
BF ₂ bnm(Br)PLA	12a	5.6	518	5.00	538	25.95
	12b	12.9	500	3.47	538	40.76
	12c	16.6	495	3.25	539	45.81

^aNumber-average molecular weight detected by GPC in THF solvent. ^bSteady-state fluorescence spectra emission maximum under air. Excitation source: 369 nm xenon lamp. ^cFluorescence lifetime excited with a 369 nm light-emitting diode (LED) monitored at the emission maximum. All fluorescence lifetimes are fitted with multi-exponential decay. ^dDelayed emission spectra maximum under N₂. Excitation source: xenon flash lamp. ^ePre-exponential weighted RTP lifetime. Excitation source: xenon flash lamp; RTP lifetime fit to triple-exponential decay.

blue-shifts with increasing polymer molecular weight. For example, polymers **9a-c** display emission wavelengths of 526, 496, and 461 nm respectively. Furthermore, the sensitivity to dye loading (i.e. M_n) varies for different dyes. For instance, for **9a** (5.4 kDa) and **9c** (16.1 kDa) the emission wavelength shifts 65 nm, while from **12a** (5.6 kDa) to **12c** (16.6 kDa) it shifts only 23 nm (Figures 3.5, 3.6 and Table 3.2).

Fluorescence lifetimes were recorded for BF₂bdkPLA films under ambient conditions (Tables 3.2) In all cases, lifetimes fit to triple exponential decay, which may be ascribed to different fluorophore associations or polymer microenvironments in the solid state. As the polymer

molecular weight increases, dye-dye interactions decrease, and the pre-exponential weighted lifetimes, τ_{pw0} , steadily decrease. For the entire molecular weight range examined in this study, dye aggregation may be present in polymer films, because only for **12c**, do lifetimes approach the value measured for monomeric structures in solution. As expected, the heavy atom has a significant influence on the fluorescence lifetime. Lifetimes for non-halogenated polymers **9a** and **11a** lifetimes are ~ 13 ns; whereas, lifetimes for brominated analogues **10a** and **12a** decrease to 3.7 ns and 5.0 ns, respectively.

Phosphorescence measurements for polymer films were performed under a nitrogen atmosphere and spectra were recorded with a 2 ms delay. Previous studies showed that BF₂bdk dyes exhibit room temperature phosphorescence (RTP) in rigid media such as poly(lactic acid) ($T_g \sim 60$ °C). Here too, RTP of varying intensities was observed for dye-polymer conjugates **9-12**. Phosphorescence data for polymer films is provided in Table 3.2. The phosphorescence maxima vary little (538-568 nm) for dyes in this series, and for different molecular weights (i.e. dye loadings) of a given dye. For example, the RTP for BF₂nbmPLA polymers **9a-c** is ~ 555 nm, and for its brominated derivatives BF₂nbm(Br)PLA **10a-d** the phosphorescence maxima slightly redshifted to ~ 565 nm. For the BF₂nbmPLA polymers **11a-c**, the RTP is ~ 545 nm and the -Br derivatives BF₂nbm(Br)PLA, **12a-c** show slightly blueshifted RTP at ~ 538 nm. From air to N₂, only BF₂nbm(Br)PLA (**10**) showed strong phosphorescence, ideal for oxygen sensing (Figure 3.6).⁵ Even though BF₂nbm(Br)PLA (**12**) has a bromide substituted, the position is ineffective to promote intersystem crossing, and enhance the phosphorescence. This is supported by the calculations, as there is not sufficient electron density on the dye scaffold where the bromide is located (Figure 3.5).

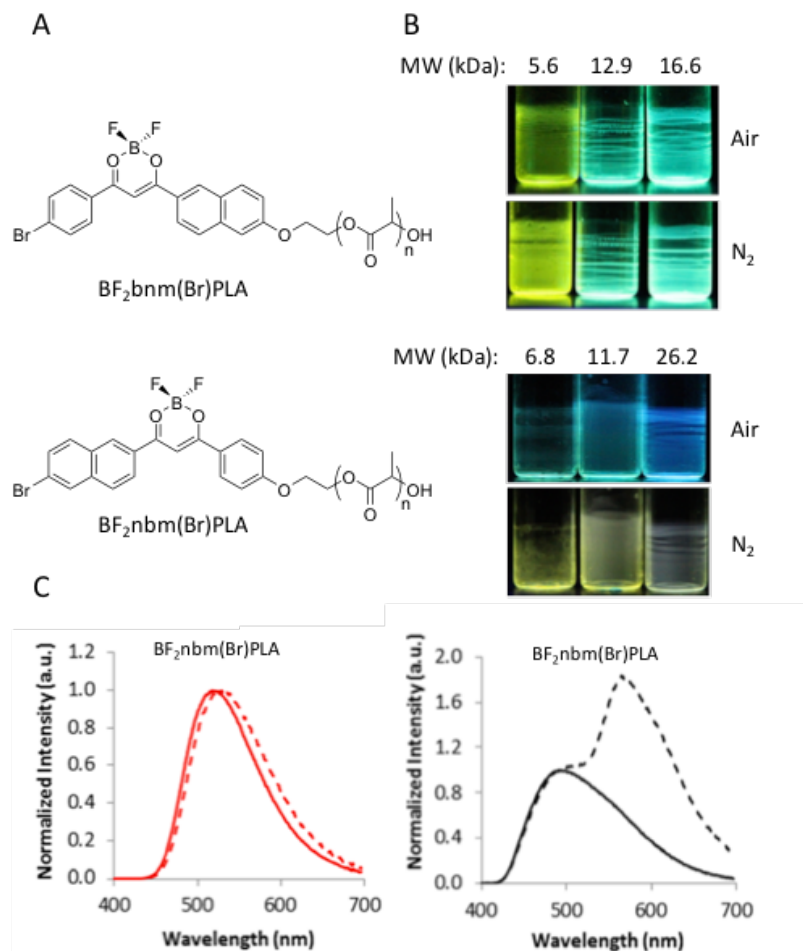


Figure 3.6. Heavy-Atom Placement and Oxygen-Sensing Response of Difluoroboron Naphthyl-Phenyl β -Diketonate PLA Polymers. A) Chemical structures of bromide substituted dyes. B) Images of polymers of variable in air and under N_2 . C) Total emission spectra of $\text{BF}_2\text{bnm}(\text{Br})\text{PLA}$ (**12a**) and $\text{BF}_2\text{nbm}(\text{Br})\text{PLA}$ (**10a**) under air (solid line) and N_2 (dashed line).

Polymer **10**, $\text{BF}_2\text{nbm}(\text{Br})\text{PLA}$ shows ideal features for ratiometric sensing. Fluorescence and phosphorescence peaks are well separated and phosphorescence intensity is strong for all samples **10a-10d** ($M_n = 7\text{-}26$ kDa) (Figure 3.7). Even the sample with the lowest dye loading has strong phosphorescence intensity and could be useful for sensing, minimizing the valuable dye reagent and possible toxicity in a biological environment.

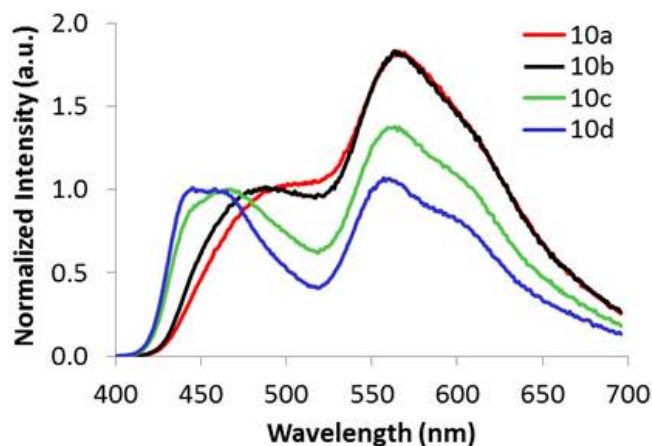


Figure 3.7. Total Emission Spectra Showing Relative Fluorescence and Phosphorescence Intensities for Films of $\text{BF}_2\text{nbm}(\text{Br})\text{PLA}$ (**10a-d**) Under N_2 .

3.2.5. Iodide-Substituted $\text{BF}_2\text{nbm}(\text{I})\text{PLA}$

Given promising properties for $\text{BF}_2\text{nbm}(\text{Br})\text{PLA}$, the naphthyl-phenyl system was extended to the iodide substituted dye, $\text{BF}_2\text{nbm}(\text{I})\text{PLA}$, as shown in Figure 3.8. The bromide sample, has a phosphorescence lifetime of ~ 13 ms, still very long, and therefore, highly sensitive to oxygen. Inclusion of the iodide should decrease the lifetime to enter a broader oxygen sensing regime. Three materials were prepared for comparison; the unsubstituted BF_2nbmPLA (**HP**),¹³ and two heavy atom analogues, $\text{BF}_2\text{nbm}(\text{Br})\text{PLA}$ (**BrP**)¹⁴ and $\text{BF}_2\text{nbm}(\text{I})\text{PLA}$ (**IP**). The polymers in this study are different molecular weights than **9** and **10**, and are named as **XP**, where X = H, Br,

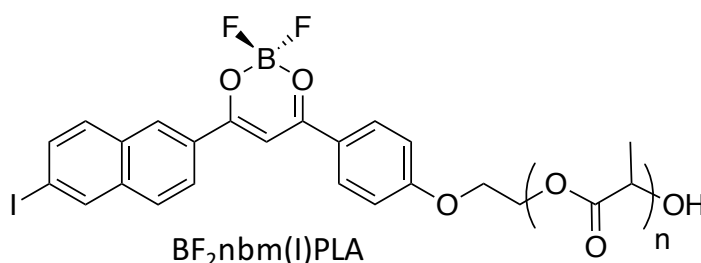


Figure 3.8. Chemical Structure of $\text{BF}_2\text{nbm}(\text{I})\text{PLA}$

or I. Polymers were prepared with similar MWs ($M_n = 16 - 20$ kDa) to ensure that differences in optical properties stem from the halide substituent and not dye concentration effects.⁴¹ Furthermore, in a previous report we discovered higher MW polymers (>16 kDa) have larger fluorescence to room temperature phosphorescence (RTP) wavelength gaps, important for ratiometric oxygen quantification techniques, and they are more photostable (Figures S3.1.-3S.5.; Appendix B).^{4,15}

The polymer luminescence was analyzed in CH_2Cl_2 solution (Table S3.1; Appendix B) and as thin films in glass vials (Table 3.3 and Figure 3.8). Dye initiators and dye-PLA conjugates had very similar properties in dilute CH_2Cl_2 solutions, indicating that the integrity of the dye is maintained during the polymerization process (i.e. negligible boron decomplexation).^{12,16}

For solid state films, all polymers have indistinguishable blue fluorescence at ~ 460 nm and lifetimes, $\tau_F < 2$ ns. Phosphorescence red-shifted and the RTP intensity increased relative to the fluorescence, while lifetimes decreased more dramatically, as is expected for the **HP** to **BrP** and **IP** series given the heavy atom effect.⁹ A weak phosphorescence shoulder and long lifetime ($\tau_p = 453$ ms) were observed for **HP**. The bromide polymer, **BrP**, showed two distinguishable peaks for fluorescence and phosphorescence, and a decreased lifetime (14.5 ms). In contrast,

Table 3.3. Optical Properties of Polymer Films

Sample		λ_F^a (nm)	τ_F^b (ns)	λ_p^c (nm)	τ_p^d (ms)
BF_2nbmPLA	HP	459	1.76	545	453
$\text{BF}_2\text{nbm(Br)PLA}$	BrP	462	0.86	561	14.5
$\text{BF}_2\text{nbm(I)PLA}$	IP	461	0.47	569	1.90

^aSteady-state fluorescence emission maximum ($\lambda_{\text{ex}} = 385$ nm) ^bFluorescence lifetime ($\lambda_{\text{ex}} = 369$ nm LED) ^cDelayed emission spectra maxima under N_2 ($\lambda_{\text{ex}} = 385$ nm) ^dPre-exponential weighted RTP lifetime.

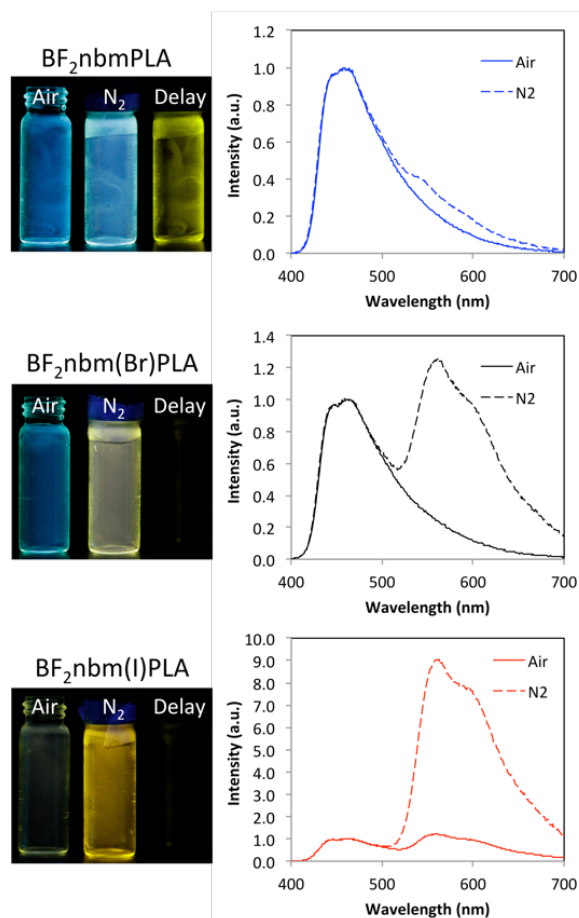


Figure 3.8. Optical Properties of Polymer Films. Photographs of dye-polymers under air, N₂, and under N₂ with the lamp turned off (delay) and corresponding total emission spectra in air and N₂ ($\lambda_{\text{ex}} = 385$ nm).

phosphorescence dominated for the iodide polymer (**IP**), and the lifetime shortened (1.9 ms).

These results show that halide substitution primarily influenced the RTP, while features of the fluorescence (e.g. color) are well maintained. Because changes in color are negligible, detection methods can be broadly applied without changing settings (e.g. filters), and the three materials can be easily interchanged to screen and identify the optimal material for a given sensing application.

3.2.6. Nanoparticles

The halide substituted dye-PLA conjugates are distinguished by their RTP intensities and unquenched lifetimes, which relate to two ways to quantify oxygen quenching (I_0/I or τ_0/τ).^{17,18}

As shown in equations 1 and 2, the unquenched RTP lifetime (τ_0) is directly correlated to the Stern-Volmer quenching constant (K_{SV}).

$$\frac{I_0}{I} = \frac{\tau_0}{\tau} = 1 + K_{SV}[Q] \quad (\text{Eq. 3.1})$$

$$K_{SV} = k_q \tau_0 \quad (\text{Eq. 3.2})$$

As a result, materials with long RTP lifetimes are more sensitive to oxygen (Q) quenching (large K_{SV}), and will operate within a narrower O_2 sensing range. Furthermore, materials with longer lifetimes can be detected with less costly instrumentation (e.g. lower frame rate). Here, we show that halide activated RTP influences the oxygen sensitivity and mode of detection via lifetime (τ/τ_0) or intensity (I/I_0) techniques. The hydrogen substituted dye-polymer (**HP**), with weak RTP and a long lifetime (~ 400 ms) serves as an ultrasensitive lifetime oxygen sensor, whereas the iodide derivative (**IP**), with a short lifetime (~ 2 ms) but intense RTP, functions as a full range ratiometric sensor. The bromide derivative showed balanced F and RTP intensities, and a relatively long RTP lifetime (~ 14 ms). Therefore, with **BrP**, oxygen can be sensed via both detection modes.

To elucidate the oxygen sensing ranges and generate materials suitable for wound application, the polymers were fabricated as nanoparticles¹⁹ (**X-NPs**, where X = H, Br, and I) and subjected to oxygen calibration⁵ (Table 3.4, Figures S3.6-S3.10; Appendix B). The nanoparticles showed similar optical properties as the dye-polymer films and, as expected given varying phosphorescence lifetimes, each derivative showed a different dynamic range (Table S3.2; Appendix B). For **H-NP**, phosphorescence lifetime vs $[O_2]$ showed an oxygen sensing range of ~ 0 -0.3% (Figure S3.6; Appendix B). Also, because the RTP is very weak compared to the F, only RTP lifetime is practical for detection, not ratiometry.

Table 3.4. Optical Properties of Nanoparticles

NP	DLS ^a		Fluorescence		Phosphorescence		
	R _H (nm)	PD	λ _F ^b (nm)	τ _F ^c (ns)	λ _P ^d (nm)	τ _P ^e (ms)	τ ₀ / τ _{1%} ^f
H	38.5	0.09	459	1.76	543	127	32.0
Br	37.0	0.11	462	0.86	559	12.3	3.3
I	41.4	0.18	461	0.47	565	1.7	0.8

^aNP hydrodynamic radius (R_H) and polydispersity (PD) determined by dynamic light scattering (DLS). ^bSteady-state fluorescence spectra emission maximum under air. Excitation source: monochromator set to 385 nm with xenon lamp. ^cFluorescence lifetime excited with a 369 nm light-emitting diode (LED) monitored at the emission maximum. ^dDelayed emission spectra maxima under N₂. Excitation source: monochromator set to 385 nm with xenon lamp. ^ePre-exponential weighted RTP lifetime. ^fSensitivity measurement of NPs.⁷

For **Br-NP**, the phosphorescence intensity is strong enough for ratiometric imaging. Ratiometric referenced intensity calibration (i.e. comparing intensities at λ_F and λ_{RTP} maxima; I_F/I_P) revealed a linear correlation from 0-1% O₂ with reliable detection to 3% (Figure S3.9; Appendix B). Although it is possible to sense oxygen to 21%, changes in the F/P ratio are minimal from 3-21%, making it difficult to distinguish the O₂ level in these ranges. This may be attributed to the tail of the broad fluorescence emission spanning into the red region of the spectrum (~430-600 nm). This causes a “jack-knife” shape in the ratiometric calibration curve (Figures S3.8 and S3.9; Appendix B).^{17,20} At higher oxygen concentrations, oxygen insensitive fluorescence interferes with the oxygen sensitive RTP observed at the same wavelength. Lifetime techniques can circumvent this problem by eliminating fluorescence effects.²¹ Because the fluorescence emission is on the order of nanoseconds, and RTP, milliseconds, an appropriately timed gate can be applied to eliminate the singlet emission. When a lifetime calibration is performed on **Br-NP**, the Stern-Volmer quenching constant (τ_P vs %O₂) had a linear correlation from 0-21% O₂ (Figure S3.7.; Appendix B). Thus, both ratiometry and lifetime methods are suitable for **Br-NPs** within appropriate [O₂] ranges.

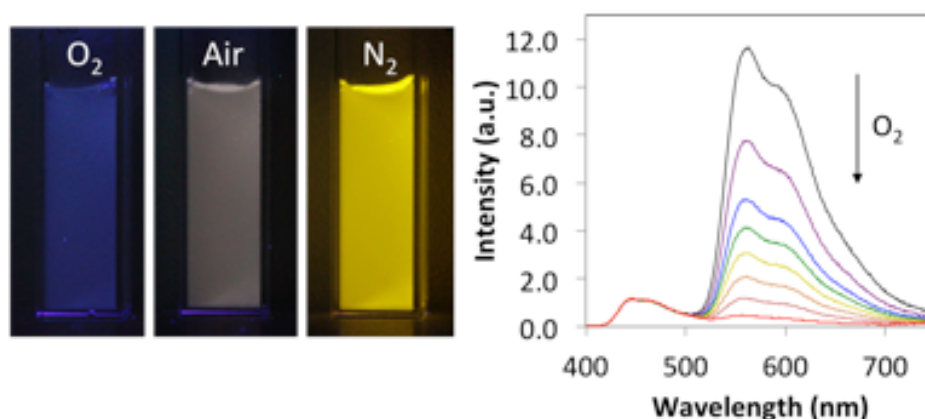


Figure 3.9. I-NP Oxygen Calibration. Images of an aqueous nanoparticle suspension under oxygen, air and nitrogen (left). Total emission spectra at 0-100% O₂ ($\lambda_{\text{ex}} = 385$ nm; black line = 0% O₂) (right).

The iodide derivative, **I-NP**, in contrast, showed oxygen-sensing capability unprecedented for boron bdk materials. From 0-100% O₂, the F/P ratio is linearly correlated ($R^2 = 0.993$; Figures 3.9 and S3.10; Appendix B). Furthermore, because the RTP is much stronger than F and is never fully quenched even in pure O₂ (Figure 3.9; red line spectrum), interference from fluorescence is negligible. Ratiometry works well for this material, while the unquenched lifetime (1.7 ms) is on the edge of the detection limits with our current camera instrumentation (2.0 ms).⁴⁷ While **H-NP** and **Br-NP** are best matched to anoxia and hypoxia (e.g. in tumors) respectively (Table S3.2; Appendix B), the reduction in oxygen sensitivity for **I-NP** dramatically increases potential uses in normoxic tissue (e.g. veins vs arteries: 10 vs 15% O₂)^{48,49} while still illuminating low O₂ and deoxygenated regions. The increased RTP intensity and decreased oxygen sensitivity of **I-NP** expands bio-imaging capabilities of BF₂bdkPLA materials.

3.2.7. Conclusion

In summary, naphthyl-substituted BF₂bdk materials with and without bromide heavy atoms were prepared for use as initiators to generate polymers with different molecular weights. Compared to previous dbm systems, the naphthyl materials displayed redshifted absorbance, fluorescence and

phosphorescence. Even when the general structure and the conjugation length of the dye are the same, the polymer attachment site—whether on the naphthyl or phenyl ring—plays an important role in electron density delocalization and optical properties.

Once an appropriate naphthyl-phenyl scaffold was identified, introduction of halide heavy atoms (Br and I) is an effective strategy to control the oxygen sensitivity in these materials. A series of naphthyl-phenyl (nbm) dye derivatives with hydrogen, bromide and iodide substituents were prepared for comparison. As nanoparticles, the hydrogen derivative was hypersensitive to oxygen (0-0.3%), while the bromide analogue was suited for hypoxia detection (0-3% O₂). The iodo derivative, BF₂nbm(I)PLA, showed excellent F to RTP peak separation and an 0-100% oxygen sensitivity range unprecedented for metal-free RTP emitting materials.

3.3. Experimental

3.3.1. Materials

3,6-Dimethyl-1,4-dioxane-2,5-dione (D,L-lactide, Sigma Aldrich) was recrystallized twice from ethyl acetate and stored under nitrogen. The ligand precursors, methyl 6-iodo-2-naphthoate,²² and 1-(4-(2-((tetrahydro-2H-pyran-2-yl)oxy)ethoxy)phenyl)ethan-1-one,⁷ and boron initiators BF₂nbmOH¹³ and BF₂nbm(Br)OH¹⁴ were prepared as previously described. Polymers were prepared by ring-opening polymerization from racemic lactide by a method previously described. Tin(II) 2-ethylhexanoate (Sn(oct)₂, Spectrum), boron trifluoride diethyl etherate (Aldrich, purified, redistilled), and all other reagents and solvents were used as received without further purification. Solvents CH₂Cl₂ and THF were dried and purified over 3 Å molecular sieves activated at 300 °C.²³ All other chemicals were reagent grade from Sigma-Aldrich and were used without further purification.

3.4.2. Methods

^1H NMR spectra were recorded on a Varian VMRS/600 (600 MHz) instrument in CDCl_3 . ^1H NMR peaks were referenced to the signals for the residual protiochloroform at 7.26 ppm. Coupling constants are given in hertz. Polymer molecular weights were determined by gel permeation chromatography (GPC) (THF, 25 °C, 1.0 mL/min, $\text{dn/dc} = 0.050$) using multiangle laser light scattering (SEC-MALS) ($\lambda = 658$ nm, 25 °C) and refractive index (RI) ($\lambda = 658$ nm, 25 °C) detection. Polymer Laboratories 5 μm mixed-C columns (guard column plus two columns) along with Wyatt Technology (Optilab T-rEX interferometric refractometer, miniDAWN TREOS multiangle static light scattering (MALS) detector, ASTRA 6.0 software) and Agilent Technologies instrumentation (series 1260 HPLC with diode array (DAD) detector, ChemStation) were used in GPC analysis. UV/vis spectra were recorded on a Hewlett-Packard 8452A diode-array spectrophotometer. Nanoparticles (~ 1 mg/mL) were prepared as previously described by DMF/ H_2O precipitation into deionized water.¹⁹

Luminescence Measurements. Steady-state fluorescence emission spectra were recorded on a Horiba Fluorolog-3 Model FL3-22 spectrofluorometer (double-grating excitation and double-grating emission monochromator). A 1 ms delay was used when recording the delayed emission spectra. Time-correlated single-photon counting (TCSPC) fluorescence lifetime measurements were performed with a NanoLED-370 ($\lambda_{\text{ex}} = 369$ nm) excitation source and a DataStation Hub as the SPC controller. Phosphorescence lifetimes were measured with a 1 ms multichannel scalar (MCS) excited with a flash xenon lamp ($\lambda_{\text{ex}} = 369$ nm; duration < 1 ms). Lifetime data were analyzed with DataStation v2.4 software from Horiba Jobin Yvon. Thin films were prepared on the inner wall of vials by dissolving polymers in CH_2Cl_2 (2 mg/mL) and evaporating the solvent by slowly rotating the vial under a low stream of nitrogen. The solution-cast films were then dried

in vacuo overnight before measurements. Fluorescence spectra and lifetimes of the films were obtained under ambient conditions (e.g., air, ~21% oxygen). The vials with the solution-cast films were purged and sealed with a Teflon cap and wrapped in parafilm in a glove box prior to phosphorescence measurements. The glove box was purged for 30 min prior to samples being sealed. Oxygen calibration of the nanoparticles was done in triplicate as previously described using analytical grade gases (Cole-Palmer flow gauges equipped with a mixing chamber; Praxair: pure N₂, 1.0% O₂, 21.0% O₂, or 100% O₂).⁵ Fluorescence and phosphorescence lifetimes were fit to double exponential decays. Spin-cast films and photostability measurements were done as previously described.⁴

6-Hydroxy-2-acetonaphthalene. 6-Methoxy-2-acetonaphthalene (1.5 g, 7.5 mmol) dissolved in 12 M HCl (500 mL) and was heated at 90 °C for 2h. The hot reaction mixture was filtered through a sintered glass frit (M) to remove a greenish black precipitate. The filtrate was allowed to cool to room temperature, and then the flask was further cooled in an ice water bath. The resulting white solid was collected by filtration and was washed with copious quantities of distilled water until the pH of the wash fraction was neutral (pH ~ 6.5). (Note: In certain preparations, when the sample was greenish or brownish in color, further purification by recrystallization from hexane/EtOAc was performed.) After drying *in vacuo*, a white powder was obtained: 1.27 g (91%). ¹H NMR (300 MHz, CDCl₃, ppm): δ 8.41 (s, 1H, 1-ArH), 8.00 (d, 1H, J = 8.7 Hz, 8-ArH), 7.89 (d, 1H, J = 9.0, 3-ArH), 7.72 (d, 1H, J = 9.0, 4-ArH), 7.20-7.16 (bm, 2H, 5, 7-ArH), 5.42 (s, 1H, OH), 2.71 (s, 3H, CH₃).

6-(2-Hydroxy)ethoxy-2-acetonaphthalene. 6-Hydroxy-2-acetonaphthalene (515 mg, 2.8 mmol) was dissolved in DMF (100 mL) in presence of K₂CO₃ (1.22 g, 8.8 mmol) and KI (50 mg, 0.3 mmol), and was refluxed at 100 °C overnight (16 h). DMF was removed via H₂O/CH₂Cl₂ extraction (1L

H₂O, 100 mL CH₂Cl₂). The organic layer was washed with H₂O (2 × 20 mL), brine (2 × 20 mL), and then was dried over Na₂SO₄, filtered and concentrated via rotary evaporation. The crude product was purified by column chromatography (3:1 hexanes / EtOAc) and dried *in vacuo* to yield a white powder: 460 mg (72%). ¹H NMR (300 MHz, CDCl₃, ppm): δ 8.40 (s, 1H, 1-ArH), 8.02 (d, 1H, J = 9, 8-ArH), 7.88 (d, 1H, J = 9.0, 3-ArH), 7.76 (d, 1H, J = 9, 4-ArH), 7.23 (d, 1H, J = 9, 7-ArH), 7.18 (s, 1H, 5-ArH), 4.23 (t, J = 4.5, 2H, -OCH₂CH₂OH), 4.05 (t, J = 4.5, 2H, -OCH₂CH₂OH), 2.06 (s, 1H, -OH).

2-(6-(2-((Tetrahydro-2H-pyran-2-yl)oxy)ethoxy)naphthalen-2-ylethanone. The ligand precursor was prepared as previously described using 6-(2-hydroxy)ethoxy-2-acetonaphthalene instead of 1-[4-(2-hydroxy-ethoxy)-phenyl]-ethanone. The crude product was purified by silica column chromatography (6:1 hexanes/EtOAc) to give a tan solid: 1.12 g (68%). ¹H NMR (300 MHz, CDCl₃, ppm): δ 8.40 (s, 1H, 1-ArH), 8.00 (d, 1H, J = 9, 8-ArH), 7.86 (d, 1H, J = 9.0, 3-ArH), 7.57 (d, 1H, J = 9.0, 4-ArH), 7.26 (d, 1H, J = 9.0, 7-ArH), 7.19 (s, 1H, 5-ArH), 4.74 (t, 1H, J = 3.5, -O-CH* (CH₂-)O-), 4.31 (t, 2H, J = 4.5, Ar-OCH₂CH₂O-R), 3.92 (t, 2H, J = 4.2, Ar-OCH₂CH₂O-R), 3.55 (t, 2H, J = 6, OCH₂-C₃H₆-CH (R)O-), 2.70 (s, 3H, -CH₃), 1.80-1.65 (bm, 6H, OCH₂-C₃H₆-CH (R)O-). HRMS (ESI, TOF) *m/z* calcd for C₁₉H₂₃O₄ 315.1596 [M]⁺, found 315.1596.

1-[4-(2-Hydroxyethoxy)-phenyl]-3-(6-bromo-2-naphthyl)-propane-1,3-dione (nbm(Br)OH) (**2**). The BrNp-Ph ligand was prepared as described for **5**. A cream-colored powder was obtained: 520 mg (59%). ¹H NMR (300 MHz, CDCl₃): δ 17.03 (s, 1H, -OH), 8.49 (s, 1H, 1''-ArH) 8.10-7.90 (m, 4H, 2', 6'-ArH, 3'', 5''-ArH), 7.88- 7.71 (m, 2H, 7'', 8''-ArH), 7.63 (d, J = 9, 1H, 3''-ArH), 7.03 (d, J = 9, 2H, 3', 5'-ArH), 6.93 (s, 1H, COCHCO), 4.19 (t, J = 4.2, -OCH₂CH₂-), 4.03 (m, 2H, -OCH₂CH₂-), 3.48 (s, 1H, CH₂CH₂OH). HRMS (ESI, TOF) *m/z* calcd for C₂₁H₁₈O₄Br 413.0388 [M+H]⁺, found 413.0401.

1-[6-(2-Hydroxyethoxy)-2-naphthyl]-3-phenyl-propane-1,3-dione (bnmOH) (**3**). The Ph-Np ligand was prepared as described for **5**. A white powder was obtained: 154 mg, (48%). ¹H NMR (300 MHz, CDCl₃): ¹H NMR (300 MHz, CDCl₃): δ 17.02 (s, 1H, -OH), 8.49 (s, 1H, 1''-ArH), 8.06-7.99 (bm, 3H, 8''-ArH, 2',6'-ArH) 7.90 (d, J = 9, 1H, 3''-ArH) 7.81 (d, J = 9, 1H, 4''-ArH), 7.57-7.51 (bm, 3H, 3',4',5'-ArH), 7.25 (d, J = 9, 1H, 7''-ArH), 7.20 (s, 1H, 5''-ArH) 6.98 (s, 1H, -COCHCO-), 4.25 (t, J = 6, 2H, ArOCH₂CH₂OH), 4.06 (t, J = 6, 2H, ArOCH₂CH₂OH), 2.2 (s, 1H, ArOCH₂CH₂OH). HRMS (ESI, TOF) *m/z* calcd for C₂₁H₁₉O₄ 335.1283. [M]⁺, found 335.1289.

1-[6-(2-Hydroxyethoxy)-2-naphthyl]-3-(4-bromophenyl)-propane-1,3-dione (bnm(Br)OH) (**4**). The BrPh-Np ligand was prepared as described for **5**. A tan powder was obtained: 110 mg (14%). ¹H NMR (300 MHz, CDCl₃): δ 16.96 (s, 1H, -OH), 8.48 (s, 1H, 1''-ArH), 8.00 (d, J = 8.7, 1H, 8''-ArH), 7.94-7.90 (m, 3H, 2', 6'-ArH, 3''-ArH), 7.81 (d, J = 8.7, 1H, 4''-ArH), 7.64 (d, J = 8.7, 2H, 3', 5'-ArH), 7.26 (d, J = 8.7, 1H, 7''-ArH), 7.19 (s, 1H, 5''-ArH), 6.94 (s, 1H, COCHCO), 4.25 (t, J = 4.2, 2H, -OCH₂CH₂-), 4.09-4.04 (m, 2H, -OCH₂CH₂-), 2.05 (s, 1H, CH₂CH₂OH). HRMS (ESI, TOF) *m/z* calcd for C₂₁H₁₈O₄Br 413.0388 [M+H]⁺, found 413.0376.

1-(4-(2-Hydroxyethoxy)phenyl)-3-(6-iodonaphtha-len-2-yl)propane-1,3-dione (nbm(I)OH). The aromatic ketone 1-{4-[2-(tetrahydropyran-2-yloxy)-ethoxy]-phenyl}-ethanone (500 mg, 1.89 mmol) and 6-iodo, 2-methyl naphthoate (710 mg, 2.27 mmol) were added to a 250 mL oven dried round bottom flask and dissolved in anhydrous THF (~100 mL). A suspension of NaH (91 mg, 3.87 mmol) in THF (20 mL) was transferred to the reaction reaction *via* cannula. The reaction was refluxed at 60 °C in a nitrogen atmosphere, and monitored by TLC. Upon consumption of the ketone limiting reagent (14 h), the reaction mixture was removed from the oil bath and allowed to cool to RT. Excess NaH was quenched with sat. NaHCO₃ (20 mL), and solvents were removed *via* rotary evaporation. The pH was fixed to ~5 with 1M HCl and the mixture was extracted with

CH₂Cl₂ (20 mL × 2) and washed with H₂O (20 mL × 2), and brine (20 mL × 2). Crude product was passed through a silica plug with CH₂Cl₂ before dissolution in THF/H₂O (40 mL/10 mL). A catalytic amount of TsOH (25 mg, 0.15 mmol) was added the reaction mixture was refluxed at 60 °C in a nitrogen atmosphere (12 h). Solvents were concentrated *via* rotary evaporation and the product was extracted with CH₂Cl₂ (100 mL × 3), and washed with H₂O (20 mL × 2), and brine (20 mL × 2). The organic layer was dried over anhydrous Na₂SO₄, filtered and solvents were removed *via* rotary evaporation. Crude product was purified by recrystallization with acetone/hexanes to yield a white powder: 326 mg (37%). ¹H NMR (600 MHz, D₆-DMSO): δ 17.37 (s, 1H, enol-OH), 8.77 (s, 1H, 1'-ArH), 8.49 (s, 1H, 5'-ArH), 8.20 (d, J = 12, 1H, 8'-ArH) 8.16 (d, J = 12, 2H, 2'', 6''-ArH), 7.99 (d, J = 12, 1H, 7'-ArH), 7.88 (s, broad, 2H, 3', 4'-ArH), 7.40 (s, 1H, COCHCO), 7.10 (d, J = 12, 2H, 3'', 5''-ArH), 4.90 (t, J = 6, 1H, Ar-OCH₂CH₂OH), 4.10 (t, J = 6, 2H, Ar-OCH₂CH₂OH), 3.73 (m, broad, 2H, Ar-OCH₂CH₂OH). HRMS (ESI, TOF) *m/z* calcd for C₂₁H₁₈O₄I, 461.0250 [M + H]⁺; found 461.0250.

BF₂nbmOH (5). The Np-Ph complex was prepared as described in the literature.¹³ A yellow powder was obtained: 296 mg (84%). ¹H NMR (300 MHz, CDCl₃): δ 8.76 (s, 1H, 2''-ArH), 8.21 (d, 2H, 2', 6'-ArH), 7.98 (m, 5H, 4'', 7'', 9'', 10''-ArH, COCHCO), 7.68 (m, 2H, 5'', 6''-ArH), 7.08 (d, 2H, 3', 5'-ArH), 4.23 (t, J = 4.2, 2H, -OCH₂CH₂-), 4.05 (t, J = 4.2, 2H, -OCH₂CH₂-). HRMS (ESI, TOF) *m/z* calcd C₂₁H₁₆BO₄F₂Na 405.1099 [M+Na]⁺, found 405.1094.

BF₂nbm(Br)OH (6). The ligand nbmOH, **2**, (250.0 mg, 0.605 mmol) was added to a flame-dried 2-neck round bottom flask under nitrogen, and was dissolved in THF/CH₂Cl₂ (20/20 mL) to give a pale yellow solution. Boron trifluoride diethyl etherate (115 μL, 0.907 mmol) was added via syringe and the solution turned bright yellow. The reaction was stirred at room temperature for 48 h. Solvents were removed via rotary evaporation resulting in a yellow solid. The crude material

was purified by recrystallization in 1:1 EtOAc/acetone to yield a yellow-orange powder: 143 mg, (53%). The BrNp-Ph complex was prepared as described for **11**. A yellow powder was obtained: 21 mg (37%). ^1H NMR (300 MHz, DMSO): δ 9.07 (s, 1H, 1''-ArH), 8.43-8.38 (bm, 4H, 3'', 8''-ArH, 2', 6'-ArH), 8.18-8.11 (bm, 2H, 5'', 7''-ArH), 7.98 (s, 1H, COCHCO), 7.81 (d, J = 9, 1H, 4''-ArH), 7.23 (d, J = 9, 2H, 3', 5'-ArH), 4.98 (t, J = 5.4, 1H, -OH), 4.19 (t, J = 4.8, 2H, -OCH₂CH₂-), 3.77 (t, J = 4.5, 2H, -OCH₂CH₂-). HRMS (ESI, TOF) m/z calcd C₂₁H₁₆BO₄F₂BrNa 483.0191 [M+Na]⁺, found 483.0180

BF₂bnmOH (**7**). The Ph-Np complex was prepared as described for **6**. A yellow powder was obtained: 154 mg (48%). ^1H NMR (300 MHz, DMSO): δ 9.07 (s, 1H, 1''-ArH), 8.39 (d, J = 9, 2H, 2', 6'-ArH), 8.31 (d, J = 9, 1H, 8''-ArH), 8.13 (d, J = 9, 1H, 3''-ArH), 8.03-7.98 (m, 2H, 4'-ArH, COCHCO), 7.81 (d, J = 9, 1H, 7''-ArH), 7.68 (t, J = 6, 2H, 3', 5'-ArH), 7.50 (s, 1H, 5''-ArH), 7.34 (d, J = 9, 1H, 4''-ArH), 5.00 (t, J = 6, 1H, OH), 4.18 (t, J = 6, 2H, -OCH₂CH₂-), 3.80 (t, J = 6, 2H, -OCH₂CH₂-). HRMS (ESI, TOF) m/z calcd C₂₁H₁₈BO₄F₂ 383.1266 [M]⁺, found 383.1252.

BF₂bnm(Br)OH (**8**). The BrPh-Np complex was prepared as described for **6**. A yellow powder was obtained: 41 mg (49%). ^1H NMR (300 MHz, DMSO): δ 9.07 (s, 1H, 1''-ArH), 8.32- 8.28 (m, 3H, 2', 6'-ArH, 8''-ArH), 8.13 (d, J = 9.0, 1H, 3''-ArH), 8.03-7.99 (m, 2H, 7''-ArH, COCHCO), 7.90 (d, J = 9, 2H, 3', 5'-ArH), 7.50 (s, 1H, 5''-ArH), 7.32 (d, 1H, 4''-ArH), 5.0 (t, J = 6, 1H, -OH), 4.18 (t, J = 6, 2H, -OCH₂CH₂-), 3.80 (t, J = 6, 2H, -OCH₂CH₂-). HRMS (ESI, TOF) m/z calcd C₂₁H₁₆BO₄F₂BrNa 483.0191 [M+Na]⁺, found 483.0193.

BF₂nbm(I)OH. The iodide dye was prepared by weighing ligand, nbm(I)OH (150 mg, 0.32 mmol), in a 250 mL round bottom flask and dissolving in anhydrous THF (150 mL). Boron trifluoride diethyl etherate (61 μL , 0.50 mmol) was added via syringe and the solution turned yellow. The reaction mixture was refluxed at 60 °C under a N₂ atmosphere and monitored by TLC until

consumption of the ligand substrate was complete (2 h). Excess boron trifluoride diethyl etherate was quenched with $K_2CO_{3(s)}$ (~30 mg) and stirred for an additional 15 min. The solution was filtered to remove solids, and solvents were removed via rotary evaporation to yield a dark yellow powder. The product was purified by recrystallization (acetone/hexanes) to yield a yellow powder: 105 mg (62 %). 1H NMR (600 MHz, D_6 -DMSO): δ 9.02 (s, 1H, 1'-ArH), 8.55 (s, 1H, 5'-ArH), 8.40 (d, J = 12, 2H, 2'', 6''-ArH), 8.35 (d, J = 12, 1H, 8'-ArH), 8.06 (d, J = 12, 1H, 7'-ArH), 7.97-7.93 (m, broad, 3H, 3', 4'-ArH, COCHCO), 7.22 (d, J = 12, 2H, 3'', 5''-ArH), 4.94 (t, J = 6, 1H, Ar-OCH₂CH₂OH), 4.18 (t, J = 6, 2H, Ar-OCH₂CH₂OH), 3.75 (m, broad, 2H, Ar-OCH₂CH₂OH). HRMS (ESI, TOF) m/z calcd for C₂₁H₁₈BO₄F₂I, 508.0154 [M + H]⁺; found 508.0149.

Boron Polymer Synthesis. Preparative scale reactions were conducted as follows.⁶ The boron initiator and D,L-lactide were placed in a Kontes flask, and sealed under N₂. The bulb of the flask was entirely submerged in an oil bath at 130 °C. After the D,L-lactide melted, Sn(Oct)₂ in hexanes was added and the reaction was heated for the designated time (~1-3 h). Crude polymer was purified by precipitation from CH₂Cl₂/cold MeOH (-20 °C). The polymer was collected by centrifugation, the filtrate was decanted, and the rubbery solid was redissolved in CH₂Cl₂ and reprecipitated in cold MeOH (-20 °C). The resulting solid was reprecipitated from CH₂Cl₂/hexanes, collected by centrifugation, the filtrate was decanted and the residue was dried *in vacuo* to give the polymers as foams. Representative 1H NMR spectral data and GPC data are provided below for each dye initiator and polymer.

BF₂nbmPLA. Polymer **9a** was obtained as a yellow crystalline solid: 81 mg (45%). M_n (GPC/RI) = 5400 Da, PDI = 1.05; M_n (NMR) = 3800 Da. 1H NMR (300 MHz, CDCl₃): δ 8.76 (s, 1H, 1'' - ArH), 8.20 (d, J = 9, 2H, 2', 6' -ArH), 8.10-7.90 (bm, 5H, 3'', 4'', 5'', 8'' -ArH, -COCHCO), 7.60-

7.55 (bm, 2H, 6'', 7'' -ArH), 7.05 (d, J = 9, 2H, 3', 5' -ArH), 5.30-5.16 (bm, 48H, PLA -CH-CH₃), 4.55 (m, 2H, -OCH₂CH₂-), 4.35 (m, 2H, -OCH₂CH₂-), 1.57 (bs, 146 H, PLA -CHCH₃).

BF₂nbm(Br)PLA (10). Polymer **10a** was obtained as a yellow crystalline solid: 151 mg (44%). M_n (GPC/RI) = 6800 Da, PDI = 1.03; M_n (NMR) = 6900 Da. ¹H NMR (300 MHz, CDCl₃): δ 8.72 (s, 1H, 1'' -ArH), 8.20 (d, J = 9, 2H, 2', 6' -ArH), 8.10-8.08 (m, 2H, 3'', 8'' -ArH), 7.89-7.87 (m, 2H, 5'', 7'' -ArH), 7.69 (d, J = 9, 1H, 4'' -ArH), 7.23 (s, 1H, -COCHCO-), 7.05 (d, J = 9, 2H, 3', 5' -ArH), 5.31-5.11 (bm, 89H, PLA -CHCH₃), 4.55 (m, 2H, -OCH₂CH₂-), 4.35 (m, 2H, -OCH₂CH₂-), 1.57 (bs, 205H, PLA -CHCH₃).

BF₂bnmPLA (11). Polymer **11a** was obtained as a yellow-orange foam: 71 mg (64%). M_n (GPC/RI) = 5200 Da, PDI = 1.04; M_n (NMR) = 3300 Da. ¹H NMR (300 MHz, CDCl₃): δ 8.73 (s, 1H, 1'' -ArH), 8.20 (d, J = 9, 2H 2', 6' -ArH), 8.10 (d, J = 9, 1H, 8'' -ArH), 7.95 (d, J = 9, 1H, 3'' -ArH), 7.85 (d, J = 9, 1H, 7'' -ArH), 7.71 (t, J = 6, 1H, 4' -ArH), 7.58 (t, J = 6, 2H, 3', 5' -ArH), 7.31-7.25 (m, 2H, -COCHCO-, 4'' -ArH), 7.19 (s, 1H, 5'' -ArH), 5.30-5.16 (bm, 45 H, PLA -CHCH₃), 4.55 (m, 2H, -OCH₂CH₂-), 4.35 (m, 2H, -OCH₂CH₂-), 1.57 (bs, 144 H, PLA -CHCH₃).

BF₂bnm(Br)PLA (12). Polymer **12a** was obtained as a bright yellow green crystalline foam: 101 mg (40%). M_n (GPC/RI) = 5600 Da, PDI = 1.07; M_n (NMR) = 3100 Da. ¹H NMR (300 MHz, CDCl₃): δ 8.73 (s, 1H, 1'' -ArH), 8.10-8.03 (bm, 4H, 8'' -ArH, 2', 6' -ArH, -COCHCO-), 7.95 (d, J = 9, 1H, 3'' -ArH), 7.85 (d, J = 9, 1H, 7'' -ArH), 7.73 (d, J = 9, 2H, 3', 5' -ArH), 7.33 (d, J = 9, 1H, 4'' -ArH), 7.19 (s, 1H, 5'' -ArH), 5.21-5.11 (bm, 72 H, PLA -CHCH₃), 4.58 (t, J = 4.8, 2H, -OCH₂CH₂-), 4.35 (t, J = 4.8, 2H, -OCH₂CH₂-), 1.57 (s, 241 H, PLA -CHCH₃).

BF₂nbm(I)PLA (IP) The iodide substituted polymer was prepared as previously described,¹⁵ except the initiator BF₂nbm(I)OH was used in place of BF₂nbm(Br)OH (loading = initiator : lactide : catalyst; 1 : 200 : 0.025), and was stirred at 130° C for 5 h, to yield a yellow crystalline powder:

345 mg (51% yield, corrected for 65% polymer conversion). M_n (GPC/MALS) = 16 300 Da, \bar{D} = 1.17; M_w (^1H NMR) = 19 300 Da. ^1H NMR (600 MHz, CDCl_3): δ 8.71 (s, 1H, 1'-ArH), 8.33 (s, 1H, 5'-ArH), 8.20 (d, J = 6, 2H, 2'', 6''-ArH), 8.09 (d, J = 6, 1H, 8'-ArH), 7.85 (m, broad, 2H, 3', 4'-ArH) 7.73 (d, J = 12, 1H, 7'-ArH), 7.16 (s, 1H, COCHCO), 7.04 (d, J = 12, 2H, 3'', 5''-ArH), 5.23-5.12 (m, broad, 268H, PLA-H), 4.55 (s, broad, 2H, Ar-OCH₂CH₂OH), 4.32 (m, broad, 2H, Ar-OCH₂CH₂OH), 1.58-1.53 (m, broad, 1137H, PLA-CH₃).

3.4. Acknowledgements

This research was published in *Macromolecules*, and *ACS Sensors*.²⁴ I thank Dr. Jelena Samonina-Kosicka, and Ziyi Fan for help in the synthesis and characterization of these BF₂dnm(X)PLA polymers, Dr. William Morris for performing the calculations, Alexander Mathew for assisting with the oxygen calibrations, Prof. Fraser, Dr. Jelena Samonina-Kosicka, and Ziyi Fan for assistance in the preparation of the manuscript, and the financial support of the National Cancer Institute of the National Institutes of Health (R01 CA167250).

3.5. References

- (1) Samonina-Kosicka, J.; DeRosa, C. A.; Morris, W. A.; Fan, Z.; Fraser, C. L. *Macromolecules* **2014**, *47*, 3736–3746.
- (2) Xu, S.; Evans, R. E.; Liu, T.; Zhang, G.; Demas, J. N.; Trindle, C. O.; Fraser, C. L. *Inorg. Chem.* **2013**, *52*, 3597–3610.
- (3) Fraser, C. L.; Zhang, G. Luminescent Diketonate Polymers. WO 2011011646, 2011.
- (4) DeRosa, C. A.; Kerr, C.; Fan, Z.; Kolpaczynska, M.; Mathew, A. S.; Evans, R. E.; Zhang, G.; Fraser, C. L. *ACS Appl. Mater. Interfaces* **2015**, *7*, 23633–23643.
- (5) Zhang, G.; Palmer, G. M.; Dewhurst, M. W.; Fraser, C. L. *Nat. Mater.* **2009**, *8*, 747–751.
- (6) Zhang, G.; Chen, J.; Payne, S. J.; Kooi, S. E.; Demas, J. N.; Fraser, C. L. *J. Am. Chem.*

- Soc.* **2007**, *129*, 8942–8943.
- (7) Bender, J. L.; Corbin, P. S.; Fraser, C. L.; Metcalf, D. H.; Richardson, F. S.; Thomas, E. L.; Urbas, A. M. *J. Am. Chem. Soc.* **2002**, *124*, 8526–8527.
 - (8) Sun, X.; Zhang, X.; Li, X.; Liu, S.; Zhang, G. *J. Mater. Chem.* **2012**, *22*, 17332–17339.
 - (9) Lower, S. K.; El-Sayed, M. A. *Chem. Rev.* **1966**, *66*, 199–241.
 - (10) Butler, T.; Morris, W. A.; Samonina-Kosicka, J.; Fraser, C. L. *ACS Appl. Mater. Interfaces* **2016**, *8*, 1242–1251.
 - (11) Frisch, M. J.; Trucks, G. W.; Schlegel, H. B.; Scuseria, G. E.; Robb, M. A.; Cheeseman, J. R.; Scalmani, G.; Barone, V.; Mennucci, B.; Petersson, G. A. . et al. *Gaussian 09 Revision A.1*; Gaussian, Inc.: Wallingford, CT. 2009.
 - (12) Zhang, G.; Evans, R. E.; Campbell, K. A.; Fraser, C. L. *Macromolecules* **2009**, *42*, 8627–8633.
 - (13) Payne, S. J.; Zhang, G.; Demas, J. N.; Fraser, C. L.; Degraff, B. A. *Appl. Spectrosc.* **2011**, *65*, 1321–1324.
 - (14) Samonina-Kosicka, J.; DeRosa, C. A.; Morris, W. A.; Fan, Z.; Fraser, C. L. *Macromolecules* **2014**, *47*, 3736–3746.
 - (15) DeRosa, C. A.; Samonina-Kosicka, J.; Fan, Z.; Hendargo, H. C.; Weitzel, D. H.; Palmer, G. M.; Fraser, C. L. *Macromolecules* **2015**, *48*, 2967–2977.
 - (16) Zhang, G.; Kooi, S. E.; Demas, J. N.; Fraser, C. L. *Adv. Mater.* **2008**, *20*, 2099–2104.
 - (17) Wang, X.; Wolfbeis, O. S. *Chem. Soc. Rev.* **2014**, *43*, 3666–3761.
 - (18) Lakowicz, J. R. *Principles of Fluorescence Spectroscopy*; Springer US: New York, 2006.
 - (19) Pfister, A.; Zhang, G.; Zareno, J.; Horwitz, A. F.; Fraser, C. L. *ACS Nano* **2008**, *2*, 1252–1258.

- (20) Moßhammer, M.; Strobl, M.; Köhl, M.; Klimant, I.; Borisov, S. M.; Koren, K. *ACS Sensors* **2016**, *1*, 681–687.
- (21) Baggaley, E.; Botchway, S. W.; Haycock, J. W.; Morris, H.; Sazanovich, I. V.; Williams, J. A. G.; Weinstein, J. A. *Chem. Sci.* **2014**, *5*, 879–886.
- (22) Irvine, M. W.; Costa, B. M.; Dlaboga, D.; Culley, G. R.; Hulse, R.; Scholefield, C. L.; Atlason, P.; Fang, G.; Eaves, R.; Morley, R.; Mayo-Martin, M. B.; Amici, M.; Bortolotto, Z. A.; Donaldson, L.; Collingridge, G. L.; Molnár, E.; Monaghan, D. T.; Jane, D. E. *J. Med. Chem.* **2012**, *55*, 327–341.
- (23) Williams, D. B. G.; Lawton, M. *J. Org. Chem.* **2010**, *75*, 8351–8354.
- (24) DeRosa, C. A.; Seaman, S. A.; Mathew, A. S.; Gorick, C. M.; Fan, Z.; Demas, J. N.; Peirce, S. M.; Fraser, C. L. *ACS Sensors* **2016**, *1*, 1366–1373.

Chapter 4:

Difluoroboron Dinaphthoylmethane Polylactide



4.1. Introduction

This study extends our exploration of boron β -diketonate materials by increasing dye conjugation using dinaphthoymethane (dnm). Previously, dnm ligands have been utilized as mechanochromic materials,^{1,2} two-photon excitable energy donors,³ in optoelectronic lanthanide complexes and in visible light absorbers for temperature sensitive europium complexes.⁴ The red-shifted absorption and increased π -conjugation of this ligand make it a good candidate for incorporation into oxygen sensing probes. Red-shifted absorbance allows for visible light absorption, which is less phototoxic compared to higher energy UV excitation. Halides, such as bromide and iodide heavy atoms are introduced to increase crossover to the triplet state by enhancing spin-orbit coupling, for shorter phosphorescence lifetimes and increased intensity of triplet emission at the expense of fluorescence. This study describes the synthesis and optical characterization of halide-substituted Difluoroboron Dinaphthoymethane Polylactide ($\text{BF}_2\text{dnm}(\text{X})\text{PLA}$; Figure 4.1) materials and probes the effects of halide substitution and polymer molecular weight on the optical properties in dilute solutions, thin films, and nanoparticles.

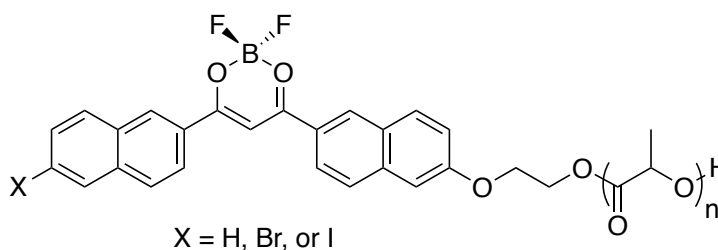


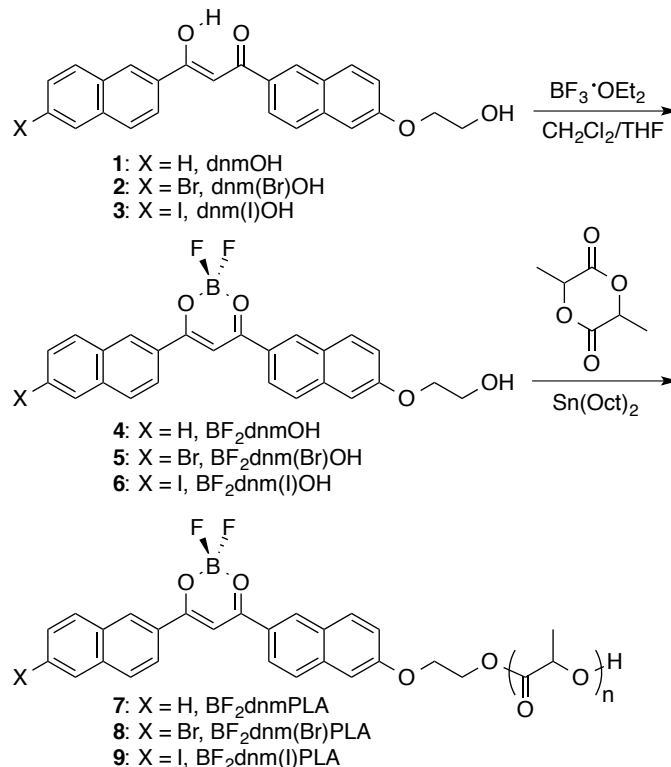
Figure 4.1. Chemical Structure of Difluoroboron Dinaphthoymethane Polylactide.

4.2. Results and Discussion

4.2.1. Synthesis

Difluoroboron dinaphthoylmethane poly(lactic acid) materials, $\text{BF}_2\text{dnm}(\text{X})\text{PLA}$ ($\text{X} = \text{H}$, Br , I) (**7-9**), are generated from $\text{BF}_2\text{dnm}(\text{X})\text{OH}$ initiators (**4-6**) via bulk polymerization of D,L-lactide in the presence of stannous octoate ($\text{Sn}(\text{oct})_2$) (Scheme 4.1). The β -diketonate ligands **1-3** were generated by Claisen condensation using NaH as the base. Corresponding boron initiators **4-6** were prepared by addition of boron trifluoride diethyl etherate in $\text{CH}_2\text{Cl}_2/\text{THF}$. Dinaphthyl boron complexes, the iodide-substituted sample in particular, showed limited solubility compared to other β -diketonate derivatives such as the previously reported phenyl-phenyl (dbm)⁵ naphthyl-phenyl (nbm)⁶ derivative. Consequently, typical column chromatographic methods proved ineffective (e.g. silica; EtOAc, THF/hexanes, acetone or THF). Instead, the boron complexes were purified by recrystallization with acetone/EtOAc (BF_2dnmOH , **4** and $\text{BF}_2\text{dnm}(\text{Br})\text{OH}$, **5**) or pure acetone ($\text{BF}_2\text{dnm}(\text{I})\text{OH}$, **6**) and were obtained as yellow-orange powders. Dye-dye interactions in polymer matrices play a key role in fluorescence properties. Though extended π -conjugation can lead to greater π stacking and aggregation, presenting challenges for purification, fortuitously, this feature presents unique benefits for optical tuning.

Scheme 4.1. Synthesis of Difluoroboron Dinaphthoylemethane-PLA Conjugates



Dye-polymer conjugates were synthesized as previously described. Polymers with various molecular weights (M_n (GPC) = 12 - 30 kDa) were generated by controlling the reaction time and lactide equivalents. The polymers were characterized by size-exclusion chromatography with multi-angle light scattering detection (SEC-MALS) and ¹H NMR spectroscopy (Table 4.1). Unlike previously studied BF₂dbmOH (phenyl-phenyl)⁵ initiators, these dinaphthyl dyes did not dissolve in lactide melts of low equivalences until after addition of the stannous octoate catalyst and polymerization commenced.⁶ Previous studies have shown that initial dissolution of the dye in the lactide melt is not crucial for growing polymers with narrow polydispersities. Previous preparations of low molecular weight polymers (5 - 10 kDa) utilized low lactide loadings (i.e. 50 equivalents). But under these conditions, dinaphthyl initiators had larger than expected MWs and large PDIs. However, increasing catalyst loading from 1/50 to 1/40 per initiator led to a decrease

Table 4.1. Polymer Synthesis and Molecular Weight Characterization

Polymer		Loading ^a	M _n ^b (NMR)	M _n ^c (GPC)	M _w ^c (GPC)	Đ ^c (GPC)
BF ₂ dnmPLA	7a	300:1/40	11800	12200	14600	1.20
	7b	300:1/40	38000	31800	41300	1.30
BF ₂ dnm(Br)PLA	8a	300:1/40	12500	12500	14900	1.19
	8b	300: 1/40	26200	26000	31500	1.21
BF ₂ dnm(I)PLA	9a	200:1/40	13000	12500	14000	1.12
	9b	300:1/40	25500	23200	27600	1.19

^a Molar ratio of monomer: Sn(oct)₂ per 1 equivalent of boron initiator. ^b Estimated from the relative integration (dye-OCH₂CH₂-OPLA/PLA-*H*). ^c Molecular weight data determined by GPC with MALS/RI detection. ^d Percent monomer conversion determined by relative integration (PLA-*H*/Lactide-*H*). ^e Corrected for monomer conversion.

in PDI (e.g. BF₂dnmOH (**4**), 1/50: PDI = 1.74 versus 1/40: PDI = 1.41). For high lactide equivalents (i.e. >200), BF₂dnm(X)OH initiators dissolved in the monomer melts more easily and narrower PDIs were obtained (Table 4.1). As previously described, reactions were typically stopped before complete monomer conversion to limit transesterification and thermal depolymerization side reactions.

4.2.2. Optical Properties in Solution

The optical properties of boron dyes and polymers were analyzed in dilute CH₂Cl₂ (Table 4.2). Extinction coefficients (ϵ), quantum yields (Φ_F), and fluorescence lifetimes (τ_F) of initiators **4-6** were determined in dilute solutions to minimize aggregation ($\sim 10^{-6}$ M and optical density < 0.10). The dye-PLA conjugates (**7-9**) dissolved easily under these conditions in comparison to dye initiators. Absorption spectra of all dinaphthyl initiators and polymers are nearly identical, with a slight red-shift in λ_{abs} for heavy atom substituted materials (λ_{abs} polymers: hydrogen (**4**) = 434 nm, bromine (**5**) = 436 nm, iodine (**6**) = 439 nm; Figure S4.1; Appendix C) and expected trends in extinction coefficients for initiators and polymers.⁷ Luminescence measurements showed green fluorescence for all initiators and polymers (e.g. initiators: λ_{em} : H (**4**) = 518 nm, Br (**5**) = 520 nm, I (**6**) = 521 nm). The efficiency of singlet emission varied substantially as evidenced by quantum

Table 4.2. Optical Properties of Boron Initiators and Polymers in CH₂Cl₂ Solution

Sample		λ_{abs}^a (nm)	ϵ^b (M ⁻¹ cm ⁻¹)	λ_{em}^c (nm)	τ_F^d (ns)	Φ_F^e
BF ₂ dnmOH	4	434	65000	518	2.47	0.66
BF ₂ dnmPLA	7a	434	45000	505	2.27	0.62
	7b	434	40000	503	2.26	0.59
BF ₂ dnm(Br)OH	5	436	50000	520	2.17	0.57
BF ₂ dnm(Br)PLA	8a	436	49000	516	2.04	0.51
	8b	436	45000	516	2.03	0.51
BF ₂ dnm(I)OH	6	439	60000	521	0.74	0.19
BF ₂ dnm(I)PLA	9a	439	51000	513	0.64	0.15
	9b	439	49000	512	0.60	0.15

^aAbsorption maxima. ^bExtinction coefficients calculated at the absorption maxima. ^cFluorescence emission maxima excited at 369 nm (xenon lamp). ^dFluorescence lifetime excited at 369 nm (LED) monitored at the emission maximum. All fluorescence lifetimes are fitted with single-exponential decay. ^eRelative quantum yield versus anthracene in EtOH as a standard.

yields of 0.66, 0.57, and 0.19 for H, Br and I dyes, respectively. Initiators with the heavy atoms Br and I exhibited lower fluorescence quantum yields due to enhanced crossover to the triplet state, followed by phosphorescence, oxygen quenching, or non-radiative decay in the organic solvent.⁸ Fluorescence lifetimes also became shorter with increasing weight of the heavy atom (τ_F : H (**4**) = 2.47 ns, Br (**5**) = 2.04 ns, I (**6**) = 0.74 ns).

4.2.3. Optical Properties of Films

Boron polymers were also studied in the solid state as films. Solution-cast films were prepared in vials by dissolving dye-PLA samples in CH₂Cl₂ followed by slow evaporation under nitrogen. Luminescence properties of the samples are summarized in Table 4.3. The increased conjugation of the dinaphthyl dyes (Np-Np) has led to red- shifted fluorescence in comparison to naphthyl-phenyl (Np-Ph)⁶ and phenyl-phenyl (Ph-Ph)⁵ dye-PLA analogues. For example, for ~12 kDa polymer films without halide heavy atoms emission maxima λ_{em} are as follows: BF₂dnmPLA (Np-Np) = 523 nm, BF₂nbmPLA (Np-Ph) = 461 nm, BF₂dbmPLA (Ph-Ph) = 437 nm. For polymers of

Table 4.3. Optical Properties of Boron Polymer Films

Sample		Polymer		Fluorescence		Phosphorescence	
		M _n ^a (kDa)	Dye Loading ^b (%)	λ _F ^c (nm)	τ _{pw0} ^d (ns)	λ _P ^e (nm)	τ _{pw0} ^f (ms)
BF ₂ dnmPLA	7a	12.2	3.5	523	11.7	541	50
	7b	31.8	1.4	494	7.1	509	156
	7c	^g	1.0	484	3.3	499	381
BF ₂ dnm(Br)PLA	8a	12.5	4.0	534	6.3	567	17
	8b	26.1	2.0	506	4.1	555	26
	7c	^g	1.0	490	3.2	564	38
BF ₂ dnm(I)PLA	9a	12.5	4.5	535	1.2	576	4.5
	9b	23.2	2.4	503	0.9	569	6.3
	9c	^g	1.0	496	0.8	566	7.0

^aNumber-average molecular weight. ^bWeight percent dye in the polymer. ^cSteady-state fluorescence emission maximum under air excited at 400 nm (xenon lamp). ^dFluorescence lifetime excited at 369 nm (LED) monitored at the emission maximum. All fluorescence lifetimes are fit with triple-exponential decay. ^eDelayed emission maxima under N₂ excited at 400 nm (xenon flash lamp; 1 ms delay). ^fPre-exponential weighted RTP lifetime excited at 400 nm (xenon flash lamp; 1 ms delay). RTP lifetime fit to triple-exponential decay. ^gBlends prepared from **7a**, **8a**, **9a** and PLA.

similar MWs, the presence of halide substituents, Br or I, results in slight redshifts in fluorescence (H; **7a** = 523 nm Br; **8a** = 534 nm I; **9a** 535 nm).

The solid-state fluorescence properties of BF₂bdks are highly dependent on the molecular weight (MW).⁷ Changing dye loading in this way is facile method for tuning fluorescence. Previously reported dbm (Ph-Ph) and nbm (Np-Ph) substituted PLA polymers exhibited red-shifted emission for low MW polymers due to increase dye-dye interactions stabilizing excited state dipoles. Longer MW polymers decreased these dye-dye interactions resulting in blue-shifted emission in the solid-state (Figure 4.2). This

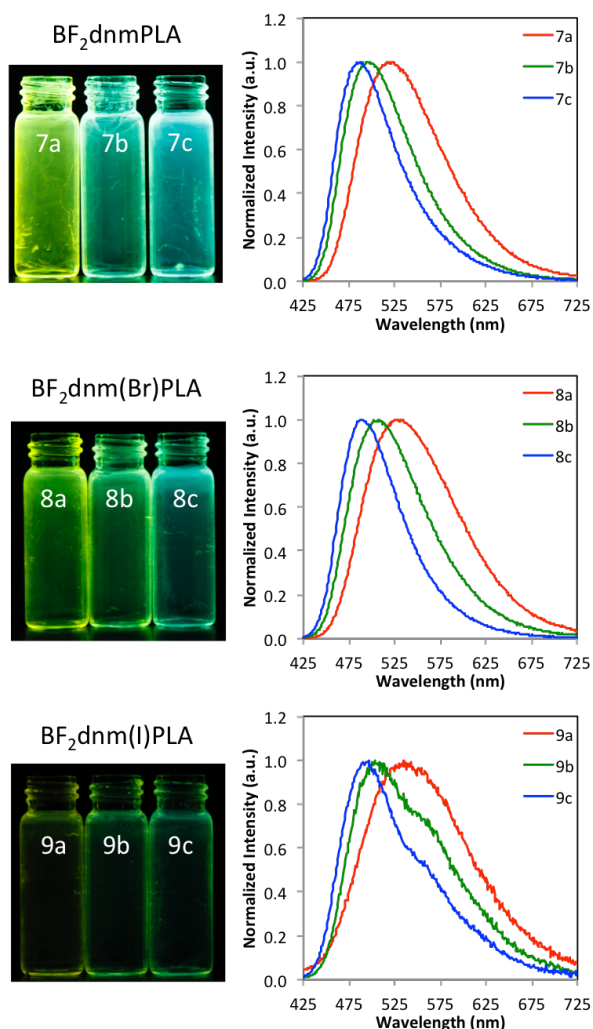


Figure 4.2. Effects of dye loading on fluorescence. Images of polymer film fluorescence ($\lambda_{\text{ex}} = 354 \text{ nm}$) and fluorescence spectra ($\lambda_{\text{ex}} = 400 \text{ nm}$) for BF_2dnmPLA (**7a-c**), $\text{BF}_2\text{dnm(Br)PLA}$ (**8a-c**), and $\text{BF}_2\text{dnm(I)PLA}$ (**9a-c**) under air.

same trend was observed in this study with dnm dyes (e.g. BF_2dnmPLA : $\sim 12.2 \text{ kDa}$ (**7a**) = 523 nm and $\sim 31.8 \text{ kDa}$ (**7b**) = 494 nm . Fluorescence lifetime (τ_F) is also influenced by polymer MW. In short polymers, neighboring fluorophores can stabilize the excited state, producing longer fluorescence lifetimes than longer polymers (e.g. BF_2dnmPLA : **7a**: $\tau_F = 11.7 \text{ ns}$, **7b**: $\tau_F = 7.1 \text{ ns}$). The halide can also influence the fluorescence lifetime. Heavy atoms increase the rate of intersystem crossing (ISC) to the triplet state by enhancing spin-orbit coupling. This resulted in

less intense fluorescence, and shorter fluorescence lifetimes (**7a**: $\tau_F = 11.7$ ns, **8a**: $\tau_F = 6.3$ ns, **9a**: $\tau_F = 1.2$ ns).

Delayed emission was investigated for the polymers under a nitrogen atmosphere. Room-temperature phosphorescence (RTP) was observed for all BF₂dnm(X)PLA materials. Iodide substituted dyes show the expected trends in phosphorescence wavelength (λ_P). Emission is redshifted with extended conjugation (λ_P : BF₂dnm(I)PLA: 565 nm versus BF₂dbm(I)PLA: 526 nm, ~12 kDa). The hydrogen derivative BF₂dnm(I)PLA, however, appears anomalous (BF₂dbmPLA: 509 nm, BF₂nbmPLA 545 nm, BF₂dnmPLA (**9a**): 541 nm, ~12 kDa). This can be explained by the fact that delayed emission maxima at room-temperature is comprised of both phosphorescence and thermally activated delayed fluorescence (TADF), which is commonly observed in BF₂bdkPLA materials.^{9–11} With increased dye conjugation the magnitude of the wavelength shift in phosphorescence ($\Delta\lambda_P$) is less than the shift in fluorescence ($\Delta\lambda_F$). Consequently, the fluorescence to phosphorescence energy gap (ΔE) gets smaller for Np-Np (dnm) systems versus Np-Ph (nbm) and Ph-Ph (dbm) systems. This has important implications for both thermally activated delayed fluorescence and ratiometric sensing with these dual emissive materials. While small singlet triplet energy gaps facilitate intersystem crossing, they also enhance thermal back population to singlet state. As illustrated by BF₂dnmPLA (**7a**), the gap between λ_F and the delayed emission maximum λ_{DE} is very small ($\lambda_F = 523$ nm, $\lambda_{DE} = 541$ nm). For this sample, the delayed emission is dominated by TADF, which accounts for the unexpected blue shift. This hypothesis is confirmed by low temperature measurements where TADF is absent and phosphorescence dominates. For example, delayed emission for BF₂dnmPLA (**7b**)

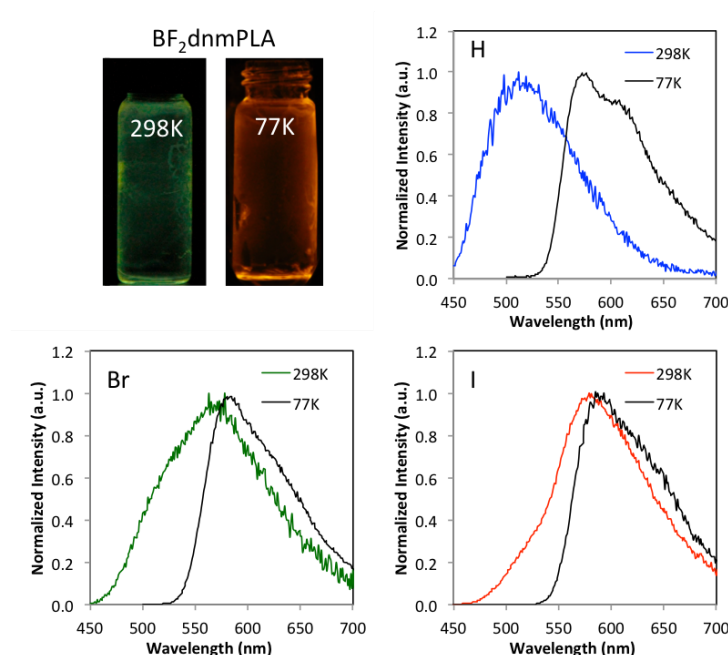


Figure 4.3. Temperature dependent delayed emission of $\text{BF}_2\text{dnm(X)PLA}$. Images of BF_2dnmPLA (**7b**) and delayed emission spectra BF_2dnmPLA (**7b**) (H), $\text{BF}_2\text{dnm(Br)PLA}$ (**8b**) (Br), and $\text{BF}_2\text{dnm(I)PLA}$ (**8b**) (I), ($\lambda_{\text{ex}} = 400 \text{ nm}$, 2 ms delay; room temperature (298 K) and liquid nitrogen (77K)).

changes from green (509 nm; delayed fluorescence plus phosphorescence) at RT to red-orange (580 nm; phosphorescence) at 77K (Figures 4.3 and S4.2; Appendix C).

Heavy atoms also influence delayed emission. Like fluorescence λ_{F} , the delayed emission maxima for the bromide dye **8a** (567 nm) and iodide dye **9a** (576 nm) are redshifted compared to the non-halogenated analogue **7a** (541 nm). Also, the singlet triplet energy gaps for the halogenated dyes are greater than for the **7a**. Rapid intersystem crossing (ISC) for the heavy atom substituted dyes results in short phosphorescence lifetimes (τ_{P}) (hydrogen (**7a**) 50.1 ms, bromine (**8a**) 16.9 ms, iodine (**9a**) 4.5 ms) and increased phosphorescence intensity relative to the hydrogen analogue (Figure 4.3). Unlike the H dye where TADF dominates at room temperature and longer wavelength phosphorescence is present at low temperature, for bromine (**8b**) and iodine (**9b**) dyes

have similar delayed emission maxima at room temperature and 77K, however, at low temperature blue region of the band corresponding to TADF disappears and the bandwidth narrows.

While materials with narrow singlet triplet gaps and strong TADF are desirable for OLEDs,^{12,13} they are problematic for ratiometric oxygen sensing, given the need for two discrete peaks, namely, stable fluorescence for use as the standard and oxygen sensitive phosphorescence as the sensor. Typical ratiometric sensing materials are multicomponent, comprised of standard and sensor dyes that are combined in a suitable matrix.^{14–16} Fluorescence and phosphorescence wavelengths and signal intensities are easily controlled by dye selection, and intensities, by dye loading. In dual emissive dyes such as BF₂bdkPLAs, different approaches to wavelength and intensity modulation are required. As previously described, halide heavy atom substitution increases phosphorescence intensity, as shown in Figure 4.4.^{5,17} Dye loading modulates the singlet to triplet energy gap, which for the dinaphthyl materials in this study also helps to address the TADF issue.

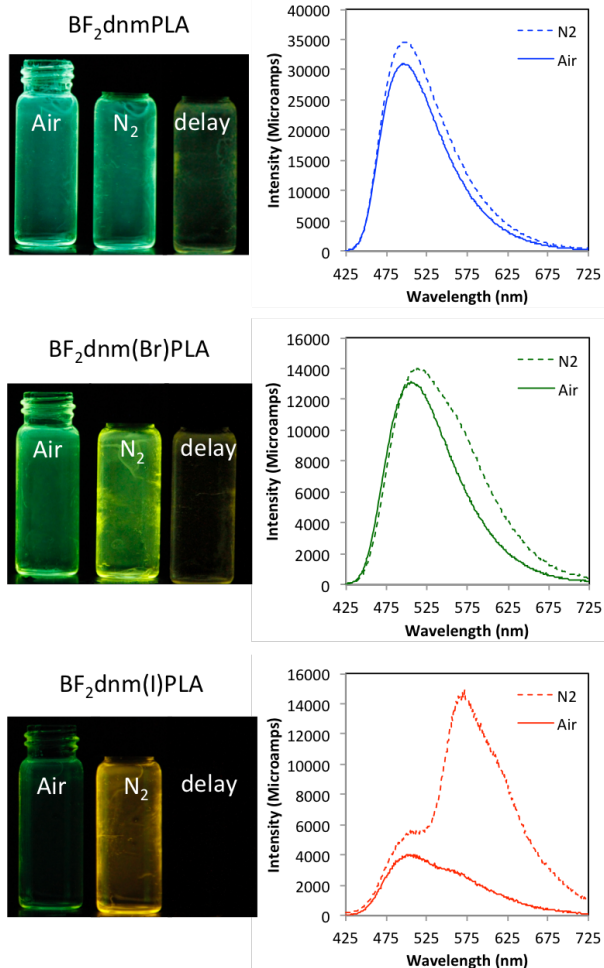


Figure 4.4. Images and total emission spectra of boron polymers BF_2dnmPLA (**7b**), $\text{BF}_2\text{dnm(Br)PLA}$ (**8b**), and $\text{BF}_2\text{dnm(I)PLA}$ (**9b**) in air and N_2 . Photographs were taken with UV lamp excitation ($\lambda_{\text{max}} = 354 \text{ nm}$); delayed emission images (i.e. delay) were captured after the UV lamp was turned off.

To adapt these materials for ratiometric sensing and achieve two discrete peaks it is necessary to increase the singlet-triplet energy gap with dye loading. All dye-polymer conjugates, **7a-9a** and **7b-9b**, exhibit TADF due to considerable overlap in fluorescence and phosphorescence peaks. Emission spectra under nitrogen appear as a single broad band with the exception of longer 23 kDa polymer of $\text{BF}_2\text{dnm(I)PLA}$, **9b**, in which fluorescence appears as a high-energy shoulder on the more intense phosphorescence peak. To test whether fluorescence and phosphorescence peaks can be separated, more dilute dye/polymer samples are required. However, attempts to grow

higher molecular weight materials did not yield the targeted products. Broad PDIs and dye degradation were observed for higher lactide loadings and longer reaction times. Higher molecular weights were not achieved. Previously it was demonstrated that spectral properties could be modeled with dye/polymer blends at high dilution.^{7,18} To avoid phase separation at higher dye loadings, in this study dye-PLA/PLA blends were prepared (Table S4.1; Appendix C). First, it was confirmed that spectral properties of **7b** (1.4%) could be replicated by blending **7a** (3.5%) and PLA. Then samples **7c-9c** were prepared in a comparable manner to achieve 1% dye loading. Although 1% loadings were not sufficient to produce peak separation in the H and Br materials, two discrete peaks are evident in the spectrum for BF₂dnm(I)PLA/PLA (**9c**) (Figure S4.4; Appendix C). Even at 1.0 % dye loading (**9c**), the phosphorescence was 3.4 times stronger than the fluorescence in air. Further dilution to 0.5 and 0.2% dye loadings shows slightly better peak resolution (Figure 4.5). However, both fluorescence and phosphorescence blue-shifted, which may indicate a change from aggregate to monomer emission, and the corresponding drop in intensity with lower dye loadings limits signal detection (e.g. lifetimes), making these blends less practical for oxygen imaging methods.¹⁵ With the exception of BF₂nbm(Br)PLA (26 kDa, 1.9 dye loading) which exhibited a fluorescence to phosphorescence intensity ratio (F/P) of 0.95,⁶ most BF₂bdkPLA materials with large singlet triplet energy gaps display weak phosphorescence at low dye loadings (i.e. high MWs).⁵ For example, BF₂dbm(I)PLA (17.6 kDa, 2.6% dye loading) showed a dramatic decrease in phosphorescence intensity (i.e. F/P = 1.67).¹⁷ The BF₂dnm(I)PLA sample **9c**

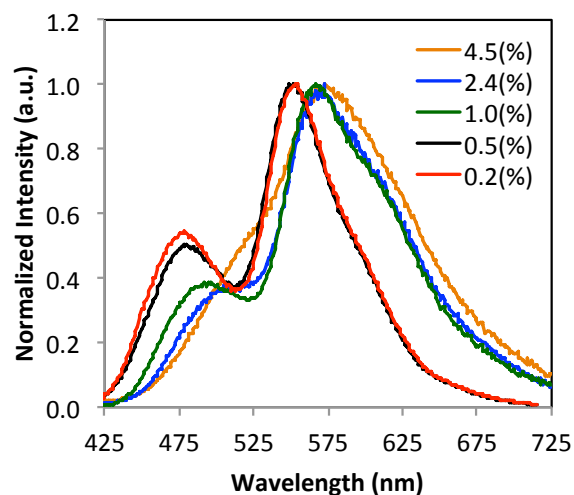


Figure 4.5. Fluorescence to phosphorescence ratio tuning for BF₂dnm(I)PLA/PLA blends at different dye loadings. (See Table S4.1.; Appendix C for blend preparation.)

with only 1% dye loading and discrete fluorescence and phosphorescence peaks exhibits the most intense relative phosphorescence to fluorescence value to date ($F/P = 0.26$).

4.2.4. Nanoparticles

Polymers were fabricated into nanoparticles to investigate their potential as oxygen nanosensors. Higher MW polymers **7b-9b** were selected for study given longer phosphorescence lifetimes that correlate with higher oxygen sensitivity, making all of these materials suitable for lifetime imaging methods. Given peak separation in film samples (Figures 4.4 and 4.5), the iodide polymer **9b** and blend **9b/PLA** served as the focus of ratiometric sensing experiments. Boron nanoparticles (BNPs) were fabricated by nanoprecipitation (i.e. solvent displacement) from DMF/H₂O by previously described methods.¹⁹

Nanoparticles were characterized with respect to size and optical properties. Nanoparticle size (hydrodynamic radius, R_H), polydispersity (PD) and luminescence properties are summarized in Table 4.4. Dynamic light scattering measurements indicated boron nanoparticle radii ranging from 29 – 47 nm, suitable for cellular uptake, and polydispersities were also typical for

Table 4.4. Nanoparticle Characterization

Sample			DLS ^a		Abs	Fluorescence		Phosphorescence	
			R_H (nm)	PD	λ_{\max} (nm)	λ_F^b (nm)	τ_F^c (ns)	λ_P^d (nm)	τ_P^e (ms)
BF ₂ dnmPLA	7b	NPH	46.0	0.29	434	493	2.87	503	71.4
BF ₂ dnm(Br)PLA	8b	NPBr	36.2	0.31	436	500	2.11	560	12.6
BF ₂ dnm(I)PLA	9b	NPI	29.1	0.15	438	498	1.20	570	5.7
BF ₂ dnm(I)PLA	9b	NPI* ^f	47.0	0.35	^g	479	0.80	565	5.9

^aBNP size and polydispersity determined by DLS (Figure S4.5.; Appendix C) ^bFluorescence maximum under air ($\lambda_{\text{ex}} = 400$ nm) ^cFluorescence lifetime at maximum emission under air ($\lambda_{\text{ex}} = 369$ nm LED) ^dPhosphorescence maxima in delayed emission spectra at room temperature under N₂ ($\lambda_{\text{ex}} = 400$ nm xenon lamp) ^ePhosphorescence lifetime at delayed emission spectra maxima under N₂ ($\lambda_{\text{ex}} = 400$ nm xenon flash lamp) ^fBNPs made by co-precipitation of polymer **9b** and PLA in 1:10 ratio by mass (0.2% loading) ^gDye absorbance is negligible (Figure S4.6; Appendix C).

BF₂bdkPLA materials. Nanoparticles made from dye-polymer conjugates **7b-9b** exhibited no changes in optical properties or DLS measurements after five days. In contrast, for the blend sample **9b/PLA**, changes were noted in spectra and DLS data after approximately two hours that became increasingly pronounced over time. For example, multimodal distributions were evident in DLS measurements and phosphorescence intensity decreased. Stereoblock formation²⁰ and PEGylation²¹ could enhance blended nanoparticle stability. Absorption properties of BNPs (Table 4.4) are nearly identical to dye solutions ($\lambda_{\max} = 435 - 440$ nm), and emission properties mirror those of films (Figure 4.6). Though fluorescence lifetimes are similar for particles and films, phosphorescence lifetimes are more sensitive to environmental changes, with BNPs showing decreased delayed emission lifetimes compared to film

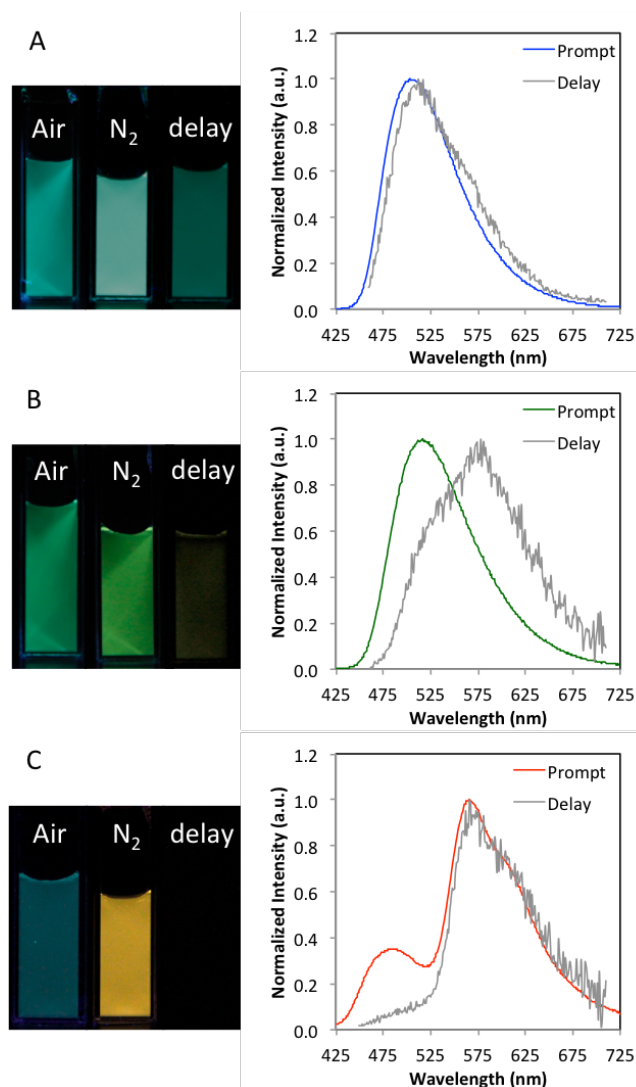


Figure 4.6. Boron nanoparticles: (A) **NPH (7b)**, (B) **NPBr (8b)**, and (C) **NPI* (9b/PLA)**. Images under air, nitrogen and delayed (i.e. under nitrogen after the UV lamp is turned off.) Total emission spectra under nitrogen (Prompt) and delayed emission spectra under nitrogen (Delay).

counterparts (hydrogen **7b**: film $\tau_p = 156$ ms, BNP $\tau_p = 71$ ms; bromine **8b**: film $\tau_p = 26$ ms, BNP $\tau_p = 12$ ms; iodine **9b**: film $\tau_p = 6.3$ ms, BNP $\tau_p = 5.7$ ms).

Given suitability for ratiometric oxygen sensing and imaging, iodide nanoparticles **NPI** were calibrated for oxygen sensitivity (Figure 4.7). Due to the small ΔE , TADF is evident in **NPI** as for **9b** films. Lifetimes for both delayed fluorescence and phosphorescence are independently measureable ($\tau_{497\text{ nm}} = 7.2$ ms and $\tau_{570\text{ nm}} = 5.7$ ms).

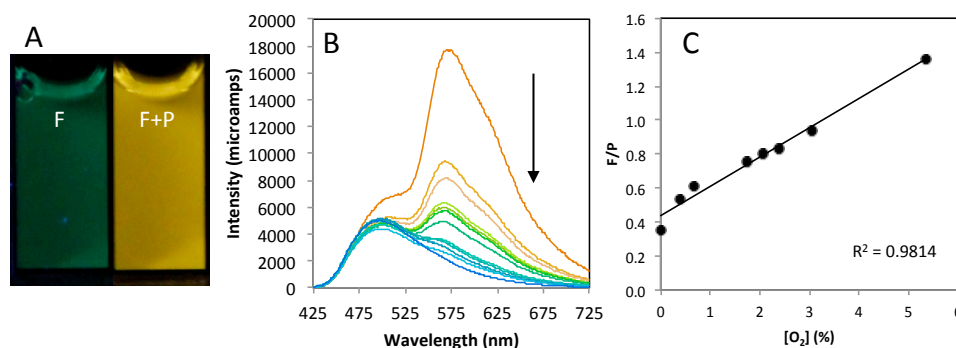


Figure 4.7. Boron nanoparticle oxygen sensing. (A) Images of BNPs made from BF₂dnm(I)PLA **9b** (NPI) in air (fluorescence) and N₂ (fluorescence + phosphorescence) ($\lambda_{\text{ex}} = 354$ nm). (B) Total emission spectra of **NPI** at O₂ levels 0-21%. Arrow indicates decreasing phosphorescence at 570 nm with increasing O₂. (C) Fluorescence intensity (505 nm) over phosphorescence intensity (565 nm) (F/P) calibration plot showing a linear fit in the 0 - 5.3% O₂ range.

Data are presented as wavelength versus intensity to illustrate this point, rather than the typical wavelength versus normalized fluorescence plots.^{3,33,58} However, fluorescence changes are minimal compared to phosphorescence and calibration plots are still essentially linear from 0-5.3% O₂ ($R^2 = 0.981$).

4.2.5. Conclusion

A series of hydroxyl-functionalized difluoroboron dinaphthoylmethane dyes were synthesized for the bulk polymerization of DL-lactide to yield new dye-PLA conjugates. Dyes showed tunable fluorescence, phosphorescence, and thermally activated delayed fluorescence in the solid state dependent upon dye loading (i.e. PLA molecular weight). At room temperature under N₂, thermally activated delayed fluorescence dominated for the non-halogenated material, BF₂dnmPLA, whereas phosphorescence was more intense for the bromide and iodide substituted polymers. Given the propensity of dinaphthyl dyes to aggregate, low dye loadings (i.e. higher MW polymers) were required to achieve good spectral separation of fluorescence and phosphorescence

signals for ratiometric oxygen sensing. Boron dye polymers were successfully fabricated into nanoparticles and were calibrated for O₂ sensing. The nanoparticles can be excited outside the ultraviolet range, which is important for biological imaging applications. The hydrogen and bromide derivatives show long phosphorescence lifetimes and high sensitivity to O₂ quenching, making them useful for lifetime based sensing methods. The iodide sample, BF₂dnm(I)PLA, on the other hand, displays distinct fluorescence and phosphorescence peaks making it compatible with ratiometric imaging.

4.3. Experimental Section

4.3.1. Materials

3,6-Dimethyl-1,4-dioxane-2,5-dione (D,L -lactide, Aldrich) was recrystallized twice from ethyl acetate and stored under nitrogen. Tin (II) 2-ethylhexanoate (Sn(oct)₂, Spectrum), boron trifluoride diethyl etherate (Aldrich, purified, redistilled) and all other reagents and solvents were used as received without further purification. Solvents CH₂Cl₂ and THF were dried and purified over 3 Å molecular sieves activated at 300 °C according to a previously described method. All other chemicals were reagent grade from Sigma Aldrich and were used without further purification. The compounds 1-(6-(2-(((tetrahydro-2H-pyran-2-yl)oxy)ethoxy)naphthalen-2-yl)ethanone⁶ and methyl 6-iodo-2-naphthoate²² were prepared as previously described. Poly(lactic-acid) was synthesized from ethylene glycol as previously described (M_n (GPC/MALS) = 13 800 Da, PDI = 1.03).⁷

4.3.2. Methods

¹H NMR (300 MHz) spectra were recorded on a Varian UnityInova 300/51 instrument in CDCl₃, or D₆-DMSO. ¹H NMR spectra were referenced to the signals for the residual protiochloroform at

7.26 ppm, protioDMSO at 2.50 ppm, and protioacetone at 2.09 ppm. Coupling constants are given in hertz. High-resolution mass spectra of ligands and dyes were recorded with a Micromass Q-TOF Ultima spectrometer using electrospray ionization (ESI) MS techniques. Polymer molecular weights were determined by gel permeation chromatography (GPC) (THF, 25 °C, 1.0 mL / min) using multi-angle laser light scattering (MALS) ($\lambda = 658$ nm, 25 °C) and refractive index (RI) ($\lambda = 658$ nm, 25 °C) detection. Polymer Laboratories 5 μ m mixed-C columns (guard column plus two columns) along with Wyatt Technology (Optilab T-rEX interferometric refractometer, miniDAWN TREOS multi-angle static light scattering (MALS) detector, ASTRA 6.0 software) and Agilent Technologies instrumentation (series 1260 HPLC with diode array (DAD) detector, ChemStation) were used in GPC analysis. UV-vis spectra were recorded on a Hewlett-Packard 8452A diode-array spectrophotometer. Steady-state fluorescence spectra were recorded on a Horiba Fluorolog-3 Model FL3-22 spectrofluorometer (double-grating excitation and double-grating emission monochromator). Time-correlated single-photon counting (TCSPC) fluorescence lifetime measurements were performed with a NanoLED-370 ($\lambda_{\text{ex}} = 369$ nm) excitation source and a DataStation Hub as the SPC controller. Phosphorescence lifetimes were measured with a 1 ms multi-channel scalar (MCS) excited with a pulsed Xenon lamp ($\lambda_{\text{ex}} = 400$ nm; duration <1 ms). Lifetime data were analyzed with DataStation v2.4 software from Horiba Jobin Yvon. Fluorescence quantum yields (Φ_{F}) for initiator and polymer samples in CH_2Cl_2 were calculated versus anthracene as a standard using a previously described method: Φ_{F} anthracene = 0.27, n_{D}^{20} EtOH = 1.360, n_{D}^{20} CH_2Cl_2 = 1.424.²³ Optically dilute CH_2Cl_2 solutions of the dyes were prepared in 1 cm path length quartz cuvettes with absorbances < 0.1 (a.u.).

Thin films were prepared on the inner wall of vials by dissolving polymers in CH_2Cl_2 (~2 mg/mL), then evaporating the solvent under a low N_2 flow. Blends of dye-PLA conjugates and

PLA were prepared by weighing dye-PLA and PLA into vials, dissolving in CH₂Cl₂ (~2 mg/mL), then evaporating the solvent under low N₂ flow (Table S4.1; Appendix C). The films were dried *in vacuo* overnight before measurements were taken. Polymers were fabricated into nanoparticles by previously described methods.¹⁹ Nanoparticle size was determined by dynamic light scattering (DLS) on a Wyatt Corporation DynaPro Plate Reader II. Ratiometric oxygen sensitivity calibration is performed as previously described.⁵⁸ Images of films and nanoparticles were taken with a Canon EOS 7D camera with handheld UV lamp excitation ($\lambda_{\text{ex}} = 354 \text{ nm}$).

1-[6-(2-Hydroxyethoxy)-2-naphthyl]-3-(2-naphthyl)-propane-1,3-dione (dnmOH) (1). The aromatic ketone, 1-(6-(2-((tetrahydro-2H-pyran-2-yl)oxy)ethoxy)naphthalen-2-yl)ethanone was prepared as previously described.⁶ 1-(6-(2-((Tetrahydro-2H-pyran-2-yl)oxy)ethoxy)naphthalen-2-yl)ethanone (740 mg, 2.35 mmol) and methyl 2-naphthoate (526 mg, 2.82 mmol) were weighed in a dry 100 mL round-bottom flask and dissolved in anhydrous THF (~20 mL). A suspension of anhydrous THF (~10 mL) and NaH (85 mg, 3.5 mmol) was transferred to the flask via cannula. The reaction mixture was heated at 60 °C and monitored by TLC until the limiting reagent (ketone) was consumed. After 1 d, the reaction mixture was cooled to room temperature and quenched by drop-wise addition of saturated NaHCO₃ (aq) (10 mL). THF was removed by rotary evaporation and the remaining aqueous layer was acidified with 1M HCl and extracted with CH₂Cl₂ (2 × 100 mL). The combined organic layers were washed with distilled water (2 × 100 mL) and brine (2 × 100 mL), then dried over Na₂SO₄, filtered, and concentrated in vacuo. The resulting brown, oily residue was dissolved in THF (50 mL) and water (15 mL), and p-TsOH (50 mg, 0.29 mmol) was added. The reaction mixture was heated at 60 °C and monitored by TLC. After 18 h, the reaction mixture was cooled to room temperature and THF was removed by rotary evaporation. The resulting residue was dissolved in CH₂Cl₂, washed with distilled water (2 × 100 mL), brine (2 ×

100 mL), and dried over anhydrous Na_2SO_4 . The solution was filtered, and solvent was removed via rotary evaporation. The tan colored crude product was purified via recrystallization with 1:1 hexanes/EtOAc to give **1** as a tan powder: 490 mg (54%). ^1H NMR (300 MHz, CDCl_3): δ 17.12 (s, 1H, -OH), 8.58 (s, 1H, 1''-ArH), 8.53 (s, 1H, 1'-ArH), 8.08 (d, $J = 3.0$, 1H, 8''-ArH), 8.05 (d, $J = 3.0$, 1H, 8'-ArH), 8.01 (d, $J = 7.2$, 1H, 4''-ArH), 7.95-7.89 (m, 3H, 4'-ArH, 3''-, 5''-ArH), 7.83 (d, $J = 8.7$, 1H, 3'-ArH), 7.59 (m, broad, 2H, 6''-, 7''-ArH), 7.26 (d, $J = 8.7$, 1H, 7'-ArH), 7.21 (s, 1H, 5'-ArH), 7.13 (s, 1H, -COCHCO), 4.35 (t, $J = 4.2$, 2H, -ArOCH₂CH₂OH), 4.09-4.05 (m, 2H, -ArOCH₂CH₂OH), 2.05 (s, 1H, -ArOCH₂CH₂OH). HRMS (ESI, TOF) m/z calcd for $\text{C}_{25}\text{H}_{21}\text{O}_4$ 385.1440 $[\text{M} + \text{H}]^+$; found 385.1433.

1-[6-(2-Hydroxyethoxy)-2-naphthyl]-3-(6-bromo-2-naphthyl)-propane-1,3-dione (dnm(Br)OH)

(2). The bromine derivative was prepared as described for **1** using methyl 6-bromo 2-naphthoate instead of methyl 2-naphthoate. A tan powder was obtained: 340 mg (46%). ^1H NMR (300 MHz, $(\text{CD}_3)_2\text{SO}$): δ 17.34 (s, 1H, -OH), 8.87 (s, 1H, 1''-ArH), 8.81 (s, 1H, 1'-ArH), 8.34 (s, 1H, 5''-ArH), 8.29 (d, $J = 8.4$, 1H, 8''-ArH), 8.20 (d, $J = 8.7$, 1H, 8'-ArH), 8.00-8.15 (m, broad, 3H, 3'-ArH, 3'', 4''-ArH), 7.95 (d, $J = 8.7$, 1H, 7''-ArH), 7.77 (d, $J = 8.7$, 1H, 7'-ArH), 7.61 (s, 1H, COCHCO), 7.45 (s, 1H, 5'-ArH), 7.25 (d, $J = 8.7$, 1H, 4'-ArH), 4.96 (t, $J = 4.2$, 1H, -ArOCH₂CH₂OH), 4.15 (t, $J = 4.2$, 2H, -ArOCH₂CH₂OH), 3.78 (m, 2H, -ArOCH₂CH₂OH). HRMS (ESI, TOF) m/z calcd for $\text{C}_{25}\text{H}_{20}\text{O}_4\text{Br}$ 463.0545 $[\text{M} + \text{H}]^+$; found 463.0538.

1-[6-(2-Hydroxyethoxy)-2-naphthyl]-3-(6-iodo-2-naphthyl)-propane-1,3-dione (dnm(I)OH) **(3).**

The iodine derivative was prepared as previously described for **1** with methyl 6-iodo 2-naphthoate instead of methyl 2-naphthoate. The crude dnm(I)OH product **3** was purified by recrystallization with acetone instead of hexanes/EtOAc to yield a tan powder: 98 mg (11%). ^1H NMR (300 MHz, $(\text{CD}_3)_2\text{SO}$): δ 17.39 (s, 1H, -OH), 8.84 (s, 1H, 1''-ArH), 8.80 (s, 1H, 1'-ArH), 8.52 (s, 1H, 5''-

ArH), 8.27 (d, $J = 9.0$, 1H, 8''-ArH), 8.18 (d, $J = 9.0$, 1H, 8'-ArH), 8.05-7.94 (m, broad, 5H, 3', 4'-ArH, 3'', 4'', 7''-ArH), 7.61 (s, 1H, COCHCO), 7.44 (s, 1H, 5'-ArH), 7.29 (d, $J = 12$, 1H, 7'-ArH), 4.95 (t, $J = 6.0$, 1H, -ArOCH₂CH₂OH), 4.15 (t, $J = 6.0$, 2H, -ArOCH₂CH₂OH), 3.78 (m, 2H, -ArOCH₂CH₂OH). HRMS (ESI, TOF) m/z calcd for C₂₅H₂₀O₄I 511.0406 [M + H]⁺; found 511.0421.

BF₂dnmOH (**4**). The ligand dnmOH (**1**), (250.0 mg, 0.705 mmol) was added to a dry 100 mL round bottom flask under nitrogen, and then dissolved in THF/CH₂Cl₂ (20/20 mL) to give a deep yellow solution. Boron trifluoride diethyl etherate (120 μ L, 0.845 mmol) was added via syringe, turning the solution bright yellow. The reaction was refluxed at 60 °C and monitored by TLC until the ligand substrate was consumed (24 h). Solvents were removed via rotary evaporation, generating a yellow solid. The crude material was purified by recrystallization with 1:1 EtOAc/acetone to yield a yellow-orange powder: 225 mg (74%). ¹H NMR (300 MHz, (CD₃)₂SO): δ 9.12 (s, 1H, 1''-ArH), 9.09 (s, 1H, 1'-ArH), 8.40-8.30 (m, 2H, 8'-ArH, 8''-ArH), 8.01 (d, $J = 8.1$, 1H, 4''-ArH), 8.16 (m, 3H, 5'', 3''-ArH, 7'-ArH), 8.06-8.00 (m, 2H, 3'-ArH, COCHCO), 7.75-7.65 (m, 2H, 6'', 7''-ArH), 7.51 (s, 1H, 5'-ArH), 7.34 (d, $J = 8.7$, 1H, 4'-ArH), 4.98 (bs, 1H, -ArOCH₂CH₂OH), 4.19 (t, $J = 4.8$, 2H, -ArOCH₂CH₂OH), 4.07 (t, $J = 4.8$, 2H, -ArOCH₂CH₂OH). HRMS (ESI, TOF) m/z calcd for C₂₅H₂₀BO₄F₂ 433.1423 [M + H]⁺; found 433.1414.

BF₂dnm(Br)OH (**5**). The bromide complex **5** was prepared as previously described for **4** using dnm(Br)OH (**2**) instead of dnm(H)OH. A yellow-orange powder was obtained: 35 mg (31%). ¹H NMR (300 MHz, (CD₃)₂SO): δ 9.12 (s, 1H, 1''-ArH), 9.09 (s, 1H, 1'-ArH), 8.48-8.33 (m, broad, 3 H, 8'', 5''-ArH, 8'-ArH), 8.18-8.14 (m, broad, 4H, 4'', 3''-ArH, 3'-ArH, -COCHCO-), 8.03 (d, $J = 8.7$, 1H, 7''-ArH), 7.83 (d, $J = 8.7$, 1H, 7'-ArH), 7.51 (s, 1H, 5'-ArH), 7.30 (d, $J = 8.7$, 1H, 4'-ArH),

4.98 (t, $J = 4.2$, 1H, -ArOCH₂CH₂OH), 4.19 (t, $J = 4.2$, 2H, -ArOCH₂CH₂OH), 3.80 (m, 2H, -ArOCH₂CH₂OH). HRMS (ESI, TOF) m/z calcd C₂₅H₁₈BO₄F₂BrNa 533.0347 [M + Na]⁺; found 533.0340.

BF₂dnm(I)OH (6). The iodide complex **6** was prepared as previously described for **4** using dnm(I)OH (**3**) in place of dnmOH with the following exception: the dnm(I)OH ligand was dissolved in anhydrous THF instead of THF/CH₂Cl₂. A yellow powder was obtained: 31 mg (44%). ¹H NMR (300 MHz, (CD₃)₂SO): δ 9.09 (s, broad, 2H, 1''-ArH, 1'-ArH), 8.59 (s, 1H, 5''-ArH), 8.41 (d, $J = 6.0$, 1H, 8''-ArH), 8.35 (d, $J = 9.0$, 1H, 8'-ArH), 8.17-7.98 (m, broad, 6H, 3''-ArH, 3'-ArH, 4''-ArH, 4'-ArH, 7''-ArH, COCHCO), 7.52 (s, 1H, 5'-ArH), 7.35 (d, $J = 12$, 1H, 7'-ArH), 4.98 (t, $J = 6.0$, 1H, -ArOCH₂CH₂OH), 4.19 (t, $J = 6.0$, 2H, -ArOCH₂CH₂OH), 3.79 (m, 2H, -ArOCH₂CH₂OH). HRMS (ESI, TOF) m/z calcd C₂₅H₁₈BO₄FI [M - F]⁺ 539.0327; found 539.0320.

Polymer Synthesis. Preparative scale reactions to produce BF₂dnmPLA (**7a-b**), BF₂dnm(Br)PLA (**8a-b**), and BF₂dnm(I)PLA (**9a-b**) were conducted as previously described.^{5t} Reagent loadings, reaction times, and monomer conversions are presented in Table 4.1. At the end of each polymerization, an aliquot was taken to determine monomer conversion by ¹H NMR spectroscopy. For polymers with low monomer conversion (< 50%), an additional precipitation into cold methanol was necessary to remove residual monomer. The polymer molecular weights were determined by ¹H NMR spectroscopy and GPC (MALS/RI). Molecular weights, polydispersity indices (PDIs), and yields are collected in Table 4.1. Yields are corrected for monomer conversion.

BF₂dnmPLA (7a). The dinaphthyl polymer **7a** was obtained as a yellow crystalline foam: 325 mg (68%). M_n (GPC/MALS) = 12,200 Da, PDI = 1.20; M_n (¹H NMR) = 11,800 Da. ¹H NMR (600 MHz, CDCl₃): δ 8.89 (s, 1H, 1'-ArH), 8.77 (s, 1H, 1''-ArH), 8.13 (m, 2H, 8'-ArH, 8''-ArH), 7.96

(m, broad, 6H, 3'-, 4'-, 5'-ArH, 3''-, 7''-ArH), 7.66 (m, broad, 2H, 7', 6'-ArH), 7.51 (s, 1H, 5''-ArH), 7.34 (d, J = 8.7, 1H, 4''-ArH), 7.19 (s, 1H, -COCHCO-), 5.16 (m, broad, 168 H, PLA-CH-CH₃), 4.59 (t, J = 4.8, 2H, -ArOCH₂CH₂-), 4.35 (t, J = 4.8, 2H, -ArOCH₂CH₂-), 1.57 (s, broad, 543 H, PLA-CHCH₃).

BF₂dnm(Br)PLA (8a). The bromo-dinaphthyl polymer **8a** was obtained as yellow crystalline foam: 212 mg (78%). *M_n* (GPC/MALS) = 12,500 Da, PDI = 1.19; *M_n* (NMR) = 12,500 Da. ¹H NMR (600 MHz, CDCl₃): δ 8.77 (m, broad, 2H, 1''-ArH, 1'-ArH), 8.17-8.11 (m, broad, 3H, 3''-, 8'', -ArH, 8'-ArH), 7.92-7.85 (m, broad, 5H, 3'-, 7', -ArH, 4''-, 5'', -7''-, ArH), 7.70 (d, J = 9, 1H, 4'-ArH), 7.42 (s, 1H, -COCHCO-), 7.18 (s, 1H, 5'-ArH), 5.31-5.11 (m, broad, 180 H, PLA -CH-CH₃), 4.55 (m, 2H, -ArOCH₂CH₂-), 4.35 (m, 2H, -ArOCH₂CH₂-), 1.57 (s, broad, 646 H, PLA -CHCH₃).

BF₂dnm(I)PLA (9a). The iodo-dinaphthyl polymer **9a** was obtained as yellow-orange foam: 98 mg (46%). *M_n* (GPC/MALS) = 12,500 Da, PDI = 1.12; (NMR) = 13,000 Da. ¹H NMR (600 MHz), (CDCl₃): δ 8.77 (s, broad, 2H, 1''-ArH, 1'-ArH), 8.36 (s, 1H, 5''-ArH), 8.19-8.10 (m, 2H, 8''-ArH, 8'-ArH), 7.95 - 7.87 (m, broad, 4H, 3'-, 4'-ArH, 3''-, 4''-ArH), 7.60 (s, 1H, 7''-ArH), 7.43 (s, 1H, COCHCO), 7.33 (s, 1H, 5'-ArH), 7.19 (d, J = 9, 1H, 5'-ArH), 5.30-5.11 (bm, 173H, PLA-CH-CH₃), 4.62 - 4.55 (m, 2H, -ArOCH₂CH₂-), 4.37 - 4.34 (m, 3H, -ArOCH₂CH₂OH, PLA-OH), 1.63-1.47 (s, broad, 596H, PLA-CH₃).

4.4. Acknowledgements

This research was published in *Macromolecules*.²⁴ I thank Ziyi Fan and Jelena Samonina-Kosicka for help in the synthesis and characterization of these BF₂dnm(X)PLA polymers, Prof. Fraser and Ziyi for assistance in the preparation of the manuscript, and the financial support of the National Cancer Institute of the National Institutes of Health (R01 CA167250).

4.5. References

- (1) Butler, T.; Morris, W. A.; Samonina-Kosicka, J.; Fraser, C. L. *Chem. Commun.* **2015**, 51, 3359–3362.
- (2) Butler, T.; Morris, W. A.; Samonina-Kosicka, J.; Fraser, C. L. *ACS Appl. Mater. Interfaces* **2016**, 8, 1242–1251.
- (3) Wang, X.-H.; Peng, H.-S.; Ding, H.; You, F.-T.; Huang, S.-H.; Teng, F.; Dong, B.; Song, H.-W. *J. Mater. Chem.* **2012**, 22, 16066–16071.
- (4) McGehee, M. D.; Bergstedt, T.; Zhang, C.; Saab, A. P.; O'Regan, M. B.; Bazan, G. C.; Srdanov, V. I.; Heeger, A. J. *Adv. Mater.* **1999**, 11, 1349–1354.
- (5) DeRosa, C. A.; Kerr, C.; Fan, Z.; Kolpaczynska, M.; Mathew, A. S.; Evans, R. E.; Zhang, G.; Fraser, C. L. *ACS Appl. Mater. Interfaces* **2015**, 7, 23633–23643.
- (6) Samonina-Kosicka, J.; DeRosa, C. A.; Morris, W. A.; Fan, Z.; Fraser, C. L. *Macromolecules* **2014**, 47, 3736–3746.
- (7) Zhang, G.; Kooi, S. E.; Demas, J. N.; Fraser, C. L. *Adv. Mater.* **2008**, 20, 2099–2104.
- (8) Lower, S. K.; El-Sayed, M. A. *Chem. Rev.* **1966**, 66, 199–241.
- (9) Daly, M. L.; DeRosa, C. A.; Kerr, C.; Morris, W. A.; Fraser, C. L. *RSC Adv.* **2016**, 6, 81631–81635.
- (10) Payne, S. J.; Zhang, G.; Demas, J. N.; Fraser, C. L.; Degraff, B. A. *Appl. Spectrosc.* **2011**, 65, 1321–1324.
- (11) Zhang, G.; Chen, J.; Payne, S. J.; Kooi, S. E.; Demas, J. N.; Fraser, C. L. *J. Am. Chem. Soc.* **2007**, 129, 8942–8943.
- (12) Reineke, S. *Nat. Photonics* **2014**, 8, 269–270.
- (13) Yang, Z.; Mao, Z.; Xie, Z.; Zhang, Y.; Liu, S.; Zhao, J.; Xu, J.; Chi, Z.; Aldred, M. P.

- Chem. Soc. Rev.* **2017**, *46*, 915–1016.
- (14) Roussakis, E.; Li, Z.; Nichols, A. J.; Evans, C. L. *Angew. Chem. Int. Ed.* **2015**, *54*, 8340–8362.
- (15) Wang, X.; Wolfbeis, O. S. *Chem. Soc. Rev.* **2014**, *43*, 3666–3761.
- (16) Wang, X.; Gorris, H. H.; Stolwijk, J. A.; Meier, R. J.; Groegel, D. B. M.; Wegener, J.; Wolfbeis, O. S. *Chem. Sci.* **2011**, *2*, 901–906.
- (17) Zhang, G.; Palmer, G. M.; Dewhurst, M. W.; Fraser, C. L. *Nat. Mater.* **2009**, *8*, 747–751.
- (18) Xu, S.; Evans, R. E.; Liu, T.; Zhang, G.; Demas, J. N.; Trindle, C. O.; Fraser, C. L. *Inorg. Chem.* **2013**, *52*, 3597–3610.
- (19) Pfister, A.; Zhang, G.; Zareno, J.; Horwitz, A. F.; Fraser, C. L. *ACS Nano* **2008**, *2*, 1252–1258.
- (20) Kersey, F. R.; Zhang, G.; Palmer, G. M.; Dewhurst, M. W.; Fraser, C. L. *ACS Nano* **2010**, *4*, 4989–4996.
- (21) Samonina-Kosicka, J.; Weitzel, D. H.; Hofmann, C. L.; Hendargo, H.; Hanna, G.; Dewhurst, M. W.; Palmer, G. M.; Fraser, C. L. *Macromol. Rapid Commun.* **2015**, *36*, 694–699.
- (22) Irvine, M. W.; Costa, B. M.; Dlaboga, D.; Culley, G. R.; Hulse, R.; Scholefield, C. L.; Atlason, P.; Fang, G.; Eaves, R.; Morley, R.; Mayo-Martin, M. B.; Amici, M.; Bortolotto, Z. A.; Donaldson, L.; Collingridge, G. L.; Molnár, E.; Monaghan, D. T.; Jane, D. E. *J. Med. Chem.* **2012**, *55*, 327–341.
- (23) Demas, J. N.; Crosby, G. A. *J. Phys. Chem.* **1971**, *75*, 991–1024.
- (24) DeRosa, C. A.; Samonina-Kosicka, J.; Fan, Z.; Hendargo, H. C.; Weitzel, D. H.; Palmer, G. M.; Fraser, C. L. *Macromolecules* **2015**, *48*, 2967–2977.

Chapter 5:

Difluoroboron Thienyl Phenyl β -Diktonate Polylactide



5.1. Introduction

Thiophene-based dyes and polymers have become some of the most versatile optical materials in the field of low-bandgap photovoltaics, metal-free phosphors and photochromic devices.^{1–6} Recent reports show that small molecule fluorophores can also benefit from substituting a phenyl ring for a thienyl unit.⁷ Ono and co-workers analyzed phenyl, furan and thiophene substituted difluoroboron β -diketonates in solution and the solid state, and found increased thiophene substitution resulted in the greatest red-shifts in optical properties.⁸ Furthermore, Meier and co-workers have investigated europium complexes of dithienyl β -diketonate for temperature sensing applications.^{9–11} The thienyl-based β -diketonate ligands are two-photon excitable and ideal to sensitize lanthanides.^{9,12} In the course of our research, we discovered thienyl substituted boron dyes blended, not conjugated, with PLA have red-shifted phosphorescence, along with benefits of higher molar absorptivity at lower energy (i.e. redder).¹³ A promising scaffold consisted of a thienyl-phenyl aromatic set. The phenyl ring with a methoxy group imitated the effect of having an ether-linked hydroxyl tail as the initiator for lactide polymerization.

In this study, the unsubstituted (H), bromide (Br), and iodide (I) substituted thienyl dyes **4–6** were prepared as initiators for the solvent-free polymerization of DL-lactide in the presence of a tin catalyst to produce dye-polymer conjugates **7–9** (Figure 5.1.). Heavy atoms, bromide and iodide, were incorporated into the dye scaffold to modulate the relative F to RTP intensities (F/P).¹⁴ Fortuitously, the iodide derivative (BF₂tbm(I)PLA, **9**) showed unprecedented singlet-triplet splitting (Δ_{ST}) with well-

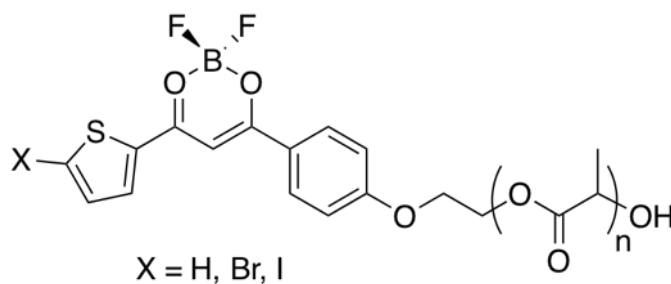


Figure 5.1. Chemical Structure of Difluoroboron Thienyl Phenyl β -Diketonate Polyactides

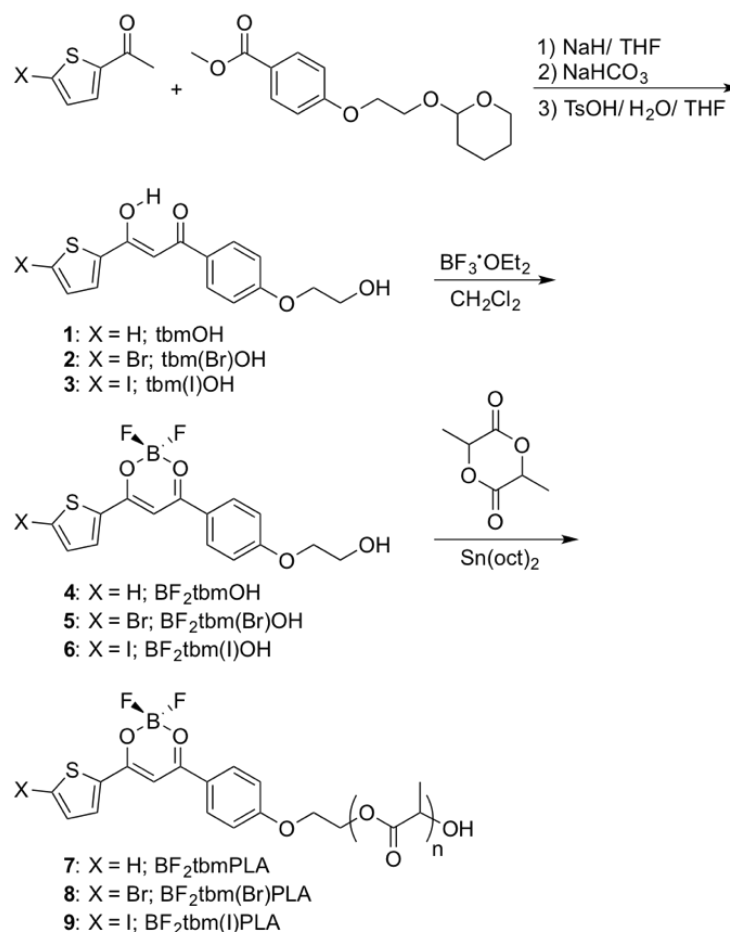
balanced **F** and **P** emissions (under N_2 ; $\text{F/P} = \sim 1$), a linear **F/P** correlation versus $[\text{O}_2]$ from 0-21% ($R^2 = 0.994$). This dye-polymer conjugated material provides a new O_2 sensitive polymer for ratiometric oxygen sensing applications.

5.2. Results and Discussion

5.2.1 Synthesis

Synthesis of the boron dye initiators was carried out as previously described,¹⁵ and is shown in Scheme 5.1. Previously, phenyl and naphthyl derivatives were developed with the same strategy. Because β -diketonates are most readily synthesized from ketone-ester pairs, there are countless combinations of commercial aromatic groups available to incorporate with the dioxaborine moiety.

Here, 2-acetylthiophene, with and without halide heavy atoms (Br and I), was condensed with a dihydropyran-protected methyl benzoate reagent using sodium hydride as the base, followed by deprotection of the crude products to generate the β -diketone ligands, **1-3**. In anhydrous methylene chloride, β -diketones were combined with boron trifluoride diethyl etherate to generate the boron initiators, **4-6**, in moderate yields after purifying by column chromatography.

Scheme 5.1. Synthesis of Thienyl Boron Dye-Polylactide Conjugates.

The dye-PLA conjugates were prepared in DL-lactide melts at 130° C in the presence of Sn(oct)₂ as a catalyst (Table 5.1). Zhang et al. previously reported lactide polymerization from a thienyl boron dye under similar reaction conditions.¹⁶ To our knowledge, the reaction kinetics have never been reported. When only 100 equivalents of lactide were used, high MW polymers with broad polydispersities were produced, which suggested uncontrolled ring-opening polymerizations¹⁷ (i.e. BF₂tbm(I)PLA; ~15 kDa; Đ = 1.30+, Figure S5.1. and S5.2.; Appendix D). One possibility is that thienyl groups or other features of the dye-PLA can couple in the presence of the tin catalyst, as suggested

Table 5.1. Polymer Synthesis and Molecular Weight Characterization

Polymer		Loading ^a	M _n ^b (NMR)	M _n ^c (GPC)	M _w ^c (GPC)	Đ ^c (GPC)
BF ₂ tbmPLA	7	300:1/40	23 300	18 600	20 400	1.10
BF ₂ tbm(Br)PLA	8	200:1/40	22 800	20 500	23 400	1.14
BF ₂ tbm(I)PLA	9	200:1/40	19 400	19 800	21 800	1.10

^a Molar ratio of monomer: Sn(oct)₂ per 1 equivalent of boron initiator. ^b Estimated from the relative integration (dye-OCH₂CH₂-OPLA/PLA-*H*). ^c Molecular weight data determined by GPC with MALS/RI detection. ^d Percent monomer conversion determined by relative integration (PLA-*H*/Lactide-*H*). ^e Corrected for monomer conversion.

by a high molecular weight (MW) shoulder on the GPC trace (Figures S5.1.; Appendix D). However, no changes in the UV/vis spectrum were observed. Furthermore, other reports of tin catalyzed polymerizations from thiophene dyes did not describe byproducts, such as bithiophene.^{18,19} Given that high molecular weight shoulders are a common occurrence in functionalized lactide polymerizations, such as poly(ethylene glycol)s and fluorescent dyes, the high MW product is likely not a chemical change in the dye, but a secondary interaction induced by the added functionality.^{16,20} Another possibility is weak binding between the sulfur atom and the tin catalyst, slowing down the initiation process. Therefore, low molecular weight polymers (<10 kDa) were not achievable in this report. Future efforts could test organocatalyst alternatives to ring opening polymerization of lactide.²¹

Given higher molecular weight polymers (>20 kDa) benefit from increased photostability, and large singlet-triplet gaps (Δ_{ST}),²² synthesis of such congeners are preferred for practical applications. In fact, when higher lactide loadings were used (200 equiv), the polymerization was controllable (Figure S5.3 and S5.4; Appendix D). The thiophene boron dye initiator BF₂tbmOH, **4**, polymerized well with high lactide loading (300 equivalents). After four hours, main chain growth ceased (53% conversion according to ¹H NMR), and increases in MW were attributed to

transesterification. Thus, reactions were stopped at low lactide conversions (~50-70%) to control the MW of the polymer product (Figure S5.5; Appendix D).

5.2.2. *Optical Properties in Solution.*

Dye initiators and polymer products were analyzed in dilute dichloromethane solution (1×10^{-5} M) (Table 2). Dye initiators and their polymer congeners have similar optical properties in solution, insuring the polymerization process did not affect the integrity of the dye.^{23,24} In solution, dyes showed violet to blue absorbances (418-433 nm; Figure S5.6.; Appendix D) with the heavier halide substituted dyes corresponding to slightly redder absorbance. Similarly, the emission red-shifted with heavier halide substituents (i.e. λ_{em} ; BF₂tbmOH = 441 nm, BF₂tbm(I)OH = 453 nm). The luminescence quantum yield was also affected by the halide substituents (Φ_F ; BF₂tbmOH = 0.53, BF₂tbm(I)OH = 0.10), likely due to increased intersystem crossing via the heavy atom effect siphoning singlet energy to the triplet state.^{22,25} However, the fluorescence quantum yield of the thienyl dyes are notably lower than many classic BF₂bdk dyes displaying quantum yields approaching unity.^{15,26,27}

Table 5.2. Optical Properties of Boron Initiators and Polymers in CH₂Cl₂ Solution

Sample		λ_{abs}^a (nm)	ε^b (M ⁻¹ cm ⁻¹)	λ_{em}^c (nm)	τ_F^d (ns)	Φ_F^e
BF ₂ tbmOH	4	418	66 000	441	1.51	0.53
BF ₂ tbmPLA	7	416	64 000	436	1.50	0.39
BF ₂ tbm(Br)OH	5	428	64 800	449	1.00	0.30
BF ₂ tbm(Br)PLA	8	425	50 800	447	0.80	0.17
BF ₂ tbm(I)OH	6	433	64 200	453	0.61	0.11
BF ₂ tbm(I)PLA	9	433	59 000	451	0.49	0.10

^aAbsorption maxima. ^bExtinction coefficients calculated at the absorption maxima. ^cFluorescence emission maxima excited at 369 nm (xenon lamp). ^dFluorescence lifetime excited at 369 nm (LED) monitored at the emission maximum. All fluorescence lifetimes are fitted with single-exponential decay. ^eRelative quantum yield versus anthracene in EtOH as a standard.

To gain further insight, density functional theory (DFT) calculations were performed on the iodide derivative, BF₂tbm(I)OMe (Figure 5.2). Previously, we reported BF₂tbmOMe, analogous to the electronic properties of the BF₂tbmOH initiator (**4**). For simplicity, calculations were performed with a methoxy substituent to mimic the electron donating features of the dye-*OCH₂CH₂OPLA* linker.²⁸ Calculated frontier molecular orbitals revealed delocalized electron density in both the highest occupied molecular orbital (HOMO) and the lowest unoccupied molecular orbital (LUMO), resembling a π - π^* transition.²⁶ This is consistent with the experimental results in CH₂Cl₂, where the absorption spectrum has structured peaks (Figure S5.6; Appendix D). Calculations also revealed significant electron density localized on the halide in both the HOMO and LUMO molecular orbitals. This is an important design feature for BF₂bdkPLA materials, as the halide heavy atom requires appropriate positioning on the scaffold in order to promote intersystem crossing for phosphorescence enhancement.²⁹

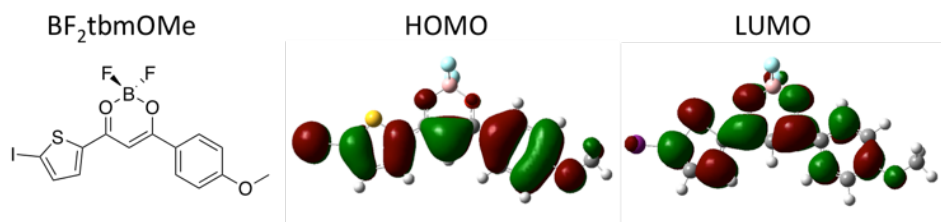


Figure 5.2. Calculated structure and HOMO/LUMO orbitals of $\text{BF}_2\text{tbm}(\text{I})\text{OMe}$.

5.2.3. Optical Properties of Polymers as Films.

The polymers were studied as solution cast films in vials. As films, the solid-state optical properties were highly dependent on the halide attached to the dye. All the polymers showed fluorescence and room-temperature phosphorescence under a nitrogen atmosphere (Figures 5.3 and Table 5.3). Typically, when the dye is covalently linked to the polymer matrix, aggregation effects are minimized and higher dye loadings are possible without phase separation than in blends.²⁴ But curiously, these thiophene derivatives had very distinct emission bands and did not follow the trends normally observed for dye-PLA conjugates.

Table 5.3. Optical Properties of Polymers as CH_2Cl_2 Cast Films

Sample		λ_{F}^a (nm)	τ_{F}^b (ns)	λ_{P}^c (nm)	τ_{P}^d (ms)
BF_2tbmPLA	7	453	1.76	545	62.0
$\text{BF}_2\text{tbm}(\text{Br})\text{PLA}$	8	467 (536) ^e	0.90 (1.83) ^e	589	4.1
$\text{BF}_2\text{tbm}(\text{I})\text{PLA}$	9	454 (541) ^e	0.24 (1.51) ^e	600	1.6

^aSteady-state fluorescence spectra emission maximum under air ($\lambda_{\text{ex}} = 385$ nm). ^bFluorescence lifetime excited with a 369 nm light-emitting diode (LED) monitored at the emission maximum.

^cDelayed emission spectra maxima under N_2 ($\lambda_{\text{ex}} = 385$ nm). ^dPre-exponential weighted RTP lifetime. ^eWavelength max and fluorescence lifetime of aggregate peak in the total emission spectra under air.

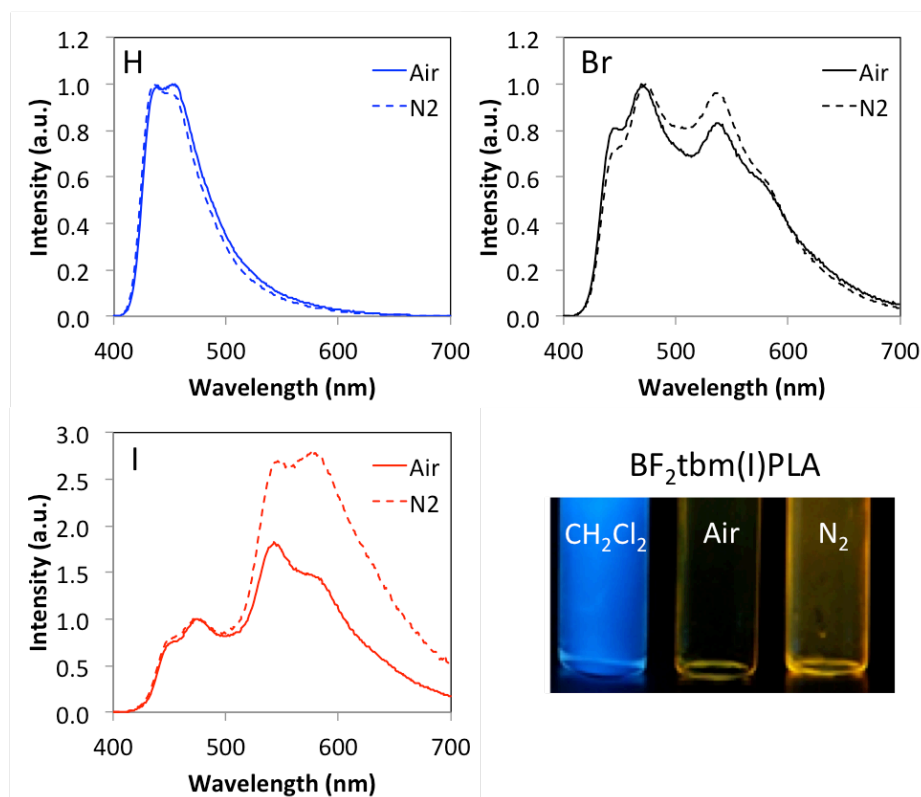


Figure 5.3. Total emission of BF₂tbm(X)PLA (**7-9**) films in air and N₂. Image: Luminescence of BF₂tbm(I)PLA dissolved in CH₂Cl₂, and a thin film under air and N₂ ($\lambda_{\text{ex}} = 369$ nm).

In air, BF₂tbmPLA (**7**) displayed a single blue peak, assigned as the fluorescence ($\lambda_{\text{F}} = 453$ nm, $\tau_{\text{F}} = 1.76$ ns). For the bromide substituted sample, BF₂tbm(Br)PLA (**8**), a blue peak at 467 nm ($\tau_{\text{F}} = 0.90$ ns) as well as a redder transition at 536 nm ($\tau_{\text{F}} = 1.86$ ns) are present. This pattern became more pronounced for the iodide derivative, BF₂tbm(I)PLA (**9**), with a weak blue fluorescence peak at 454 nm ($\tau_{\text{F}} = 0.24$ ns) and a second peak at 541 nm ($\tau_{\text{F}} = 1.51$ ns). Given these redder transitions only existed in the solid state, and not in dilute CH₂Cl₂ solutions (Figure 5.3.), these observations suggest aggregation-induced changes within the PLA matrix. Heavy atom substituted dyes have notoriously low solubility; therefore, the aggregation-induced red emission from the

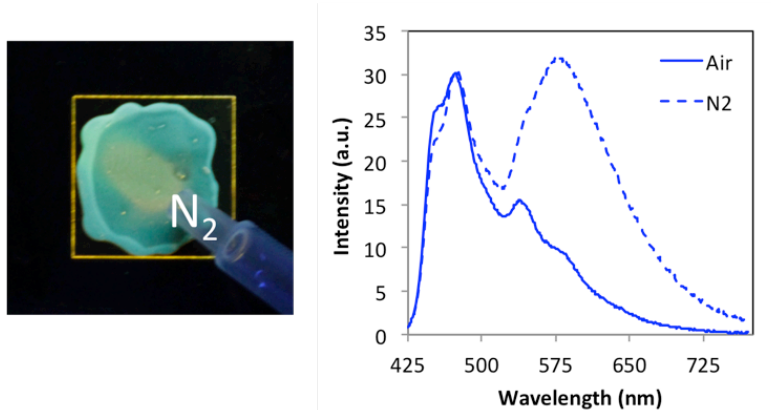


Figure 5.4. Total emission of BF₂tbm(I)PLA (**9**) blended with PLA (~1.0% dye) as toluene cast films in air and N₂.

iodide sample can be expected. To determine the origin of the red-shifted peak as aggregate or excimer emission, excitation spectra were recorded for the two peaks of **8** and **9** (Figure S5.7; Appendix D).³⁰ Excitation spectra reveal that distinct ground state species (i.e. aggregates vs. monomers) are responsible for the fluorescence peaks. In PLA, the heavy atom substituted thienyl dyes have a higher propensity to aggregate than non-heteroaromatic dyes.^{13,24,26,31}

To tailor aggregation induced dye-dye interactions, dye concentration (i.e. dye loading) was used to control the emission and a different solvent was tested. When polymer **9** was dissolved with excess PLA in toluene (~1.0% dye total) and evaporated onto a glass slide, aggregation diminished, yielding comparable F and RTP intensities under N₂, which is promising for oxygen sensing applications (Figure 5.4. and Table S5.1; Appendix D).

The room temperature phosphorescence (RTP) properties are analogous to previously described heavy atom-substituted boron dyes.²² For example, in the total emission spectra of BF₂tbmPLA (**7**), no changes are observed in the total emission from air to N₂ (F > RTP). The bromide dye showed the same result (F > RTP), likely a result of the RTP residing near the same wavelength as the aggregate emission. Among these thienyl dyes, only the iodo-substituted derivative (**9**) showed distinct F and RTP signals required for ratiometric O₂ sensing. Also, a

decrease in phosphorescence lifetime occurred, which is an important factor influencing oxygen sensitivity (τ_p ; BF₂tbmPLA = 62 ms; BF₂tbm(I)PLA = 1.6 ms).²²

5.2.4. Nanoparticles

The dye-polymer conjugates were prepared as nanoparticles as previously described.³² Nanoparticles are easily fabricated and suitable for topical application to image oxygen levels in tumors³³ or cells.¹⁴ The dynamic light scattering (DLS), and luminescence data are summarized in Table 5.4. When fabricated as nanoparticles (BF₂tbmPLA; **HNP**, BF₂tbm(Br)PLA; **BrNP**, BF₂tbm(I)PLA; **INP**), the luminescence properties were dramatically altered compared to emission as films. The effect is most prominent in the bromide sample, **BrNP**. As a film, two fluorescence peaks were present; one ascribed to the monomer at 467 nm, and another assigned as the aggregate peak at 536 nm. When fabricated as nanoparticles, the aggregate peak disappears and a distinct RTP peak emerges from the total emission spectra under N₂, yielding a color change from blue (F) to white (F + RTP) luminescence (Figure 5.5.). For the iodide sample (**INP**), the aggregate emission is reduced, but is still a prominent feature in the total emission spectra under air. No change is observed for **HNP**, as the dye did not show aggregation in the film state either.

Table 5.4. BF₂tbm(X)PLA Nanoparticle Properties

Sample	R _H ^a (nm)	λ_{abs} ^b (nm)	λ_{F} ^c (nm)	τ_{F} ^d (ns)	λ_{P} ^e (nm)	τ_{P} ^f (ms)
HNP	52.1	417	437	1.66	562	89.2
BrNP	45.6	426	449	0.78	600	7.62
INP	39.6	431	452 (543)	0.64 (1.58)	580	1.92
INP ^{*h}	42.3	433	449	0.65	581	2.02

^aHydrodynamic radius (R_H) according to DLS. ^bAbsorbance maxima. ^cSteady-state fluorescence spectra emission maximum under air (λ_{ex} = 385 nm). ^dFluorescence lifetime excited with a 369 nm light-emitting diode (LED) monitored at the emission maximum. ^eDelayed emission spectra maxima under N₂ (λ_{ex} = 385 nm). ^fPre-exponential weighted RTP lifetime (λ_{ex} = 385 nm from a xenon flash lamp). ^gSecond fluorescence transition (aggregate). ^hNanoparticles fabricated from a 1:1 ratio of BF₂tbm(I)PLA (**9**) and PLA.

During the nanoprecipitation process, it is possible the dyes become solvated by water, decreasing dye/dye interactions in the nanoparticle. Nanoprecipitation (DMF/water solvent system) may also influence aggregation processes, as the dye-polymers do not assemble in the same way in CH_2Cl_2 or toluene evaporation, as evidenced by different optical properties. Further investigation is necessary to elucidate the mechanism of aggregation or solvation of the molecule in PLA when precipitated from various solvents.

Each dye-polymer conjugate is adapted for different oxygen sensing regimes. For example, the nanoparticles fabricated from BF_2tbmPLA (**7**) have long phosphorescence lifetimes (89 ms), well suited for lifetime-based hypoxia imaging. For a larger oxygen sensing range (i.e. 0-21% O_2), materials with stronger RTP and shorter lifetimes are required. The optical properties of $\text{BF}_2\text{tbm(I)PLA}$ (**9**), particularly diluted with PLA, are the most promising for ratiometric techniques with comparable F and RTP and short RTP lifetime (2.3 ms) (Figure 5.6).

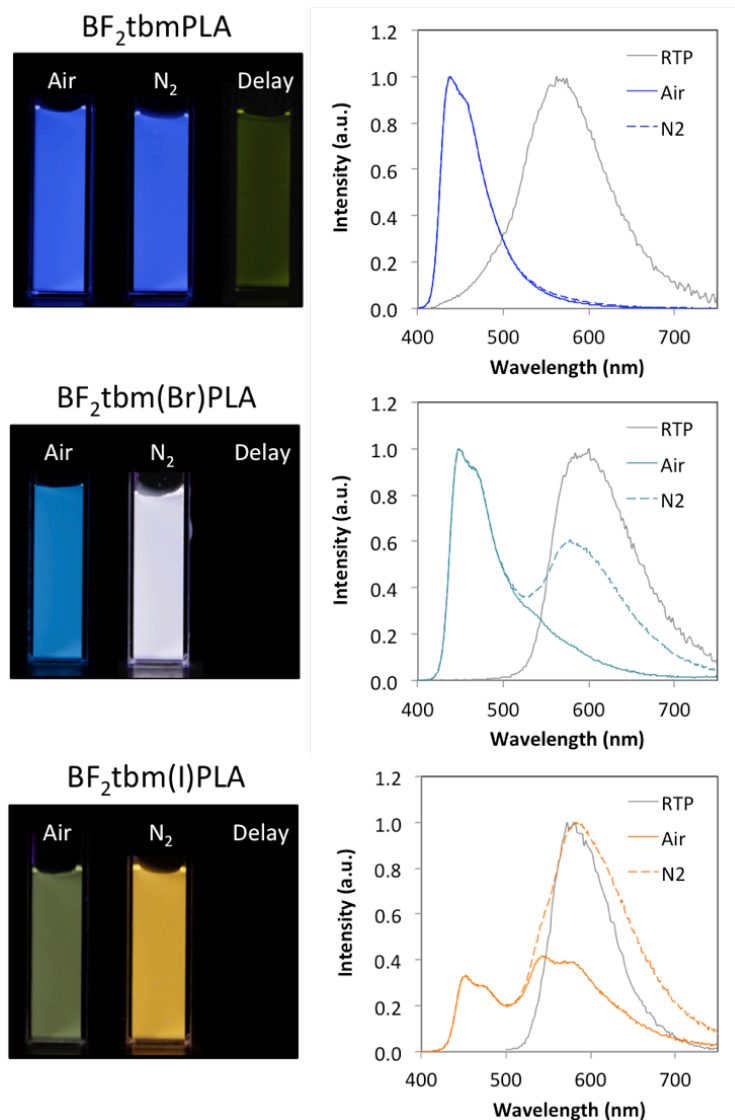


Figure 5.5. Optical properties of thienyl boron dye-polymers fabricated as nanoparticles. Images in air (F), N₂ (F+RTP) and after the UV lamp was turned off (i.e. delayed; RTP). Steady state emission spectra taken under air and N₂ and delayed emission spectra (RTP) taken under N₂ (1 ms delay).

To achieve nanoparticle optical properties analogous to the 1% dye-PLA film, a coprecipitation was performed with BF₂tbm(I)PLA and PLA (1:1 mass ratio) to yield **INP***. The nanoparticles thus prepared were subjected to ratiometric oxygen calibration, shown in Figure 5. Fortunately, the nanoparticles showed large singlet-triplet splitting ($\Delta_{ST} = \sim 140$ nm), balanced F and RTP intensities (F/P = ~ 1 under N₂), and linear correlation between the F/P ratio and oxygen concentration from 0-21% O₂ ($R^2 = 0.995$).

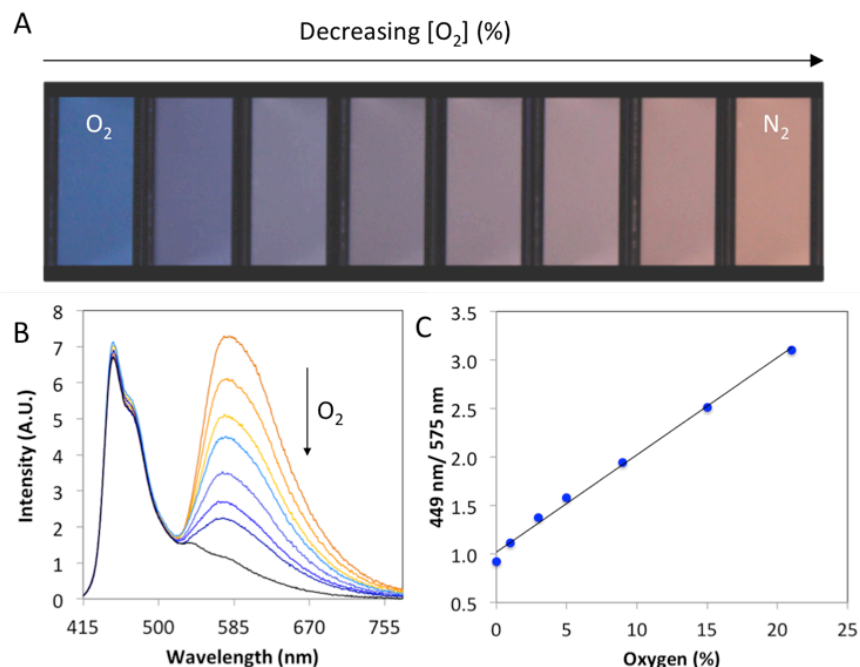


Figure 5.6. Oxygen Calibration of BF₂tbm(I)PLA/PLA (INP*) Nanoparticles. A) Images of nanoparticles with decreasing oxygen level left to right. B) Changes in total emission spectra at various oxygen levels; arrow indicating decreasing RTP with increasing O₂ concentration. C) Stern-Volmer F/P ratiometric calibration.

This is the first boron-based oxygen sensor to meet all three of these important sensing requirements, namely, a large singlet-triplet gap, comparable F and P intensities and 0-21% O₂ sensitivity.

5.2.5. Conclusions

In this report, three BF₂bdks with thienyl aromatic groups and halide substituents (Br, and I) were prepared as initiators for lactide polymerization. The resulting materials possess fluorescence and oxygen sensitive room-temperature phosphorescence. The optical properties in solution and solid-state films were characterized. Unlike previously described boron dye-PLA materials, the halide substituted derivatives aggregated readily in PLA, showing both monomer and aggregate emission in films. Aggregation was reduced by dilution in PLA to minimize dye-dye interactions, which yielded distinct fluorescence and phosphorescence peaks for O₂ sensing

applications. When fabricated as nanoparticles, the iodide substituted dye, BF₂tbm(I)PLA, has many benefits such as equal intensity F and P peaks, 0-21% O₂ sensitivity and red-shifted emission, that previous scaffolds did not have. Future reports will focus on using these materials as therapeutic indicators of health and healing for biomedical applications.

5.3. Experimental Section

5.3.1. Materials

3,6-Dimethyl-1,4-dioxane-2,5-dione (DL-lactide, Sigma Aldrich) was recrystallized twice from ethyl acetate and stored under nitrogen. Tin(II) 2-ethylhexanoate (Sn(oct)₂, Spectrum), boron trifluoride diethyl etherate (Aldrich, purified, redistilled), and all other reagents and solvents were used as received without further purification. The ketones, 2-acetyl-5-bromothiophene and 2-acetyl-5-iodothiophene, were purchased from Alfa Aesar. Solvents CH₂Cl₂ and THF were dried and purified over 3 Å molecular sieves activated at 300 °C. All other chemicals were reagent grade from Sigma-Aldrich and were used without further purification. The ligand precursor, methyl 4-(2-((tetrahydro-2H-pyran-2-yl)oxy)ethoxy)benzoate, was prepared as previously described.³⁴

5.3.2. Methods

Ligands were prepared as previously described by combining the appropriate thienyl ketone (2-acetylthiophene, 2-acetyl-5-bromothiophene, or 2-acetyl-5-iodothiophene) in place of acetophenone with an ester building block.³⁴ Boron coordination of the ligands was performed as previously described, except the corresponding thienyl-phenyl ligand was used.¹⁵ Solvent-free polymerizations of DL-lactide were performed as previously described, but the appropriate thienyl-substituted boron complex was used as the initiator. Reaction conditions for each polymer are described with the physical characterization data. ¹H NMR (600 MHz) spectra were recorded on a Varian VMRS 600/51 instrument in CDCl₃ or D₆-DMSO. ¹H NMR peaks were referenced to

the signals for the residual protiochloroform at 7.26 ppm, protioDMSO peaks at 2.50, or protioacetone peaks at 2.09. Coupling constants are given in Hertz. For the boron coordinated dye initiators (**4-6**), because of limited solubility in common organic solvents (CDCl_3 and $\text{d}_6\text{-DMSO}$), the concentration of the dyes in the NMR solvent was not high enough to observe the initiator tail $-\text{OH}$ signals. Polymer molecular weights were determined by gel permeation chromatography (GPC) (THF, 25 °C, 1.0 mL/min, $dn/dc = 0.050$) using size-exclusion chromatography, multiangle laser light scattering (SEC-MALLS) ($\lambda = 658$ nm, 25 °C) and refractive index (RI) ($\lambda = 658$ nm, 25 °C) detection. Polymer Laboratories 5 μm mixed-C columns (guard column plus two columns) along with Wyatt Technology (Optilab T-rEX interferometric refractometer, miniDAWN TREOS multiangle static light scattering (MALS) detector, ASTRA 6.0 software), and Agilent Technologies instrumentation (series 1260 HPLC with diode array (DAD) detector, ChemStation) were used in GPC analysis. UV-vis spectra were recorded on a Hewlett-Packard 8452A diode-array spectrophotometer. Nanoparticle fabrication was performed as previously described,³² and nanoparticle hydrodynamic radius (R_H) was determined by a DynaPro dynamic light scattering (DLS) plate reader (Wyatt).

Luminescence Measurements. Steady-state fluorescence emission spectra were recorded on a Horiba Fluorolog-3 Model FL3-22 spectrofluorometer (double-grating excitation and double-grating emission monochromator). A 2 ms delay was used when recording the delayed emission spectra. Time-correlated single-photon counting (TCSPC) fluorescence lifetime measurements were performed with a NanoLED-370 ($\lambda_{\text{ex}} = 369$ nm) excitation source and a DataStation Hub as the SPC controller. Phosphorescence lifetimes were measured with a 1 ms multichannel scalar (MCS) excited with a flash xenon lamp ($\lambda_{\text{ex}} = 369$ nm; duration <1 ms). Lifetime data were analyzed with DataStation v2.4 software from Horiba Jobin Yvon. Fluorescence quantum yields

(Φ_F) of initiator and polymer samples in CH_2Cl_2 were calculated against anthracene as a standard as previously described, using the following values: $\Phi_F(\text{anthracene}) = 0.27$,³⁵ $n_D^{20}(\text{EtOH}) = 1.360$, $n_D^{20}(\text{CH}_2\text{Cl}_2) = 1.424$. Optically dilute CH_2Cl_2 solutions of the dyes, with absorbances <0.1 au, were prepared in 1 cm path length quartz cuvettes. Thin films were prepared on the inner wall of vials by dissolving polymers in CH_2Cl_2 (2 mg/mL) and evaporating the solvent by slowly rotating the vial under a low stream of nitrogen. The solution-cast films were then dried *in vacuo* for at least 15 min before measurements. Fluorescence spectra and lifetimes were obtained under ambient conditions (e.g., air, ~21% oxygen). Phosphorescence measurements were performed under a N_2 atmosphere (Praxair). The vials with the solution-cast films were purged and sealed with a Teflon cap and wrapped in parafilm in a nitrogen atmosphere glove box prior to measurements. The glove box was purged with nitrogen for 30 min prior to samples being sealed. Fluorescence and phosphorescence lifetimes were fit to double or triple exponential decays in solid-state films. Ratiometric calibration was performed as previously described with Cole-Palmer flowmeters and mixing air (Praxair; 21% O_2) and analytical grade N_2 (Praxair).³³

Computational Details. The compound $\text{BF}_2\text{tbm}(\text{I})\text{OMe}$ was modeled using the Gaussian 09 suite of programs using density functional theory (DFT).³⁶ We chose B3LYP/6-31+G(d) to simulate the B, S, O, C, and F atoms and B3LYP/SDD to simulate the I heavy atom for ground state geometry optimization with a Tomasi polarized continuum for dichloromethane solvent.² The vibrational frequencies for the optimized geometries were all positive, assuring that the geometries are at least a local minimum. Single point energy calculations were used to generate the molecular orbital diagrams utilizing B3LYP/6-31G(d). We used time-dependent density functional theory, TD-B3LYP/6-311+G(d) for estimates of the absorption spectra, at the respective optimized geometries. In all calculations, B3LYP/SDD was used to simulate the iodine atom. The first three

excited states were computed for the compound. Molecular orbitals were depicted by GaussView 5 software.

1-(4-(2-Hydroxyethoxy)phenyl)-3-(thiophen-2-yl)propane-1,3-dione (tbmOH: **1**) The unsubstituted thiophenyl diketone ligand was prepared as previously described with 2-acetylthiophene in place of 1-(4-(2-((tetrahydro-2H-pyran-2-yl)oxy)ethoxy)phenyl)ethan-1-one,³⁴ to yield a light tan solid, 143 mg (19 %). ¹H NMR (600 MHz, CDCl₃): δ 16.48 (s, 1H, -OH), 7.92 (d, J = 6, 2H, 2',6'-Ph-H), 7.77 (d, J = 3, 1H, 3''-Thio-H), 7.61 (d, J = 3, 1H, 5''-Thio-H), 7.15 (t, J = 3, 1H, 4''-Thio-H), 6.99 (d, J = 6, 2H, 3',5'-Ph-H), 6.61 (s, 1H, COCHCO), 4.16 (t, J = 6, 2H, Ar-OCH₂CH₂-OH), 4.0 (s, 2H, Ar-OCH₂CH₂-OH), 4.0 (s, 1H, Ar-OCH₂CH₂-OH). HRMS (ESI, TOF) m/z calcd for C₁₅H₁₅O₄S, 291.0686 [M + H]⁺; found 291.0691.

1-(5-Bromothiophen-2-yl)-3-(4-(2-hydroxyethoxy)phenyl)propane-1,3-dione (tbm(Br)OH: **2**) The bromo-substituted thio-phenyl diketone was prepared as previously described with 5-bromo-2-acetylthiophene in place of 1-(4-(2-((tetrahydro-2H-pyran-2-yl)oxy)ethoxy)phenyl)ethan-1-one,³⁴ to yield a light tan solid, 147 mg (42 %). ¹H NMR (600 MHz, CDCl₃): δ 7.90 (d, J = 3, 2H, 2',6'-Ph-H), 7.51 (d, J = 3, 1H, 3''-Thio-H), 7.12 (d, J = 3, 1H, 5''-Thio-H), 6.99 (d, J = 3, 2H, 3',5'-Ph-H), 6.50 (s, 1H, COCHCO), 4.16 (t, J = 3, 2H, Ar-OCH₂CH₂-OH), 4.0 (s, 2H, Ar-OCH₂CH₂-OH). HRMS (ESI, TOF) m/z calcd for C₁₅H₁₄O₄SBr, 368.9796 [M + H]⁺; found 368.9793.

1-(5-Iodothiophen-2-yl)-3-(4-(2-hydroxyethoxy)phenyl)propane-1,3-dione (tbm(I)OH: **3**) The iodo-substituted thio-phenyl diketone was prepared as previously described with 5-iodo-2-acetylthiophene in place of 1-(4-(2-((tetrahydro-2H-pyran-2-yl)oxy)ethoxy)phenyl)ethan-1-one,³⁴ to yield a brown solid, 128 mg (49 %). ¹H NMR (600 MHz, CDCl₃): δ 16.33 (s, 1H, -OH), 7.90 (d, J = 3, 2H, 2',6'-Ph-H), 7.40 (d, J = 3, 1H, 3''-Thio-H), 7.32 (d, J = 9, 1H, 5''-Thio-H), 6.99 (d, J = 3, 2H, 3',5'-Ph-H), 6.50 (s, 1H, COCHCO), 4.16 (t, J = 3, 2H, Ar-OCH₂CH₂-OH), 4.01 (s, 2H,

Ar-OCH₂CH₂-OH). HRMS (ESI, TOF) *m/z* calcd for C₁₅H₁₄O₄SI, 416.9657 [M + H]⁺; found 416.9655.

Difluoroboron-1-(4-(2-hydroxyethoxy)phenyl)-3-(thiophen-2-yl)propane-1,3-dione (BF₂tbmOH:

4) The boron complex was obtained as a light yellow solid after column chromatography (toluene), 81 mg (53 %). ¹H NMR (600 MHz, DMSO): δ 8.79 (d, *J* = 6, 1H, 5''-Thio-*H*), 8.49 (d, *J* = 6, 1H, 3''-Thio-*H*) 8.46 (d, *J* = 12, 2H 2',6'-Ph-*H*) 7.91 (s, 1H, COCHCO), 7.60 (d, *J* = 6, 1H, 4''-Thio-*H*), 7.35 (d, *J* = 3, 2H, 3',5'-Ph-*H*), 5.10 (s, broad, 1H, Ar-OCH₂CH₂-OH) 4.33 (t, *J* = 6, 2H, Ar-OCH₂CH₂-OH), 3.92 (s, broad, 2H, Ar-OCH₂CH₂-OH). HRMS (ESI, TOF) *m/z* calcd for C₁₅H₁₂BO₄F₂S, 416.9779 [M - H]⁺; found 416.9782.

Difluoroboron-1-(5-bromothiophen-2-yl)-3-(4-(2-hydroxyethoxy)phenyl)propane-1,3-dione

(BF₂tbm(Br)OH: **5**) The boron complex was obtained as a yellow solid after column chromatography (toluene), 72 mg (52 %). ¹H NMR (600 MHz, CDCl₃): δ 8.10 (d, *J* = 3, 2H, 2',6'-Ph-*H*), 7.78 (d, *J* = 3, 1H, 3''-Thio-*H*), 7.22 (d, *J* = 3, 1H, 5''-Thio-*H*), 7.04 (d, *J* = 6, 2H, 3',5'-Ph-*H*), 6.78 (s, 1H, COCHCO), 4.21 (t, *J* = 3, 2H, Ar-OCH₂CH₂-OH), 4.04-4.02 (s, broad, 2H, Ar-OCH₂CH₂-OH). HRMS (ESI, TOF) *m/z* calcd for C₁₅H₁₃BO₄F₂SBr, 416.9779 [M + H]⁺; found 416.9782.

Difluoroboron-1-(5-iodothiophen-2-yl)-3-(4-(2-hydroxyethoxy)phenyl)propane-1,3-dione

(BF₂tbm(I)OH: **6**) The boron complex was obtained as a yellow solid after column chromatography (toluene), 33 mg (25 %). ¹H NMR (600 MHz, CDCl₃): δ 8.09 (d, *J* = 6, 2H, 2',6'-Ph-*H*), 7.64 (s, 1H, 3''-Thio-*H*), 7.42 (s, 1H, 5''-Thio-*H*), 7.04 (d, *J* = 3, 2H, 3',5'-Ph-*H*), 6.77 (s, 1H, COCHCO), 4.20 (s, 2H, Ar-OCH₂CH₂-OH), 4.02 (s, 2H, Ar-OCH₂CH₂-OH). HRMS (ESI, TOF) *m/z* calcd for C₁₅H₁₁BO₄F₂SI, 462.9479 [M - H]⁺; found 462.9484.

BF₂tbmPLA (7). The solvent-free DL-lactide polymerization to form the dye-PLA conjugate was performed as previously described¹⁴ with *BF₂tbmOH (4)* as the initiator and the following reaction conditions: initiator-OH: lactide: Sn(Oct)₂ = 1:300:0.025 for 4h at 130 °C, to yield an orange microcrystalline powder upon purification by precipitation into hexanes and ice cold methanol (×2), 315 mg (79%, corrected for 56% monomer conversion). *M_n* (GPC/RI) = 18 600 Da, *Đ* = 1.10; *M_n* (¹H NMR) = 23 300 Da. ¹H NMR (600 MHz, CDCl₃): δ 8.56 (s, broad, 1H, 3''-Thio-*H*), 8.30 (d, *J* = 6, 2H, 2',6'-Ph-*H*), 8.10 (s, broad, 1H, 5''-Thio-*H*), 7.30 (s, broad, 1H, 4''-Thio-*H*), 7.26 (s, 1H, COCHCO), 7.04 (d, *J* = 3, 2H, 3',5'-Ph-*H*), 5.28-5.13 (m, broad, 283H, PLA-*H*), 4.20 (s, broad, 2H, Ar-OCH₂CH₂-OH), 4.02 (s, 2H, broad, Ar-OCH₂CH₂-OH), 1.67-1.52 (m, broad, 541H, PLA-CHCH₃).

BF₂tbm(Br)PLA (8). The solvent-free DL-lactide polymerization to form the dye-PLA conjugate was performed as previously described¹⁴ with *BF₂tbm(Br)OH (5)* as the initiator with the following reaction conditions: initiator-OH:lactide: Sn(Oct)₂ = 1:200:0.025 for 7 h at 130 °C, to yield an orange microcrystalline powder upon purification from precipitation into hexanes and ice cold methanol (×2), 470 mg (50%, corrected for 70% monomer conversion). *M_n* (GPC/RI) = 20 500 Da, *Đ* = 1.14; *M_n* (¹H NMR) = 22 800 Da. ¹H NMR (600 MHz, CDCl₃): δ 8.10 (d, *J* = 3, 2H, 2',6'-Ph-*H*), 7.78 (d, *J* = 3, 1H, 3''-Thio-*H*), 7.22 (d, *J* = 3, 1H, 5''-Thio-*H*), 7.04 (d, *J* = 6, 2H, 3',5'-Ph-*H*), 6.78 (s, 1H, COCHCO), 5.23-5.13 (m, broad, 283H, PLA-*H*), 4.21 (t, *J* = 3, 2H, Ar-OCH₂CH₂-OH), 4.04-4.02 (s, broad, 2H, Ar-OCH₂CH₂-OH), 1.65-1.52 (m, broad, 541H, PLA-CHCH₃).

BF₂tbm(I)PLA (9). The solvent-free DL-lactide polymerization to form the dye-PLA conjugate was performed as previously described¹⁴ with *BF₂tbm(I)OH (6)* as the initiator and the following reaction conditions: initiator-OH: lactide: Sn(Oct)₂ = 1:200:0.025 for 2.5 hat 130 °C, to yield an orange microcrystalline powder upon purification via precipitation into hexanes and ice cold

methanol ($\times 2$), 375 mg (82%, corrected for 72% monomer conversion). M_n (GPC/RI) = 19 800 Da, $\bar{D} = 1.10$; M_n (^1H NMR) = 19 400 Da. ^1H NMR (600 MHz, CDCl_3): δ 8.09 (d, $J = 6$, 2H, 2',6'-Ph-*H*), 7.64 (s, 1H, 3''-Thio-*H*), 7.42 (s, 1H, 5''-Thio-*H*), 7.04 (d, $J = 3$, 2H, 3',5'-Ph-*H*), 6.77 (s, 1H, COCHCO), 5.28-5.13 (m, broad, 272H, PLA-*H*), 4.20 (s, 2H, Ar-OCH₂CH₂-OH), 4.02 (s, 2H, Ar-OCH₂CH₂-OH), 1.67-1.52 (m, broad, 867H, PLA-CHCH₃).

5.4. Acknowledgements

This research was published in *ChemPlusChem*.³⁷ I thank Dr. Milena Kolpaczynska, Caroline Kerr, and Margaret Daly for help in the synthesis and characterization of these BF₂tbm(X)PLA polymers, Dr. William Morris for the help with the calculations, Prof. Fraser for assistance in the preparation of the manuscript, and the financial support of the National Cancer Institute of the National Institutes of Health (R01 CA167250).

5.5. References

- (1) Ren, Y.; Jäkle, F. *Dalt. Trans.* **2016**, *45*, 2537–2574.
- (2) Yin, X.; Chen, J.; Lalancette, R. A.; Marder, T. B.; Jäkle, F. *Angew. Chem. Int. Ed.* **2014**, *53*, 9761–9765.
- (3) Poon, C.-T.; Wu, D.; Lam, W. H.; Yam, V. W.-W. *Angew. Chem. Int. Ed.* **2015**, *127*, 10715–10719.
- (4) Poon, C.-T.; Lam, W. H.; Wong, H.-L.; Yam, V. W.-W. *J. Am. Chem. Soc.* **2010**, *132*, 13992–13993.
- (5) Matsumoto, T.; Tanaka, K.; Chujo, Y. *Macromolecules* **2015**, *48*, 1343–1351.
- (6) Gutierrez, G. D.; Sazama, G. T.; Wu, T.; Baldo, M. A.; Swager, T. M. *J. Org. Chem.* **2016**, *81*, 4789–4796.
- (7) Morris, W. A.; Butler, T.; Kolpaczynska, M.; Fraser, C. L. *Mater. Chem. Front.* **2017**, *1*,

- 158–166.
- (8) Ono, K.; Yoshikawa, K.; Tsuji, Y.; Yamaguchi, H.; Uozumi, R.; Tomura, M.; Taga, K.; Saito, K. *Tetrahedron* **2007**, *63*, 9354–9358.
- (9) Wang, X.; Wolfbeis, O. S.; Meier, R. J. *Chem. Soc. Rev.* **2013**, *42*, 7834–7869.
- (10) Wang, X.; Meier, R. J.; Schäferling, M.; Bange, S.; Lupton, J. M.; Sperber, M.; Wegener, J.; Ondrus, V.; Beifuss, U.; Henne, U.; Klein, C.; Wolfbeis, O. S. *Adv. Opt. Mater.* **2016**, *4*, 1854–1859.
- (11) Ondrus, V.; Meier, R. J.; Klein, C.; Henne, U.; Schäferling, M.; Beifuss, U. *Sens. Actuat. A: Phys.* **2015**, *233*, 434–441.
- (12) Peng, H.; Stich, M. I. J.; Yu, J.; Sun, L.; Fischer, L. H.; Wolfbeis, O. S. *Adv. Mater.* **2010**, *22*, 716–719.
- (13) Kolpaczynska, M.; DeRosa, C. A.; Morris, W. A.; Fraser, C. L. *Aust. J. Chem.* **2016**, *69*, 537–545.
- (14) DeRosa, C. A.; Samonina-Kosicka, J.; Fan, Z.; Hendargo, H. C.; Weitzel, D. H.; Palmer, G. M.; Fraser, C. L. *Macromolecules* **2015**, *48*, 2967–2977.
- (15) Zhang, G.; Chen, J.; Payne, S. J.; Kooi, S. E.; Demas, J. N.; Fraser, C. L. *J. Am. Chem. Soc.* **2007**, *129*, 8942–8943.
- (16) Zhang, X.; Cui, M.; Zhou, R.; Chen, C.; Zhang, G. *Macromol. Rapid Commun.* **2014**, *35*, 566–573.
- (17) Chen, J.; Gorczynski, J. L.; Zhang, G.; Fraser, C. L. *Macromolecules* **2010**, *43*, 4909–4920.
- (18) Ho, V.; Boudouris, B. W.; McCulloch, B. L.; Shuttle, C. G.; Burkhardt, M.; Chabiny, M. L.; Segalman, R. A. *J. Am. Chem. Soc.* **2011**, *133*, 9270–9273.
- (19) Boudouris, B. W.; Frisbie, C. D.; Hillmyer, M. A. *Macromolecules* **2010**, *43*, 3566–3569.

- (20) Mackiewicz, N.; Nicolas, J.; Handké, N.; Noiray, M.; Mougin, J.; Daveu, C.; Lakkireddy, H. R.; Bazile, D.; Couvreur, P. *Chem. Mater.* **2014**, *26*, 1834–1847.
- (21) Dove, A. P. *ACS Macro Lett.* **2012**, *1*, 1409–1412.
- (22) DeRosa, C. A.; Kerr, C.; Fan, Z.; Kolpaczynska, M.; Mathew, A. S.; Evans, R. E.; Zhang, G.; Fraser, C. L. *ACS Appl. Mater. Interfaces* **2015**, *7*, 23633–23643.
- (23) Zhang, G.; Evans, R. E.; Campbell, K. a.; Fraser, C. L. *Macromolecules* **2009**, *42*, 8627–8633.
- (24) Zhang, G.; Kooi, S. E.; Demas, J. N.; Fraser, C. L. *Adv. Mater.* **2008**, *20*, 2099–2104.
- (25) Lower, S. K.; El-Sayed, M. A. *Chem. Rev.* **1966**, *66*, 199–241.
- (26) Xu, S.; Evans, R. E.; Liu, T.; Zhang, G.; Demas, J. N.; Trindle, C. O.; Fraser, C. L. *Inorg. Chem.* **2013**, *52*, 3597–3610.
- (27) Nguyen, N. D.; Zhang, G.; Lu, J.; Sherman, A. E.; Fraser, C. L. *J. Mater. Chem.* **2011**, *21*, 8409–8415.
- (28) Samonina-Kosicka, J.; DeRosa, C. A.; Morris, W. A.; Fan, Z.; Fraser, C. L. *Macromolecules* **2014**, *47*, 3736–3746.
- (29) DeRosa, C. A.; Samonina-Kosicka, J.; Fan, Z.; Hendargo, H. C.; Weitzel, D. H.; Palmer, G. M.; Fraser, C. L. *Macromolecules* **2015**, *48*, 2967–2977.
- (30) Prieto, I.; Teetsov, J.; Fox, M. A.; Vanden Bout, D. A.; Bard, A. J. *J. Phys. Chem. A* **2000**, *105*, 520–523.
- (31) Daly, M. L.; DeRosa, C. A.; Kerr, C.; Morris, W. A.; Fraser, C. L. *RSC Adv.* **2016**, *6*, 81631–81635.
- (32) Pfister, A.; Zhang, G.; Zareno, J.; Horwitz, A. F.; Fraser, C. L. *ACS Nano* **2008**, *2*, 1252–1258.

- (33) Zhang, G.; Palmer, G. M.; Dewhurst, M. W.; Fraser, C. L. *Nat. Mater.* **2009**, 8, 747–751.
- (34) Bender, J. L.; Shen, Q.-D.; Fraser, C. L. *Tetrahedron* **2004**, 60, 7277–7285.
- (35) Demas, J. N.; Crosby, G. A. *J. Phys. Chem.* **1971**, 75, 991–1024.
- (36) Frisch, M. J.; Trucks, G. W.; Schlegel, H. B.; Scuseria, G. E.; Robb, M. A.; Cheeseman, J. R.; Scalmani, G.; Barone, V.; Mennucci, B.; Petersson, G. A. . et al. *Gaussian 09 Revision A.1*; Gaussian, Inc.: Wallingford, CT. 2009.
- (37) DeRosa, C. A.; Kolpaczynska, M.; Kerr, C.; Daly, M. L.; Morris, W. A.; Fraser, C. L. *ChemPlusChem* **2016**, 82, 399–406.

Chapter 6:

Difluoroboron β -Diketonate-PLA-PEG Materials as Full-Color Luminescent Nanoparticles



6.1. Introduction

Polymer conjugates of luminescent and therapeutic molecules are of great interest.¹⁻⁵ Preparation of the polymer-conjugated materials requires lengthy, multi-step organic synthesis compared to small molecule/polymer blend formulations. However, increased stability or controlled release of macromolecular products are beneficial for long-term applications, where side effects such as “burst” release are essentially eliminated. Three methods are commonly employed for generating polymer conjugated small molecules; 1) material (e.g. dye or drug) initiated polymerization,⁶⁻⁸ 2) polymerizable side chains on the material of interest⁹⁻¹¹ and 3) post-polymerization modification.¹²⁻¹⁴ In standard protocols, BF₂bdks have been covalently linked to PLA via dye initiation of lactide polymerization to yield BF₂bdkPLA. For PEGylated nanoparticles, our first approach was stereocomplexation through blending BF₂bdkPLLA (poly(L-lactic acid)) and PEG-PDLA (poly(D-lactic acid)) to create stealth nanoparticles for IV injection and tumor accumulation.¹⁵ Another approach was post polymerization modification to attach a carboxyl-PEG to the BF₂bdkPLA.¹⁶ In this report, we simplify and considerably streamline the process for generating BF₂bdkPLA-PEG materials by preparing the boron dye with an acidic phenol for the post polymerization modification of a PEG-PLA block copolymer via the Mitsunobu reaction.^{17,18}

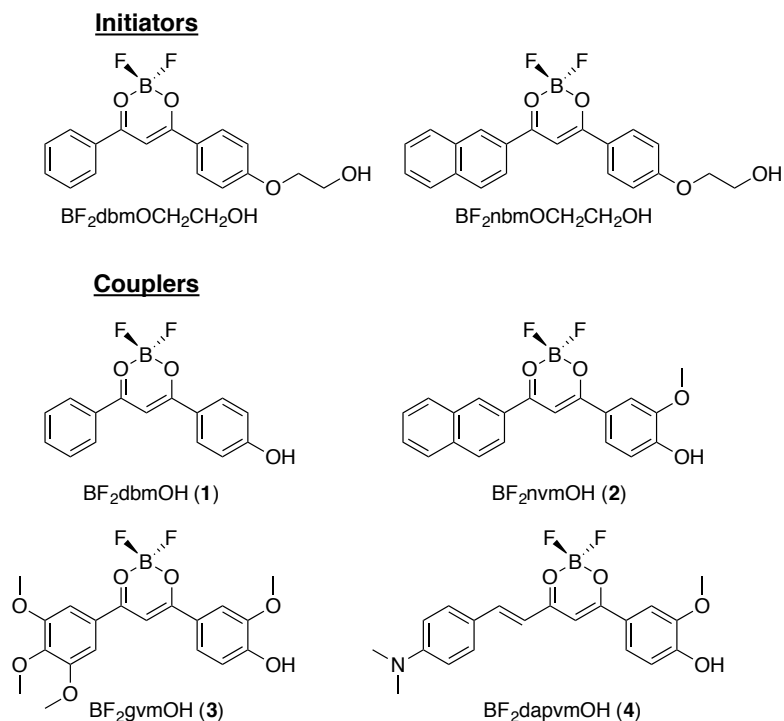


Figure 6.1. Boron dyes for polymer initiation (initiators) or post polymerization modification (couplers).

Phenolic dyes, shown in Figure 6.1., are prepared in fewer steps than dye initiators (e.g. $\text{BF}_2\text{dbmCH}_2\text{CH}_2\text{OH}$), and a single batch of PEG-PLA copolymer can be used in multiple coupling reactions with different luminescent dyes to yield full color luminescent polymers. In this report, we describe the synthesis and characterization of dual emissive $\text{BF}_2\text{bdkPLLA}$ -PEG materials with a range of emission colors for future biomedical applications. Stereocomplexes with PDLA-PEG are fabricated to tailor color (i.e. dye loading) and stability in different media.^{19–21}

6.2. Results and Discussion

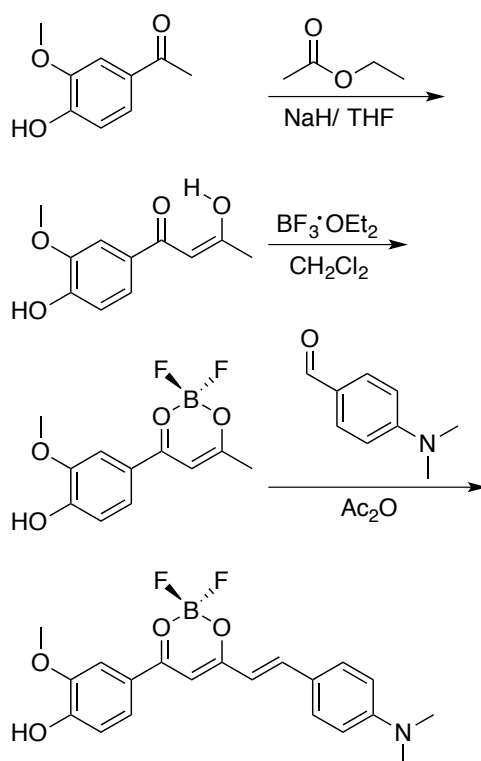
6.2.1. Synthesis

The β -diketones were prepared by a method reported by Jin et al.,²² with commercially available ketones and esters, followed by coordination of difluoroboron in anhydrous CH_2Cl_2 . To prepare the dimethyl amino derivative, a synthetic protocol reported by Fedorenko et al.²³ was

used involving a condensation reaction of the boron dye ketone and an amino-substituted aldehyde (Scheme 6.1.). For dyes **2-4**, methoxy-substituted acetovanillinone was employed as the ketone for the Claisen condensations to increase the donor ability of the dye, potentially red-shifting the luminescence wavelengths (Figure 6.1.). The boron dyes showed excellent solubility in common organic solvents (i.e. acetone, CH_2Cl_2 , THF). These phenol dye couplers for post polymerization modification were prepared in moderate yields (35-72%) in two to three steps. This contrasts with dye initiators for lactide polymerization that take 5-7 steps to synthesize, and where issues with dye solubility are common when larger aromatics (e.g. naphthalene) are present in the dye scaffold. For naming protocol, refer to Table S6.1. and Scheme 6.1. in Appendix E.

Dye-polymer conjugates were successfully prepared via Mitsunobu reaction conditions (Figure 6.2.).¹⁷ The coupling process could be monitored visually through color changes. Upon addition of the DIAD reagent, the yellow solution of BF_2gvmOH became red, and the strong green

Scheme 6.1. Synthesis of $\text{BF}_2\text{dapvmOH}$ (**4**).



emission was quenched (Figure S6.1.; Appendix E). This is likely due to deprotonation of the phenol, inducing a stronger dipole, also seen in BF₂Curcumin dyes.²⁴ Over the course of the reaction, the solution became yellow again, as expected for the ether functionality formed in the coupled product. The reaction was allowed to proceed for three days under N₂ to insure maximum coupling efficiency. After this time, the THF solvent was removed via rotary evaporation, and the reaction mixture was dissolved in minimal CH₂Cl₂ for purification via precipitation. The oxidized triphenylphosphine generated during the reaction, excess boron dye, and DIAD reagents were easily removed from the final product via precipitation into cold methanol (50 mL at 0° C × 2), as dye-PLLA-PEG materials were insoluble in MeOH, whereas the byproducts remained in MeOH solution.

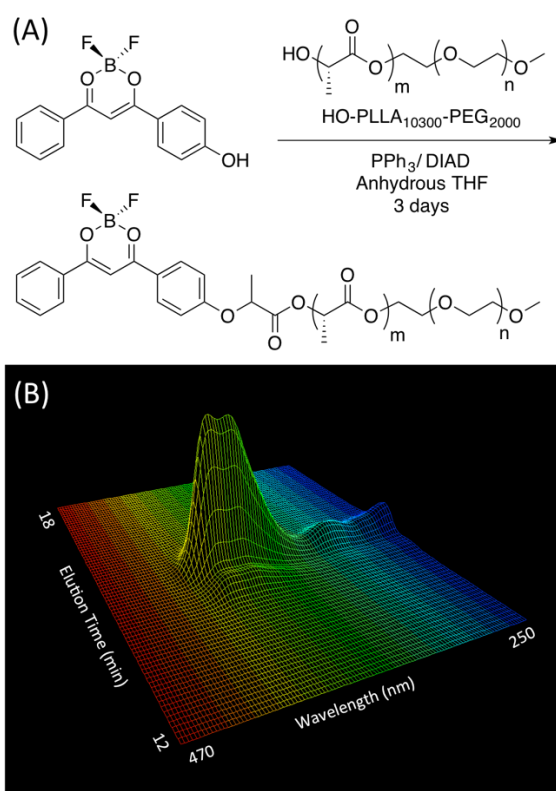


Figure 6.2. Dye-Polymer Conjugation. A) Mitsunobu coupling of BF₂dbmOH to PLLA-PEG. B) 3-D GPC trace of **1P** showing the dye coupled to the PLLA-PEG polymer via UV-Vis detection. Plot shows elution time (min) versus wavelength (nm) versus relative absorbance.

Coupling was confirmed by ^1H NMR spectroscopy and gel permeation chromatography (GPC). The GPC trace of the uncoupled PLLA-PEG has no UV absorbance. However, after dye functionalization, the elution of the polymer coincides with the absorbance of the dye via GPC (Figures 6.2. and Figures S6.2. and S6.3.). Upon dye coupling to the polymer, the MW and PDI increased slightly as shown in Table S6.2 in Appendix E (i.e. MW: HO-PLLA-PEG = 10 300, \bar{D} = 1.05; **2P** = 11 700, \bar{D} = 1.07). This is likely a result of purification, as lower MW polymers are more soluble and less likely to precipitate from solution than the higher MW polymers, causing the overall MW to increase.^{25,26} Furthermore, the coupling is confirmed by the disappearance of the ^1H NMR signal at ~ 2.5 ppm corresponding to the PLLA-*OH* end group. Coupling efficiency is estimated to be ~ 80 -95% based on NMR integration for dye arene and PEG- OCH_3 peaks. Importantly, no degraded dye byproducts were observed in GPC (UV trace) or NMR analysis (e.g. ligand enol peaks), which has been a problem for boron dye-PLA analogues previously with heat and certain base mediated reactions.^{27,28} This is further supported by the optical properties in dilute CH_2Cl_2 solutions, as the polymer conjugates and the uncoupled dye precursors have similar optical properties (Table S6.3; Appendix E). A small high molecular weight shoulder was present in the GPC trace, possibly due to polymer backbiting²⁹ and recombination of chains.²⁶ High molecular weight shoulders are a common observation in PEG-polyester materials with functionalized moieties (e.g. bioconjugates, ligands, fluorophores).³⁰ Despite this, the PDI values are low, indicating a narrow distribution of products. Therefore, the Mitsunobu reaction method is a reliable means for coupling boron dyes to polymers.

6.2.2. Nanoparticles

Nanoparticles were fabricated by precipitation of DMF solutions of the polymer into water with stirring.³¹ Two nanoparticle formulations were studied for each dye; namely, nanoparticles

were prepared from the dye-PLLA-PEG homopolymer (**1-4NP**), and from a ~1:1 mixture of dye-PLLA-PEG and PDLA-PEG to form the stereocomplex systems (**1-4scNP**) (Figure 6.3.). In previous reports, stereocomplexation is a simple method to alter stability and size of the nanoparticles.^{32,33} Based on literature precedent, stereocomplexed PLA materials should offer more stable, yet biodegradable nanoparticle systems, more resistant to changes in pH.²⁰ During the fabrication process, BF₂dbmPLLA-PEG (**1NP**) readily dissolved in DMF and formed nanoparticles as expected. For the stereocomplex nanoparticles, the PDLA-PEG/BF₂dbmPLLA-PEG mixture showed limited solubility in DMF. The addition of other solvents, such as acetone, THF or acetonitrile did not increase solubility. As a result, during precipitation into water, aggregation visibly increased. Thus, precipitated polymer suspensions were passed through filter paper (Whatman, quantitative) before dialysis to produce uniform nanoparticles. Other nanoparticles prepared from **2P-4P** polymers were treated similarly.

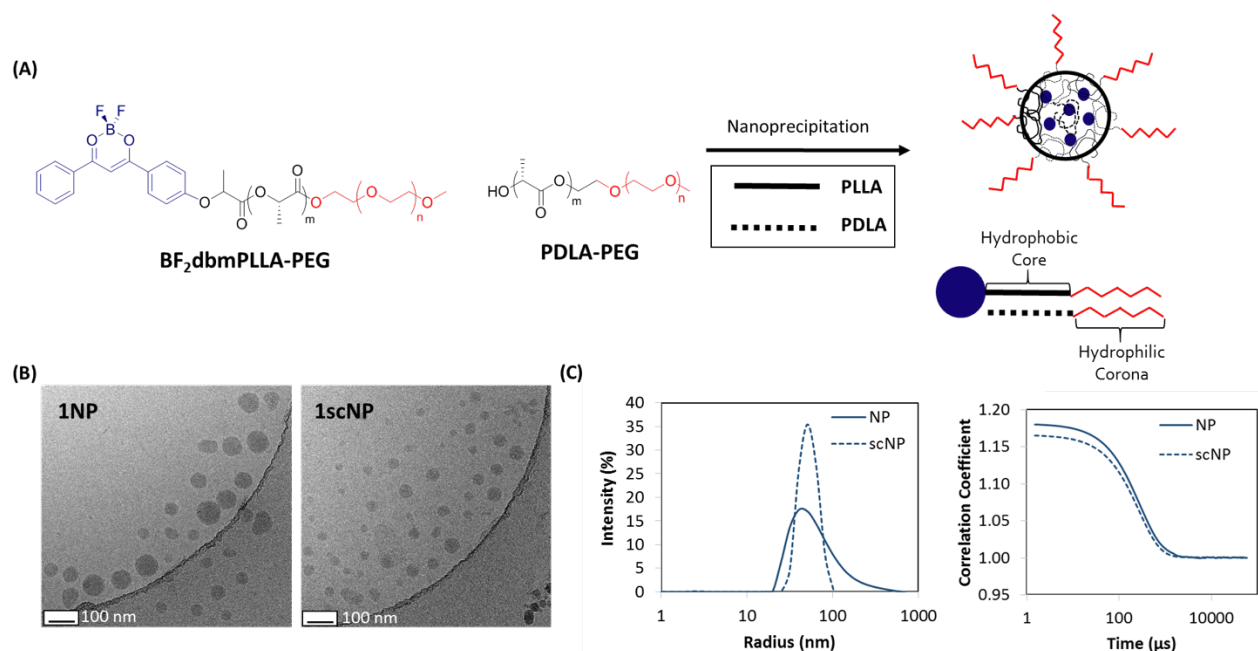


Figure 6.3. Nanoparticle Fabrication. (A) Schematic of stereocomplex (scPLA) nanoparticle self-assembly. (B) CryoTEM of concentrated **1NP** and **1scNP** nanoparticles (3.0 mg/mL). (C) BNP size and polydispersity determined by DLS (left) and autocorrelation functions and size distribution of nanoparticles (right) (1.0 mg/mL).

Homopolymer and stereocomplex nanoparticles showed expected radius and size distributions. According to DLS measurements, the homopolymer nanoparticles showed slightly larger radii compared to the stereocomplexes (R_H ; **1NP** = 53.6 nm, **1scNP** = 52.0 nm). Greater differences were noted in polydispersities (PD) of **1NP** and **1scNP**. The homopolymer nanoparticles showed a broader distribution of sizes compared to the stereocomplex congener (PD (%); **1NP** = 23.3 nm, **1scNP** = 13.6 nm) (Figure 6.3.). The cryoTEM results are in good agreement with the DLS results. On average, the cryoTEM revealed smaller, somewhat more regular nanoparticles for the **scNP** samples compared to the **NP** samples. However, according to DLS, all dye-polymer and dye-polymer stereocomplex nanoparticles showed similar radii and distribution results. One outlier was the BF₂nvm dye derivative, as the homopolymer nanoparticles were slightly larger than the **scNP** counterpart, as shown in Table 6.1 and Figure S6.4 (Appendix E) (R_H ; **2NP** = 34.3 nm, **2scNP** = 45.5 nm). Differences in size and distribution can vary depending on drop rate and stirring speed from the nanoprecipitation process. Nevertheless, all nanoparticles are well under the size ranges needed for enhanced permeation and retention (EPR) in tumors and for renal clearance.³⁴ More in depth analysis to understand ways to further control the nanoparticle size, and influences of filtering, concentration, and stir rate on the resultant nanoparticles, may be performed when this is merited for specific biological investigations.

Table 6.1. Nanoparticle Properties.

Boron Dye	Sample	DLS ^a		Abs ^b	F		RTP	
		R _H (nm)	PD (%)	λ _{max} (nm)	λ _F ^c (nm)	τ _F ^d (ns)	λ _{RTP} ^e (nm)	τ _{RTP} ^f (ms)
BF ₂ dbm	1NP	53.6	23.3	380	426	1.98	520	104
	1scNP	52.0	13.6	379	418	1.96	516	167
BF ₂ nvm	2NP	34.3	25.1	417	503	5.01	556	77.4
	2scNP	45.5	23.1	419	479	2.42	550	159
BF ₂ gvm	3NP	68.7	15.5	417	553	17.73	556	36.6
	3scNP	37.7	25.9	419	499	4.42	552	90.7
BF ₂ dapvm	4NP	61.0	15.4	531	639	1.28	^g	^g
	4scNP	57.2	23.6	533	618	1.52	^g	^g

^aDynamic light scattering (DLS) of NPs; hydrodynamic radius (R_H) radii and polydispersity (PD) determined by DLS. ^bAbsorption maxima. ^cFluorescence emission maxima excited at 369 nm, except sample **4** (λ_{ex} = 475 nm). ^dFluorescence lifetime excited with a 369 nm light-emitting diode (LED) monitored at the emission maximum. All fluorescence lifetimes are fitted with multiexponential decays. ^eDelayed emission spectra maxima under N₂ at 298 K. Excitation source: xenon flash lamp. ^fPre-exponential weighted RTP lifetime. Excitation source: xenon flash lamp; RTP lifetime fit to double-exponential decay. ^gNo phosphorescence was observed.

6.2.3. Fluorescence

The optical properties of PLLA-PEG and scPLA-PEG nanoparticles are shown in Table 6.1. Fluorescence attributed to the dye scaffold was elucidated by comparing homopolymer nanoparticles (**1-4NP**). Using BF₂dbmPLLA-PEG (**1**) for comparison, increased π-conjugation and addition of a methoxy group (**1NP** vs **2NP**) resulted in a red-shift (Δλ_{max} = 77 nm), and emission color change from blue-violet to green (Figure 6.4). The yellow emission of compound **3NP** is due to the increased number of -OMe electron-donating groups, shown to red-shift emissive properties in previous reports (Δλ_{max} = 127 nm vs **1NP**).^{35,36} Extended conjugation with a vinyl spacer group and the dimethyl amino substitution resulted in further red-shifting for **4NP** (Δλ_{max} = 213 nm vs **1NP**). This red fluorescence makes compound **4NP** a promising candidate for tissue imaging, given greater tissue penetration of red light; however, all derivatives have useful fluorescence properties. For example, nanoparticles based on **1-3** have high extinction coefficients (ε = 28 000 – 61 000 M⁻¹ cm⁻¹) with absorbance wavelengths between 375-420 nm,

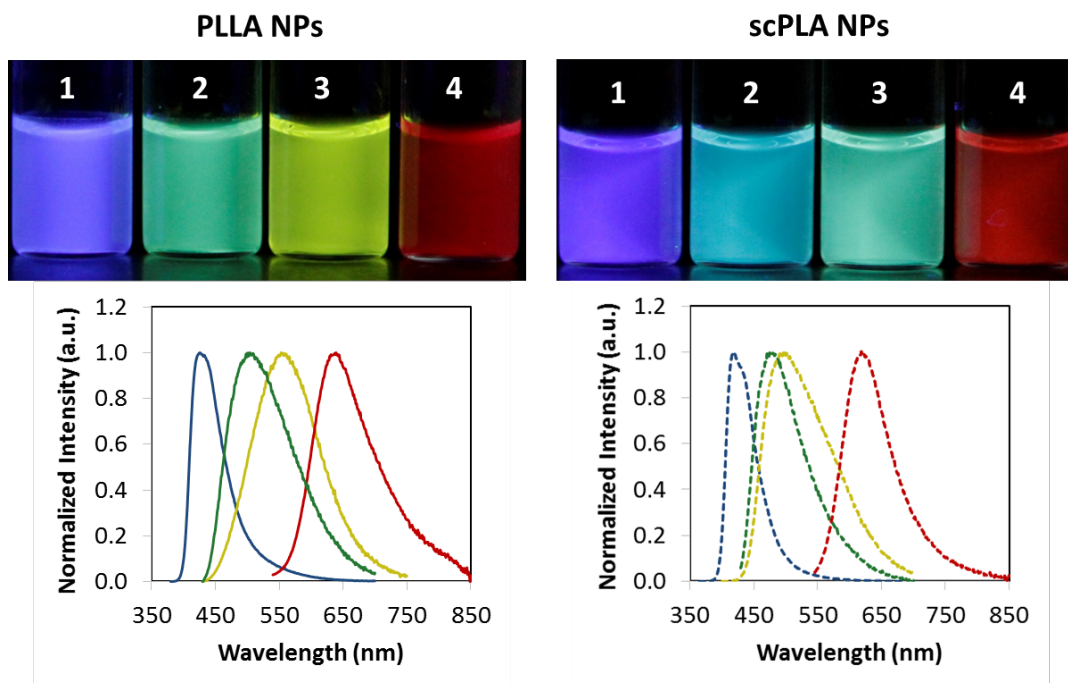


Figure 6.4. Images and total emission spectra of **1-4NP** (solid lines) and **1-4scNP** (dashed lines) in air. (**1** = blue, **2** = green, **3** = yellow, **4** = red). Fluorescence emission maxima excited at 369 nm, except sample **4** ($\lambda_{\text{ex}} = 475$ nm).

well aligned with a 405 nm violet laser, commonly used for hydroxycoumarins.³⁷ The red fluorescent nanoparticle, **4NP** with redder absorption, can be used in combination with a 515 nm Ar-ion gas laser, typically used for rhodamine dyes.³⁸ Boron β -diketonates also typically have good two-photon cross sections in alignment for Ti-sapphire pulsed lasers. Therefore, these materials could find ready application in fluorescence imaging techniques, such as two-photon fluorescence lifetime imaging microscopy (TP-FLIM).³⁹

When nanoparticles are formed from polymers **1-4-PLLA-PEG** and PDLA-PEG through stereocomplexation, dye loading is decreased by $\sim 50\%$. It is well known that optical properties of BF₂bdk materials are affected by dye loading.^{40,41} As expected based on previous results with dye blends and dye-PLA conjugates of variable molecular weights, the fluorescence blue-shifted in stereocomplexes (i.e. λ_{F} ; **3NP** = 553 nm, **3scNP** = 499 nm), while the absorption is essentially unchanged (Figure S6.5. and S6.6; Appendix E). The blue-shifted fluorescence was accompanied

by a decrease in fluorescence lifetime (i.e. τ_F ; **3NP** = 17.63 ns, **3scNP** = 4.34 ns). Stereocomplexation-induced changes in luminescence based on dye loading serve as an additional way to modulate emission wavelength (i.e. color) and lifetimes in dye-PLA materials, and lifetime is related to oxygen sensitivity.

6.2.4. Phosphorescence

The delayed emission of **1-3** was studied at room temperature (298 K) and in liquid nitrogen (77 K) (Figure 6.5 and Figures S6.7 and S6.8; Appendix E). Phosphorescence was not detected for compound **4**, possibly due to twisting and non-radiative decay due to the vinyl spacer. For compounds **1-3**, the delayed emission at room temperature red-shifted with dye modifications, similar to the fluorescence (NPs: λ_{RTP} ; **1NP** = 520 nm, **2NP** = 556 nm, **3NP** = 556 nm). Surprisingly, in **3NP** the RT fluorescence and phosphorescence bands completely overlapped. To better understand this phenomenon, low temperature phosphorescence (LTP) measurements at 77 K (liquid N₂) were performed. The LTP of **3** red-shifted to λ_{em} = 596 nm (Figure S6.8; Appendix E). This suggests that the triplet state of **3** is observable as orange-red phosphorescence at low temperature (596 nm), but at room temperature, thermally activated delayed fluorescence (TADF) is the dominant transition. The TADF is a result of the decrease in the singlet-triplet gap of dye **3**, and reverse intersystem crossing; that is, triplet excited state electrons can back populate the singlet excited state, if the barrier is low enough. Because this is a thermal process, the TADF is absent at low temperature (i.e. 77K; liq. N₂). The TADF of organic materials is a desirable feature for organic light emitting diodes (OLEDs).^{42,43} Nanoparticles **1NP** and **2NP** had large singlet-triplet gaps, decreasing the probability of TADF. The emission spectra at 77 K did not change dramatically, indicating minimal TADF (Figure S6.7.; Appendix E). Stereocomplex nanoparticles (**1-3scNP**) showed similar RTP wavelengths as the homopolymer

analogues (i.e. λ_{RTP} ; **1NP** = 520 nm, **1scNP** = 516 nm). However, when the dye loading was decreased via stereocomplexation, the RTP lifetime (τ_{RTP}) increased (i.e. τ_{RTP} ; **1NP** = 104 ms, **1scNP** = 167 ms). With the long RTP lifetimes of these nanoparticles, gated techniques can be utilized for image capture and oxygen concentration imaging.⁴⁴ These multi-color dual-emitters are promising starting points for generating oxygen sensors with stronger phosphorescence.^{40,45,46} Ratiometric oxygen sensing may be enabled by introducing halide heavy atoms into these boron dye-PLA-PEG nanoparticle materials.

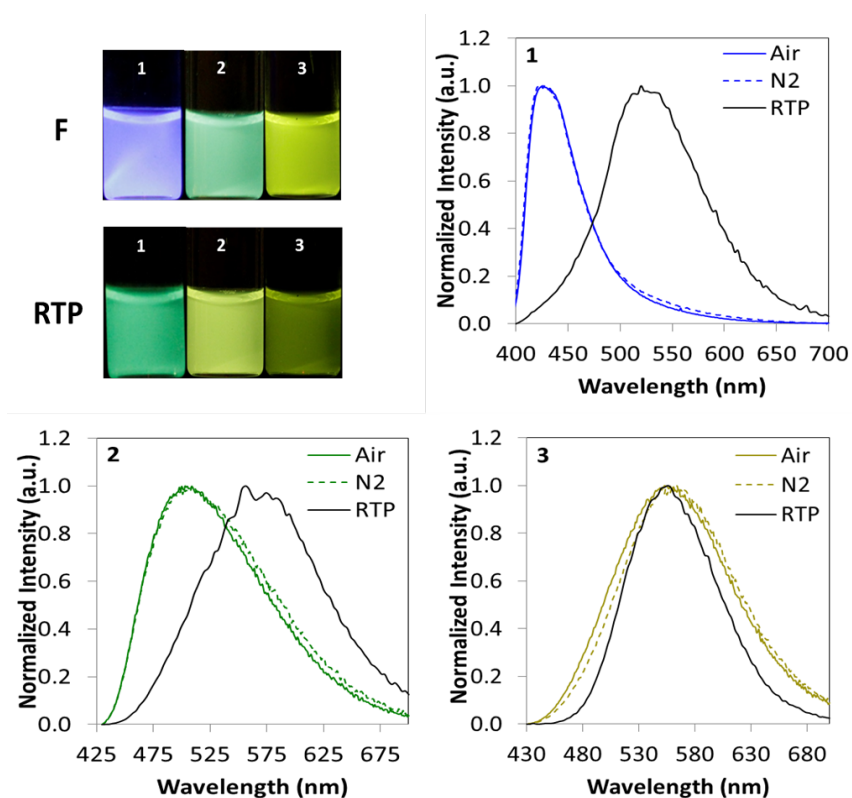


Figure 6.5. Images and total emission of **1-3NP**. Images: photos taken in air with UV illumination (365 nm; F) and afterglow emission under N_2 after UV lamp is turned off (RTP) Spectra: total emission in air and N_2 (λ_{ex} = 385 nm, note: the spectra are very similar) and the delayed emission under N_2 (RTP, λ_{ex} = 385 nm, 2 ms delay).

6.2.5 Stability

The stability of **3NP** and **3scNP** nanoparticles (0.5 mg/mL) was studied over the course of three days in deionized (DI) water, phosphate buffered saline (PBS), and Dulbecco's modified Eagle's medium (DMEM). Dye **3** nanoparticles were selected for the stability experiments because **3NP** and **3scNP** samples had the largest difference in size and color, suggesting that there might be a greater difference in stability/aggregation that can be easily tracked by DLS and fluorescence. Nanoparticles were prepared in DI water, but this is unsuitable for cells, as application of NPs in DI water would cause cell lysing through differences in osmotic pressure. Thus, PBS and DMEM are commonly used in conjunction with cells and IV injection. The size and polydispersity of the nanoparticles were monitored at 37 °C (body and incubation temperature) by dynamic light scattering (DLS) for each medium. Also, the emission spectra of the NPs were monitored at room temperature and at 37 °C for three days, to account for changes at elevated temperatures. Three days was chosen for analysis as a reasonable timeframe for tumor accumulation via passive targeting and the EPR effect. Nanoparticles appear to be stable on the timescale for imaging the biological process of interest (e.g. tumor uptake), as the EPR effect typically occurs within 24 hours post injection.⁹

In deionized water and PBS, changes in size and luminescence for **3NP** and **3scNP** formulations were similar. Over the course of three days, the radii (R_H) and polydispersity (PD) of the NPs increased slightly. This is a result of the concentration gradients of ions (PBS; Na^+ and Cl^-) in the solution and NP matrix causing swelling.⁴⁷ This effect can be observed after incubation for 12 hours at 37 °C (Figures S6.9-12.; Appendix E). Although the nanoparticle size did not remain constant over time, the emission spectra were consistent. Therefore, both PLLA-PEG and scPLA-

PEG formulations showed good stability in DI water and PBS for three days at room and body temperatures.

In Dulbeccos modified Eagle's medium (DMEM), a common medium for cell culture, radii and polydispersity increased over time, and significant aggregation was observed (Figure S6.10.), again due to the concentration gradients of ions in DMEM (Ca^{2+} , Na^+ , K^+ , Cl^- , HCO_3^-) causing swelling (**3scNP**: start = 55.8 nm, end = 131.3 nm).¹⁰⁰ In DMEM, two peaks were present in the total emission spectra (Figures S6.11. and S6.12.; Appendix E). The peak absorbance of the phenol red pH indicator in the DMEM occurs at the same wavelength as the peak emission of **3NP** in DI water. Phenol red has a weak emissive band at 600 nm, but when combined with the boron dye, sensitization occurred, increasing the phenol red emission. Overlaying the absorbance spectra of the DMEM with the emission spectra of the NPs confirmed these results (Figure S6.13.; Appendix E). This overlap is strongest with the **3NP** sample, which is why the energy transfer is not observed as significantly in the emission spectra of the other three samples in DMEM. This is surprising considering that phenol red is virtually non-emissive, however BF_2bdks have been utilized for energy transfer donors in previous reports.⁴⁴ While stereocomplexed nanoparticles offered no advantages in DI water or PBS at room (25 °C) and body temperature (37 °C), in DMEM, the fluorescence properties of **3scNP** showed greater stability (Figure S6.12.; Appendix E). According to previous reports, DMEM selectively degrades PLLA over the PDLA isomer.⁴⁸ Our results suggest that the stereocomplexation of PLLA with the PDLA isomer can overcome this.

The consistency of the emission spectra suggests that these materials could be used as imaging agents in vivo, provided delivery and uptake occur before aggregation and degradation in the three-day time period, given aggregation limits the potential for NP biodistribution and the usefulness of the materials as imaging agents.⁴⁹ Aggregation was also more significant in the

stereocomplex nanoparticles. Similar aggregation results for tri-block copolymers of PDLA-PEG-PDLA and PLLA-PEG-PLA flower-like micelles in water.³² When stereocomplex PLA cores interact, gels can readily form and precipitate from water.^{50,51} However, these PEGylated nanoparticles have superior aqueous stability in media and buffers compared to the pure PLA analogues published previously.^{31,46} In future studies, longer PEG chains will be investigated to tune the stability of boron dye polymers in different media to the specific biomedical application of interest.

6.2.6 Conclusion

Color tuning strategies based on dye structure and loading were employed to achieve full color emissions for BF₂bdk-PLA-PEG nanoparticles. These multicolored nanoparticles show promise for multiplexing in vitro and in vivo. The red emission of the amino derivative (**4**) has potential for greater tissue penetration and reduction in autofluorescence noise. Both the red emission and the full color emission are useful characteristics for in vivo fluorescence imaging for applications such as image-guided surgery. Additionally, the long phosphorescence lifetimes and distinct fluorescence and phosphorescence peaks of **1-3NP** indicate utility of these materials for hypersensitive lifetime-based oxygen sensing. The **4scNP** sample was imaged in vivo and accumulated in a murine flank tumor 24 hours after IV injection, showing the efficacy of PEG for passive targeting. After dye scaffold modification with a heavy atom to increase phosphorescence intensity, materials **1P** and **2P**, with well separated fluorescence and phosphorescence peaks, may be compatible with ratiometric oxygen sensing. The self-assembly of the boron dye-PLLA-PEG conjugates with PDLA-PEG can be extended, in future work, to PDLA-PEG-bioconjugates for active targeting to tumors or other biological targets. This is an important first step to generating modular multicolor nanosensors with specialized surfaces for passive and active targeting.

6.3. Experimental Section

6.3.1. Materials

The lactide monomers (L-lactide and D-lactide) were generous gifts from Corbion Purac®. Lactide was recrystallized twice from EtOAc and dried in vacuo overnight (10 h) prior to use. Poly(ethylene glycol) (PEG) was purchased from Sigma Aldrich (2 000 Da, $\bar{D} = \sim 1.05$) and dried via azeotropic distillation in toluene according to a previously described protocol.⁵² The PEG was stored under nitrogen in a glovebox prior to use as a macroinitiator. The polymers PEG-PLLA-OH (GPC: $M_n = 10\,300$, $\bar{D} = 1.05$, $^1\text{H NMR} = 12\,600$) and PEG-PDLA-OH ($M_n = 12\,500$, $\bar{D} = 1.08$, $^1\text{H NMR} = 13\,800$),¹⁵ the ligand, dbmOH,²² and the boron coordinated dye, BF₂dbmOH (**1**),⁵³ were prepared as previously described and $^1\text{H NMR}$ spectra are in accord with literature values. In this report, dbmOH and BF₂dbmOH refer to the phenol dibenzoylmethane ligand and difluoroboron dye. In previous reports by our group these abbreviations referred to a primary alcohol ligand and boron dye initiators for lactide polymerization, renamed in this manuscript as dbmOC₂H₄OH and BF₂dbmOC₂H₄OH.⁵⁴ Solvents CH₂Cl₂ and THF were dried over 3 Å molecular sieves activated at 300 °C, transferred via cannula, and dried a second time over 3 Å molecular sieves activated at 300 °C.⁵⁵ The solvents were stored in a dry pot prior to use. All other chemicals were reagent grade from Sigma-Aldrich and were used without further purification. Phosphate buffered saline (PBS) and Dulbecco's Modified Eagle's Medium (DMEM) were obtained from Life Technologies.

6.3.2. Methods

^1H (600 MHz) and ^{13}C (150 MHz) NMR spectra were recorded on a Varian VMRS 600/51 instrument in CDCl₃ or d₆-DMSO. ^1H NMR spectra were referenced to the residual signals for protiochloroform (7.26 ppm), protioDMSO (2.50 ppm), and protioacetone (2.09 ppm). ^{13}C NMR spectra were referenced to the residual signals for chloroform (76.97 ppm), DMSO (39.95 ppm).

In the ^1H NMR assignments, aromatic positions are defined as follows; phenyl (Ph), vanillinone (v-Ph), naphthyl (Np), trimethyl gallate (g-Ph), and dimethylamino-phenyl (a-Ph). For a guide to the nomenclature of the ligands and boron dyes, refer to Table S6.1 and Scheme S6.1 (Appendix E). Coupling constants are given in hertz. Number average molecular weights (M_n), weight average molecular weights (M_w) and polydispersity index (\mathcal{D}) were determined by gel permeation chromatography (GPC) (THF, 25 °C, 1.0 mL/min) using multiangle laser light scattering (MALLS; $\lambda = 658$ nm, 25 °C) and refractive index ($\lambda = 658$ nm, 25 °C) detection. A Polymer Laboratories 5 μm mixed-C guard column and two GPC columns along with Wyatt Technology Corp. (Optilab REX interferometric refractometer, miniDawn TREOS laser photometer) and Agilent Technologies instrumentation (series 1260 HPLC) and Wyatt Technology software (ASTRA 6.0) were used for analysis. The incremental refractive index (dn/dc) was determined by a single-injection method assuming 100% mass recovery from the columns. UV–vis spectra were recorded on a Hewlett-Packard 8452A diode-array spectrophotometer.

Luminescence Measurements. Steady-state fluorescence emission spectra were recorded on a Horiba Fluorolog-3 Model FL3-22 spectrofluorometer (double-grating excitation and double-grating emission monochromator). A 2 ms delay was used when recording the delayed emission spectra. Time-correlated single-photon counting (TCSPC) fluorescence lifetime measurements were performed with a NanoLED-370 ($\lambda_{\text{ex}} = 369$ nm) excitation source and a DataStation Hub as the SPC controller. Phosphorescence lifetimes were measured with a 1 ms multichannel scalar (MCS) excited with a flash xenon lamp ($\lambda_{\text{ex}} = 369$ nm; duration <1 ms). Lifetime data were analyzed with DataStation v2.4 software from Horiba Jobin Yvon. Fluorescence quantum yields (Φ_F) of initiator and polymer samples in CH_2Cl_2 were calculated against anthracene or Rhodamine G6 (Exciton) as a standard as previously described, using the following values: Φ_F (anthracene) =

0.27,⁵⁶ Φ_F (Rhodamine G6) = 0.97, n_D^{20} (EtOH) = 1.360, n_D^{20} (CH₂Cl₂) = 1.424, Optically dilute CH₂Cl₂ solutions of the dyes, with absorbances <0.1 au, were prepared in 1 cm path length quartz cuvettes. Fluorescence spectra and lifetimes were obtained under ambient conditions (e.g., air, ~21% oxygen). Phosphorescence measurements were performed under a N₂ atmosphere. Dilute nanoparticle solutions (absorbance = ~0.1) were purged with N₂ (Praxair) in a cuvette and sealed with a 12 mm PTFE/silicone/PTFE seal (Chromatography Research Supplies), connected by a screw cap. Vials were continuously purged in the headspace between the solution and the vial cap with analytical grade N₂ (Praxair) during measurements. For 21% O₂ (i.e. air), measurements were taken under ambient conditions (open vial, no cap). Fluorescence and phosphorescence lifetimes were fit to double or triple exponential decays in nanoparticles. Fluorescence lifetimes in CH₂Cl₂ were fit to single exponential decays.

Nanoparticle Characterization. Nanoparticles were fabricated as previously described.³¹ Nanoparticle sizes and polydispersities were analyzed via dynamic light scattering (DLS, Wyatt, DynaPro) and cryo transmission electron microscopy (cryoTEM, 120kV Tecnai Spirit is equipped with a tungsten filament electron source, and a 2k × 2k UltraScan CCD camera). For cryoTEM, nanoparticles were concentrated by centrifugation at 4000 rpm for 5 min in a cellulose filter tube (Amicon, Ultra -15, 30,000 Da MW cutoff).

1-(4-Hydroxy-3-methoxyphenyl)-3-(naphthalen-2-yl)propane-1,3-dione (nvmOH). The naphthyl-vanillin phenolic ligand was prepared as described by Jin et. al.,²² except the ketone, acetovanillinone, was used in place acetophenone, and the ester, methyl 2-naphthoate, was used in place of methyl benzoate to yield a tan powder after recrystallization from acetone/hexanes: 720 mg (39%). ¹H NMR: (600 MHz, CDCl₃): δ 17.05 (s, 1H, -OH), 8.52 (s, 1H, 1-Np-H), 7.99 (m, 2H, 3, 8-Np-H), 7.92 (m, 2H, 4, 5-Np-H), 7.62 (m, 2H, 2, 6-Ph-H), 7.59 (m, 2H, 6, 7-Np-H), 7.01 (d,

$J = 6$, 1H, 5-Ph-*H*) 6.93 (s, 1H, COCHCO), 6.03 (s, 1H, Ph-OH), 4.00 (s, 3H, Ph-OCH₃). ¹³C NMR: (150 MHz, CDCl₃) δ 187.10, 182.53, 153.40, 135.22, 132.82, 132.35, 129.70, 128.75, 128.71, 128.49, 128.12, 127.36, 126.63, 123.76, 122.92, 115.92, 111.44, 93.16, 56.32. HRMS (ESI, TOF) m/z calcd for C₂₀H₁₇O₄: 321.1127 [M + H]⁺; found 321.1125.

1-(4-Hydroxy-3-methoxyphenyl)-3-(3,4,5-trimethoxyphenyl)propane-1,3-dione (gvmOH). The trimethyl-gallate phenolic ligand was prepared as described for nvmOH, but the ester methyl 3,4,5-trimethoxybenzoate was used in place of methyl 2-naphthoate to yield a tan powder after purification by silica column chromatography (3:1 hexanes/EtOAc): 550 mg (16%). ¹H NMR: (600 MHz, DMSO) δ 17.53 (s, broad, 1H, -OH), 10.07 (s, broad, 1H, 4-v-Ph-OH), 7.75 (d, $J = 6$, 1H, 6-v-Ph-*H*), 7.58 (s, 1H, 1H, 2-v-Ph-*H*), 7.35 (s, 2H, 2, 6-g-Ph-*H*), 7.14 (s, 1H, COCHCO), 6.90 (d, $J = 6$, 1H, 5-v-Ph-*H*), 3.86 (s, broad, 6H, 3, 5-g-Ph-OCH₃), 3.84 (s, broad, 3H, 3-v-Ph-OCH₃), 3.72 (s, broad, 3H, 4-g-Ph-OCH₃). ¹³C NMR: (150 MHz, CDCl₃) δ 188.75, 183.65, 153.22, 149.91, 146.71, 130.81, 128.08, 121.78, 114.16, 109.37, 107.00, 104.48, 92.07, 60.98, 56.37, 56.13. HRMS (ESI, TOF) m/z calcd for C₁₉H₂₁O₇: 361.1287 [M + H]⁺; found 361.1287.

1-(4-Hydroxy-3-methoxyphenyl)butane-1,3-dione (mvmOH). The methyl phenolic ligand was prepared as described for nvmOH, but the ester, ethyl acetate, was used in place of methyl 2-naphthoate to yield a white powder after purification by silica column chromatography (3:1 hexanes/EtOAc): 854 mg (28 %). ¹H NMR: (CDCl₃) δ 16.28 (s, 1H, -OH), 6.94 (d, $J = 6$, 1H, 5-Ph-*H*), 7.47 (s, 1H, 2-Ph-*H*), 7.44 (d, $J = 12$, 1H, 6-Ph-*H*), 6.10 (s, 1H, COCHCO), 5.98 (s, 1H, Ph-OH), 3.95 (s, 3H, Ph-OCH₃). ¹³C NMR: (150 MHz, CDCl₃) δ 196.76, 150.36, 146.57, 130.19, 123.97, 113.72, 109.67, 56.04, 26.16. HRMS (ESI, TOF) m/z calcd for C₁₁H₁₁O₄: 207.0658 [M - H]⁺; found 207.0657.

Difluoroboron-1-(4-hydroxy-3-methoxyphenyl)-3-(naphthalen-2-yl)propane-1,3-dione,

BF₂nvmOH (**2**). The boron dye was prepared according to a method previously described for BF₂dbmOC₂H₄OH,⁵³ except the naphthyl ligand nvmOH was used in place of dbmOC₂H₄OH, to yield a yellow-orange solid after recrystallization from acetone/hexanes: 108 mg (35%). ¹H NMR (600 MHz, CDCl₃): δ 8.74 (s, 1H, 1-Np-*H*), 8.07 (d, *J* = 6, 1H, 3-Np-*H*), 8.01 (d, *J* = 12, 6-*v*-Ph-*H*), 7.96 (d, *J* = 6, 1H, 4-Np-*H*), 7.91 (d, *J* = 6, 1H, 8-Np-*H*), 7.80 (d, *J* = 6, 1H, 5-Np-*H*), 7.75 (s, 1H, 2-*v*-Ph-*H*), 7.66 (t, *J* = 6, 1H, 7-Np-*H*), 7.60 (t, *J* = 6, 1H, 6-Np-*H*), 7.06 (d, *J* = 12, 1H, 5-*v*-Ph-*H*), 6.35 (s, 1H, COCHCO), 4.03 (s, 3H, 3-*v*-Ph-OCH₃), 3.73 (s, broad, 1H, 4-*v*-Ph-OH). ¹³C NMR: (150 MHz, DMSO) δ 181.98, 179.63, 155.96, 147.67, 136.22, 132.67, 131.34, 140.31, 130.07, 129.56, 129.28, 128.26, 127.85, 126.46, 124.23, 122.61, 112.66, 94.13, 56.53. HRMS (ESI, TOF) *m/z* calcd for C₂₀H₁₄O₄BF₂: 367.0953 [*M* - H]⁺; found 367.0943.

Difluoroboron-1-(4-hydroxy-3-methoxyphenyl)-3-(3,4,5-trimethoxyphenyl)propane-1,3-dione

BF₂gvmOH (**3**). The boron dye was prepared according to a method previously described for BF₂dbmOC₂H₄OH, except the trimethyl gallate, ligand (gvmOH) was used in place of dbmOC₂H₄OH, to yield a yellow-orange solid after recrystallization from acetone/hexanes: 311 mg (69%). ¹H NMR: (600 MHz, DMSO) δ 10.85 (s, 1H, *v*-Ph-OH), 8.06 (d, *J* = 12, 1H, 6-*v*-Ph-*H*), 7.69 (m, 2H, 2-*v*-Ph-*H*, COCHCO), 7.51 (s, 2H, 2, 4-*g*-Ph-*H*), 7.01 (d, *J* = 12, 1H, 5-*v*-Ph-*H*), 3.90 (s, broad, 9H, 3,4,5-*g*-Ph-OCH₃), 3.79 (s, 3H, 3-*v*-Ph-OCH₃). ¹³C NMR: (150 MHz, DMSO) δ 181.44, 179.34, 155.71, 153.51, 148.61, 144.14, 127.16, 126.44, 122.63, 116.43, 112.46, 106.90, 93.67, 60.87, 56.90, 56.43. HRMS (ESI, TOF) *m/z* calcd for C₁₉H₁₈O₇BF₂: 407.1114 [*M* - H]⁺; found 407.1111.

Difluoroboron-1-(4-hydroxy-3-methoxyphenyl)butane-1,3-dione, BF₂mvmOH. The boron dye was prepared according to a method previously described for BF₂dbmOC₂H₄OH, except the

methyl-vanilin ligand, mvmOH, was used in place of dbmOC₂H₄OH, to yield a yellow solid after recrystallization from acetone/hexanes: 544 mg (72%). ¹H NMR: (600 MHz, CDCl₃) δ 7.62 (m, 2H, 2, 6-v-Ph-*H*), 7.00 (d, *J* = 6, 1H, 5-v-Ph-*H*), 6.45 (s, 1H, COCHCO), 6.31 (s, 1H, 4-v-Ph-OH), 3.99 (s, 3H, 3-v-Ph-OCH₃), 2.36 (s, 3H, -OC-CH₃). ¹³C NMR: (150 MHz, DMSO) δ 190.49, 181.08, 155.55, 148.56, 125.62, 121.69, 116.51, 112.33, 97.25, 56.31, 24.38. HRMS (ESI, TOF) *m/z* calcd for C₁₁H₁₀O₄BF₂: 255.0640 [M - H]⁺; found 255.0640.

Difluoroboron-(E)-5-(4-(dimethylamino)phenyl)-1-(4-hydroxy-3-methoxyphenyl)pent-4-ene-1,3-dione, BF₂dapvmOH (**4**). The amino substituted dye was prepared by a method described by Fedorenko et. al,²³ except the boron dye BF₂mvmOH was used in place of 2,2-difluoro-4-(9H-fluorene-2-yl)-6-methyl-1,3,2-dioxaborine to yield a blue solid with metallic luster after precipitation from diethyl ether, filtration, and washing with copious amounts of ice cold diethyl ether (250 mL): 107 mg (56%). ¹H NMR: (600 MHz, CDCl₃) δ 8.10 (d, *J* = 12, 1H, -COCH=CH-a-Ph), 7.68 (s, broad, 1H, 2-v-Ph-*H*), 7.58 (d, *J* = 6, 1H, 6-v-Ph-*H*), 7.54 (d, *J* = 12, 2H, 2, 6-a-Ph-*H*), 7.14 (d, *J* = 12, 1H, 5-v-Ph-*H*), 6.69 (d, *J* = 6, 2H, 3, 5-a-Ph-*H*), 6.54 (d, *J* = 12, 1H, -COCH=CH-a-Ph), 6.46 (s, 1H, COCHCO), 3.92 (s, 3H, 3-v-Ph-OCH₃), 3.09 (s, 6H, 4-a-Ph-CH₃NCH₃), phenolic hydrogen was not observed. ¹³C NMR: (150 MHz, DMSO) δ 181.16, 175.70, 168.57, 154.08, 151.78, 150.52, 144.39, 133.21, 131.36, 124.20, 121.84, 121.61, 114.04, 112.64, 111.89, 97.54, 56.62, 21.47, 20.84. HRMS (ESI, TOF) *m/z* calcd for C₂₀H₁₉BNO₄F₂: 386.1375 [M - H]⁺; found 386.1374.

BF₂dbmPLLA-PEG (**1P**). The BF₂dbmOH dye was coupled to the PLLA-PEG block copolymer via a Mitsunobu reaction with diisopropyl azodicarboxylate (DIAD) as the activating reagent, as described by Balog et al.¹⁷ In an oven dried, 100 mL round bottom flask, PEG-PLLA-OH (250 mg, 0.024 mmol), BF₂dbmOH (**1**) (28 mg, 0.097 mmol) and triphenyl phosphine (PPh₃, 25 mg,

0.097 mmol) were dissolved in anhydrous THF (50 mL). The reaction mixture was chilled to -10 °C (acetone/ice bath) for 30 min before the DIAD reagent was added via syringe (10 μ L, 0.049 mmol). The reaction was removed from the chilled bath, and allowed to warm to room temperature. After stirring for 3 d, the THF was removed via rotary evaporation. The polymer was dissolved in minimal CH₂Cl₂ and the viscous solution was precipitated (2 \times) into cold methanol (50 mL, -20 °C), filtered, and washed with cold methanol (-20 °C). After drying in vacuo, a white, fluffy solid was collected: 223 mg (81%). M_n (GPC/MALLS) = 11 500, \bar{D} = 1.09 (¹H NMR) = 13 500; ¹H NMR: (600 MHz, CDCl₃) δ 8.12 (m, 4H, 2', 6'-Ph-*H*, 2'', 6''-Ph-*H*), 7.65 (t, *J* = 6, 1H, 4'-Ph-*H*), 7.53 (t, *J* = 6, 2H, 3', 5'-Ph-*H*), 7.09 (s, 1H, COCHCO), 7.04 (d, *J* = 6, 2H, 3'', 5''-Ph-*H*) 5.14 (q, *J* = 6, 172H, PLLA-*H*), 3.62 (s, broad, 152H, PEG-OC₂H₄-O), 3.36 (s, 3H, PEG-OCH₃), 1.57 (m, broad, 560H, PLLA-CH₃).

BF₂nvmPLLA-PEG (2P). The naphthyl dye was coupled to PEG-PLLA-OH as previously described for **1P**, but BF₂nvmOH (**2**) was used in place of BF₂dbmOH (**1**) to yield a yellow, fibrous solid: 185 mg (74%). M_n (GPC/MALLS) = 11 700, \bar{D} = 1.07 (¹H NMR) = 15 400; ¹H NMR: (600 MHz, CDCl₃) δ 8.76 (s, 1H, 1-Np-*H*), 8.08 (d, *J* = 6, 1H, 3-Np-*H*), 8.02 (d, *J* = 6, 1H, 6-v-Ph-*H*), 7.97 (d, *J* = 6, 1H, 4-Np-*H*), 7.91 (d, *J* = 6, 1H, 8-Np-*H*), 7.79 (d, *J* = 6, 1H, 5-Np-*H*), 7.73 (s, 1H, 2-v-Ph-*H*), 7.66 (t, *J* = 6, 1H, 7-Np-*H*), 7.61 (t, *J* = 6, 1H, 6-Np-*H*), 7.07 (s, 1H, COCHCO), 6.98 (d, *J* = 12, 1H, 5-v-Ph-*H*), 5.15 (q, *J* = 6, 188H, PLLA-*H*), 3.98 (s, 3H, 3-v-Ph-OCH₃), 3.62 (s, broad, 183H, PEG-OC₂H₄-O), 3.36 (s, 3H, PEG-OCH₃), 1.57 (m, broad, 712H, PLLA-CH₃).

BF₂gvmPLLA-PEG (3P). The trimethyl gallate dye was coupled to PEG-PLLA-OH as previously described for **1P**, but BF₂gvmOH (**3**) was used in place of BF₂dbmOH (**1**) to yield a yellow solid: 245 mg (64%). M_n (GPC/MALLS) = 12 600, \bar{D} = 1.13 (¹H NMR) = 14 900; ¹H NMR: (600 MHz, CDCl₃) δ 7.70 (s, broad, 2H, 2, 6-v-Ph-*H*), 7.34 (s, broad, 2H, 2, 6-g-Ph-*H*), 7.00 (s, 1H,

COCHCO), 6.93 (d, $J = 6$, 1H, 5-*v*-Ph-*H*), 5.17 (q, $J = 6$, 170H, PLLA-*H*), 3.94 (m, broad, 12H, 3, 4, 5-*g*-Ph-OCH₃, 3-*v*-Ph-OCH₃), 3.66 (s, broad, 154H, PEG-OC₂H₄-O), 3.36 (s, 3H, PEG-OCH₃), 1.57 (m, broad, 554H, PLLA-CH₃).

BF₂dapvmPLLA-PEG (**4P**). The dimethyl amino dye was coupled to PEG-PLLA-OH as previously described for **1P**, but BF₂dapvmOH (**4**) was used in place of BF₂dbmOH (**1**) to yield a magenta, fibrous solid: 95 mg (29%). M_n (GPC/MALLS) = 15 200, $\bar{D} = 1.15$ (¹H NMR) = 16 000; ¹H NMR: (600 MHz, CDCl₃) δ 8.05 (d, $J = 18$, 1H, -COCH=CH-*a*-Ph), 7.59 (m, 2H, 2, 6-*v*-Ph-*H*) 7.53 (d, $J = 6$, 2H, 2, 6-*a*-Ph-*H*) 6.90 (d, $J = 6$, 1H, 5-*v*-Ph-*H*) 6.69 (d, $J = 6$, 2H, 3, 5-*a*-Ph-*H*), 6.53 (d, $J = 12$, 1H, -COCH=CH-*a*-Ph), 6.44 (s, 1H, COCHCO) 5.15 (q, $J = 6$, 197H, PLLA-*H*), 3.93 (s, 3H, 3-*v*-Ph-OCH₃), 3.66 (s, broad, 183H, PEG-OC₂H₄-O), 3.36 (s, 3H, PEG-OCH₃), 3.08 (s, 6H, 4-*a*-Ph-CH₃NCH₃), 1.57 (m, broad, 699H, PLLA-CH₃).

6.4. Acknowledgements

This research was published in *Biomacromolecules*.⁵⁷ I thank Dr. Gina Fiore for the literature report of the Mitsunobu reaction to couple the dye to the polymer, Caroline Kerr and Margaret Daly for helping in the synthesis and characterization of these BF₂bdk-PLA-PEG block copolymers, Prof. Kelly Dryden for acquiring the cryoTEM images, Purac Corbion© for the generous donation of the D- and L-lactide monomers, Prof. Fraser, Caroline Kerr, and Margaret Daly for assistance in the preparation of the manuscript, and the financial support of the National Cancer Institute of the National Institutes of Health (R01 CA167250).

6.5. References

- (1) Shi, H.; Ma, X.; Zhao, Q.; Liu, B.; Qu, Q.; An, Z.; Zhao, Y.; Huang, W. *Adv. Funct. Mater.* **2014**, *24*, 4823–4830.
- (2) Wang, R.-F.; Peng, H.-Q.; Chen, P.-Z.; Niu, L.-Y.; Gao, J.-F.; Wu, L.-Z.; Tung, C.-H.;

- Chen, Y.-Z.; Yang, Q.-Z. *Adv. Funct. Mater.* **2016**, *26*, 5419–5425.
- (3) Kim, K. S.; Hyun, H.; Yang, J.-A.; Lee, M. Y.; Kim, H.; Yun, S.-H.; Choi, H. S.; Hahn, S. K. *Biomacromolecules* **2015**, *16*, 3054–3061.
- (4) Morais, M.; Campello, M. P. C.; Xavier, C.; Heemskerk, J.; Correia, J. D. G.; Lahoutte, T.; Caveliers, V.; Hernot, S.; Santos, I. *Bioconjug. Chem.* **2014**, *25*, 1963–1970.
- (5) Nicolas, J. *Chem. Mater.* **2016**, *28*, 1591–1606.
- (6) Zhang, X.; Cui, M.; Zhou, R.; Chen, C.; Zhang, G. *Macromol. Rapid Commun.* **2014**, *35*, 566–573.
- (7) DeRosa, C. A.; Kerr, C.; Fan, Z.; Kolpaczynska, M.; Mathew, A. S.; Evans, R. E.; Zhang, G.; Fraser, C. L. *ACS Appl. Mater. Interfaces* **2015**, *7*, 23633–23643.
- (8) Chen, X.; Xu, C.; Wang, T.; Zhou, C.; Du, J.; Wang, Z.; Xu, H.; Xie, T.; Bi, G.; Jiang, J.; Zhang, X.; Demas, J. N.; Trindle, C. O.; Luo, Y.; Zhang, G. *Angew. Chem. Int. Ed.* **2016**, *55*, 9872–9876.
- (9) Sun, X.; Wang, X.; Li, X.; Ge, J.; Zhang, Q.; Jiang, J.; Zhang, G. *Macromol. Rapid Commun.* **2015**, *36*, 298–303.
- (10) Barnes, J. C.; Bruno, P. M.; Nguyen, H. V.-T.; Liao, L.; Liu, J.; Hemann, M. T.; Johnson, J. A. *J. Am. Chem. Soc.*, **2016**, *138*, 12494–12501.
- (11) Liao, L.; Liu, J.; Dreaden, E. C.; Morton, S. W.; Shopsowitz, K. E.; Hammond, P. T.; Johnson, J. A. *J. Am. Chem. Soc.* **2014**, *136*, 5896–5899.
- (12) Borchmann, D. E.; ten Brummelhuis, N.; Weck, M. *Macromolecules* **2013**, *46*, 4426–4431.
- (13) Borchmann, D. E.; Tarallo, R.; Avendano, S.; Falanga, A.; Carberry, T. P.; Galdiero, S.; Weck, M. *Macromolecules* **2015**, *48*, 942–949.

- (14) Foster, J. C.; Matson, J. B. *Macromolecules* **2014**, *47*, 5089–5095.
- (15) Kersey, F. R.; Zhang, G.; Palmer, G. M.; Dewhirst, M. W.; Fraser, C. L. *ACS Nano* **2010**, *4*, 4989–4996.
- (16) Samonina-Kosicka, J.; Weitzel, D. H.; Hofmann, C. L.; Hendargo, H.; Hanna, G.; Dewhirst, M. W.; Palmer, G. M.; Fraser, C. L. *Macromol. Rapid Commun.* **2015**, *36*, 694–699.
- (17) Thévenaz, D. C.; Monnier, C. A.; Balog, S.; Fiore, G. L. *Biomacromolecules* **2014**, *15*, 3994–4001.
- (18) Burnworth, M.; Tang, L.; Kumpfer, J. R.; Duncan, A. J.; Beyer, F. L.; Fiore, G. L.; Rowan, S. J.; Weder, C. *Nature* **2011**, *472*, 334–337.
- (19) Tsuji, H.; Hyon, S. H.; Ikada, Y. *Macromolecules* **1991**, *24*, 5657–5662.
- (20) Tsuji, H. *Macromol. Biosci.* **2005**, *5*, 569–597.
- (21) Farah, S.; Anderson, D. G. *Adv. Drug Deliv. Rev.* **2016**, *107*, 367–392.
- (22) Jin, H.; Zhang, W.; Wang, D.; Chu, Z.; Shen, Z.; Zou, D.; Fan, X.; Zhou, Q. *Macromolecules* **2011**, *44*, 9556–9564.
- (23) Fedorenko, E. V.; Mirochnik, A. G.; Beloliptsev, A. Y.; Isakov, V. V. *Dye. Pigment.* **2014**, *109*, 181–188.
- (24) Chaicham, A.; Kulchat, S.; Tumcharern, G.; Tuntulani, T.; Tomapatanaget, B. *Tetrahedron* **2010**, *66*, 6217–6223.
- (25) Chen, J.; Gorczynski, J. L.; Zhang, G.; Fraser, C. L. *Macromolecules* **2010**, *43*, 4909–4920.
- (26) Vora, A.; Wojtecki, R. J.; Schmidt, K.; Chunder, A.; Cheng, J. Y.; Nelson, A.; Sanders, D. *P. Polym. Chem.* **2016**, *7*, 940–950.

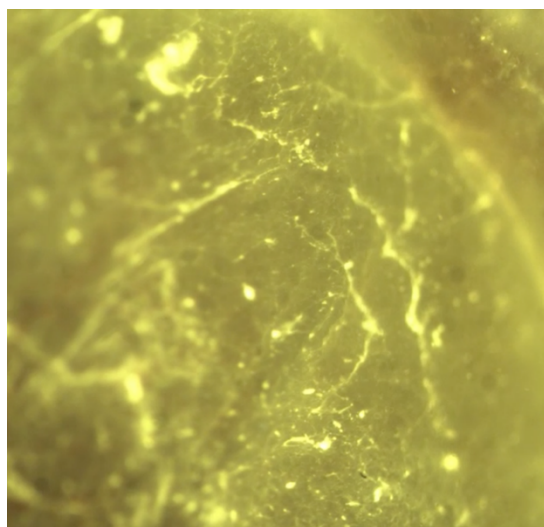
- (27) Beauchamp, C. O.; Gonias, S. L.; Menapace, D. P.; Pizzo, S. V. *Anal. Biochem.* **1983**, *131*, 25–33.
- (28) Kim, S. W.; Jeong, B.; Bae, Y. H.; Lee, D. S.; Kim, S. W. *Nature* **1997**, *388* (6645), 860–862.
- (29) Tam, Y. T.; Gao, J.; Kwon, G. S. *J. Am. Chem. Soc.* **2016**, *138*, 8674–8677.
- (30) Mackiewicz, N.; Nicolas, J.; Handké, N.; Noiray, M.; Mougín, J.; Daveu, C.; Lakkireddy, H. R.; Bazile, D.; Couvreur, P. *Chem. Mater.* **2014**, *26*, 1834–1847.
- (31) Pfister, A.; Zhang, G.; Zareno, J.; Horwitz, A. F.; Fraser, C. L. *ACS Nano* **2008**, *2*, 1252–1258.
- (32) Abebe, D. G.; Fujiwara, T. *Biomacromolecules* **2012**, *13*, 1828–1836.
- (33) Fujita, M.; Sawayanagi, T.; Abe, H.; Tanaka, T.; Iwata, T.; Ito, K.; Fujisawa, T.; Maeda, M. *Macromolecules* **2008**, *41*, 2852–2858.
- (34) Aryal, S.; Hu, C.-M. J.; Zhang, L. *Mol. Pharm.* **2011**, *8*, 1401–1407.
- (35) Sánchez, I.; Núñez, C.; Campo, J. A.; Torres, M. R.; Cano, M.; Lodeiro, C. *J. Mater. Chem. C* **2014**, *2*, 9653–9665.
- (36) Xu, S.; Evans, R. E.; Liu, T.; Zhang, G.; Demas, J. N.; Trindle, C. O.; Fraser, C. L. *Inorg. Chem.* **2013**, *52*, 3597–3610.
- (37) Lavis, L. D.; Raines, R. T. *ACS Chem. Biol.* **2008**, *3*, 142–155.
- (38) Grimm, J. B.; English, B. P.; Chen, J.; Slaughter, J. P.; Zhang, Z.; Revyakin, A.; Patel, R.; Macklin, J. J.; Normanno, D.; Singer, R. H.; Lionnet, T.; Lavis, L. D. *Nat. Methods* **2015**, *12*, 244–250.
- (39) Baggaley, E.; Botchway, S. W.; Haycock, J. W.; Morris, H.; Sazanovich, I. V.; Williams, J. A. G.; Weinstein, J. A. *Chem. Sci.* **2014**, *5*, 879–886.

- (40) Zhang, G.; Palmer, G. M.; Dewhurst, M. W.; Fraser, C. L. *Nat. Mater.* **2009**, *8*, 747–751.
- (41) Zhang, G.; Kooi, S. E.; Demas, J. N.; Fraser, C. L. *Adv. Mater.* **2008**, *20*, 2099–2104.
- (42) Daly, M. L.; DeRosa, C. A.; Kerr, C.; Morris, W. A.; Fraser, C. L. *RSC Adv.* **2016**, *6*, 81631–81635.
- (43) Reineke, S. *Nat. Photonics* **2014**, *8*, 269–270.
- (44) Mathew, A. S.; DeRosa, C. A.; Demas, J. N.; Fraser, C. L. *Anal. Methods* **2016**, *8*, 3109–3114.
- (45) Xu, S.; Chen, R.; Zheng, C.; Huang, W. *Adv. Mater.* **2016**, *28*, 9920–9940.
- (46) DeRosa, C. A.; Samonina-Kosicka, J.; Fan, Z.; Hendargo, H. C.; Weitzel, D. H.; Palmer, G. M.; Fraser, C. L. *Macromolecules* **2015**, *48*, 2967–2977.
- (47) Proikakis, C. S.; Mamouzelos, N. J.; Tarantili, P. A.; Andreopoulos, A. G. *Polym. Degrad. Stab.* **2006**, *91*, 614–619.
- (48) Carfi Pavia, F.; La Carrubba, V.; Piccarolo, S.; Brucato, V. *J. Biomed. Mater. Res. - Part A* **2008**, *86*, 459–466.
- (49) Maeda, H.; Wu, J.; Sawa, T.; Matsumura, Y.; Hori, K. *J. Control. Release* **2000**, *65*, 271–284.
- (50) Mao, H.; Pan, P.; Shan, G.; Bao, Y. *J. Phys. Chem. B* **2015**, *119*, 6471–6480.
- (51) Ma, C.; Pan, P.; Shan, G.; Bao, Y.; Fujita, M.; Maeda, M. *Langmuir* **2015**, *31*, 1527–1536.
- (52) Kinard, L. A.; Kasper, F. K.; Mikos, A. G. *Nat. Protoc.* **2012**, *7*, 1219–1227.
- (53) Cammack, J. K.; Marder, S. R.; Kippelen, B. 2005. US 2005/0209478 A1, 2005.
- (54) Zhang, G.; Chen, J.; Payne, S. J.; Kooi, S. E.; Demas, J. N.; Fraser, C. L. *J. Am. Chem. Soc.* **2007**, *129*, 8942–8943.
- (55) Williams, D. B. G.; Lawton, M. *J. Org. Chem.* **2010**, *75*, 8351–8354.

- (56) Demas, J. N.; Crosby, G. A. *J. Phys. Chem.* **1971**, *75*, 991–1024.
- (57) Kerr, C.; DeRosa, C. A.; Daly, M. L.; Zhang, H.; Palmer, G. M.; Fraser, C. L. *Biomacromolecules* **2017**, *18*, 551–561.

Chapter 7:

Oxygen-Sensing Capabilities and Performance of Difluoroboron β -Diketonate-PLA Materials



7.1. Introduction

Optimization of difluoroboron β -diketonate-poly(lactic acid) materials has enabled applications beyond our initial report of tumor hypoxia imaging.¹ New iodide substituted derivatives have expanded the range of absorption (λ_{abs}), fluorescence (F) and phosphorescence (P) wavelengths. Furthermore, we have developed methods to systematically tune the phosphorescence lifetime (τ_{p}) to modulate the oxygen sensing range. Properties for four iodide-substituted derivatives are summarized in Table 7.1. (Structures are shown in Figure 7.1).

This chapter summarizes the types of functional boron dye materials developed over the last five years. Features achieved through chemical modulation are compared and contrasted, in order to critically analyze advantages and disadvantages for practical applications. Differences in photostabilities, fluorescence and phosphorescence wavelengths (e.g. peak separation required oxygen-sensing techniques), and oxygen-sensing dynamic ranges are discussed. Biological applications such as wound hypoxia imaging, cellular imaging, nanoparticle biodistribution, and radiation therapy efficacy are presented to show advancements made possible with newly developed dyes and polymers.

Table 7.1. Optical Properties of BF₂bdkPLA Nanoparticles

Sample	λ_{abs}^a (nm)	λ_{F}^b (nm)	λ_{P}^c (nm)	τ_{P}^d (ms)	F to P	O ₂ Range (%)	References
BF ₂ dbm(I)PLA	407	437	525	4.5	F = P	0-21	1
BF ₂ nbm(I)PLA	417	460	562	1.9	F << P	0-100	2
BF ₂ dnm(I)PLA	433	503	575	6.0	F < P	0-5	3
BF ₂ tbm(I)PLA	433	449	581	2.1	F = P	0-21	4

^aAbsorbance maxima. ^bSteady-state fluorescence spectra emission maximum under air. ^cDelayed emission spectra maxima under N₂. ^dPre-exponential weighted RTP lifetime. ^eRelative F and P intensities under nitrogen.

7.2. Results and Discussion

7.2.1. Photostability

Stable emission from the dye is paramount for imaging and sensing functionality. Because the fluorescence to phosphorescence emission ratio (F/P) is a commonly utilized parameter for quantifying oxygen, if those ratios change over time, given dye degradation, determination of oxygen levels will be inaccurate. To be clear, some dye degradation is expected, but clear understanding of the the effect of dye degradation on emissive properties is important. For example, when the boron dye degrades, a decrease in dye density results, but if the F/P ratios remain stable during degradation (i.e. at a given oxygen level), the emission can still serve as a reliable oxygen concentration reporter. If, however, dye degradation changes the fluorescence wavelength, then collecting intensity data on the initial fluorescence wavelength (i.e. prior to degradation) to determine the F/P ratio will no longer be reliable, as is the case for high dye-density polymers (i.e. low molecular weights).⁵ Therefore, identifying materials with stable F/P signals (or alternatively, developing data processing methods for migrating signals and other changes to F/P ratios and sample calibration due to degradation and other factors) is the first priority for developing nanosensors that are practical for long periods of time *in vivo*. While photobleaching is a drawback, the reality is that all luminescent materials will photobleach.^{6,7} What is important is to determine the onset and degree of degradation over the course of a given experiment, and also, reasonable expectations for nanoparticles when used *in vivo*. We focused photostability measurements on the iodide-substituted dyes given their optimal fluorescence to phosphorescence ratios. Ratiometry is a steady-state technique; therefore, the UV lamp is continuously illuminating the sample to gather information on the F/P ratios. In non-heavy atom substituted derivatives with

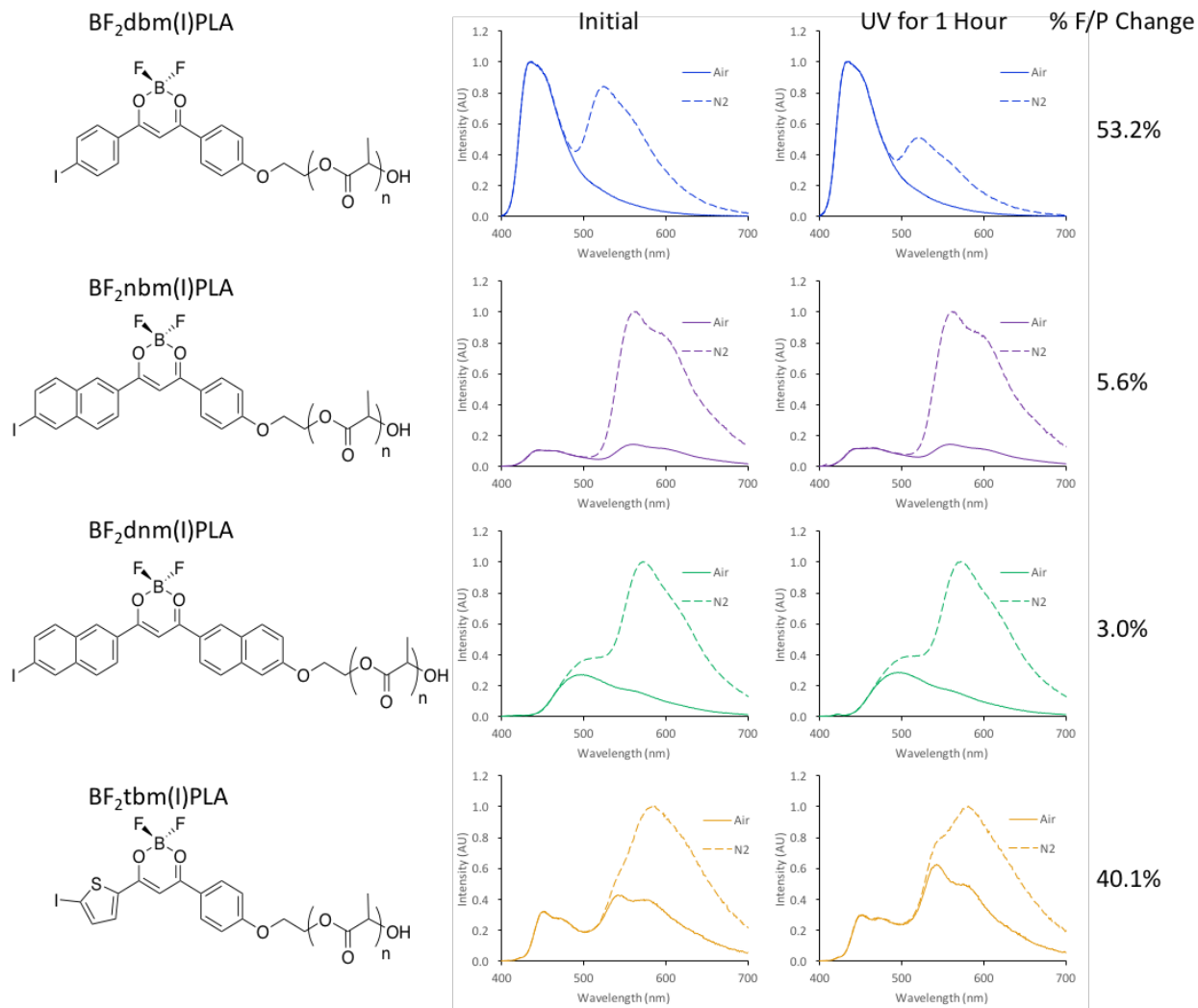


Figure 7.1. Structures and Photostability of BF₂bdkPLA Nanoparticles. The initial spectra were recorded right after nanoparticle fabrication. The photobleached samples were recorded after 1 hour of intense UV illumination (The Blak-Ray B-100 Series high powered UV lamp). The percent change is the calculated changes in F/P ratios before and after UV illumination.

long afterglows, steady-state methods are ineffective because the phosphorescence is too weak to be observed, and relatively to the fluorescence is too strong. For lifetime sensing, the UV lamp is on for only a short period of time, and photobleaching is less of an issue.

Photostability measurements were performed on newly fabricated nanoparticles of BF₂dbm(I)PLA (phenyl-phenyl; 19 kDa polymer),⁵ BF₂nbm(I)PLA (naphthyl-phenyl; 25 kDa polymer),² BF₂dnm(I)PLA (naphthyl-naphthyl; 24 kDa polymer),³ and BF₂tbm(I)PLA (thienyl-

phenyl; 22 kDa polymer), as shown in Figure 7.1.⁴ Polymers of higher molecular weights were chosen based on our previous studies with dibenzolymethane derivatives.⁵ In this experiment, we used a high-power lamp, similar to those on fluorescence microscopes, to expedite the photobleaching process for nanoparticles. For many experiments, lower power excitation is utilized, so this also probes upper limits of degradation. The nanoparticles were illuminated for 1 hour with stirring (Figure 7.1). The changes in F/P ratios before and after photobleaching are revealing. The BF₂dbm(I)PLA polymer photobleached the most, with a 53% decrease in the phosphorescence intensity. This is in agreement with our previous study.⁵ The thienyl derivative, BF₂dbm(I)PLA, experienced a 40% change in ratio, but unexpectedly, the aggregate emission (peak at ~530 nm) was stable, and the blue monomer emission (peak at ~450 nm), decreased intensity. More work is required to explain these results, as it contradicts our previous reports involving aggregation effects on the photostability. Regardless, this analogue appears to be the least reliable. The naphthyl derivatives, BF₂nbm(I)PLA and BF₂dnm(I)PLA, showed impressive resilience to photobleaching, with only 5.6% and 3.0% changes, respectively. Given the advantages in wavelengths and sensitivity (Table 7.1), these two scaffolds (BF₂nbm and BF₂dnm) are the preferred dye materials for imaging.

7.2.2. Camera-Based Oxygen Sensing via Lifetime

Many commercial oxygen sensing techniques based on luminescence already exist. For example, ©Presens has developed a convenient hand-held system that utilizes the red/green/blue (RGB) channels of a camera to perform ratiometric imaging.^{8,9} The hand-held camera, in combination “sensor foils” generates oxygen maps to gather spatial and temporal information. Commercial lifetime-based oxygen sensors are primarily fabricated as fiber optic lifetime decay O₂ sensors, such as the ©Piccolo₂ developed by ©PyroScience. These provide highly reliable O₂

measurements, but only point measurements based on the location of the probe tip, and can be invasive in a biological context. Lifetime based measurements can be performed spatially with high-speed cameras, but depending on the particular phosphor that is used, costs and feasibility can differ greatly.

Recently, Meier et al., compared several camera-based imaging techniques.¹⁰ Of those reviewed, lifetime imaging was shown to be the most expensive (\$15,000 - \$60,000), the most complex, and the least portable. In the Fraser lab, in collaboration with Prof. Demas, we developed a low-cost, real-time oxygen imaging system that takes advantage of the unusually long lifetimes of heavy-atom free BF₂bdkPLA materials ($\tau_p = >100$ ms). The unusually long lifetimes reduce equipment costs given decays can be captured by a lower frame rate camera. Our setup costs less than \$5000, easily fits into a backpack, and can operate on battery power alone, as shown in Figure S7.1 (Appendix F). A schematic is shown in Figure 7.2. For complete details refer to Mathew et al., *Anal. Methods* **2016**, 8, 3109–3114.¹¹ Other materials, such as metal porphyrins, cannot use this cost-effective method because the phosphorescence is too short (μ s). For lifetime detection, our system trades resolution (frame-rate) for the reduction in costs. Steady-state emission, however, is comparable to the commercially available O₂-sensing platforms, and ratiometry can also be performed with this setup, even dual mode lifetime/ratiometric imaging.⁸

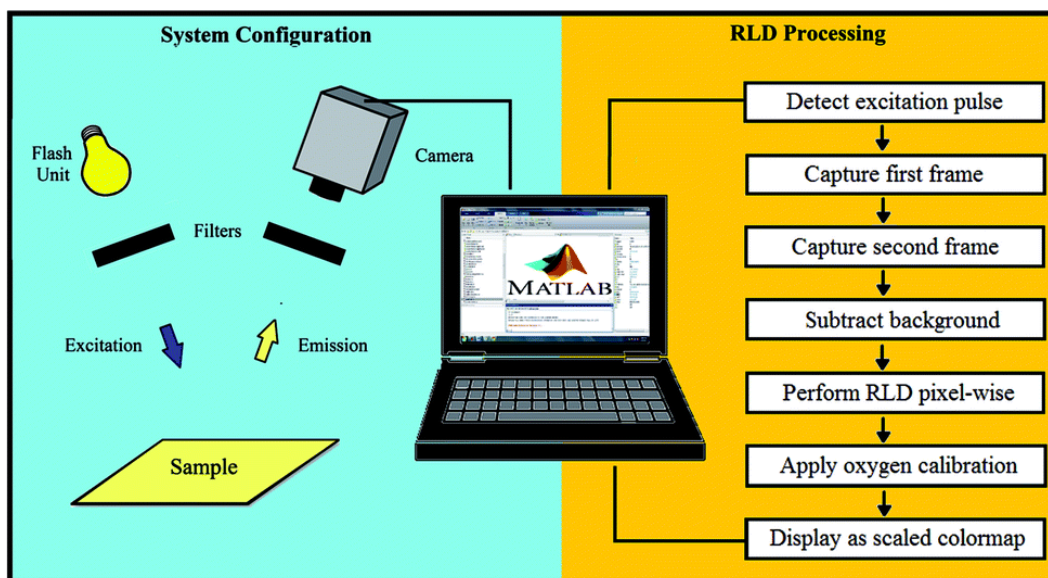


Figure 7.2. Schematic of the System Setup (left) and Data Processing for Real-Time Rapid Lifetime Determination Imaging (right). Image reproduced with permission from Mathew et al., *Anal. Methods* **2016**, 8, 3109–3114.¹¹ Copyright the Royal Society of Chemistry 2016.

Lifetime-based oxygen sensing is demonstrated with BF_2nbmPLA nanoparticles, shown in Figure 7.3.² As expected, the long-lived RTP of the nanoparticles was quenched very quickly (i.e. in ~ 6 s) when 1% O_2 is bubbled into a nitrogen purged sample. Because the RTP is ultrasensitive to oxygen, this type of probe could be deployed for “turn-on” sensing to detect the most oxygen-starved regions (e.g. anoxic, ischemic, necrotic tissue).^{12,13}

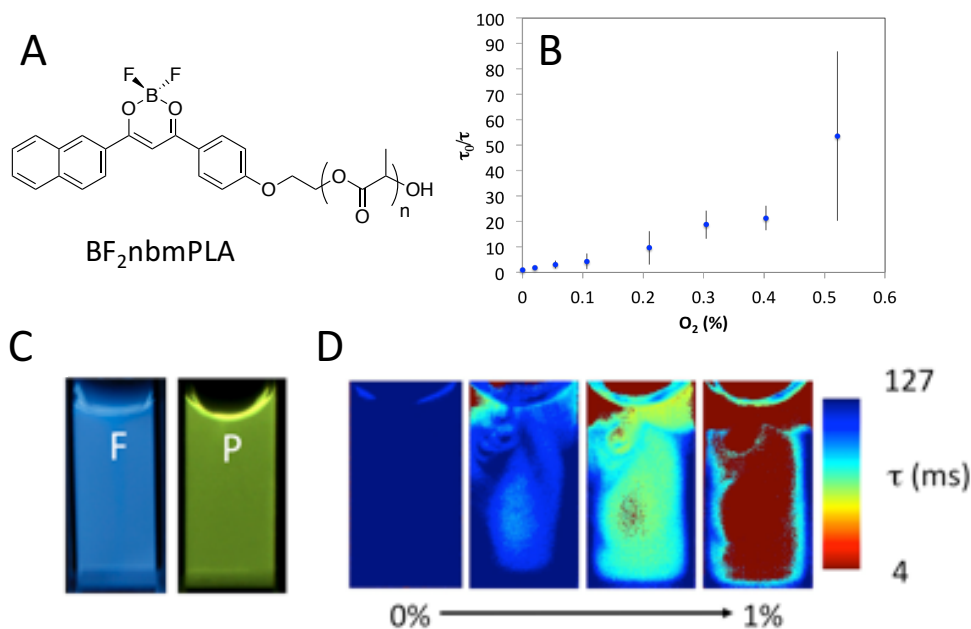


Figure 7.3. Lifetime Imaging with BF_2nbmPLA . A) Chemical structure. B) Stern-Volmer relationship of oxygen quenching. C) Photographs of BF_2nbmPLA nanoparticles in air (F) (UV lamp on) and under N_2 (P) (UV lamp turned off). (B) Selected video frames of oxygen quenching from 0% (N_2 ; start) to 1% oxygen, as a steady stream of 1% O_2 (Praxair) is blown into the nanoparticle suspension.

7.2.3. RGB Camera Imaging

Camera imaging captures emission on the red, green, and blue (RGB) channels of a color camera. This method is both powerful and accessible, because most everyone has camera technologies in their pocket in the forms of phones and devices. Simple and user-friendly instrumentation is key to the adoption of research technologies in the clinical setting.

For RGB imaging to work optimally, material design compatible with imaging technology is critical. Klimant and co-workers recently reported a dual O_2 and pH optical sensing using three fluorophores embedded in a polystyrene matrix.¹⁴ In particular, the europium complex red channel O_2 sensor was crucial. Europium dyes emit through the distinct and narrow $^5\text{D}_0 \rightarrow ^7\text{F}_2$ emission peak ($\lambda_{\text{max}} = 615 \text{ nm}$) with virtually no overlapping emission into the green and blue channels.¹⁵

For RGB camera sensing, ideally the fluorescence and phosphorescence peaks should be distinct, such that the peak emissions do not “bleed” into or interfere with the other channels. In our work, this was achieved by using boron dye materials with large singlet-triplet splitting (Δ_{ST}). The naphthyl-phenyl dye fit the key requirements best (Figure 7.4). Furthermore, this scaffold is highly tunable by varying naphthyl substituent (i.e. H, Br or I). These materials, in conjunction with a portable cost effective camera, are well tuned to anoxia, hypoxia (<3% O₂), normoxia (0-21% O₂) and even full range (0-100% O₂) imaging in real time via lifetime (τ), ratiometric (RGB), or dual lifetime/ratiometric modes.

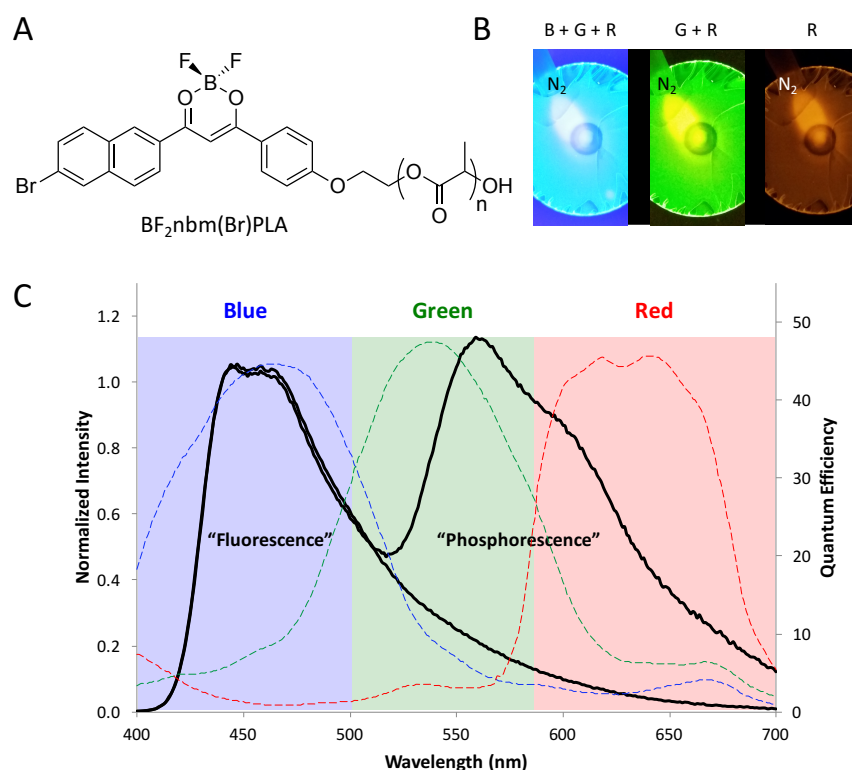


Figure 7.4. RGB Camera Channels. A) Chemical Structure of BF₂nbm(Br)PLA. B) Images of spin-cast film with a steady flow of N₂ and filters to reveal the response in different channels (B+G+R = no filter, G+R = 520 nm cut-on filter, R = 590 nm cut-on filter). C) Spectra of BF₂nbm(Br)PLA under air (“fluorescence”) and N₂ (“fluorescence” + “phosphorescence”) overlaid with the quantum efficiency of the channels of the camera (blue, green and red).

Specifically, $\text{BF}_2\text{nbm}(\text{Br})\text{PLA}$ nanoparticles enable simultaneous, multimodal lifetime and ratiometric detection (Figure 7.5). Unlike BF_2nbmPLA , the phosphorescence of the brominated derivative is strong and the red/green/blue (RGB) color channels of the camera can be used to independently monitor changes in F and P for referenced (F/P) oxygen sensing. RGB camera calibration of $\text{BF}_2\text{nbm}(\text{Br})\text{PLA}$ revealed that using the blue channel for the reference (F) and the red channel as the sensor (P) generated the best calibration curve for this material. The green channel was excluded from the measurements to provide the most spectrally isolated F and P signals. It is common for the camera RGB calibration to have reduced precision compared to spectral referenced intensity (RI) as shown in Figure S7.2 (Appendix F). However, these are goals for further optimization, namely, either to push the material F and P signals farther apart, into better alignment with camera channels, or to better tailor the instrumentation to the material via camera selection, filter selection and customization.

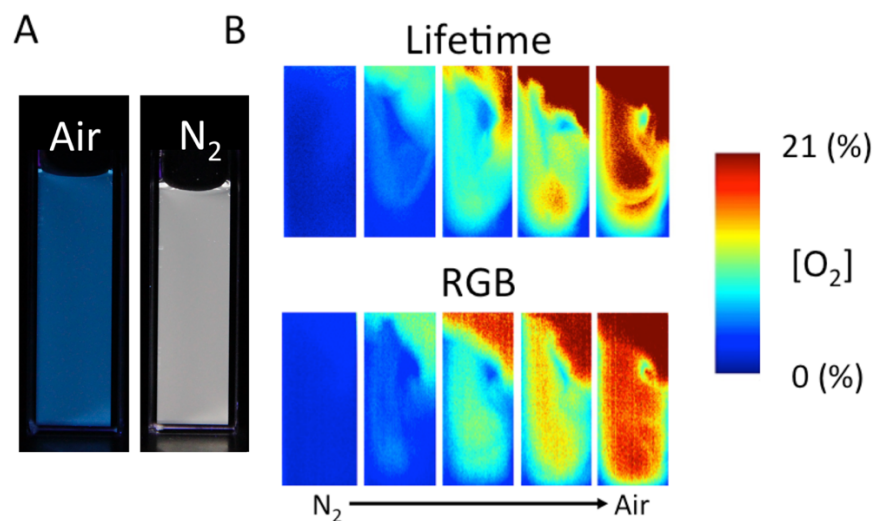


Figure 7.5. Dual-Mode Oxygen Sensing with $\text{BF}_2\text{nbm}(\text{Br})\text{PLA}$ Nanoparticles. A) Images of nanoparticles in N_2 and air. B) Selected video frames of oxygen quenching from 0% (N_2) to 21% oxygen (Praxair) as a steady stream of 21% O_2 (Praxair) is blown into the nanoparticle suspension.

Side by side comparison of lifetime and RGB imaging of BF₂nbm(Br)PLA nanoparticles contrasts the two techniques nicely. Although it is possible to sense oxygen to 21%, changes in the F/P ratio are minimal from 3-21%, making it difficult to distinguish the O₂ level in these ranges via RGB, as discussed earlier in Chapter 3. Because the fluorescence emission is on the order of nanoseconds, and RTP, milliseconds, an appropriately timed gate can be applied to eliminate the singlet emission. When a lifetime calibration is performed on BF₂nbm(Br)PLA, the Stern-Volmer quenching constant (τ_p vs %O₂) had a linear correlation from 0-21% O₂.

7.2.4. RGB Wound Hypoxia Imaging

Tissue healing requires energy to facilitate increased extracellular matrix synthesis and cell proliferation.¹⁶ The production of adenosine triphosphate (ATP) and other activated carrier molecules requires oxygen, so tissues are dependent on proper oxygenation to provide the energy to enable healing. Wounds that do not heal properly, given incomplete repair, are known as chronic wounds and they can be hypoxic. In fact, tissue oxygenation (e.g. hyperbaric chamber) is a chronic wound treatment.¹⁷ To test the usability of the nanoparticles, we chose to use BF₂nbm(I)PLA nanoparticles because of the full-range oxygen sensing capabilities (Figure 7.6).

To demonstrate the utility of nanoparticle/camera imaging for biological oxygen sensing, the camera was mounted onto a microscope, and nanoparticles were applied to a murine (mouse) full thickness skin wound (Figures S7.3.and S7.4.; Appendix F). Upon BF₂nbm(I)PLA application (Figure 7.7), the wound bed displayed bright yellow emission (strong P + weak F) even without covering the wound. When BF₂nbm(I)PLA treated wounds were later covered, the phosphorescence signal persisted and intensified over the course of image acquisition. Finer wound bed detail is also evident in certain UV and processed RGB oxygenation images. For

example, some $\text{BF}_2\text{nbm(I)PLA}$ ratiometric images reveal microvasculature (Figure 7.7 and Figures S7.5 and S7.6; Appendix F).

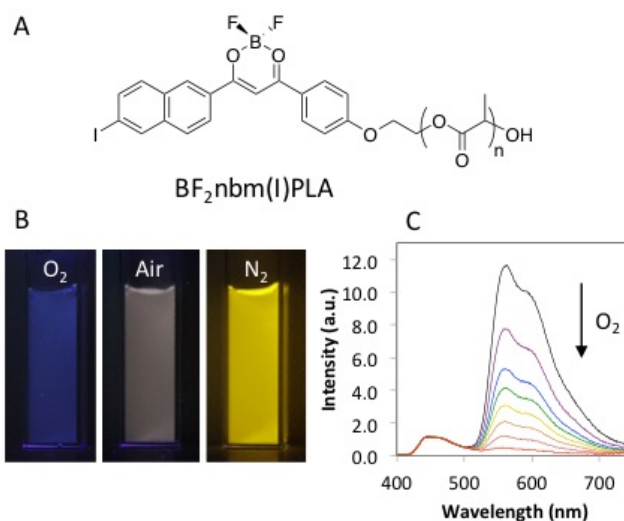


Figure 7.6. Optical Properties of $\text{BF}_2\text{nbm(I)PLA}$. A) Chemical structure $\text{BF}_2\text{nbm(I)PLA}$. B) Images on the nanoparticles at different oxygen concentrations, and C) total emission spectra at different oxygen concentrations.

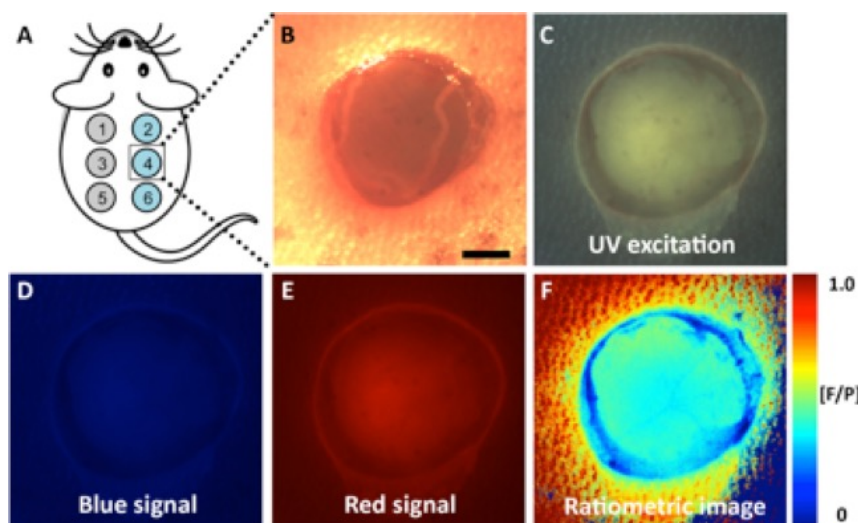


Figure 7.7. In Vivo Camera Imaging with $\text{BF}_2\text{nbm(I)PLA}$ Nanoparticles. (A) Illustration of mouse dorsal wounds (gray circles = control wounds, blue circles = NP treated wounds) (B) Bright field image. (C) Raw image under UV excitation (D) Blue channel (fluorescence). (E) Red channel (phosphorescence). (F) RGB image (blue/red channel).

Because $\text{BF}_2\text{nbm}(\text{Br})\text{PLA}$ nanoparticles possess a narrower sensing range, they too, were tested, in attempts to detect details and microenvironmental changes at higher resolution. For example, on day 0, the periphery of the $\text{BF}_2\text{nbm}(\text{I})\text{PLA}$ treated wound bed appeared to be highly deprived of oxygen (Figure 7.8; Day 0). However, this effect was less evident when $\text{BF}_2\text{nbm}(\text{Br})\text{PLA}$ were applied to the wound, as ratio changes were barely above the baseline fluorescence. When attempting lifetime mode imaging with $\text{BF}_2\text{nbm}(\text{Br})\text{PLA}$, no delayed emission was observed, or it was too short-lived for detection (<2 ms). This could be a result of the increased O_2 sensitivity of the material, or because wounds can be situational and diverse, and the same features did not arise between trials. When isolated from air (covered) however, RTP did activate. However, the response of $\text{BF}_2\text{nbm}(\text{Br})\text{PLA}$ was less dynamic than $\text{BF}_2\text{nbm}(\text{I})\text{PLA}$, indicating that $\text{BF}_2\text{nbm}(\text{Br})\text{PLA}$ are not as well suited for wound imaging as $\text{BF}_2\text{nbm}(\text{I})\text{PLA}$, which gave consistent measurements of the oxygen levels day to day for covered and uncovered measurements. Biological mechanisms of nanoparticle cell uptake, differences in oxygen diffusion, and tissue accumulation may all influence hypoxia responses, and are under investigation.

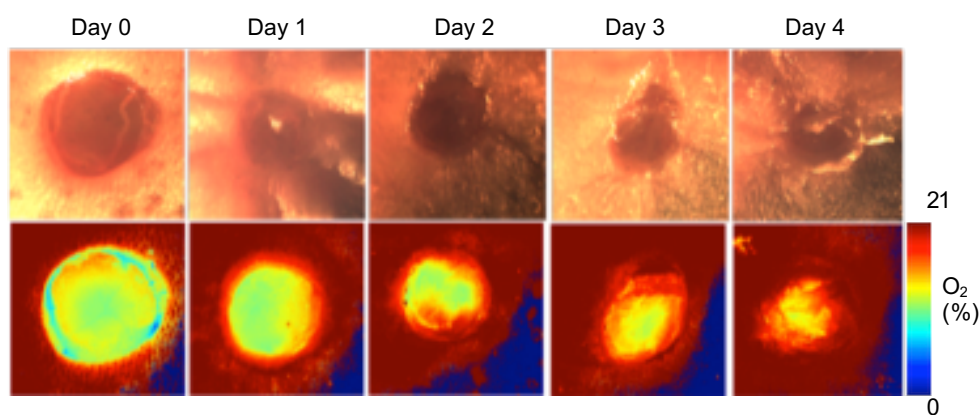


Figure 7.8. Wound oxygenation and healing time course monitored by $\text{BF}_2\text{nbm}(\text{I})\text{PLA}$. Top row: Brightfield images of the uncovered wound. Bottom row: Ratiometric images of the uncovered wound taken 5 min after nanoparticle application.

Unlike first generation materials with no heavy atom and very bright emission, the BF₂nbm(I)PLA were not bright enough to allow for one application, with repeated imaging every day. Instead, serial applications were applied fresh each day prior to imaging to see strong nanoparticle emission. Mechanisms of degradation in the wounds and new Band-Aid type foil formulations are now under investigated.

7.2.5. Cell Imaging

Imaging the oxygen levels in cells lends insights into how BF₂bdkPLA materials interact in biological environments.¹⁸ In most cases, the PLA-based nanoparticles are applied directly to the region of interest, such as wounds² or tumors,¹ and ratios are recorded within the hour. However, for cellular uptake, incubation for a period of time is required. Given suitability for ratiometric oxygen sensing, and increased photostability, nanoparticles based on BF₂dnm(I)PLA, a more red-shifted derivative, were prepared and utilized in tumor cell O₂ imaging studies. Images are presented as wavelength versus intensity to illustrate this point, rather than the typical wavelength versus normalized fluorescence plots. However, fluorescence changes are minimal compared to phosphorescence and calibration plots are still essentially linear from 0-5.3% O₂ ($R^2 = 0.981$).³ Because the F and P wavelengths are close (See Table 7.1.), a quadview imaging system was used.³ The quadview has a beam-splitter that allows for simultaneous monitoring of four different wavelengths of the user's choice. The RGB technique does not work well for this dye, given that both the F and P maxima are in the green channel.

BNPs were taken up by 4T1 cells and maintained in two different oxygen environments overnight (~18 hours). The cellular luminescence properties were recorded every minute over a 45-minute time course (Figure 7.9). Cells maintained under normoxia conditions showed a relatively steady F/P ratio over this time (~1.1 F/P). BNP-loaded cells incubated under hypoxic

conditions were exposed to normoxia (air; ambient) and monitored by microscopy. A robust increase in the F/P ratio was observed as the oxygen levels equilibrated to room air (0.8 – 1.2). These changes occurred very slowly in the first ten minutes, but rapidly in the next ten minutes as the F/P ratios approach those observed under normoxia conditions. Thus, these nanoparticles demonstrated a rapid and dynamic oxygen-sensing activity within cells. Interestingly, nanoparticles under either condition demonstrated an upward drift of the F/P ratio as the imaging proceeded. This may be due to partial dye degradation over the course of the experiment, changes in the dye environment, or other factors that influence polymer and nanoparticle properties.

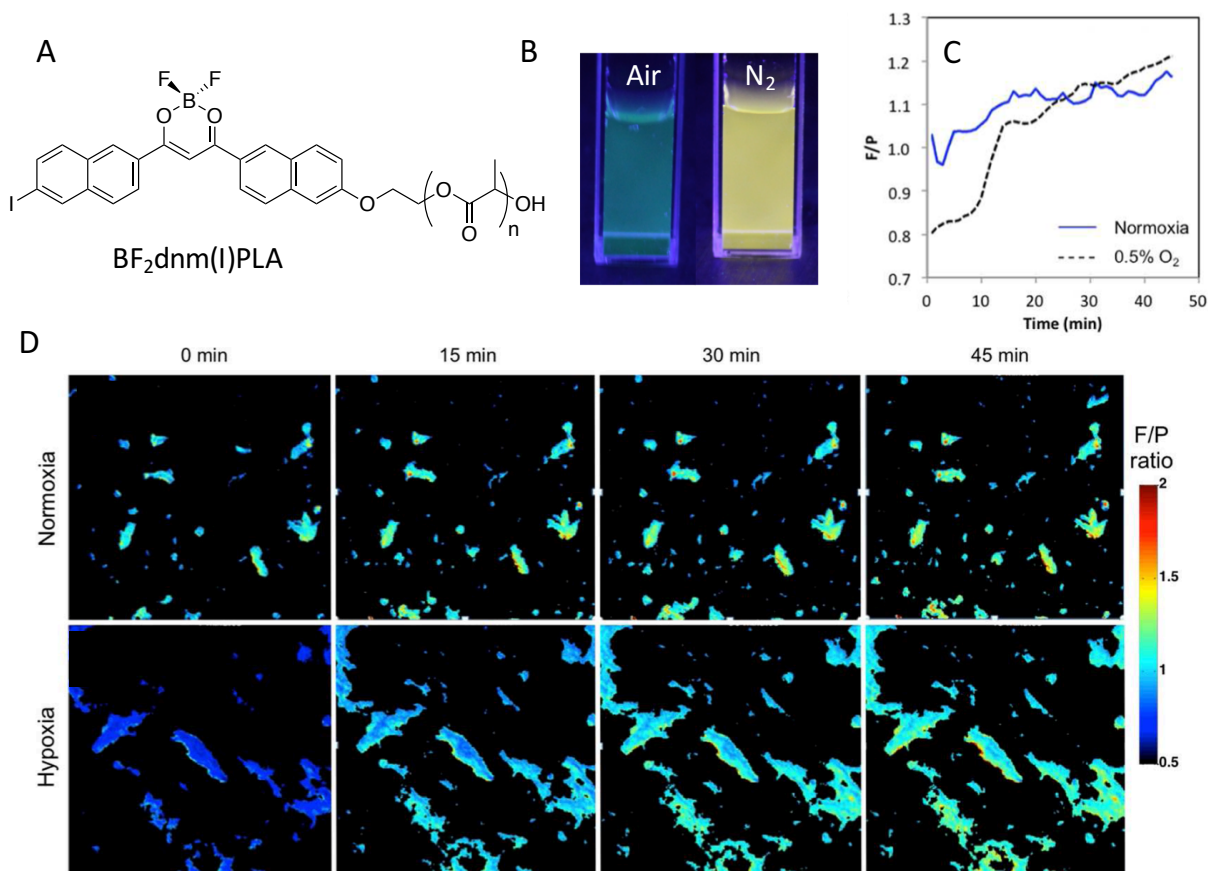


Figure 7.9. Cellular Imaging with $\text{BF}_2\text{dnm(I)PLA}$ Nanoparticles. A) Chemical Structure of $\text{BF}_2\text{dnm(I)PLA}$. B) Images of the Nanoparticles in air and N_2 under UV illumination. C) QuadView microscope quantification of F/P intensity ratio monitored for 45 min. E) QuadView microscope images of **NPI** within 4T1 cells under normoxia Top; air; ambient). And QuadView microscope images of the hypoxia (0.5% O_2) to normoxia transition (bottom).

7.2.6. Tumor Imaging

In cancer, low tissue oxygenation or hypoxia is correlated with increased tumor invasion and metastasis, as well as resistance to radiation and chemotherapy. In radiotherapy, oxygen helps to produce irreparable DNA adducts via singlet oxygen generation.¹⁹ Given the importance of oxygenation for understanding cancer biology, determining prognosis, and monitoring treatment response, it is of critical importance to measure oxygen levels dynamically in heterogeneous tumor microenvironments before and after therapy. Oxygen-sensing nanoparticles could provide this insight into the tumor microenvironment and drug response for both traditional cytotoxic drugs as well as newer molecularly specific treatments that alter microenvironmental properties (e.g. anti-angiogenic drugs).

Besides direct application or injection of nanoparticles into the tumor, another challenge is IV delivery of the nanoparticle imaging agent to the tumor. To achieve this, a hydrophilic block of poly(ethylene glycol) (PEG) was added to the nanoparticles.^{20–23} The PEG provides stealth properties to enable passive uptake of the nanoparticles to the tumor via the enhanced permeation and retention effect (EPR). Biodistribution studies were performed to determine the passive targeting efficacy of boron dye imaging agents. These studies served to elucidate the timescale of accumulation and circulation of the NPs and to assess the NP metabolism after imaging. To characterize the distribution of BF₂bdk-PLA-PEG nanoparticles in a live mouse, either saline (control or PBS) or NPs were intravenously infused into mice bearing flank tumors. For this experiment, the polymer BF₂dapvm-PLLA-PEG²³ was mixed and co-precipitated with PDLA-PEG block copolymers to form stereocomplexed nanoparticles with red emission (RED-NPs). After infusion, RED-NPs were detected in the bloodstream for at least eight hours. At 24 hours after IV infusion no RED-NPs signal was detected in the bloodstream (Figure 7.10). IVIS live

imaging of mice showed good accumulation of RED-NPs in the tumor area ($6.03 \times 10^7 \pm 2.91 \times 10^7$ to $1.73 \times 10^8 \pm 5.89 \times 10^7$ average radiant efficiency [$\text{p/s/cm}^2/\text{sr}$] / [$\mu\text{W/cm}^2$]). This result indicated successful delivery of RED-NPs to tumors and good efficacy of PEG as a passive targeting agent by the EPR effect. IVIS imaging of the dissected organs from the control mice (saline injected) and a RED-NPs injected mouse further indicated significant accumulation in the tumor and liver (Figure 7.11). The presence of NPs in the liver suggests metabolism in that organ. No significant accumulation was detected in heart, skeletal muscle, lung, kidney and spleen.

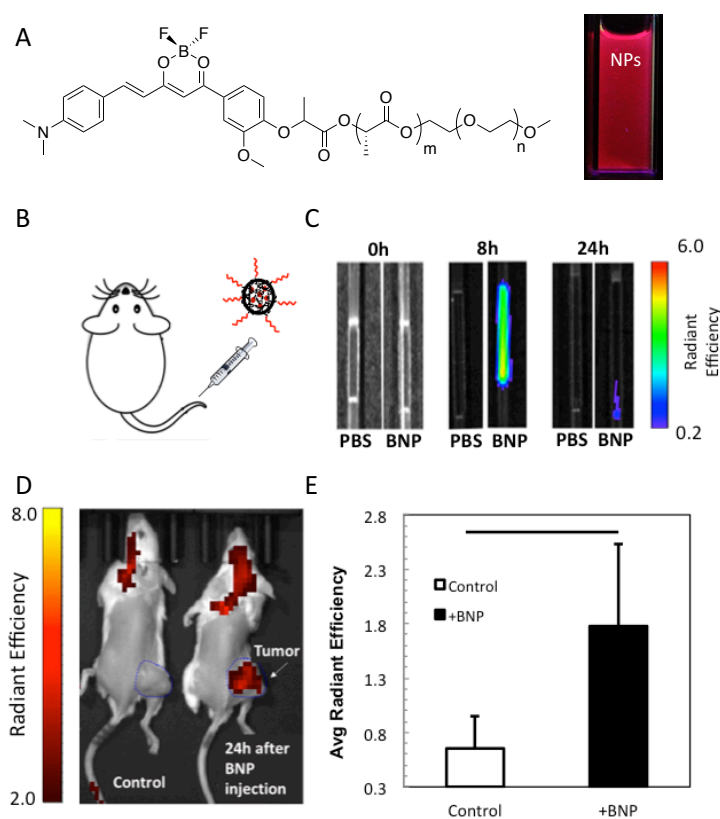


Figure 7.10. Biodistribution of RED-NPs. (A) Schematic of RED-NPs injection via tail vein infusion. (B) Pharmacokinetic study of nanoparticles in mouse bloodstream (units in [$\text{p/s/cm}^2/\text{sr}$]/ $[\mu\text{W/cm}^2] \times 10^7$). (C) Epifluorescence images of RED-NPs accumulation in a flank tumor 24 hours after IV injection. A negative control mouse injected with saline is shown on the left. The color bar on the left indicates the fluorescence intensity (units: [$\text{p/s/cm}^2/\text{sr}$]/ $[\mu\text{W/cm}^2] \times 10^8$). (D) Plots of average epifluorescence intensity from the control and RED-NPs (units: [$\text{p/s/cm}^2/\text{sr}$]/ $[\mu\text{W/cm}^2] \times 10^8$).

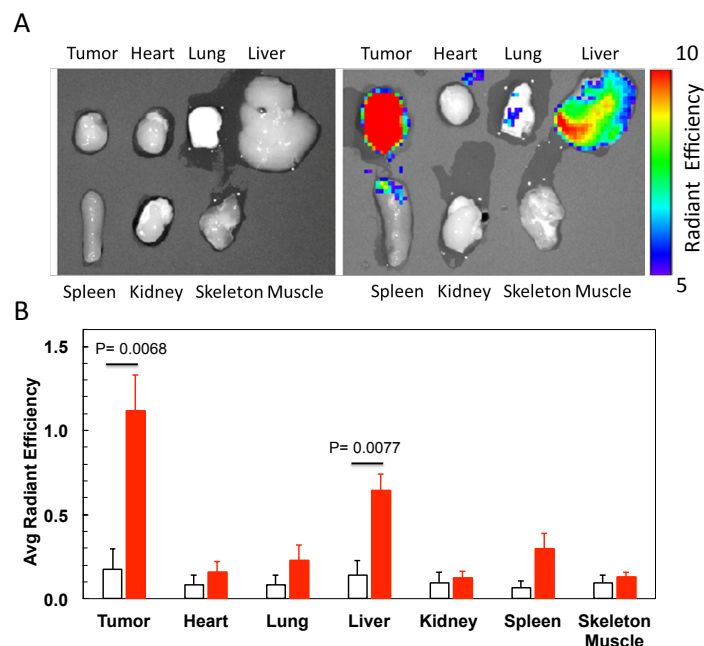


Figure 7.11. IVIS Imaging of Harvested Organs. (A) Radiant efficiency images of harvested organs from control mice (saline: n = 3) and **4scNP** injected mice (n = 6). (B) Plotted average of **4scNP** distribution in mouse organs 24 hours after injection (units given in $[p/s/cm^2/sr]/[\mu W/cm^2] \times 10^7$).

To analyze oxygenation and the effect of radiotherapy, $BF_2nbm(I)PLLA-PEG$ nanoparticles were prepared. The RED-NPs successfully accumulated in the tumor environment. The next obvious steps are to use dyes were ratiometric capabilities, such as $BF_2nbm(I)PLLA-PEG$ (Figure 7.10). However, these nanoparticles were not visible in blood draws or the tumor after, or during, the 24-hour EPR circulation. We tried many ways to alleviate this to determine why the O_2 sensing derivatives were not accumulating as the RED-NPs. One theory was the wavelength, so $BF_2dnm(I)PLLA-PEG$, a green derivative, was prepared, but this was still not visible. Then, a third poly(ϵ -caprolactone) block was included, $BF_2dnm(I)PLLA-PCL-PEG$, so the crystalline block would increase the water stability. However, the PCL diminished the phosphorescence properties, and the emission was very dim, and accumulation was still not detected. Therefore, more work is required for the ratiometric oxygen sensing polymers to be taken

up by tumors and remain stable for longer term imaging.

Radiation therapy can still be analyzed when the nanoparticles are applied directly to the tumor area (Figure 7.12). Initially, the tumor environment is resistant to changes in oxygenation (Figure 7.12D). After 2 days of radiation therapy, the ratios showed marked increases in the oxygen levels, suggesting changes in the tumor environment.

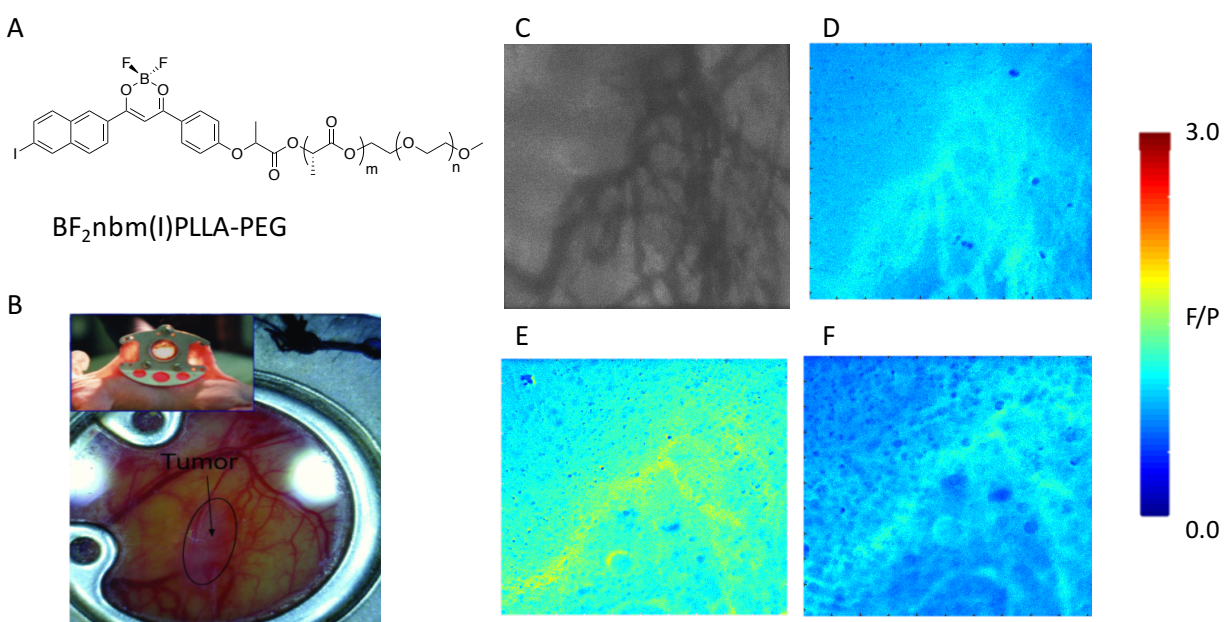


Figure 7.12. BF₂nbm(I)PLLA-PEG Nanoparticle Imaging and Radiation Therapy Efficacy in Mouse EO771. A) Chemical structure of the nanoparticle composition. B) Example image of a backpack-dorsal window chamber used in the experiment. C) Brightfield image D) Ratio acquired before radiation while mouse was breathing 10% O₂ E) 2 days after radiation before breathing 10% O₂ and F) after breathing 10% O₂. Image in B was reproduced with permission from Palmer et al. *J. Biomed. Opt.* **2010**, *15*, 066021–066021.²⁴

7.2.7. Conclusion

As described in the chapter, BF₂bdk polymeric materials have successfully been prepared for oxygen-sensing applications. Some of the newly synthesized naphthalene dyes showed better photostability and were then utilized in biological imaging of wounds, cells, and tumors, with varying degrees of success. Future work must be focused on optimizing wavelengths into the red and near-IR region to overcome difficulties with PEGylated materials for tumor accumulation, or to use active targeting groups to expedite delivery and the accumulation process.

7.3. Experimental

7.3.1. Materials

The polymers BF₂dbm(I)PLA (19 kDa),⁵ BF₂nbm(I)PLA (25 kDa)² BF₂dnm(I)PLA (24 kDa),³ BF₂tbm(I)PLA (22 kDa), BF₂nbmPLA (19 kDa),²⁵ BF₂nbm(Br)PLA (16 kDa),²⁶ BF₂dapvm-PLLA-PEG²³ and BF₂nbm(I)PLLA-PEG²³ were prepared as previously described.

7.3.2. Methods

Luminescence Measurements. Steady-state fluorescence emission spectra were recorded on a Horiba Fluorolog-3 Model FL3-22 spectrofluorometer (double-grating excitation and double-grating emission monochromator). A 1 ms delay was used when recording the delayed emission spectra. Time-correlated single-photon counting (TCSPC) fluorescence lifetime measurements were performed with a NanoLED-370 ($\lambda_{\text{ex}} = 369$ nm) excitation source and a DataStation Hub as the SPC controller. Phosphorescence lifetimes were measured with a 1 ms multichannel scalar (MCS) excited with a flash xenon lamp ($\lambda_{\text{ex}} = 369$ nm; duration <1 ms). Lifetime data were analyzed with DataStation v2.4 software from Horiba Jobin Yvon. and evaporating the solvent by slowly rotating the vial under a low stream of nitrogen. Oxygen calibration of the nanoparticles was done in triplicate as previously described using analytical grade gases (Cole-Palmer flow

gauges equipped with a mixing chamber; Praxair: pure N₂, 1.0% O₂, 21.0% O₂, or 100% O₂).¹ Fluorescence and phosphorescence lifetimes were fit to double exponential decays. Photostability measurements were performed as previously described.⁵

Nanoparticle Fabrication. Nanoparticles (~1 mg/mL) were prepared as previously described by DMF/H₂O precipitation into deionized water.¹⁸ Cellular isotonic conditions were achieved by the addition of dextrose to yield a 5% dextrose/NP/H₂O solution. The NP solution (~6 mL of ~1 mg/mL) was concentrated by centrifugation at 4000 rpm (room temperature) for 3 min (Sorval, ThermoScientific, Legend RT) in a concentrator centrifuge tube (Amicon Ultra, Regenerated Cellulose, 30,000 MW cutoff) to yield ~3 mL of a ~2 mg/mL NP solution. To remove aggregates, ~2 mg/mL NP solution (1 mL) was passed through a 200 nm filter (Whatman). Then 10% dextrose solution (1 mL) was added to yield 2 mL of ~1 mg/mL solution at 5% dextrose concentration. The NP solutions were stored at 5 °C prior to use, and were filtered (200 nm Whatman) to sterilize just prior to wound application.

Murine Full Thickness Skin Wound Model. All procedures were performed in accordance with the University of Virginia Institutional Animal Care and Use Committee. Female 12-16 week old C57BL/6 mice were used for the studies. A previously published non-splinted full thickness skin wound model was adapted and used for in vivo imaging trials.²⁷

Wound Area Quantification. Brightfield, 200x images of wounds were acquired at each time point and were imaged as described above. ImageJ²⁸ was used to quantify the wound bed area at each day by manually tracing the wound bed and calculating the area. To keep measurements consistent, the periphery of the wound was traced at the outermost edge of the wound barrier in each image.

Cell Culture in Cell Imaging. 4T1 cells (American Type Culture Collection, Manassas, VA) were maintained in Dulbecco's Modified Eagle's Medium (DMEM) supplemented with 10% fetal

bovine serum (Life Technologies, Carlsbad, CA) in a humidified incubator with 5% carbon dioxide. Cells were plated at a density of 10,000 cells per well of a 48-well plate. On the following day, cells were loaded with nanoparticles as described.²⁹ Briefly, following media removal, the wells were rinsed with PBS plus calcium and magnesium (PBS+Ca,Mg), and media without serum was added. Nanoparticle solution (50 μ g) was incubated with the cells for 1 h at 37 °C. Upon uptake completion, cells were rinsed with PBS+Ca,Mg (3X) to remove any unbound nanoparticles then growth media was replaced. Plates were placed in incubators at either 0.5% oxygen or ambient conditions for 18 h. Hypoxic plates were wrapped in parafilm following the incubation period and were unwrapped immediately before imaging.

Microscopic Imaging of Cells. Fluorescence optical imaging was performed on an inverted Zeiss Axio Observer microscope with a mercury lamp. A QV2 multichannel imager (Photometrics) employed a sequence of beamsplitters to separate the emitted fluorescent light from the sample onto different quadrants on a Hamamatsu Orca Flash4 CMOS camera. The fluorescence and phosphorescence signals were filtered at 505 nm and 565 nm, respectively, with $\Delta \lambda = 25$ nm.

Image Data Analysis of Cell Data. Acquired images were first cropped to produce individual images of the 505 nm fluorescence and 565 nm phosphorescence. Images were corrected to a background reference, regions with low signal were removed with a mask, and then spatially aligned with an affine transformation. Ratios of the 505 nm image relative to the 565 nm image (F/P) were calculated for each time point. The F/P and brightfield images were superimposed for visualization.

Animal Preparation for Biodistribution. Female mice (BALB/c), 6-8 weeks old, were purchased from Charles River Laboratory. All mice were maintained in pathogen-free barrier facilities at Duke University and were used in accordance with protocols approved by the Division of

Laboratory Animal Resources and Institutional Animal Care & Use Committee at Duke University. Before implanting flank tumors, mouse hair was first removed from the dorsal area and right leg by using Nair hair remover lotion. Mouse breast cancer cells (4T1, 2.5×10^5 cells per mouse) were then subcutaneously injected into the flank of the right leg. Flank tumors typically grow to a measurable size within a week.

IVIS Imaging for Biodistribution. In order to characterize the biodistribution of RED-NP dye-PEG-PLA nanoparticles, mice were anaesthetized and slowly, intravenously infused with either saline (negative control) or RED-NP suspensions (0.05 mg/g). IVIS Kinetic (Perkin-Elmer Corp) was used to study distribution of RED-NP in the mice after IV injection. For pharmacokinetic analysis (PKA), a small amount ($\sim 10 \mu\text{l}$) of blood was also collected with a capillary tube with a cheek-pouch in a given time interval after infusion of RED-NP into bloodstream. The collected blood sample was first centrifuged for three minutes, then immediately imaged with the IVIS Kinetic. One day after RED-NP injection, mice were sacrificed and organs were collected, rinsed with saline, and then fluorescence images were taken.

7.4. Acknowledgements

Parts of this chapter are adapted from manuscripts in *ACS Sensors*,² *Macromolecules*,³ and *Biomacromolecules*.²³ I would like to thank Ziyi Fan, Caroline Kerr, Dr. Milena Kolpacynska, and Margaret Daly for aid in the synthesis and characterization of the materials, Alexander Mathew and Prof. James N. Demas for development of the camera we used for photostability, lifetime and RGB imaging, Dr. Scott Seaman, Catherine Gorick, and Prof. Shayn M. Peirce for the work with the wound studies, Prof. Greg Palmer, Dr. Douglas Weitzel, Dr. Hansford Hendargo, and Dr. Hengtao Zhang for the cell and tumor studies, Prof. Fraser for helping with the many manuscripts

and the financial support of the National Cancer Institute of the National Institutes of Health (R01 CA167250).

7.5. References

- (1) Zhang, G.; Palmer, G. M.; Dewhirst, M. W.; Fraser, C. L. *Nat. Mater.* **2009**, *8*, 747–751.
- (2) DeRosa, C. A.; Seaman, S. A.; Mathew, A. S.; Gorick, C. M.; Fan, Z.; Demas, J. N.; Peirce, S. M.; Fraser, C. L. *ACS Sensors* **2016**, *1*, 1366–1373.
- (3) DeRosa, C. A.; Samonina-Kosicka, J.; Fan, Z.; Hendaro, H. C.; Weitzel, D. H.; Palmer, G. M.; Fraser, C. L. *Macromolecules* **2015**, *48*, 2967–2977.
- (4) DeRosa, C. A.; Kolpaczynska, M.; Kerr, C.; Daly, M. L.; Morris, W. A.; Fraser, C. L. *Chempluschem* **2016**, *82*, 399–406.
- (5) DeRosa, C. A.; Kerr, C.; Fan, Z.; Kolpaczynska, M.; Mathew, A. S.; Evans, R. E.; Zhang, G.; Fraser, C. L. *ACS Appl. Mater. Interfaces* **2015**, *7*, 23633–23643.
- (6) Altman, R. B.; Terry, D. S.; Zhou, Z.; Zheng, Q.; Geggier, P.; Kolster, R. A.; Zhao, Y.; Javitch, J. A.; Warren, J. D.; Blanchard, S. C. *Nat. Methods* **2011**, *9*, 68–71.
- (7) Grimm, J. B.; English, B. P.; Chen, J.; Slaughter, J. P.; Zhang, Z.; Revyakin, A.; Patel, R.; Macklin, J. J.; Normanno, D.; Singer, R. H.; Lionnet, T.; Lavis, L. D. *Nat. Methods* **2015**, *12*, 244–250.
- (8) Wolfbeis, O. S. *BioEssays* **2015**, *37*, 921–928.
- (9) Wang, X.; Wolfbeis, O. S. *Chem. Soc. Rev.* **2014**, *43*, 3666–3761.
- (10) Meier, R. J.; Fischer, L. H.; Wolfbeis, O. S.; Schäferling, M. *Sens. Actuat. B: Chem.* **2013**, *177*, 500–506.
- (11) Mathew, A. S.; DeRosa, C. A.; Demas, J. N.; Fraser, C. L. *Anal. Methods* **2016**, *8*, 3109–3114.

- (12) Babilas, P.; Lamby, P.; Prantl, L.; Schreml, S.; Jung, E. M.; Liebsch, G.; Wolfbeis, O. S.; Landthaler, M.; Szeimies, R.-M.; Abels, C. *Ski. Res. Technol.* **2008**, *14*, 304–311.
- (13) Giaccia, A. J.; Simon, M. C.; Johnson, R. *Genes Dev.* **2004**, *18*, 2183–2194.
- (14) Moßhammer, M.; Strobl, M.; Köhl, M.; Klimant, I.; Borisov, S. M.; Koren, K. *ACS Sensors* **2016**, *1*, 681–687.
- (15) Thévenaz, D. C.; Monnier, C. A.; Balog, S.; Fiore, G. L. *Biomacromolecules* **2014**, *15*, 3994–4001.
- (16) Schreml, S.; Szeimies, R. M.; Prantl, L.; Karrer, S.; Landthaler, M.; Babilas, P. *Br. J. Dermatol.* **2010**, *163*, 257–268.
- (17) Bishop, A. J. *Wound Care* **2008**, *17*, 399–402.
- (18) Pfister, A.; Zhang, G.; Zareno, J.; Horwitz, A. F.; Fraser, C. L. *ACS Nano* **2008**, *2*, 1252–1258.
- (19) Egusquiaguirre, S. P.; Igartua, M.; Hernández, R. M.; Pedraz, J. L. *Clin. Transl. Oncol.* **2012**, *14*, 83–93.
- (20) Maeda, H.; Wu, J.; Sawa, T.; Matsumura, Y.; Hori, K. *J. Control. Release* **2000**, *65*, 271–284.
- (21) Maeda, H. *Bioconjug. Chem.* **2010**, *21*, 797–802.
- (22) Samonina-Kosicka, J.; Weitzel, D. H.; Hofmann, C. L.; Hendargo, H.; Hanna, G.; Dewhirst, M. W.; Palmer, G. M.; Fraser, C. L. *Macromol. Rapid Commun.* **2015**, *36*, 694–699.
- (23) Kerr, C.; DeRosa, C. A.; Daly, M. L.; Zhang, H.; Palmer, G. M.; Fraser, C. L. *Biomacromolecules* **2017**, *18*, 551–561.
- (24) Palmer, G. M.; Fontanella, A. N.; Zhang, G.; Hanna, G.; Fraser, C. L.; Dewhirst, M. W. *J.*

- Biomed. Opt.* **2010**, *15*, 066021–066021.
- (25) Payne, S. J.; Zhang, G.; Demas, J. N.; Fraser, C. L.; Degraff, B. A. *Appl. Spectrosc.* **2011**, *65*, 1321–1324.
- (26) Samonina-Kosicka, J.; DeRosa, C. A.; Morris, W. A.; Fan, Z.; Fraser, C. L. *Macromolecules* **2014**, *47*, 3736–3746.
- (27) Liu, M.; Saeki, K.; Matsunobu, T.; Okuno, T.; Koga, T.; Sugimoto, Y.; Yokoyama, C.; Nakamizo, S.; Kabashima, K.; Narumiya, S.; Shimizu, T.; Yokomizo, T. *J. Exp. Med.* **2014**, *211*, 1063–1078.
- (28) Schneider, C. A.; Rasband, W. S.; Eliceiri, K. W. *Nat. Methods* **2012**, *9*, 671–675.
- (29) Contreras, J.; Xie, J.; Chen, Y. J.; Pei, H.; Zhang, G.; Fraser, C. L.; Hamm-Alvarez, S. F. *ACS Nano* **2010**, *4*, 2735–2747.

Chapter 8:

Future Directions



8.1. Introduction

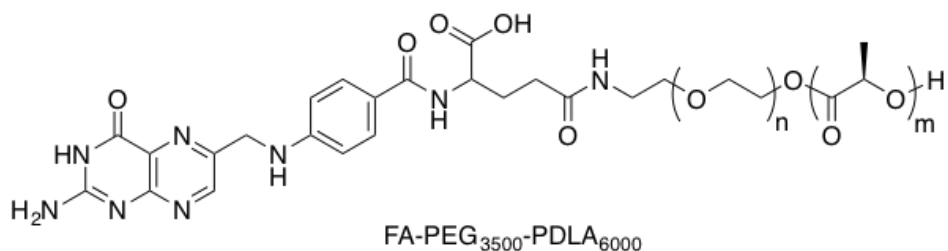
Optimization of these oxygen-sensing materials is still in the early stages. While strides have been made, challenges still need to be addressed for these materials to be realized as common tools for bioimaging. Among them are improving efficient and quick delivery of the nanoparticles to tumors, streamlining fabrication processes, optimizing peak separation for camera methods, and above all, red and near-IR emission must be achieved. Also important is to use low-cost reagents to make these alternatives commercially competitive with the current methods employed.¹ In this chapter, preliminary results and fortuitous “dead-ends” will be discussed. In some cases, serendipitous discoveries led to promising new avenues of research involving pH, viscosity and temperature responsive materials.

8.2. Ongoing Research

8.2.1. Folate-Conjugated Nanoparticles

Our previous oxygen-sensing nanoparticle designs for passive tumor accumulation worked well for short term imaging but greater stability is needed for monitoring tumor microenvironments over time.^{2,3} An active uptake mechanism could be one solution to achieving this. This can be achieved with the addition of a bioactive molecule that can bind to receptors on the cell surface and expedite intracellular accumulation. Tumors often overexpress certain biomarkers, for example, the folate-receptor α -protein.^{4,5} Because folic acid molecules have a greater affinity for the tumor than healthy cells and tissues, nanoparticles decorated with folic acid molecules are often used to tag the tumors.

To achieve this synthetically, we adapted a method reported by Xiong et al. (Scheme 8.1).⁶ This approach generated ~60% folic acid functionalization, which should be sufficient for binding and cell uptake, as it is possible to have too many targeting groups on the nanoparticle surface.⁷ In

Scheme 8.1. Folate-PEG-PDLA

our experiments, we used the D-isomer of poly(lactic acid) (PDLA) in the synthesis of a folic acid-poly(ethylene glycol)-poly(d-lactic acid) block copolymer (FA-PEG-PDLA). The D-isomer can be combined the L-isomer of poly(lactic acid) to form stereocomplexes in water, a strong, non-covalently interaction between the polymers.^{8,9}

The folic-acid functionalized polymer can be coprecipitated with O₂ sensing dye-PLA-PEG block copolymers to yield oxygen sensing nanoparticles, or with other boron dye-polymer conjugates for full color luminescent nanoparticles for multiplexing applications. This approach is illustrated in Figure 8.1 for multicolor dye-polymers. The emission properties are similar to the non-bioconjugated nanoparticles, but in the UV/Vis spectra, the folate absorbance can be detected at ~290 nm. This has great potential as a multiplexing platform because the folate polymer can be coprecipitated with many different dye-polymer conjugate. This modular “mix and match” approach can conveniently accommodate different dyes (i.e. colors) and bioconjugates. These preliminary results set the stage for future cell uptake and in vivo experiments to determine the efficacy of this method in various biological and medical contexts.

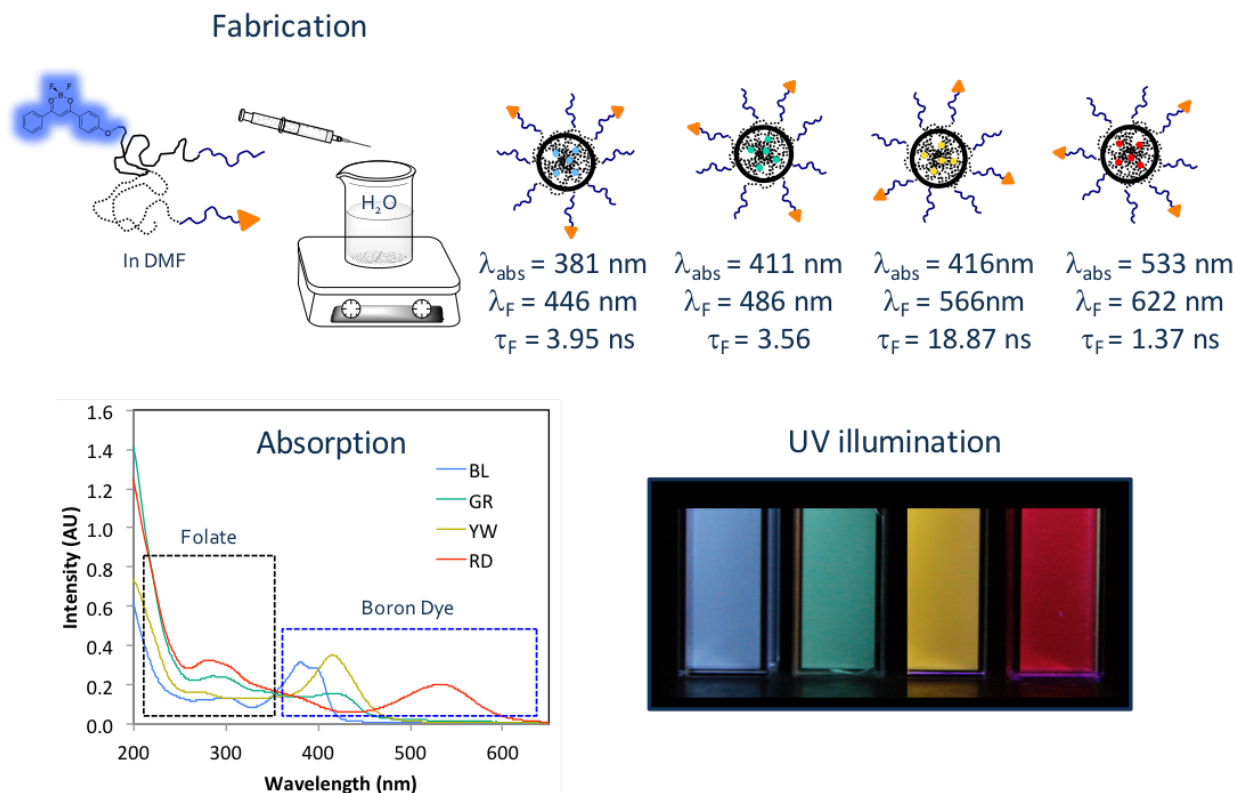


Figure 8.1. Fabrication and Optical Properties of Folate-Conjugated Nanoparticles.

8.2.2. Optimization of Dyes for Camera Techniques

For camera RGB imaging, spectral separation of the peaks, and alignment with camera channels is vital. Therefore, dyes with discrete blue, green or red emission are ideal. Wavelengths between the channels, such as yellow and teal, are less reliable because the emission will interfere with the reference channel. To approach this problem, we designed new dye scaffolds, shown in Figure 8.2. Also, rather than conjugating the dye to the PLA, we decided to add a fatty C12 alkoxy chain. The C12 alkoxy chain serves two purposes. First, it improves the solubility of the dye during synthesis, as iodide substituted dyes are notoriously difficult to dissolve. Second, it enhances the hydrophobicity of the dye material. In this pilot study, we used non-covalent interactions to prepare dye-embedded nanoparticles, analogous to the “cocktail” formulations Wolfbeis et al., and other investigators in the field commonly employ.¹⁰ Though less synthetically rigorous, and materials

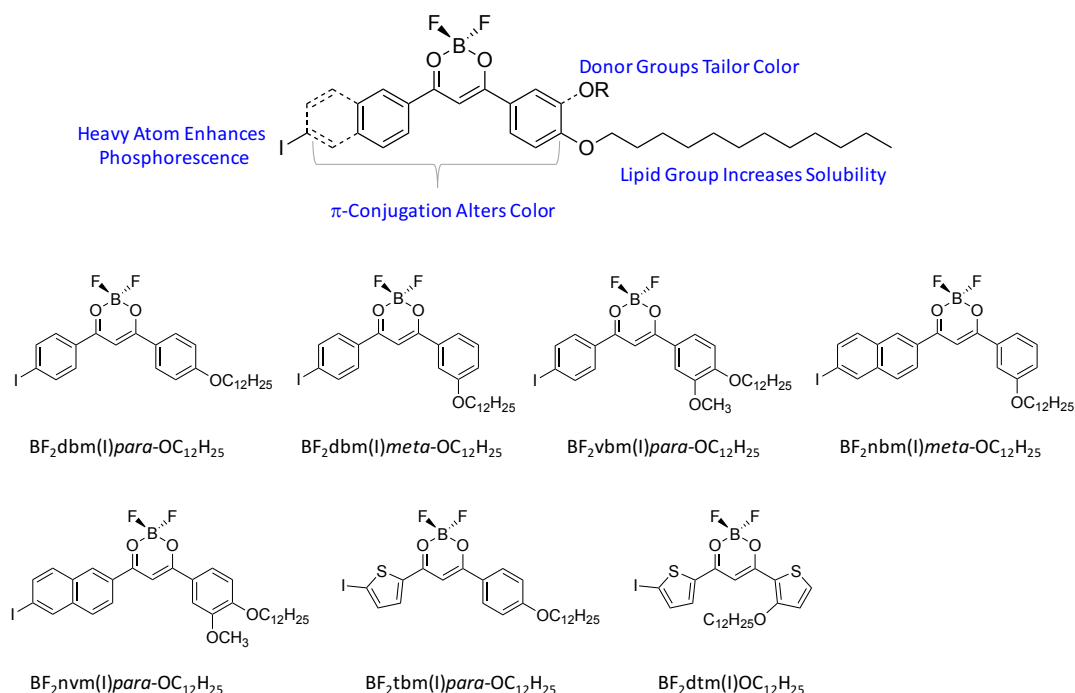


Figure 8.2. Design Strategy for Synthesizing Dye Candidates with Optimal RGB Properties.

are less uniform, large scale preparation and processing are more convenient. Synthesis, nanoparticle fabrication, physical (dynamic light scattering) and optical characterization (fluorescence and phosphorescence), and stability measurements are currently underway.

Selected preliminary results are shown in Figure 8.3 with meta-alkoxy substituted dibenzoylmethane (DBM) scaffolds, and a dithienylmethane derivative (DTM). The dye and a block copolymer of PLA-PEG were dissolved in DMF and co-precipitated into water to form nanoparticles. Dynamic light scattering suggests the nanoparticles have comparable properties to those fabricated from covalently attached dye-polymer congeners. The meta-substituted dye had usually strong phosphorescence, much stronger than the para-substituted derivatives commonly explored by our group. Furthermore, the reference emission corresponds nicely with the blue channel, and the phosphorescence spans the green channel. The narrow peaks also leave the red-channel mostly open, meaning a third dye could be used in the red-channel (e.g. rhodamine,

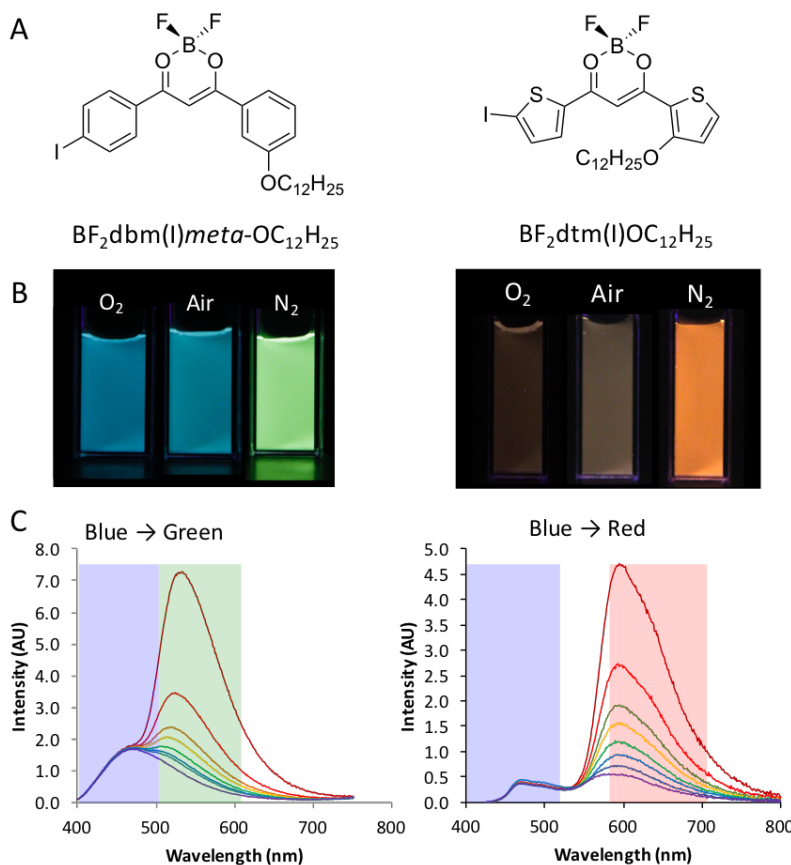


Figure 8.3. Examples of Dual-Emissive Dyes with Emission Peaks Optimal for RGB Imaging.

live/dead staining, or a pH sensor). The thienyl dye showed the reddest phosphorescence to date, with a peak wavelength at 592 nm (8 nm short of being officially red). For this dye, the blue channel is appropriate for the reference, and the red channel, for phosphorescence sensing. This however, leaves the green channel unusable, as the phosphorescence spans both the green and red channels. This dye does have promising red-shifted emission, thus enhancing the materials toolkit available to accommodate specific optical requirements or given applications.

With these two derivatives in hand, we are equipped with sensors for the blue/green and blue/red channels. While useful for other purposes, the remaining dyes were less optimal for ratiometric oxygen sensing, given overlapping fluorescence and phosphorescence peaks, weak phosphorescence, or broad emission colors. For wound or skin-care applications, the blue channel

is not a reliable reference, as endogenous species glow blue.¹¹ New derivatives must be synthesized, optically screened, and biologically tested to find the perfect chemical combination to yield a green/red channel dye for skin applications. Furthermore, these nanoparticles prepared through a non-covalent route showed limited stability. In contrast to nanoparticles prepared from materials wherein dyes are covalently linked to the polymer that are stable in the fridge for years, these dye/polymer mixtures form large precipitates after ~ 3 months. After filtering, the solution showed diminished optical properties. As the PLA matrix degrades, the dye may leach out of the nanoparticle, perhaps undergo hydrolysis, and precipitate out of solution. Thus, without further tailoring and optimization of dye/matrix interactions, these cocktailed nanoparticles may have limited usage. If the matrix were polystyrene beads, for instance, the nanoparticles could be stable for months. This hypothesis is worth investigating.

8.2.3. Biphenyl Derived Dyes

In another attempt to tune the emission colors, we extended our work with π -conjugated materials to biphenyl substitution, a common modification in the development of fluorescent materials. In the crystal structure of a biphenyl boron dye elucidated by Mirochnik et al., a slight twist was observed between the two phenyl groups of the biphenyl moiety in the ground state.¹² We hypothesized that a twisted structure induced by the biphenyl groups might result in blue-shifted delayed emission (TADF), whereas planar structures may produce red-shifted delayed emission (RTP).

While extended phenyl conjugation can tune the phosphorescence, it also decreases the singlet-triplet energy gap (ΔE_{ST}). As shown in BF₂dbpm (Figure 8.4), two distinct peaks were present in the delayed emission spectra at room-temperature. We hypothesize that the blue-shifted

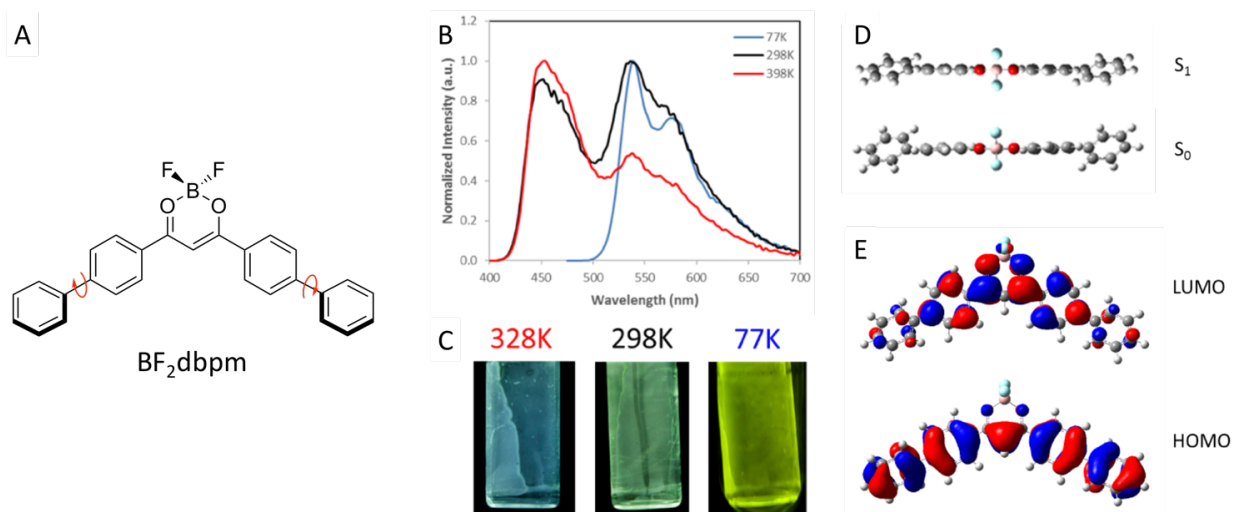


Figure 8.4. Thermally-Activated Delayed Fluorescence Properties of BF₂dbpm. A) Chemical structure with points of rotation labeled. B) Delayed emission spectra at variable temperatures. C) Images of the afterglow emission at variable temperatures. D) Optimized ground state (S₀) and excited state (S₁) geometries. E) Fronteier molecular orbital diagrams (π - π^*).

peak is thermally activated delayed fluorescence (TADF: $\lambda_{\text{TADF}} \approx 450$ nm), and the redder transition is the room temperature phosphorescence (RTP) from the dye ($\lambda_{\text{RTP}} = 536$ nm).

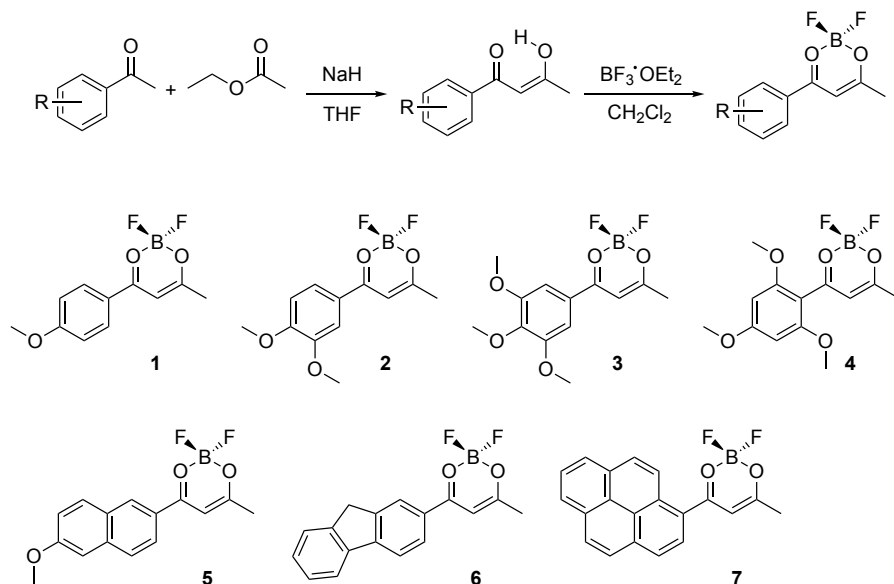
The TADF properties of BF₂dbpm were confirmed by investigating the temperature dependence of the delayed emission (Figure 8.4). When the sample was submerged in liquid nitrogen (77 K), thermal back population was eliminated, resulting in only phosphorescence at 535 nm in the delayed emission spectrum. Conversely, when the sample was heated (< 60 °C), reverse intersystem crossing was promoted. Thus, TADF became the dominant feature in the delayed emission to produce a blue afterglow. Prolonged heating quenched all delayed emission. When PLA is heated above the glass transition temperature ($T_g = \sim 60$ °C), all delayed emission is turned off as a result of a change in the matrix and availability of non-radiative decay pathways.¹³ In previous work, Adachi *et al.* reported that enhanced twisting in a molecule induces TADF.¹⁴

Density Functional Theory (DFT) calculations further support the TADF exhibited in the BF₂dbpm. The geometry of the dye in the ground state shows twisting ($\theta_{S_0} = 36^\circ$) about the phenyl-

phenyl bond of the biphenyl moieties (Figure 8.4). In the HOMO, the electron density is delocalized around the phenyl rings. Electron density of the LUMO is localized around the dioxaborine subunit. Furthermore, from the ground state to the singlet excited state, a change in the torsion angles between the phenyl moieties on either half of the dye was observed. The dye appeared to planarize slightly upon excitation ($\theta_{S1} = 24^\circ$). These twisted structures, coupled with the charge transfer character induced by the dioxaborine moiety, produce twisted intramolecular charge transfer (TICT), a feature commonly linked to blue TADF emitting materials.¹⁵ Molecules exhibiting TADF are commonly used for organic light emitting diodes (OLED). Further experiments should be carried out to analyze the performance of the biphenyl dye in an OLED device. For a complete analysis, refer to Daly et al., *RSC Adv.* **2016**, *6*, 81631–81635.¹⁶

8.2.4. Dyes with a Single Aromatic Unit

To date, red phosphorescence from difluoroboron β -diketonate dyes as yet to be achieved, with previous structural modifications associated with bathochromic shifts (e.g. thiophene, naphthalene, alkoxy donors). A deeper understanding of the mechanism and factors controlling the phosphorescence wavelength is required. Because the electronics of large conjugated systems are complicated, here, we attempted to focus on a single aromatic unit to better understand how alkoxy-substitution patterns or aromatic conjugation can influence the fluorescence and phosphorescence properties. Boron dyes consisting of a single aromatic moiety with variable number and substitution patterns of methoxys were studied in solution and PLA films. A benefit of this fundamental study is that monoaromatic dye synthesis consists of only two steps, and pure dyes can be prepared in a few hours (Scheme 8.2.)

Scheme 8.2 Synthesis of Difluoroboron β -Diketonates with a Single Aromatic Unit


Most of the dyes in this set show bright fluorescence and color tunable phosphorescence. The pyrene derivative did not show any phosphorescence though. This was surprising considering pyrene by itself is a bright blue phosphor commonly used as an industrial oxygen sensor,¹⁷ but upon chemical modification with the dioxaborine, phosphorescence was no longer present. For the other derivatives, all the fluorescence wavelengths were blue, and the phosphorescence varied according to alkoxy-substitution number and pattern. With increasing number of –OMe groups in compounds **1**, **2**, and **3**, the phosphorescence red-shifted from 503 nm, to 545 nm and 565 nm, respectively. Substitution in the 2 and 6 positions of the benzene ring (compound **4**) resulted in blue-shifted phosphorescence (450 nm). Increased π -conjugation (compound **5**), showed broad emission with a mixture of TADF and RTP in the delayed emission.

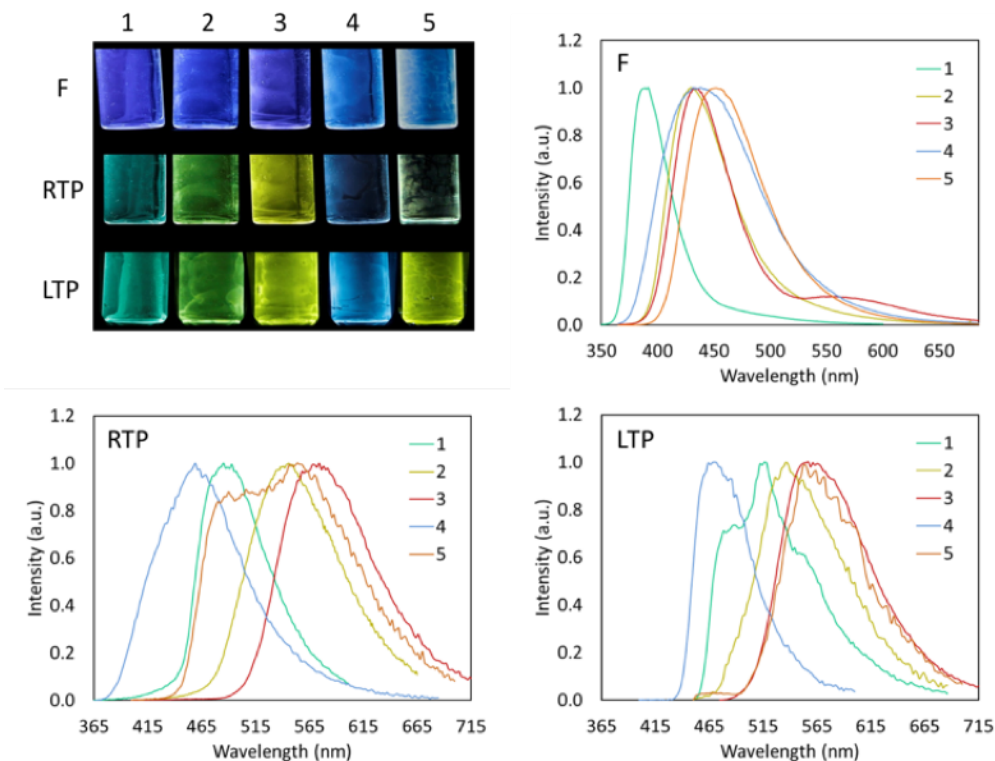


Figure 8.5. Optical Properties of Difluoroboron β -Diketones with a Single Aromatic Unit in PLA Blends (2% by weight). Top left: Images of dye embedded PLA films. F: total emission spectra at room temperature under N_2 . RTP: delayed emission spectra at room temperature under N_2 . LTP: delayed emission spectra at low temperature (liq. N_2 ; 77K).

Density functional theory was used to evaluate the frontier molecular orbitals.¹⁸ All dyes showed π - π^* electronic character upon excitation. Calculated energy levels are useful to illustrate the relationship between the molecules, as shown in Figure 8.6. Compounds **1-3** showed the desired trend of phosphorescence red-shifting with additional donor groups on the scaffold, but there is no obvious trend in energy levels. According to the calculations, compound **2** has the smallest bandgap, and highest HOMO energy, so it would be expected to have the reddest emission. Clearly, more calculations, possibly of the triplet state energies and orbitals, are required to explain the observed trends.

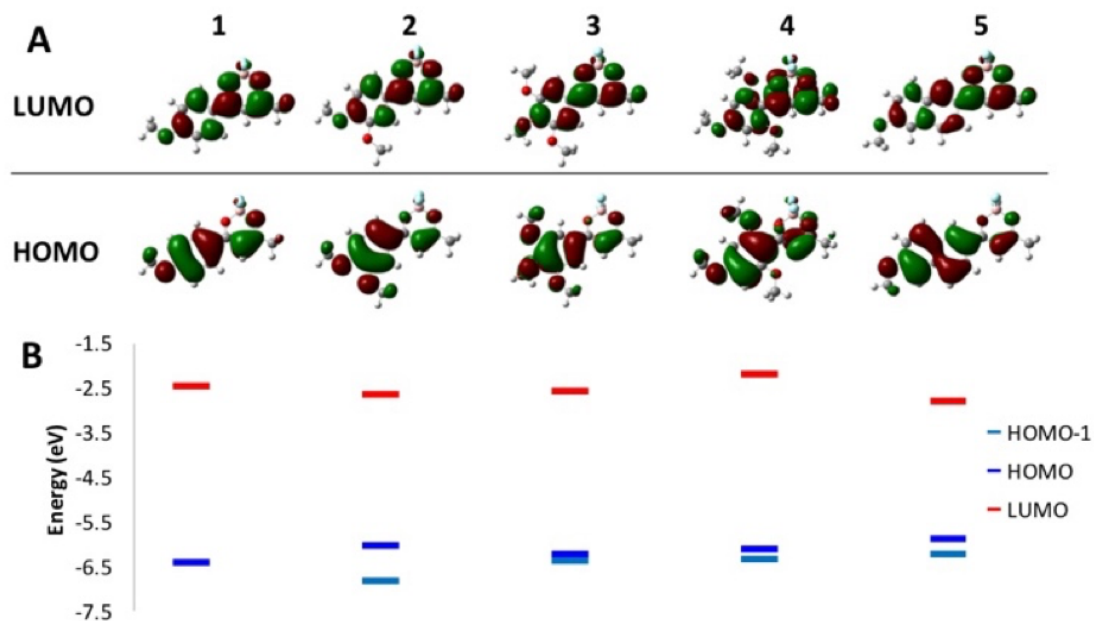


Figure 8.6. Frontier Molecular Orbitals of Difluoroboron β -Diketonates with a Single Aromatic Unit. A) HOMO/LUMO diagrams and B) energy levels of participating orbitals.

Calculations of compound **4** can explain the blue phosphorescence. The aromatic ring is twisted compared to the dioxaborine ring (Figure 8.7). This likely results in a loss of π -conjugation. Also, highly twisted blue emitters are very rare, and very desirable for OLED applications.¹⁹ While this difluoroboron β -diketonate is less realistic for red-phosphorescence oxygen sensing, it is more promising as an emitter for light emitting diodes and electronic devices. The blue phosphorescence and bluer thermally activated delayed fluorescence should be tested in LED devices to evaluate luminescence efficiency.

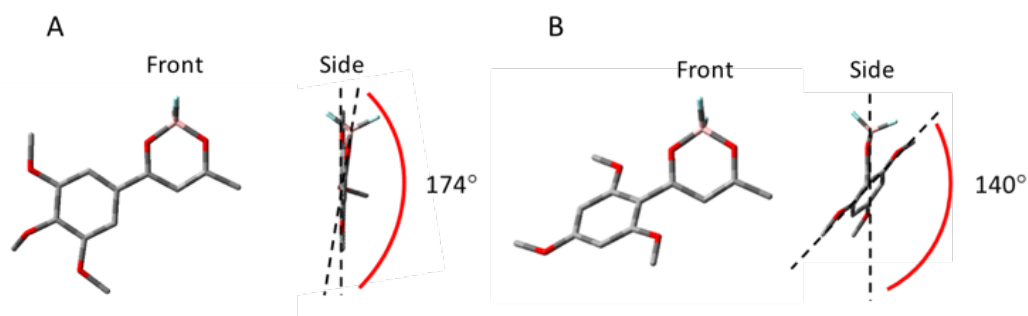


Figure 8.7. Calculated Ground-State Geometries of Compounds **3** (A) and **4** (B).

8.2.5. Calculations for Screening Red-Shifted Difluoroboron β -Diketonates

In the previous set of experiments, we identified that increasing the number of donor substituents on the dye phenyl rings red-shifted the phosphorescence in a controllable way. However, the energy levels did not reflect any trend that could be used for rational, systematic optimization. For the next set of experiments, we considered the effect of donating groups and π -conjugation on the HOMO and the LUMO energies, shown for Jablonski diagrams in Figure 8.8. Assuming that we could selectively alter the HOMO and LUMO energies with substitution and not alter the other energies dramatically, which is a big assumption, we thought it would be more beneficial to raise the energy of the HOMO to red-shift optical properties. Our reasoning is as follows. Previously we employed strategies that lower the LUMO energies, but this often resulted in intramolecular charge transfer (ICT). Dyes with ICT typically have degenerate F and RTP wavelengths, and the RTP is generally weak. However, we hypothesize that raising the HOMO energy will not affect the gap between the singlet and triplet excited states, and fluorescence and phosphorescence peaks would remain isolated.

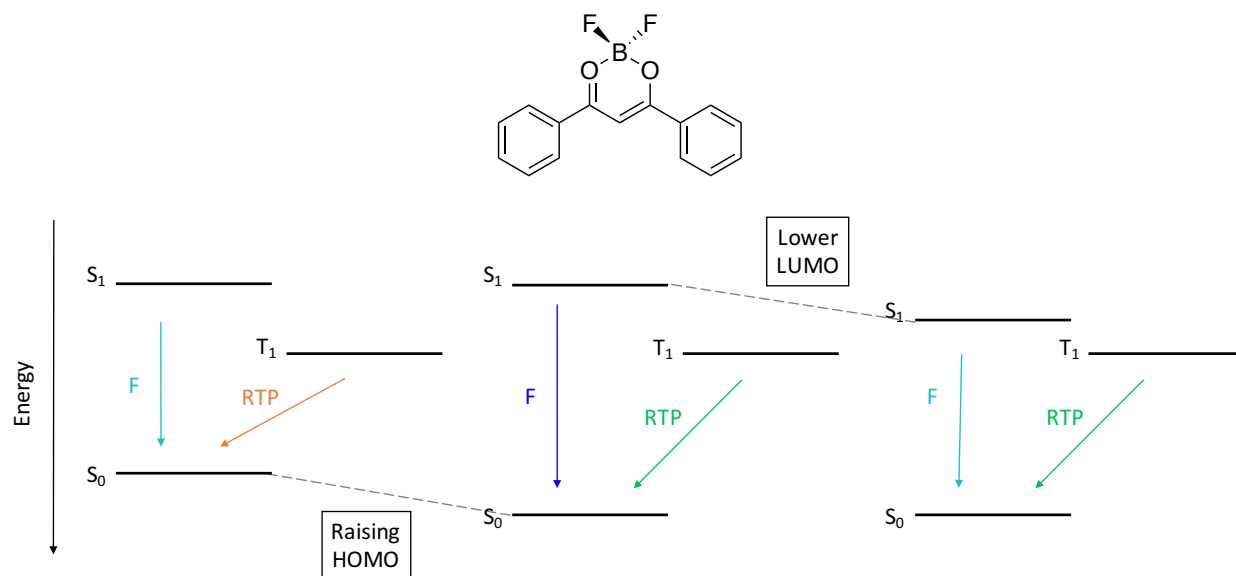


Figure 8.8. Bandgap Engineering Strategy Involving Raising the HOMO Energy (left) or Lowering the LUMO Energy (right) versus the Unsubstituted DBM Dye (center).

With this idea, we performed calculations for many foreseeable combination of commercially available starting points (~60 dye calculations), and used this computationally informed starting point to design, prepare and test new dye derivatives. Some energies are displayed in Figure 8.9. Many derivatives have been made (~35 dyes), but for many dyes in this set, experimental data must still be collected. Selected dyes are shown in Figure 8.9, illustrating dyes with large gaps, small gaps, low LUMOs and high HOMO energies. Further investigation of rationally designed dyes with distinguishing properties predicted by computation is merited.

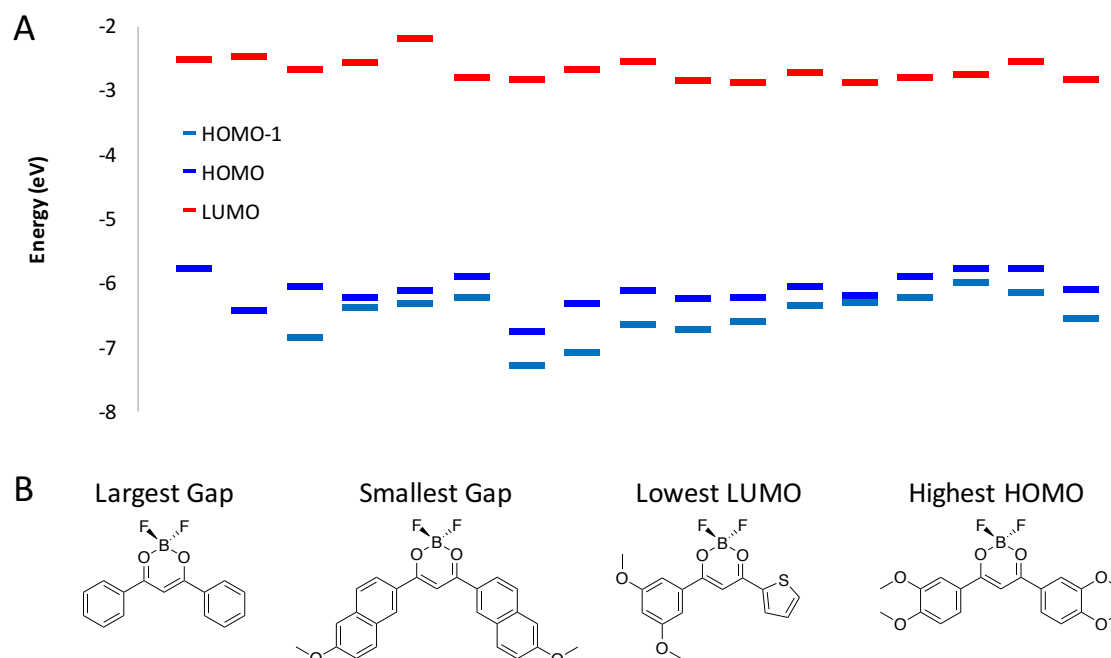


Figure 8.9. Examples of Dual-Emissive Dyes with Emission Peaks Optimized for RGB Imaging.

In general, symmetrical dyes have the highest HOMO energies compared to others. Also, the electronic character is always $\pi-\pi^*$, such as the compound shown in Figure 8.10. In previous reports, these dyes have shown optical properties with spectrally isolated peaks, and red-shifted properties. These dyes should be further pursued based on our previous successes. When the aromatic rings are different, the dye emission is typically ICT in character. Generally, these dyes are not the best for oxygen sensing, given the fluorescence and phosphorescence are close in energy, but recent reports by Chen et al., reveal that ICT transitions can, in fact, also induce strong phosphorescence. Experimental data is still needed to support these calculations, but we hope to build upon a growing body of knowledge reported by our lab and others, to identify clear trends in the optical properties so that we can develop a more targeted approach to difluoroboron β -diketonate dye molecular design.

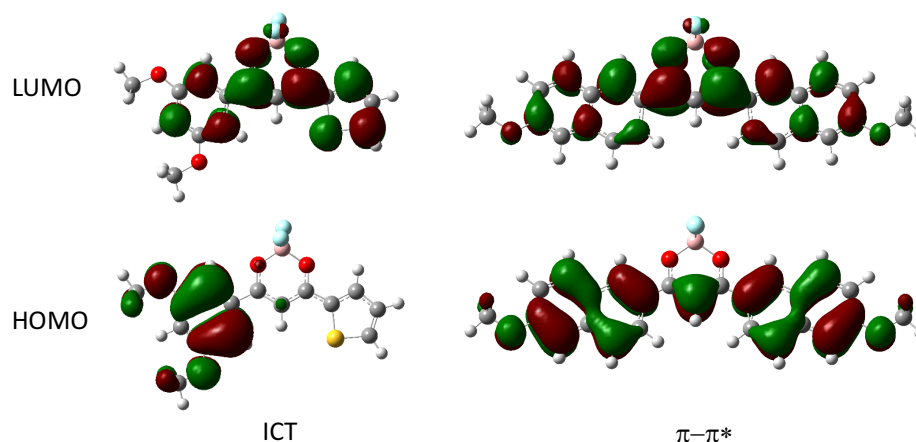


Figure 8.10. Selected Dyes Identified in Computational Screening with Promising Features for Future Investigation. Left = ICT Character dye, Right = π - π^* dye.

8.2.6. Dimethylamino-Substituted Dyes

Another obvious solution to red-shifting the absorption and emission is to increase the donor strength with an amino group. Amino groups are incredibly versatile substituents. There is a large commercial feedstock of functional amines, and substitution is straightforward synthetically.²⁰ To test the effect of amino substitution on optical properties, three derivatives were prepared, where one ring consisted of a para-dimethylamino benzene, in combination with various arene conjugation (e.g. methyl, phenyl and 2-naphthyl) (Figure 8.11). The dyes showed colorful emission in PLA blends with differing dye loading. Emission colors for these three derivatives span from blue-green to red (470–590 nm). It is likely that the stronger donor produced solvatochromic effects,^{21,22} the range of colors may be due to the dye interacting with and reporting on its surroundings. These features can be exploited for polarity and viscosity sensing.

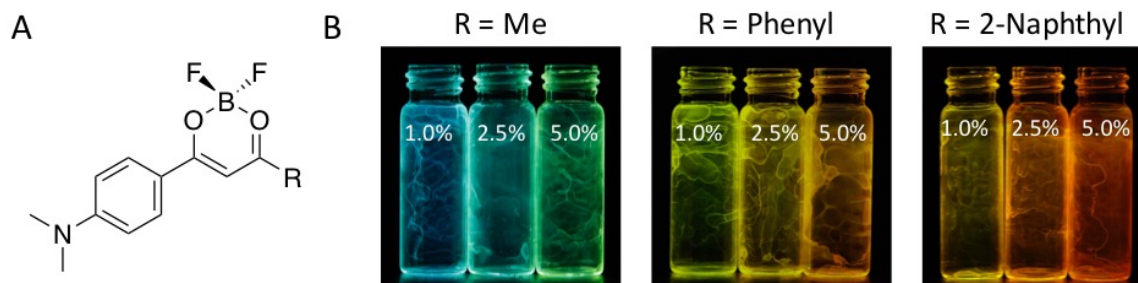


Figure 8.11. Dimethylamino-Substituted Dyes. A) Chemical Structure. B) Images of the Dyes at variable dye loading in PLA (% weight)

However, the geometry of the functional group induces twisted, intramolecular charge transfer (TICT) upon excitation,^{23–25} which destroys the phosphorescence intensity, likely through increased non-radiative decay pathways. While these dyes have bright, colorful emission, the oxygen-sensing capabilities are completely lost. But the environmental sensitive emission can be used for other biological purposes. Environmental-sensitive can be highly useful for studying the physical properties of cells and liposomal materials. Fluorescence solvatochromism can be highly applicable to cell biology, where differences in non-polar domains such as lipid vesicles and membrane bilayers, can have dielectric constants and physical features distinct from other regions and organelles. Polarity and viscosity are two defining factors that markedly influence nutrient delivery, metabolism, and signaling through changes in protein configuration and cell membrane engulfment (endocytosis) or release (exocytosis).

Dimethylamino-substituted dyes designed in our lab show emission enhancement in viscous environments. Chemical structures of the para-dimethylamino phenyl and styryl systems are shown in Figure 8.12. The push-pull electronics of the fluorophore, easily influenced by and highly sensitive to the surroundings, have the potential to sense minute environmental differences.^{26–28} This is demonstrated by comparing the emission color and brightness in different solutions. Methylene chloride is a non-polar, fluid solvent, and thus, the quantum yield is low. In 1,4-dioxane, a non-polar, viscous solution, brightness is enhanced and emission blue shifts.

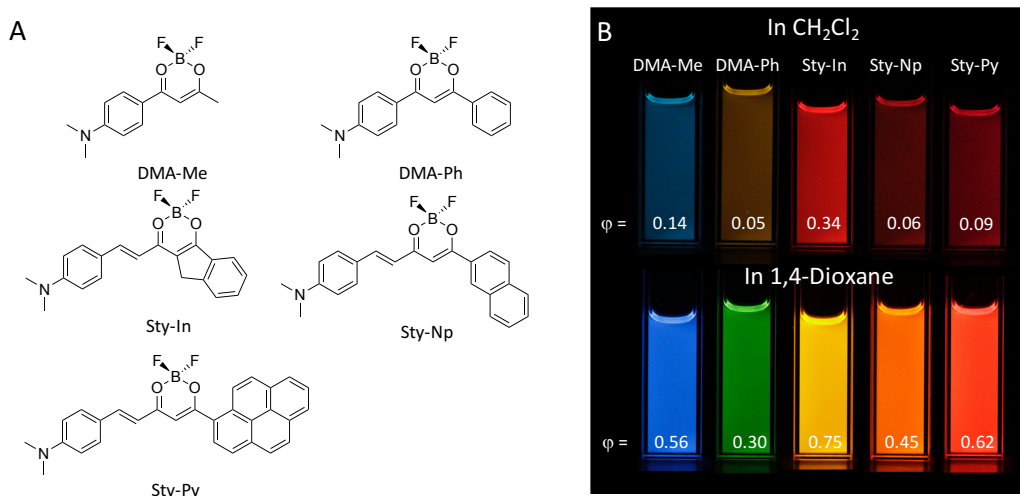


Figure 8.12. Environment-Sensitive Emission from Difluoroboron β -Diketonates. A) Chemical structures and B) Images of the dyes dissolved in CH_2Cl_2 and 1,4-Dioxane ($1 \times 10^{-5} \text{ M}$)

Fluorophores can be applied as wash-free probes, where differences in organelle polarity are expressed in the fluorescence color or intensity.²⁹ Localization can be controlled with affinity groups for organelles or via side chain interactions. Mitochondrial specific lipids such as cardiolipin,³⁰ can be tagged with charged moieties (i.e. triphenyl phosphonium),^{31,32} or charge neutral alkyl chains for liposomal tracking with a morpholine moiety.^{33,34}

8.3. Conclusion

Research the last 5 years on tuning the optical properties of difluoroboron β -diketonates has brought to light many discoveries. The primary goal of preparing optical-oxygen sensors has been achieved and utilized in cells, wounds, and tumors for measuring oxygen levels. Future developments should be driven towards red phosphorescence, in order to improve imaging performance, and compete commercially in the sensor market. Even though red phosphorescence was not achieved, our research efforts on structure-dependence luminescence has yielded many more avenues for research. Most importantly, the presence of thermally-activated delayed fluorescence can be used in electronic applications. There is no doubt that this group of boron dye is fascinating and will be studied for many years to come.

8.4. References

- (1) Wolfbeis, O. S. *BioEssays* **2015**, *37*, 921–928.
- (2) Kerr, C.; DeRosa, C. A.; Daly, M. L.; Zhang, H.; Palmer, G. M.; Fraser, C. L. *Biomacromolecules* **2017**, *18*, 551–561.
- (3) Samonina-Kosicka, J.; Weitzel, D. H.; Hofmann, C. L.; Hendargo, H.; Hanna, G.; Dewhirst, M. W.; Palmer, G. M.; Fraser, C. L. *Macromol. Rapid Commun.* **2015**, *36*, 694–699.
- (4) van Dam, G. M.; Themelis, G.; Crane, L. M.; Harlaar, N. J.; Pleijhuis, R. G.; Kelder, W.; Sarantopoulos, A.; de Jong, J. S.; Arts, H. J.; van der Zee, A. G.; Bart, J.; Low, P. S.; Ntziachristos, V. *Nat Med* **2011**, *17*, 1315–1319.
- (5) Singh, R.; Ho, D.; Lim, L. Y.; Iyer, K. S.; Smith, N. M. *ACS Omega* **2016**, *1*, 1114–1120.
- (6) Xiong, J.; Meng, F.; Wang, C.; Cheng, R.; Liu, Z.; Zhong, Z.; Meins, J. F. Le; Farooque, A.; Chandraiah, G.; Jain, A. K.; Misra, A.; Lecommandoux, S. *J. Mater. Chem.* **2011**, *21*, 5786.
- (7) Gindy, M. E.; Ji, S.; Hoye, T. R.; Panagiotopoulos, A. Z.; Prud'homme, R. K. *Biomacromolecules* **2008**, *9*, 2705–2711.
- (8) Kersey, F. R.; Zhang, G.; Palmer, G. M.; Dewhirst, M. W.; Fraser, C. L. *ACS Nano* **2010**, *4*, 4989–4996.
- (9) Tsuji, H. *Macromol. Biosci.* **2005**, *5*, 569–597.
- (10) Wang, X.; Wolfbeis, O. S. *Chem. Soc. Rev.* **2014**, *43*, 3666–3761.
- (11) Li, Z.; Roussakis, E.; Koolen, P. G. L.; Ibrahim, A. M. S.; Kim, K.; Rose, L. F.; Wu, J.; Nichols, A. J.; Baek, Y.; Birngruber, R.; Apiou-Sbirlea, G.; Matyal, R.; Huang, T.; Chan, R.; Lin, S. J.; Evans, C. L. *Biomed. Opt. Express* **2014**, *5*, 3748–3764.

- (12) Mirochnik, A. G.; Fedorenko, E. V.; Karasev, V. E. *Russ. Chem. Bull.* **2008**, *57*, 1190–1193.
- (13) Zhang, G.; Fiore, G. L.; Clair, T. L. S.; Fraser, C. L. *Macromolecules* **2009**, *42*, 3162–3169.
- (14) Lee, S. Y.; Yasuda, T.; Yang, Y. S.; Zhang, Q.; Adachi, C. *Angew. Chem. Int. Ed.* **2014**, *126*, 6520–6524.
- (15) Zhang, P.; Dou, W.; Ju, Z.; Yang, L.; Tang, X.; Liu, W.; Wu, Y. *Org. Electron.* **2013**, *14*, 915–925.
- (16) Daly, M. L.; DeRosa, C. A.; Kerr, C.; Morris, W. A.; Fraser, C. L. *RSC Adv.* **2016**, *6*, 81631–81635.
- (17) Ye, J.-W.; Zhou, H.-L.; Liu, S.-Y.; Cheng, X.-N.; Lin, R.-B.; Qi, X.-L.; Zhang, J.-P.; Chen, X.-M. *Chem. Mater.* **2015**, *27*, 8255–8260.
- (18) Frisch, M. J.; Trucks, G. W.; Schlegel, H. B.; Scuseria, G. E.; Robb, M. A.; Cheeseman, J. R.; Scalmani, G.; Barone, V.; Mennucci, B.; Petersson, G. A. . et al. *Gaussian 09 Revision A.1*; Gaussian, Inc.: Wallingford, CT. 2009.
- (19) Reineke, S. *Nat. Photonics* **2014**, *8*, 269–270.
- (20) Grimm, J. B.; English, B. P.; Chen, J.; Slaughter, J. P.; Zhang, Z.; Revyakin, A.; Patel, R.; Macklin, J. J.; Normanno, D.; Singer, R. H.; Lionnet, T.; Lavis, L. D. *Nat. Methods* **2015**, *12*, 244–250.
- (21) Jangwon, S.; Kim, S.; Park, S. Y. *J. Am. Chem. Soc.* **2004**, *126*, 11154–11155.
- (22) Kubota, Y.; Ozaki, Y.; Funabiki, K.; Matsui, M. *J. Org. Chem.* **2013**, *78*, 7058–7067.
- (23) Li, J.; Qian, Y.; Xie, L.; Yi, Y.; Li, W.; Huang, W. *J. Phys. Chem. C* **2015**, *119*, 2133–2141.

- (24) Sasaki, S.; Drummen, G. P. C.; Konishi, G. *J. Mater. Chem. C* **2016**, *4*, 2731–2743.
- (25) Haidekker, M. A.; Theodorakis, E. A. *Org. Biomol. Chem.* **2007**, *5*, 1669–1678.
- (26) Liu, H.; Xu, X.; Shi, Z.; Liu, K.; Fang, Y. *Anal. Chem.* **2016**, *88*, 10167–10175.
- (27) Reichardt, C. *Chem. Rev.* **1994**, *94*, 2319–2358.
- (28) Dell'Acqua, M.; Ronda, L.; Piano, R.; Pellegrino, S.; Clerici, F.; Rossi, E.; Mozzarelli, A.; Gelmi, M. L.; Abbiati, G. *J. Org. Chem.* **2015**, *80*, 10939–10954.
- (29) Pitter, D. R. G.; Brown, A. S.; Baker, J. D.; Wilson, J. N. *Org. Biomol. Chem.* **2015**, *13*, 9477–9484.
- (30) Chicco, A. J.; Sparagna, G. C. *Am. J. Physiol. - Cell Physiol.* **2007**, *292*, C33–C44.
- (31) Maftah, A.; Petit, J. M.; Ratinaud, M.-H.; Julien, R. *Biochem. Biophys. Res. Commun.* **1989**, *164*, 185–190.
- (32) Wang, X.-H.; Peng, H.-S.; Yang, L.; You, F.-T.; Teng, F.; Hou, L.-L.; Wolfbeis, O. S. *Angew. Chem. Int. Ed.* **2014**, *53*, 12471–12475.
- (33) Liu, T.; Xu, Z.; Spring, D. R.; Cui, J. *Org. Lett.* **2013**, *15*, 2310–2313.
- (34) Yu, H.; Xiao, Y.; Jin, L. *J. Am. Chem. Soc.* **2012**, *134*, 17486–17489.

Appendix A:

Supporting Information to Chapter 2

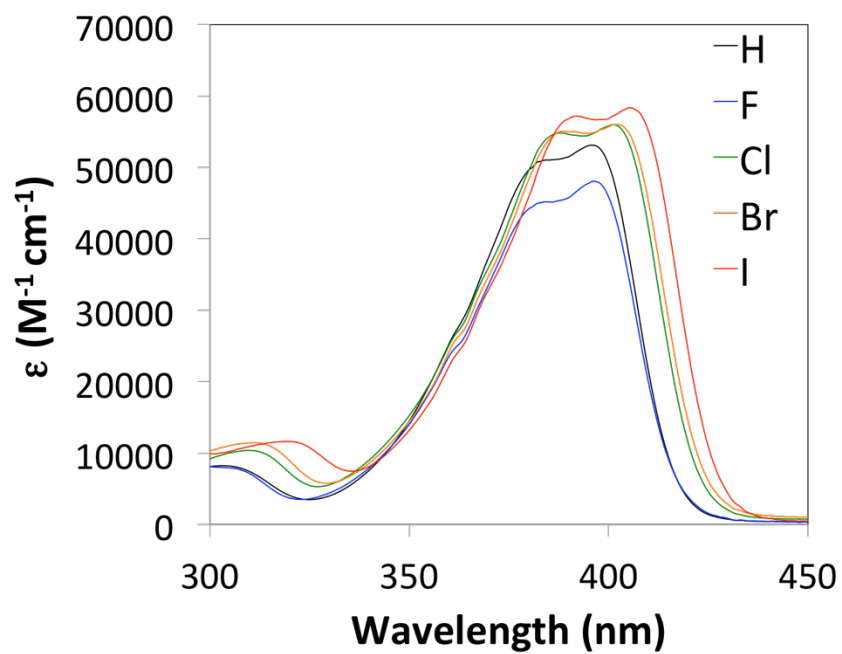


Figure S2.1. Absorbance spectra of dye initiators (6-10) in CH_2Cl_2 (Concentration = $1.0 \times 10^{-5} \text{ M}$).

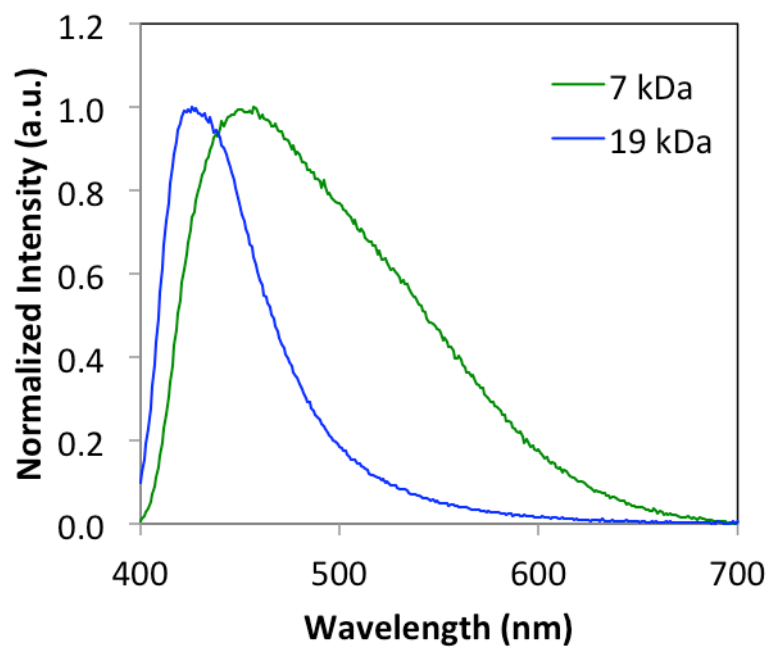


Figure S2.2. Total emission in air of BF₂dbmPLA (**11**) at different molecular weights ($\lambda_{\text{ex}} = 369$ nm).

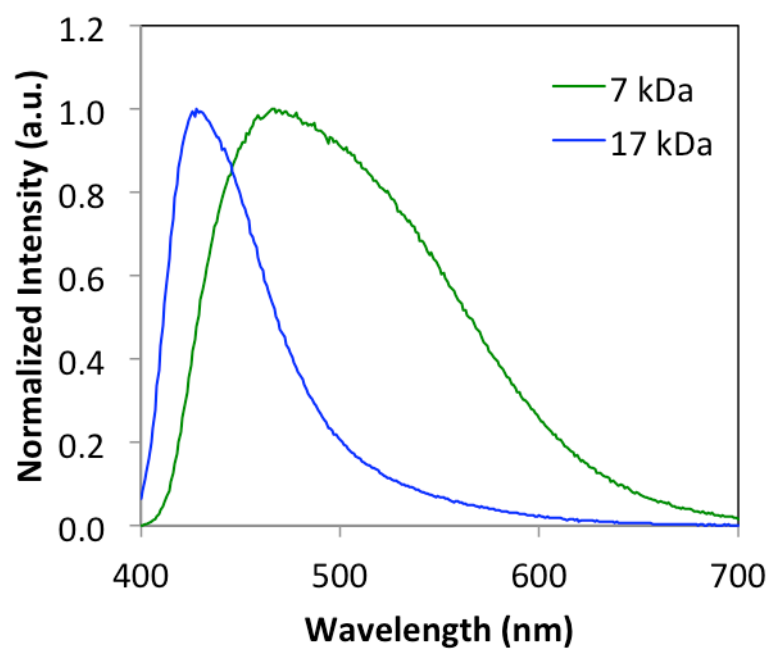


Figure S2.3. Total emission in air of BF₂dbm(Cl)PLA (**13**) at different molecular weights ($\lambda_{\text{ex}} = 369$ nm).

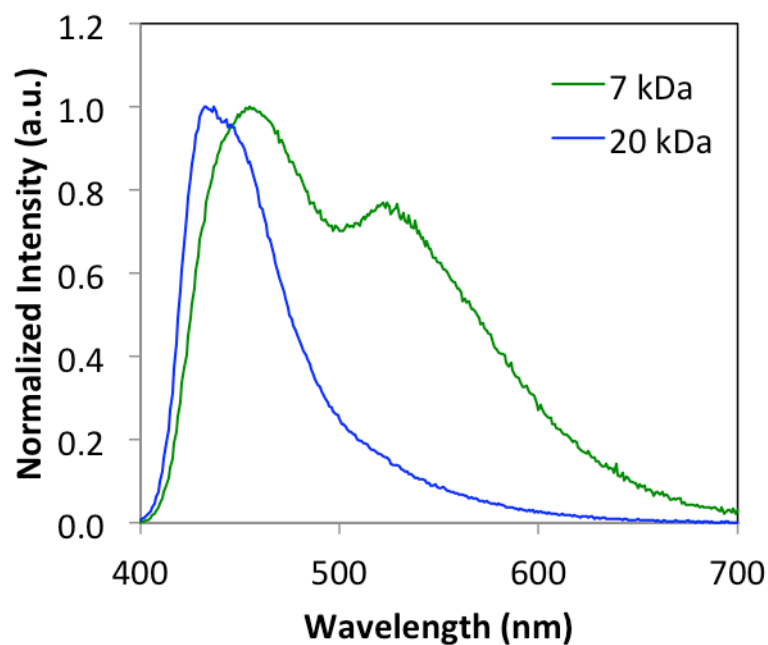


Figure S2.4. Total emission in air of BF₂dbm(I)PLA (**15**) at different molecular weights (λ_{ex} = 369 nm).

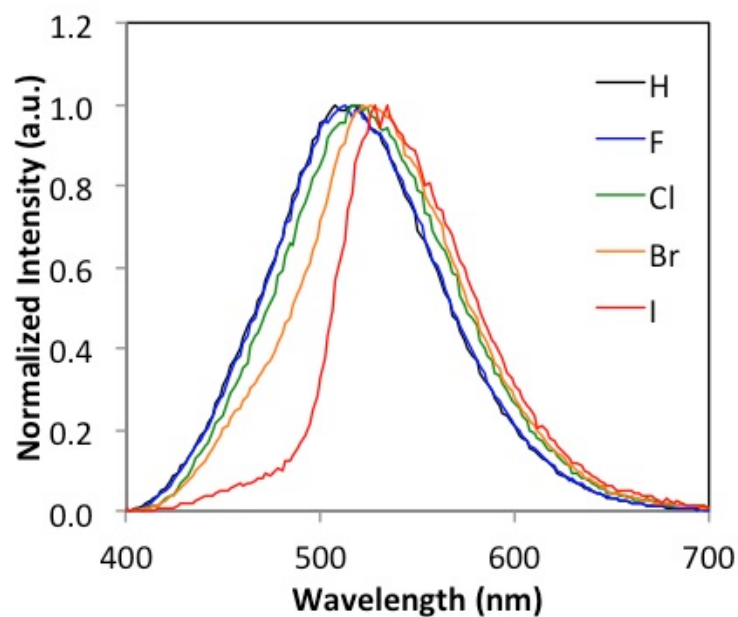


Figure S2.5. Phosphorescence of high molecular weight BF₂dbm(X)PLA polymer films (**11b-15b**) Delayed emission spectra of films (excitation = xenon flash lamp with 2 ms delay).

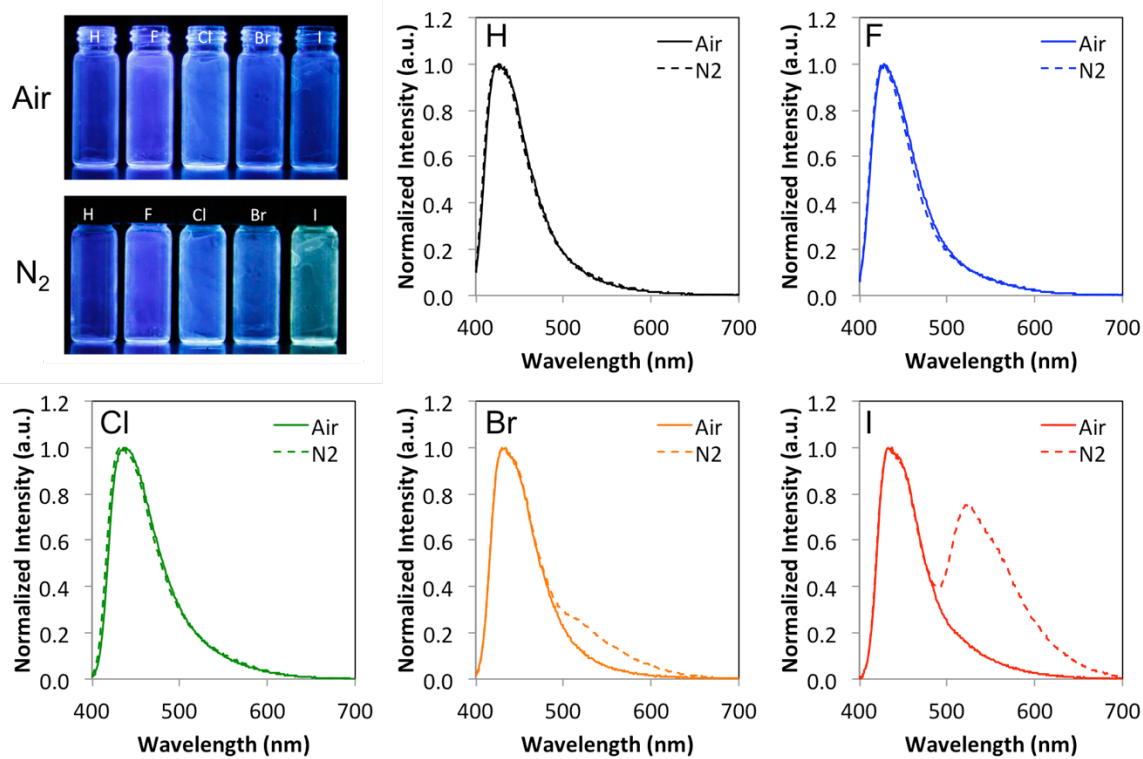


Figure S2.6. Images and total emission spectra of high molecular weight polymer films (**11b-15b**) under air and nitrogen ($\lambda_{\text{ex}} = 369$ nm).

Appendix B:

Supporting Information to Chapter 3

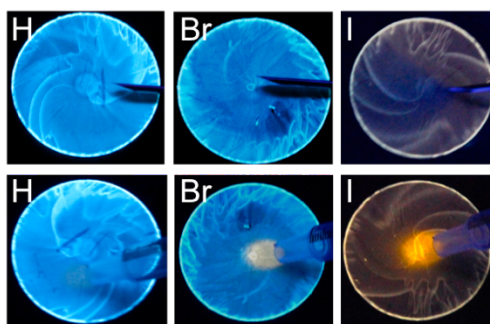


Figure S3.1. Images of spin-cast films used in photostability tests and their response to low flow gases, O₂ (top) and N₂ (bottom).

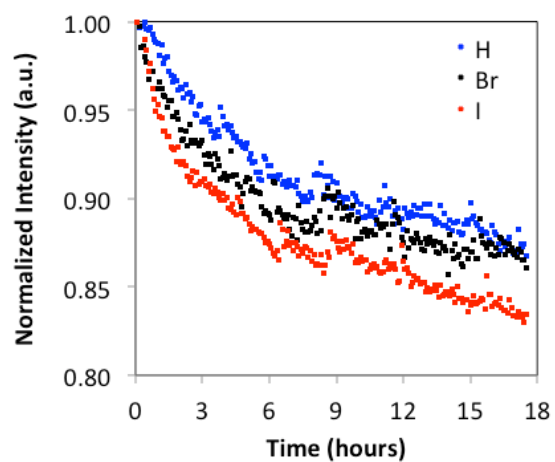


Figure S3.2. Photostability plot for BF₂nbm(X)PLA spin-cast films.

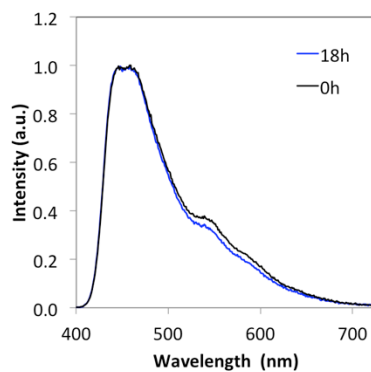


Figure S3.3. Total emission under N_2 of **HP** before (0 h) and after (18 h) photobleaching.

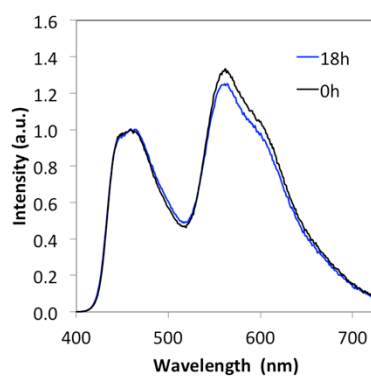


Figure S3.4. Total emission under N_2 of **BrP** before (0 h) and after (18 h) photobleaching.

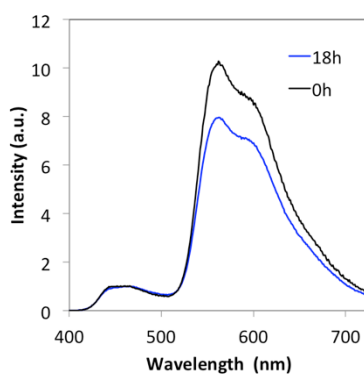


Figure S3.5. Total emission under N_2 of **IP** before (0 h) and after (18 h) photobleaching.

Table S3.1. Optical Properties of Boron Dye Initiators and Polymers in CH_2Cl_2

Sample		λ_{abs}^a (nm)	ε^b (M ⁻¹ cm ⁻¹)	λ_{em}^c (nm)	τ_F^d (ns)	Φ_F^e
BF ₂ nbmOH		414	59 000	452	1.55	0.40
BF ₂ nbmPLA	HP	414	53 200	456	1.54	0.40
BF ₂ nbm(Br)OH		417	65 000	448	0.53	0.19
BF ₂ nbm(Br)PLA	BrP	417	60 400	448	0.49	0.20
BF ₂ nbm(I)OH		419	66 100	444	0.20	0.05
BF ₂ nbm(I)PLA	IP	419	62 500	445	0.20	0.05

^aAbsorption maxima. ^bExtinction coefficients calculated at the absorption maxima. ^cFluorescence emission maxima excited at 369 nm. ^dFluorescence lifetime excited with a 369 nm light-emitting diode (LED) monitored at the emission maximum. All fluorescence lifetimes are fitted with single-exponential decay. ^eRelative quantum yield,

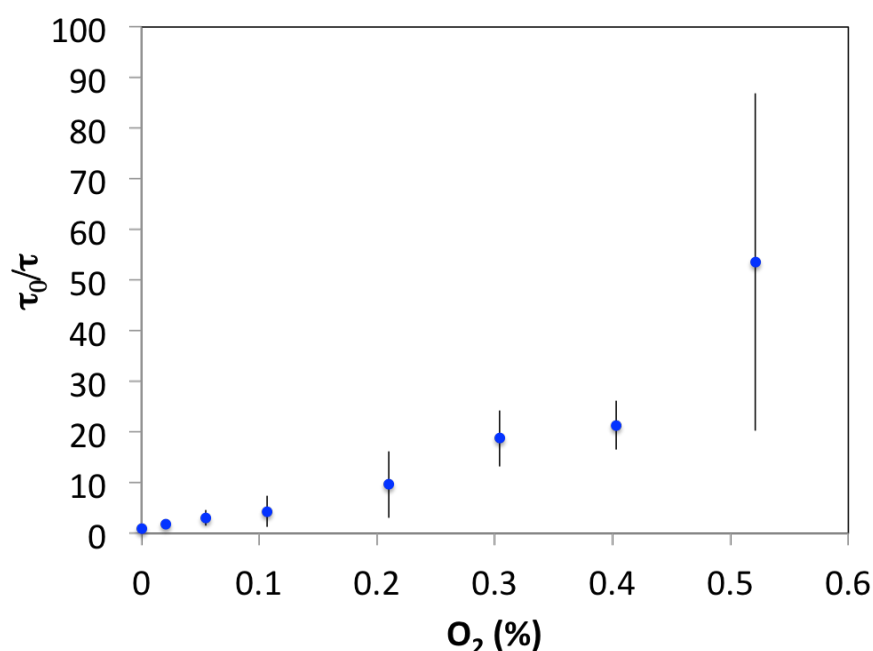


Figure S3.6. Lifetime Stern-Volmer plot for BF₂nbmPLA nanoparticles (**H-NP**) n = 3.

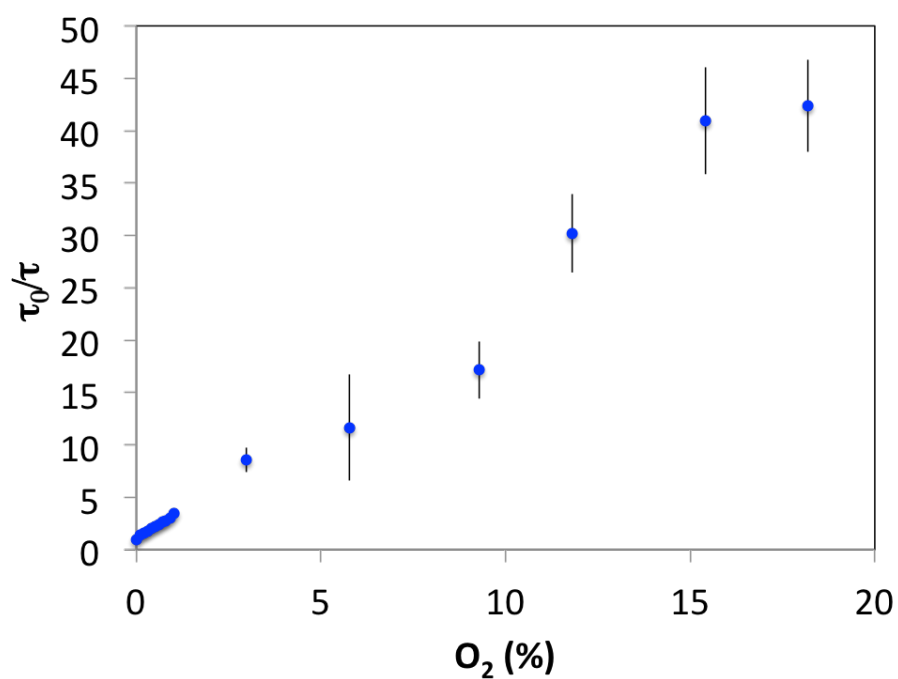


Figure S3.7. Lifetime Stern-Volmer plot of BF₂nbm(Br)PLA nanoparticles (**Br-NP**) (n = 3).

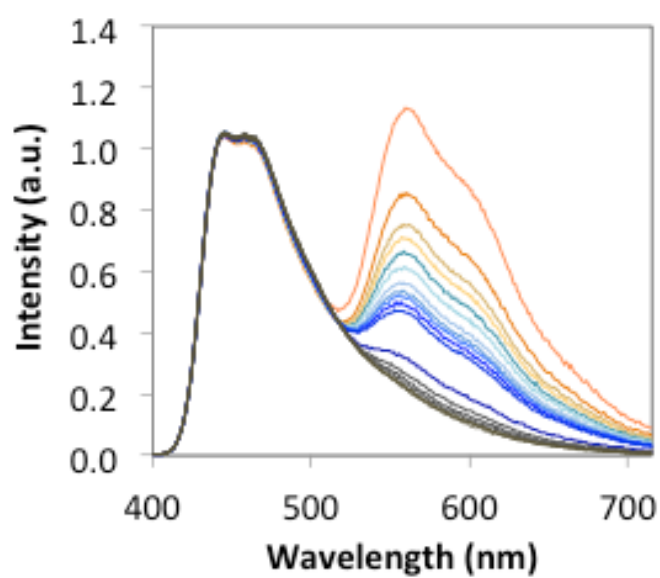


Figure S3.8. Ratiometric calibration and F/P Stern-Volmer plot of BF₂nbm(Br)PLA nanoparticles (**Br-NP**).

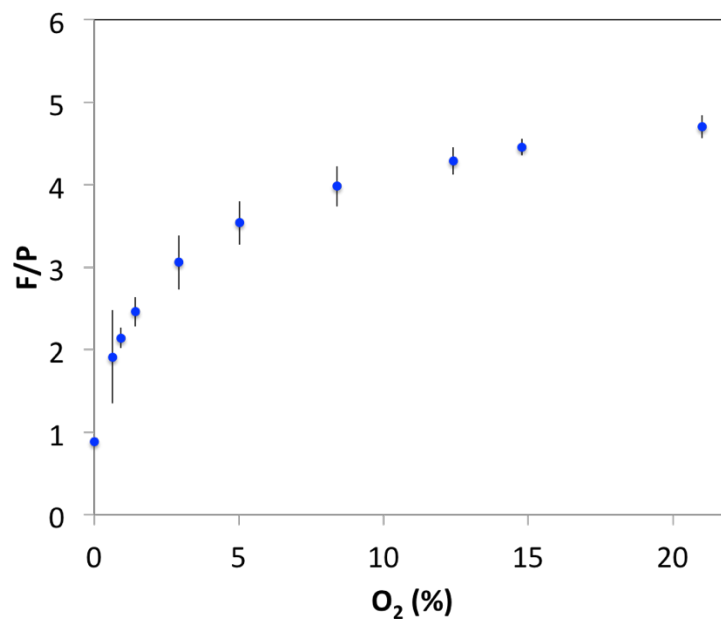


Figure S3.9. Br-NP Ratiometric Oxygen Calibration. Stern-Volmer (F/P) plot displayed as referenced intensity (RI; fluorescence and phosphorescence peaks from the total emission spectra) ($n = 3$).

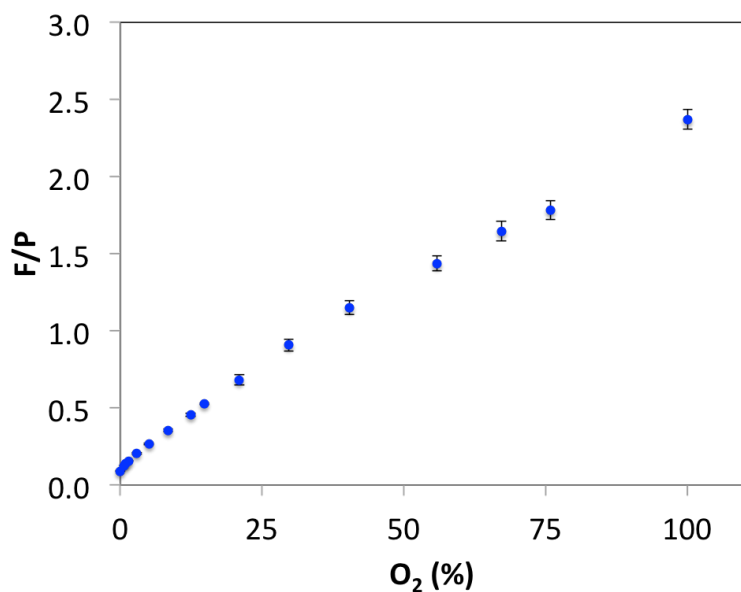


Figure S3.10. Stern-Volmer F/P ratiometric calibration of BF₂nbm(I)PLA nanoparticles (I-NP) from 0-100% oxygen ($n = 3$).

Table S3.2. Oxygen Sensing Characteristics of Nanoparticles

Sample		K_{SV}^a (O ₂ %) ⁻¹	Lower LOD ^b (%)	Upper LOD ^c (%)
BF ₂ nbmPLA	H-NP	50.87 ^d	0.01 ^d	0.75 ^d
BF ₂ nbm(Br)PLA	Br-NP	2.058 ^d	0.05 ^d	21.0 ^d
		1.875 ^e	0.05 ^e	21.0 ^e
BF ₂ nbm(I)PLA	I-NP	0.024 ^e	0.50 ^e	100 ^e

^a Single site Stern-Volmer quenching constant per percent O₂. $(F/P_0 \div F/P)/\%O_2 = P/P_0$ per % O₂, where P = phosphorescence intensity and $K_{SV} = P/P_0$. ^b Estimated lower limit of detection defined as $\tau/\tau_0 = 0.99$ (i.e. when 1% of phosphorescence is quenched). ^c Estimated upper limit of detection defined as $\tau/\tau_0 = 0.01$ (i.e. when 99% of phosphorescence is quenched). ^d Values based on lifetime calibration data. ^e Values based on ratiometric calibration data.

Appendix C:

Supporting Information to Chapter 4

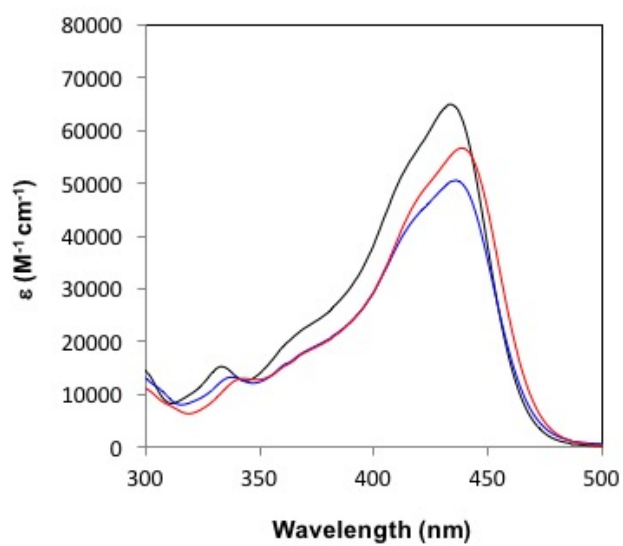


Figure S4.1. Absorption spectra of boron complexes **4-6** in CH_2Cl_2 (Optical Density < 0.1).

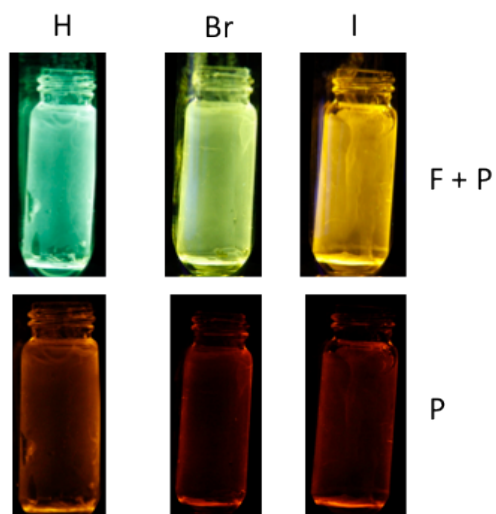


Figure S4.2. Images of polymers **7b** (H), **8b** (Br), and **9b** (I), in liquid nitrogen (77K) with lamp on (F + P) and lamp off (P).

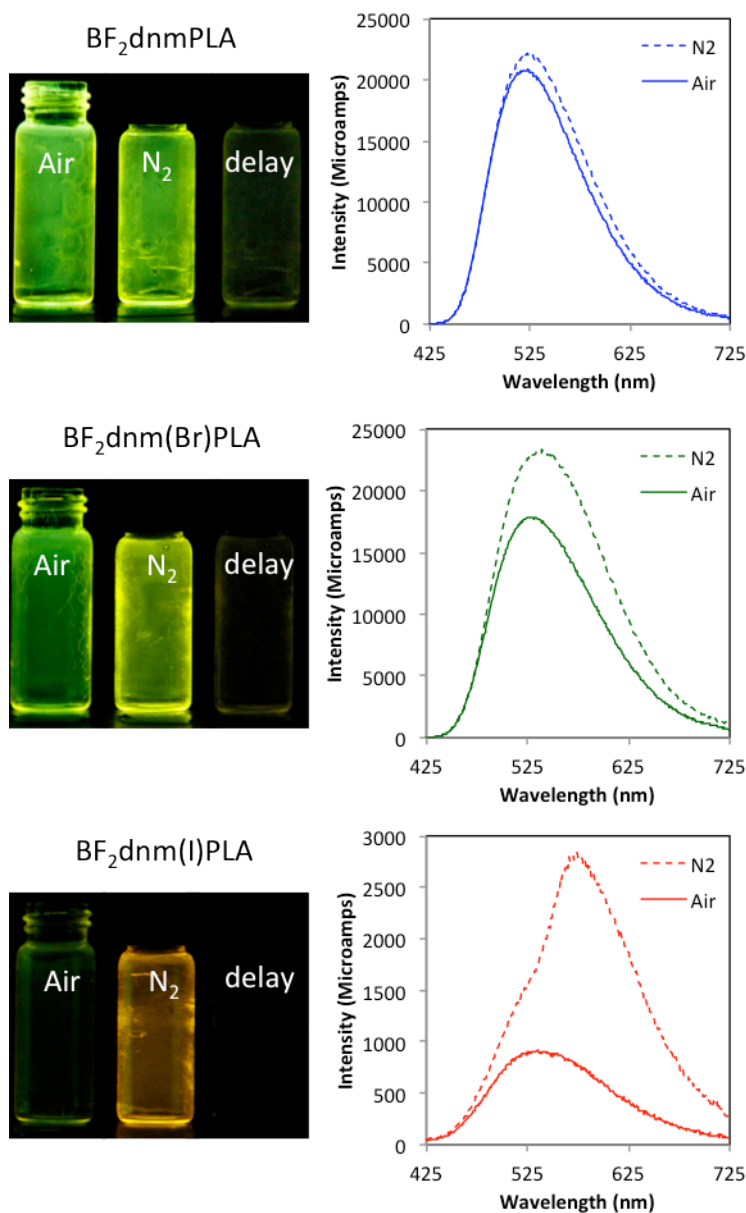


Figure S4.3. Images and total emission spectra of boron polymers BF_2dnmPLA (7a), $\text{BF}_2\text{dnm(Br)PLA}$ (8a), and $\text{BF}_2\text{dnm(I)PLA}$ (9a) in air and N_2 . Photographs were taken with UV lamp excitation ($\lambda_{\text{max}} = 354 \text{ nm}$); delayed emission images (i.e. delay) were captured after the UV lamp was turned off.

Table S4.1. Boron Dye PLA Blend Preparation

Blend	Dye-PLA	Dye-PLA (mg)	PLA ^a (mg)	Dye % (w/w)
7c	7a	2.0	7.0	1.0
8c	8a	2.0	8.2	1.0
9c	9a	2.0	9.0	1.0
9d	9b	2.0	10.0	0.5
9e	9b	2.0	30.0	0.2

^a Linear PLA M_n = 13,800 PDI = 1.03 (GPC).

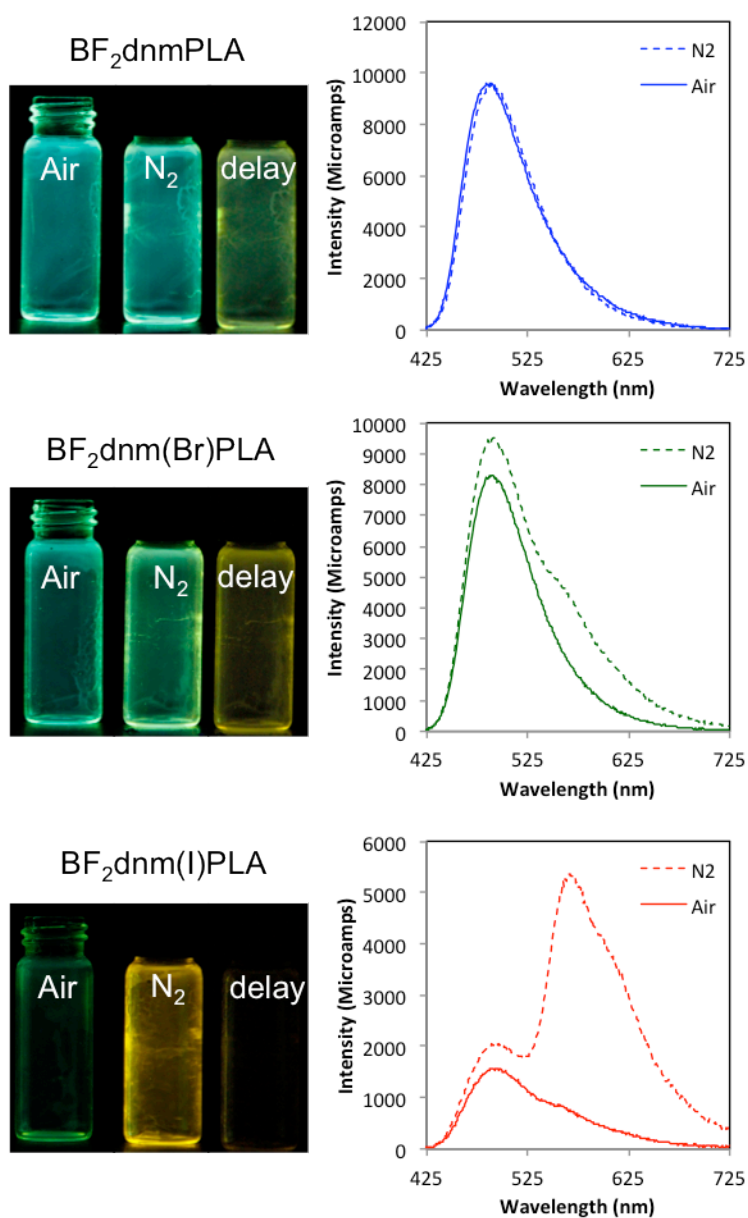


Figure S4.4. Images and total emission spectra of boron polymers BF_2dnmPLA (**7c**), $\text{BF}_2\text{dnm(Br)PLA}$ (**8c**), and $\text{BF}_2\text{dnm(I)PLA}$ (**9c**) in air and N_2 . Photographs were taken with UV lamp excitation ($\lambda_{\text{max}} = 354 \text{ nm}$); delayed emission images (i.e. delay) were captured after the UV lamp was turned off.

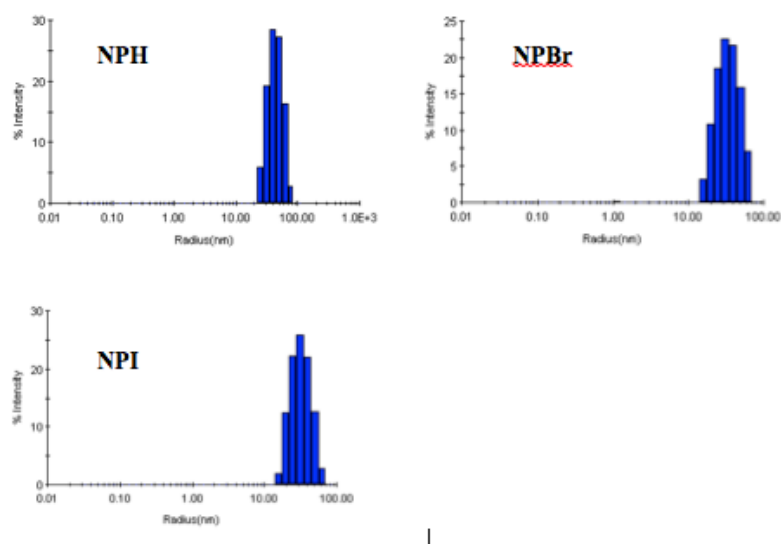


Figure S4.5. Size distribution of nanoparticles via dynamic light scattering. \

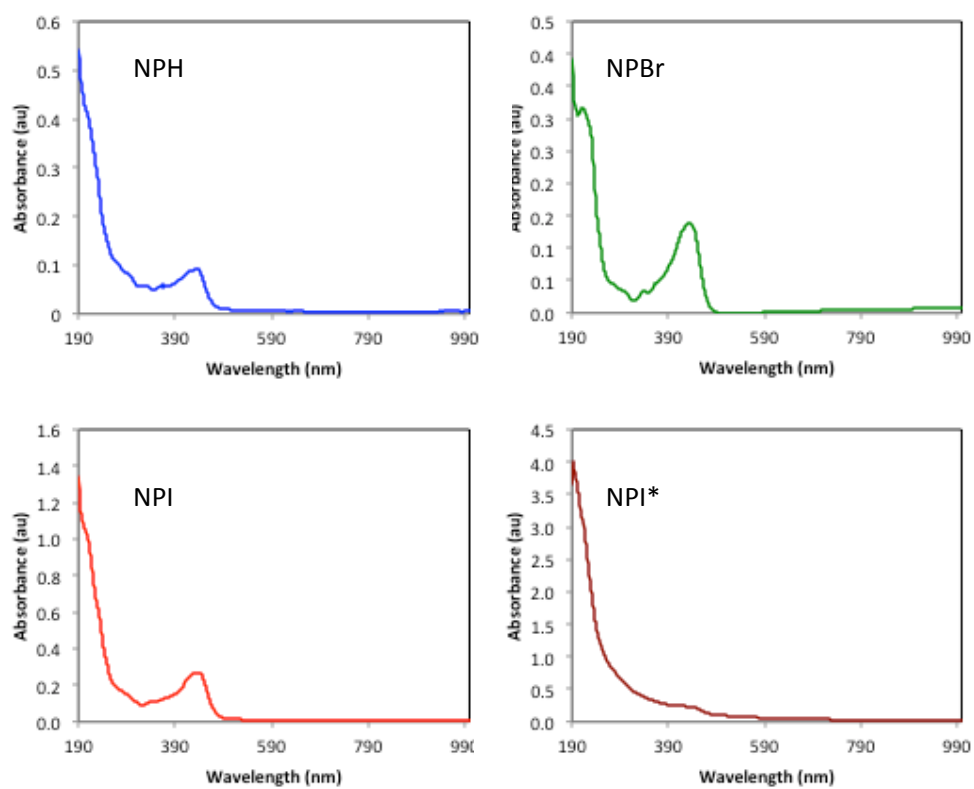


Figure S4.6. Absorbance spectra of BNPs in water (OD ~0.1 - 0.3).

Appendix D:

Supporting Information to Chapter 5

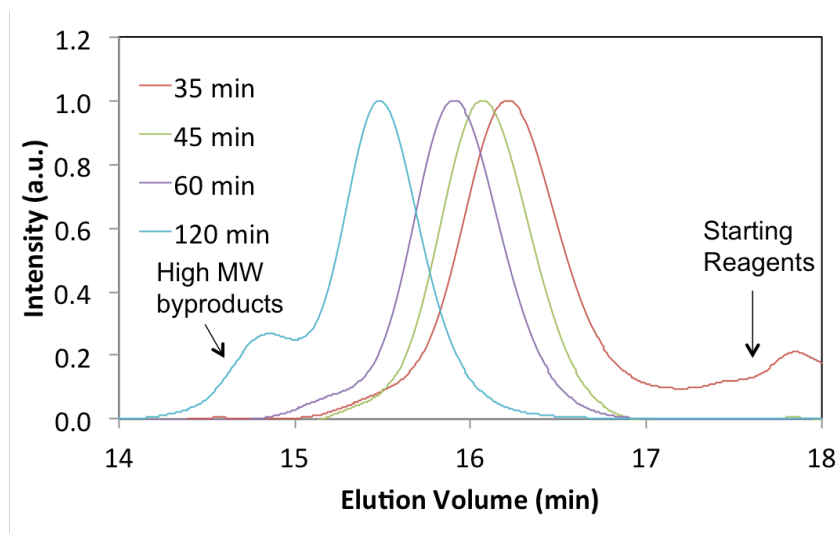


Figure S5.1. GPC traces of $\text{BF}_2\text{tbm(I)PLA}$ (**6**) with 100 equivalents of lactide at different times. Elution traces of the changes in refractive indices (dRI) of the polymers.

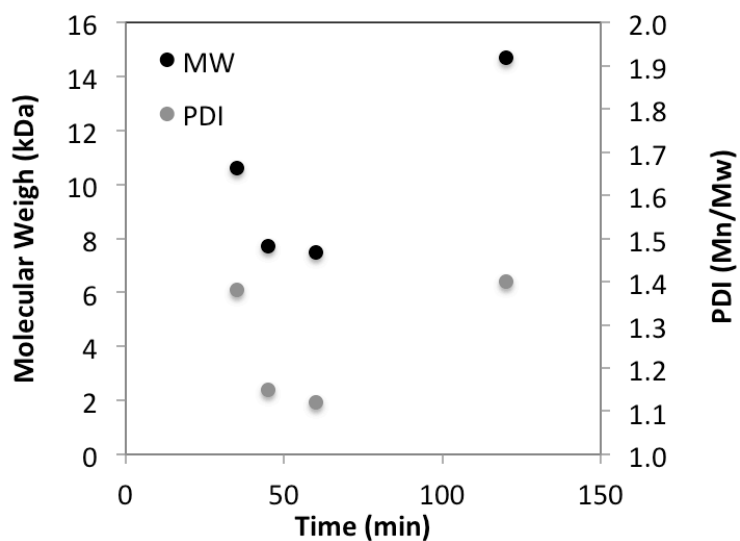


Figure S5.2. Reaction kinetics of $\text{Sn}(\text{oct})_2$ catalyzed polymerization of lactide from $\text{BF}_2\text{tbm(I)OH}$ (**6**) with 100 equivalents

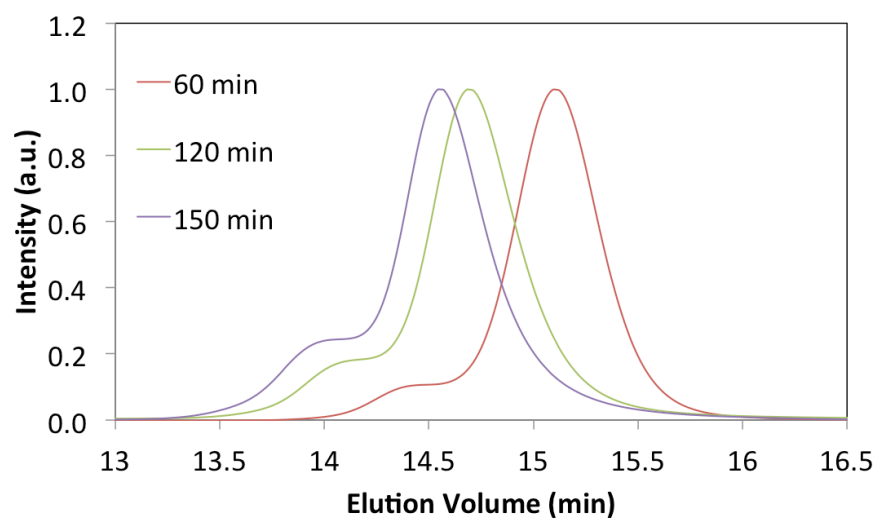


Figure S5.3. GPC traces of $\text{BF}_2\text{tbm(I)PLA}$ (**6**) with 200 equivalents of lactide at different reaction times. Elution traces of the changes in refractive indices (dRI) of the polymers.

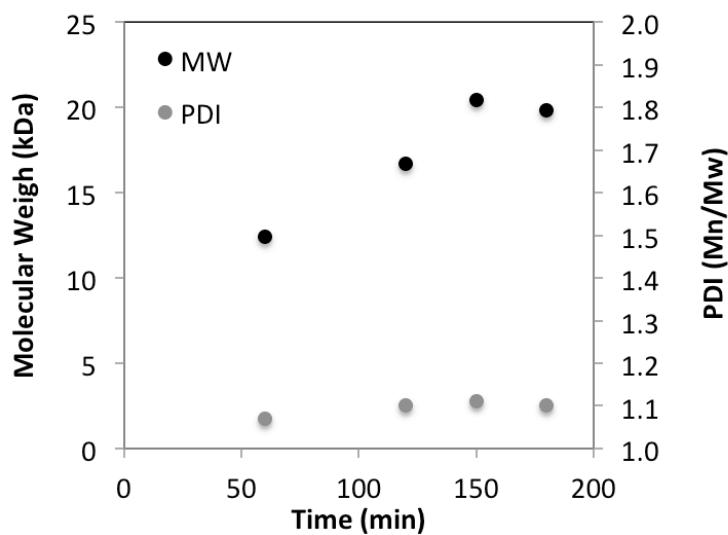


Figure S5.4. Reaction kinetics of $\text{Sn}(\text{oct})_2$ catalyzed polymerization of lactide from $\text{BF}_2\text{tbm(I)OH}$ (**6**) with 200 equivalents of lactide

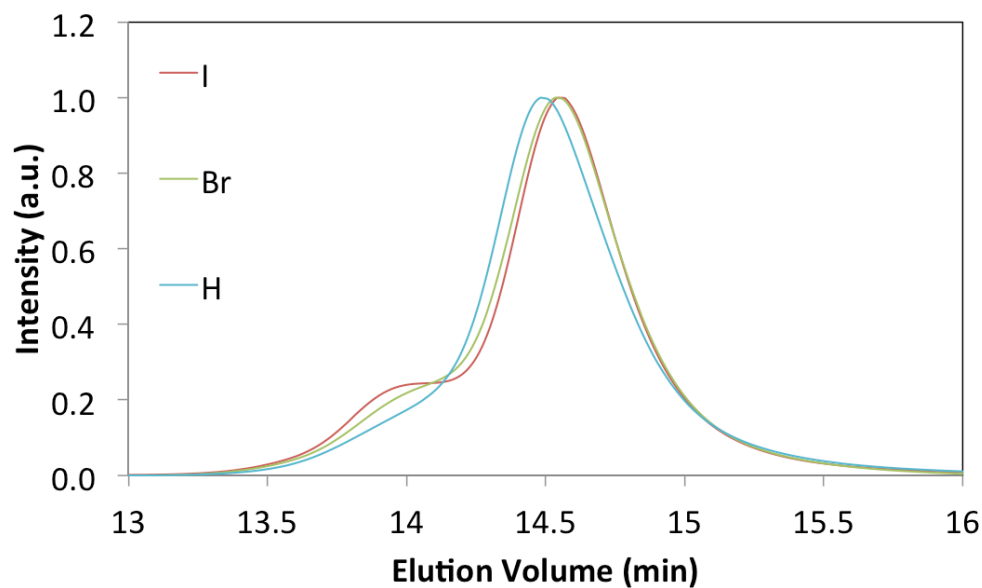


Figure S5.5. GPC elution traces of the changes in refractive indices (dRI) of the thienyl boron dye polymers used for fluorescence characterization.

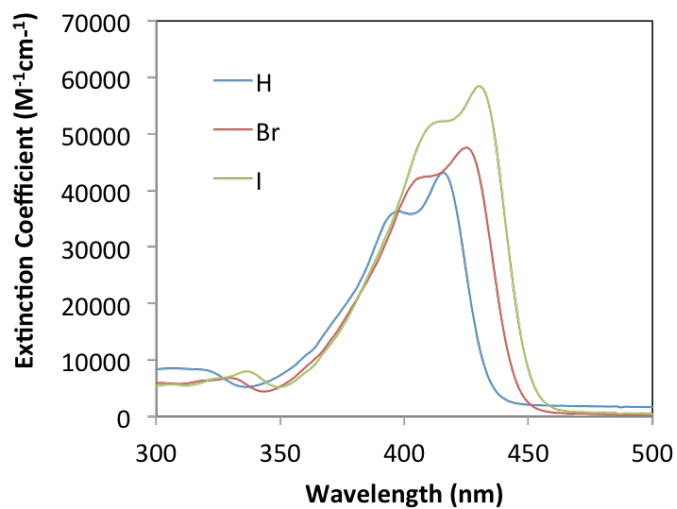


Figure S5.6. Heavy atom dependence of absorbance spectra of boron dye initiators conjugates (concentration; $M = 1.0 \times 10^{-5}$), BF_2tbmOH (**4**); $\text{BF}_2\text{tbm}(\text{Br})\text{OH}$ (**5**); $\text{BF}_2\text{tbm}(\text{I})\text{OH}$ (**6**).

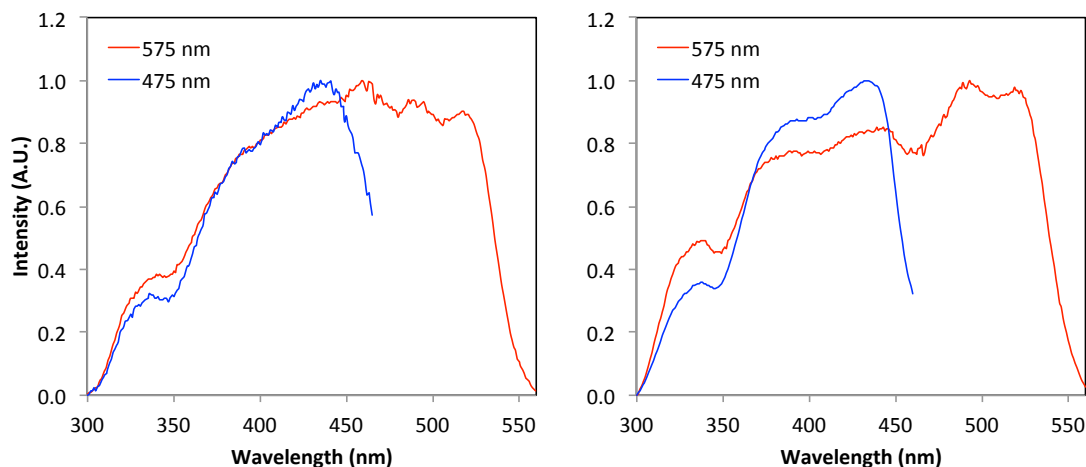


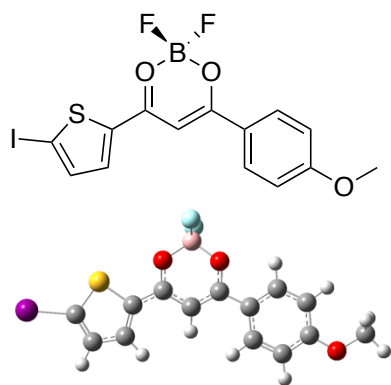
Figure S5.7. Excitation spectra of BF₂tbm(Br)PLA (**8**; left) and BF₂tbm(I)PLA (**9**; right) monitored at different regions on the fluorescence spectra (blue line = 475 nm and red line = 575 nm).

Table S1. Optical Properties of Toluene Cast Polymer Films of BF₂tbm(I)PLA.

BF ₂ tbm(I)PLA		Loading ^a (%)	λ_F^b (nm)	τ_F^c (ns)	λ_p^d (nm)	τ_p^e (ms)
20 kDa	9	2.3	465	0.24	586	1.7
			575	1.51 ^g		
20kDa+PLA ^f	9*	1.0	474	0.34	579	2.3
			533	1.40 ^g		

^aDye concentration by total mass. ^bSteady-state fluorescence spectra emission maximum under air ($\lambda_{ex} = 385$ nm). ^cFluorescence lifetime excited with a 369 nm light-emitting diode (LED) monitored at the emission maximum. ^dDelayed emission spectra maxima under N₂ ($\lambda_{ex} = 385$ nm). ^ePre-exponential weighted RTP lifetime.

Computational Data:



E = -1399.79476750 a.u

Dipole Moment = 11.0523 Debye

B, -1.194905, 2.592006, 0.011488

F, -1.196014, 3.130162, 1.30189

F, -1.175815, 3.590479, -0.952211

O, -2.421629, 1.77317, -0.171394
 C, -2.438844, 0.46947, -0.014033
 C, -1.236554, -0.236391, 0.126323
 H, -1.237927, -1.30383, 0.284627
 O, 0.021521, 1.745885, -0.154688
 C, -0.022221, 0.442455, 0.005163
 C, 1.264261, -0.218685, 0.019711
 C, 1.557655, -1.571817, 0.080118
 S, 2.729995, 0.739508, -0.046272
 C, 2.946676, -1.846218, 0.077272
 H, 0.802824, -2.349195, 0.120137
 C, 3.697857, -0.692046, 0.012504
 H, 3.368538, -2.843235, 0.118744
 I, 5.802089, -0.579129, -0.01977
 C, -3.760937, -0.152894, -0.018821
 C, -3.935645, -1.556747, -0.026153
 C, -4.912027, 0.659318, -0.016934
 C, -5.201218, -2.115877, -0.026823
 H, -3.079572, -2.222345, -0.044266
 C, -6.189675, 0.109028, -0.015554
 H, -4.799454, 1.737643, -0.009904
 C, -6.342724, -1.288572, -0.019859
 H, -5.33538, -3.193002, -0.037159
 H, -7.050567, 0.766717, -0.008468
 O, -7.533818, -1.928713, -0.019494
 C, -8.743118, -1.158141, -0.019239
 H, -8.806775, -0.532565, -0.916167
 H, -9.552362, -1.888381, -0.021281
 H, -8.808529, -0.535913, 0.879892

Excitation energies and oscillator strengths:

Excited State 1: Singlet-A 2.9295 eV 423.23 nm

f=1.2990 <S2>=0.000**

82 -> 83 0.70549

Excited State 2: Singlet-A 3.5645 eV 347.83 nm

f=0.0518 <S2>=0.000**

81 -> 83 0.69534

Excited State 3: Singlet-A 3.8958 eV 318.25 nm

f=0.0095 <S2>=0.000**

80 -> 83 0.68460

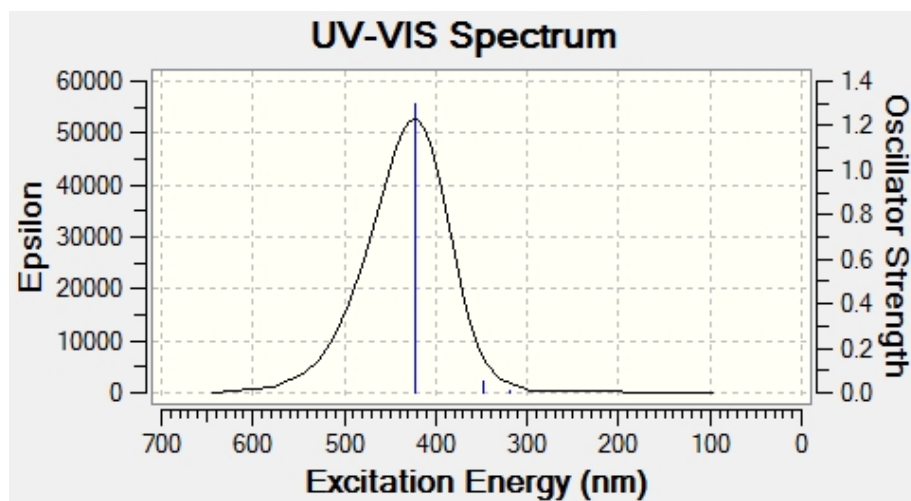
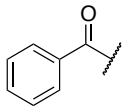
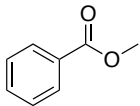
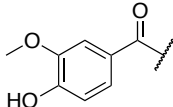
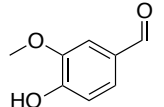
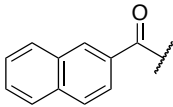
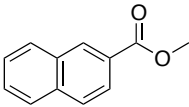
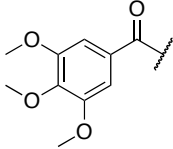
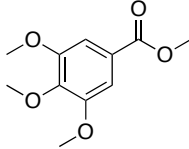
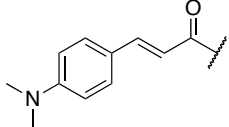
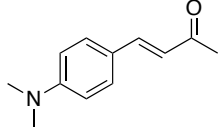


Figure S5.8. Calculated Absorption Spectrum.

Appendix E:

Supporting Information to Chapter 6

Table S6.1. Nomenclature of Aromatic Groups

Aromatic Group ^a	Similar Compound ^b	Name ^c	Abbreviation ^d
		methyl benzoate	“b”
		Vanillin	“v”
		methyl 2-naphthoate	“n”
		methyl trimethylgallate	“g”
		(E)-4-(4-(dimethylamino)phenyl)but-3-en-2-one	“dap”

^aAromatic group in boron dye. ^bStructure of compound of similar structure with a common name or distinguishable IUPAC name to simplify the abbreviation. ^cCommon or IUPAC name of the similar compound. ^dLetter representation in the boron dye name.

Scheme S6.1. System of Naming Boron Dyes

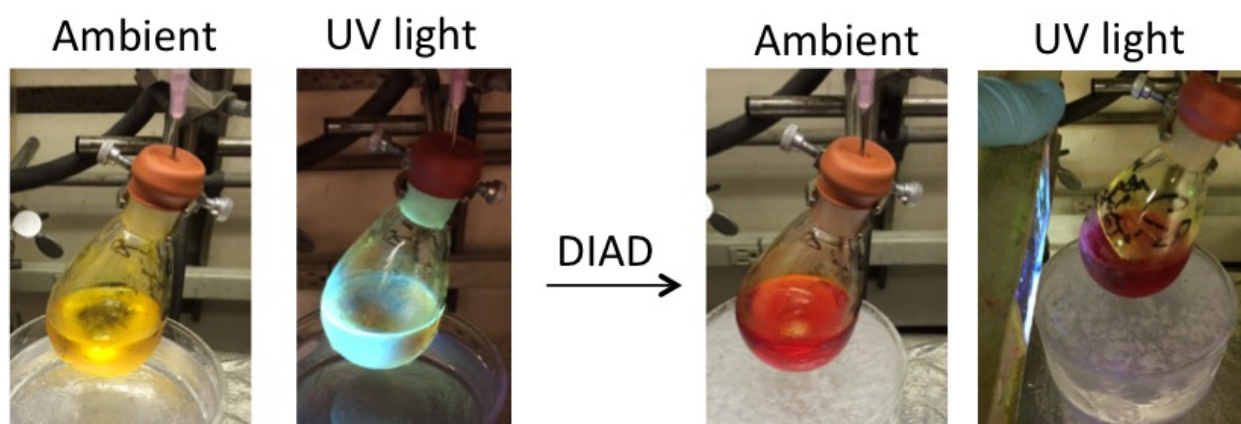
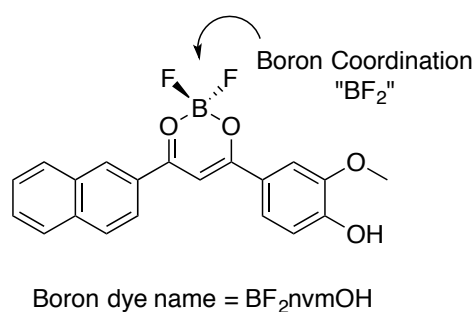
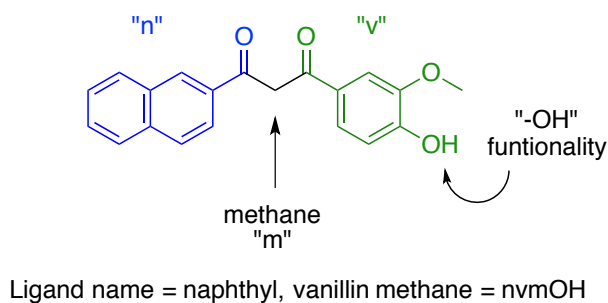


Figure S6.1. Mitsunobu Reaction of BF₂gvmoH (**3**) with PLLA-PEG. Note: After addition of DIAD, the solution is non-fluorescent. A compact UV light (UVP, 365 nm) was used for excitation and pictures were taken with an iPhone 5. Note, the DIAD reagent was added while the flask was in the acetone/ice bath (-10 °C) and then removed.

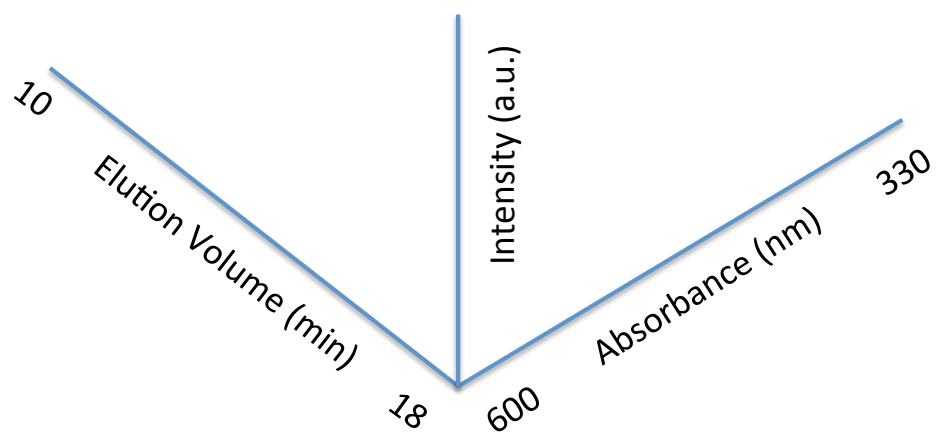


Figure S6.2. Schematic of axis values for the GPC plots in Figure S3 for comparison.

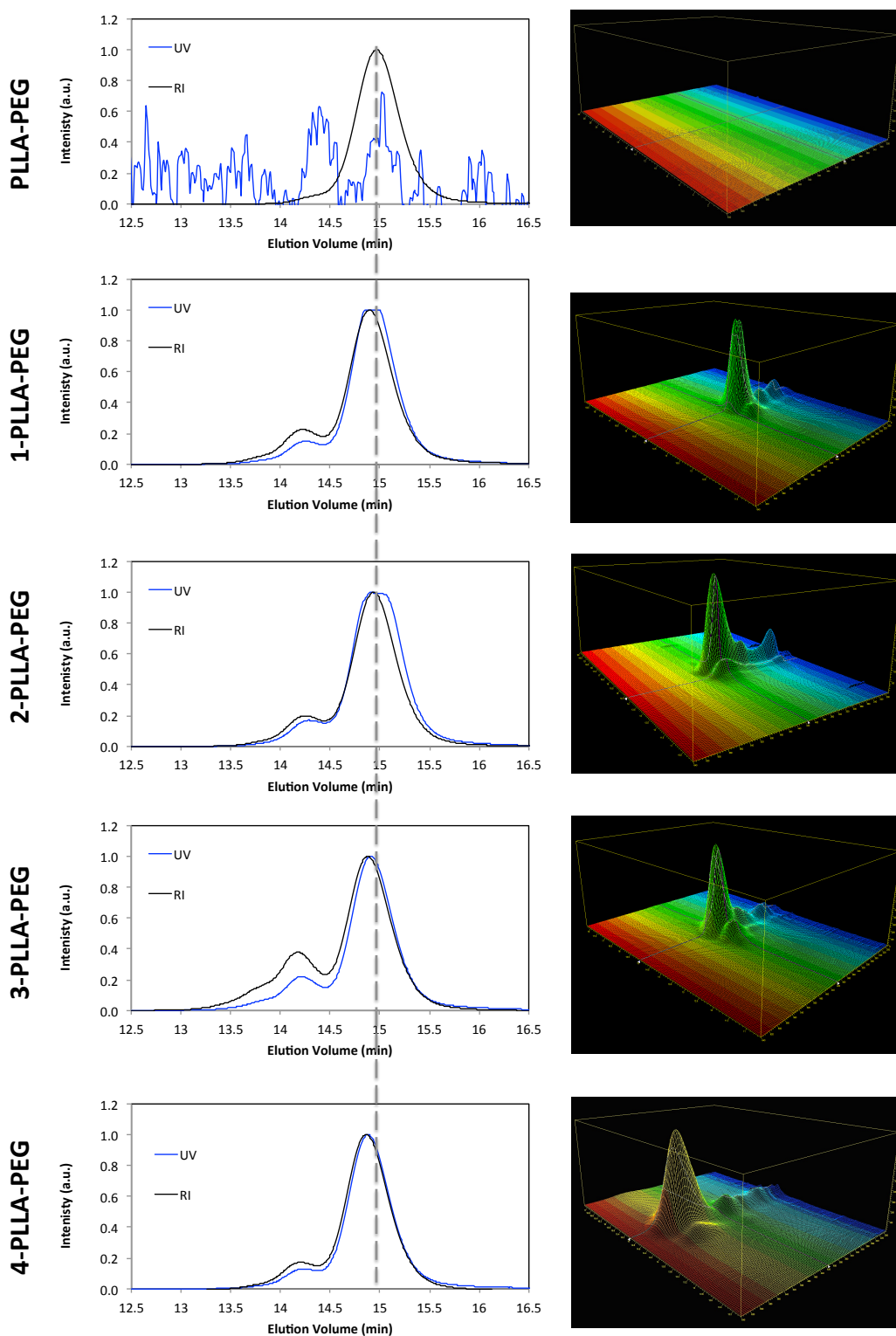


Figure S6.3. 2D (left column) and 3D (right column) GPC plots PLLA-PEG polymers. The gray dashed line is included to aid comparison of the retention volumes. UV = absorbance and RI = refractive index of the polymers. Note that the UV signal in pure PLLA-PEG is simple normalized noise. Refer to Figure S2 for the axis values of the 3D GPC plots.

Table S6.2. Polymer Molecular Weight Data

Sample	ID	M _n (NMR) ^a	M _n (GPC) ^b	M _w (GPC) ^b	Đ ^b
HO-PLLA-PEG		12 600	10 300	10 500	1.05
HO-PDLA-PEG		13 800	12 500	13 400	1.08
1 -PLLA-PEG	1P	13 500	11 500	12 500	1.09
2 -PLLA-PEG	2P	15 400	11 700	12 400	1.07
3 -PLLA-PEG	3P	14 900	12 600	14 200	1.13
4 -PLLA-PEG	4P	16 000	15 200	17 400	1.15

a. Determined by ¹H NMR end group analysis (-PEG-OCH₃ vs PLA-H).

b. Determined by SEC-MALS 100% mass recovery method.

Table S6.3. Optical Properties of Dye Phenols and Dye-Polymers in CH₂Cl₂

Sample	ID	λ _{abs} ^a	ε ^b	λ _{em} ^c	τ _F ^d	Φ _F ^e
		(nm)	(M ⁻¹ cm ⁻¹)	(nm)	(ns)	
BF ₂ dbmOH	1	394	28 000	422	1.8	67
BF ₂ dbmPLLA-PEG	1P	396	23 000	426	1.9	68
BF ₂ nvmOH	2	423	53 000	478	1.8	40
BF ₂ nvmPLLA-PEG	2P	423	39 000	501	2.3	41
BF ₂ gnmOH	3	424	54 000	504	2.1	41
BF ₂ gnmPLLA-PEG	3P	425	61 100	503	1.6	30
BF ₂ dapvmOH	4	542	75 100	633	43.2	8
BF ₂ dapvmPLLA-PEG	4P	539	83 500	626	1.0	17

^aAbsorption maxima. ^bExtinction coefficients calculated at the absorption maxima. ^cFluorescence emission maxima excited at 369 nm (except **1**, excited at 350 nm, and **4** at 488 nm).

^dFluorescence lifetime excited with a 369 nm light-emitting diode (LED) monitored at the emission maximum. All fluorescence lifetimes are fitted with single-exponential decay.

^eRelative quantum yield, with anthracene in EtOH as a standard for dyes **1-3** and Rhodamine G6 in EtOH for dye **4**.

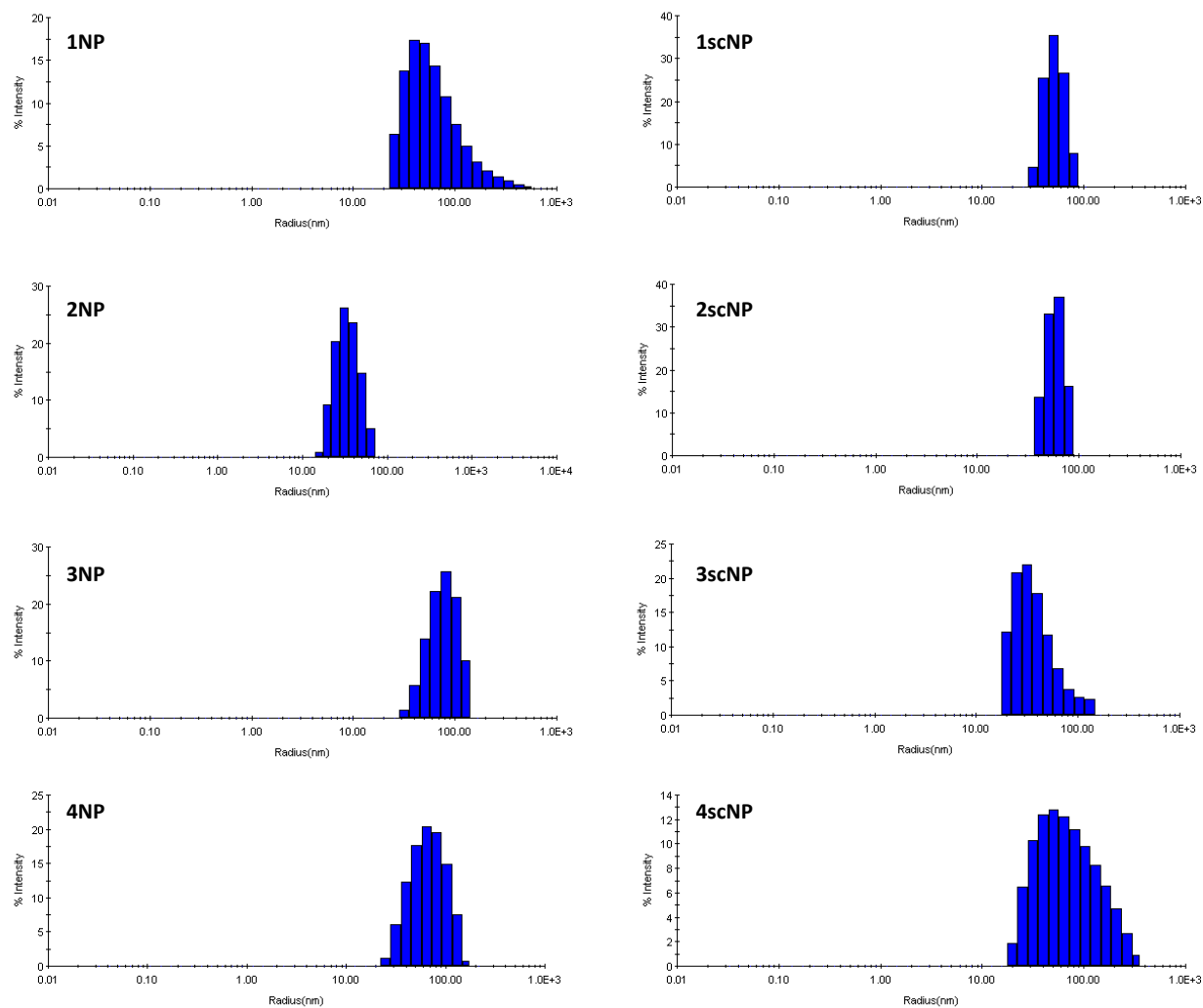


Figure S6.4. DLS histograms of nanoparticle size distributions.

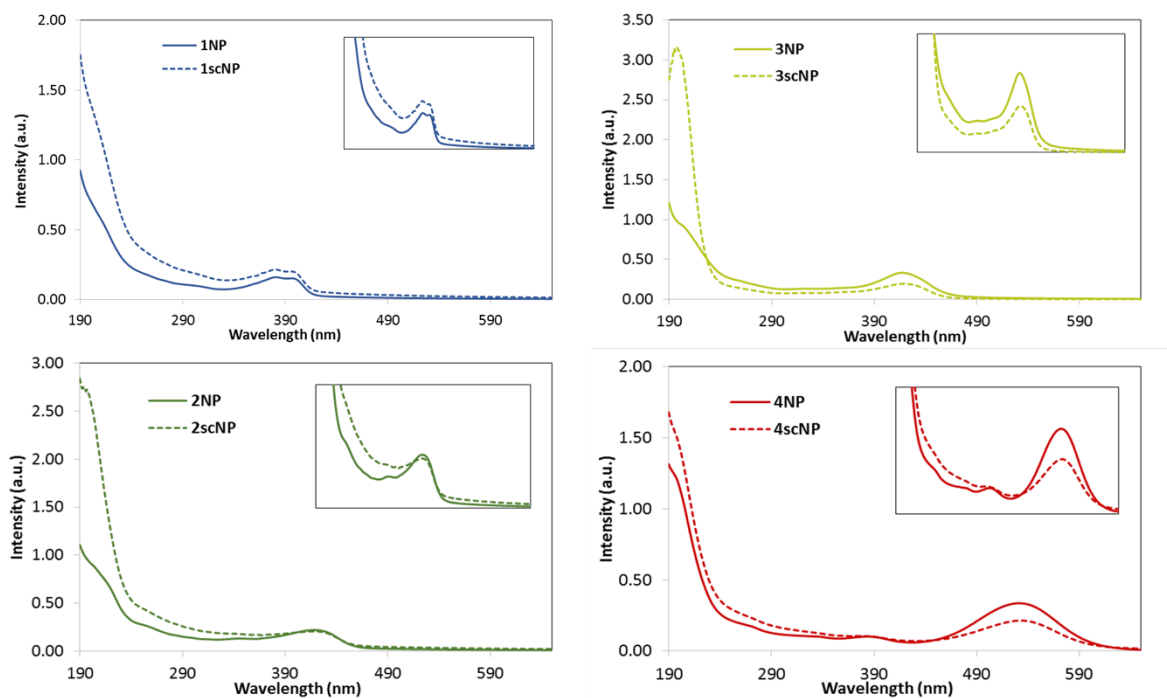


Figure S6.5. Absorbance spectra of BF₂dbm (1), BF₂nvm (2), BF₂gvm (3), and BF₂dapvm (4) nanoparticles (XNP and XscNPs, where X = 1-4).

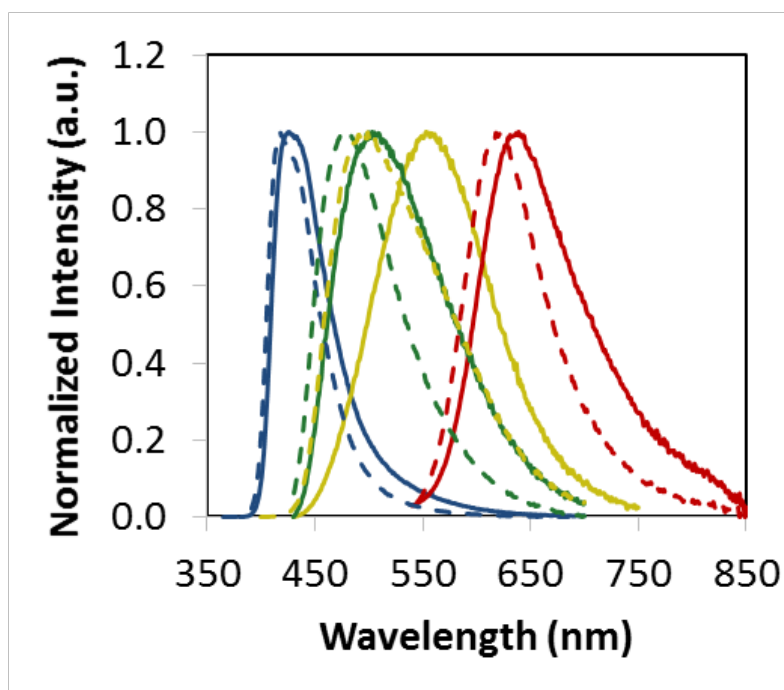


Figure S6.6. Nanoparticle emission spectra overlays. **1-4NP** (solid lines) and **1-4scNP** (dashed lines) in air. (1 = blue, 2 = green, 3 = yellow, 4 = red). Fluorescence emission maxima excited at 369 nm, except sample 4 ($\lambda_{\text{ex}} = 475$ nm).

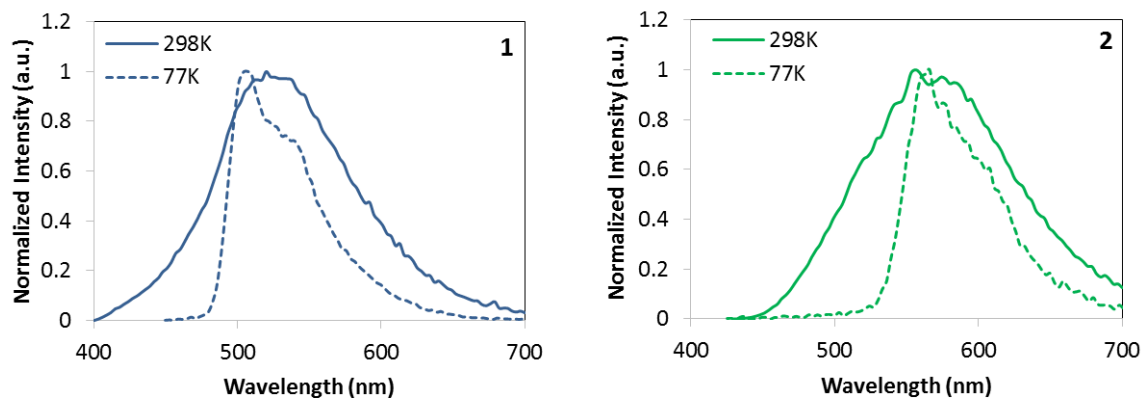


Figure S6.7. Temperature dependent delayed emission spectra of **1NP** and **2NP** under N_2 (350 nm excitation from xenon flash lamp, and 2 ms delay).

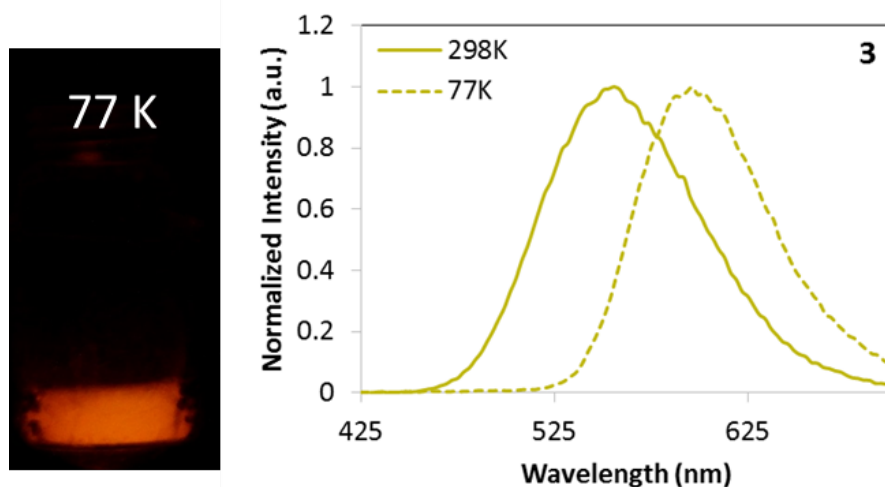


Figure S6.8. Image of delayed emission of **3NP** at 77 K and delayed emission spectra of **3NP** under N_2 at 77 K and 298 K (350 nm excitation from xenon flash lamp, and 2 ms delay).

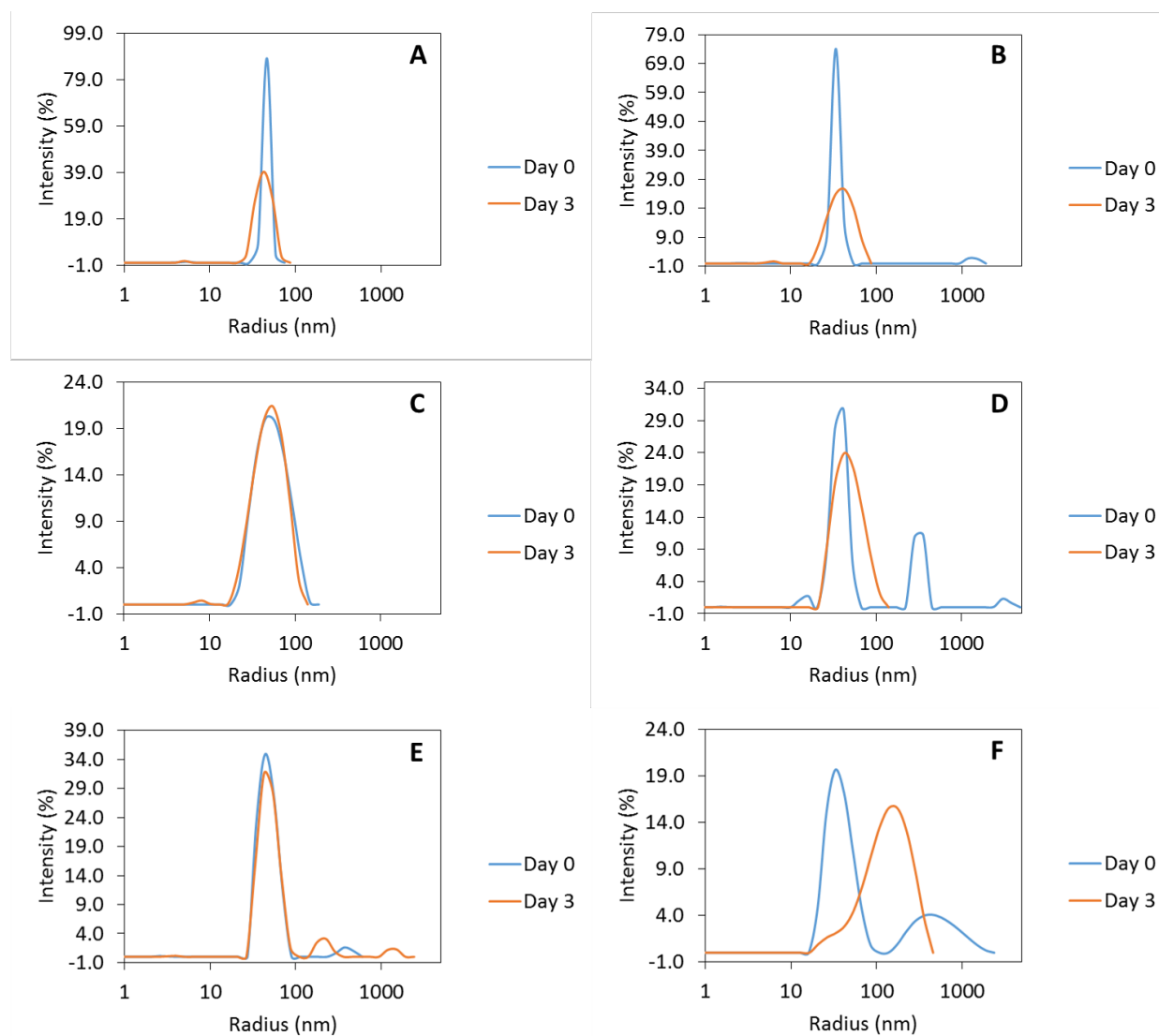


Figure S6.9. Size distribution of nanoparticles (0.5 mg/ml) over three days at 37 °C. BNP size and polydispersity determined by DLS. (A) **3NP** in DI water. (B) **3scNP** in DI water. (C) **3NP** in PBS. (D) **3scNP** in PBS. (E) **3NP** in DMEM. (F) **3scNP** in DMEM.

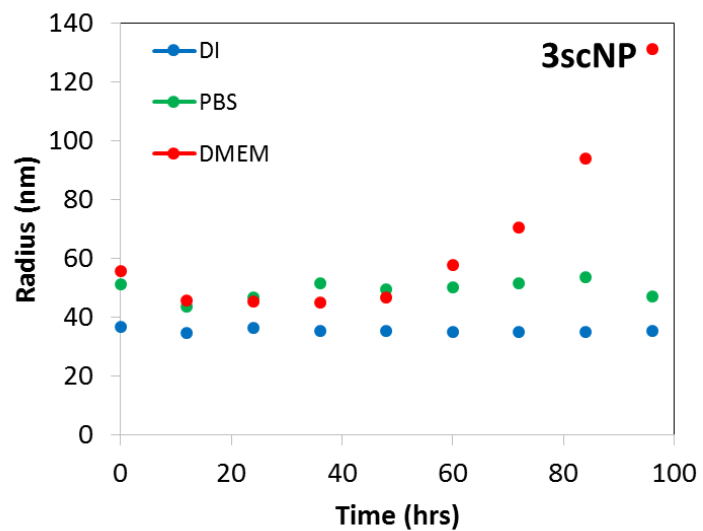
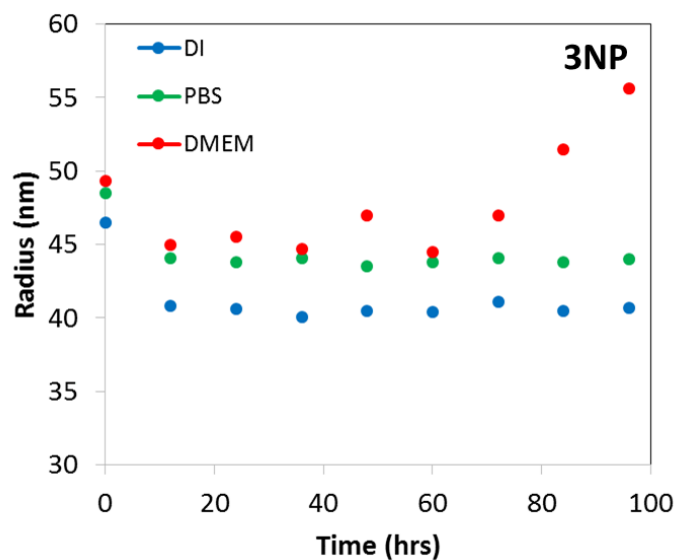


Figure S6.10. Average nanoparticle radii over time for **3NP** and **3scNP** in DI water, PBS, and DMEM determined by DLS.

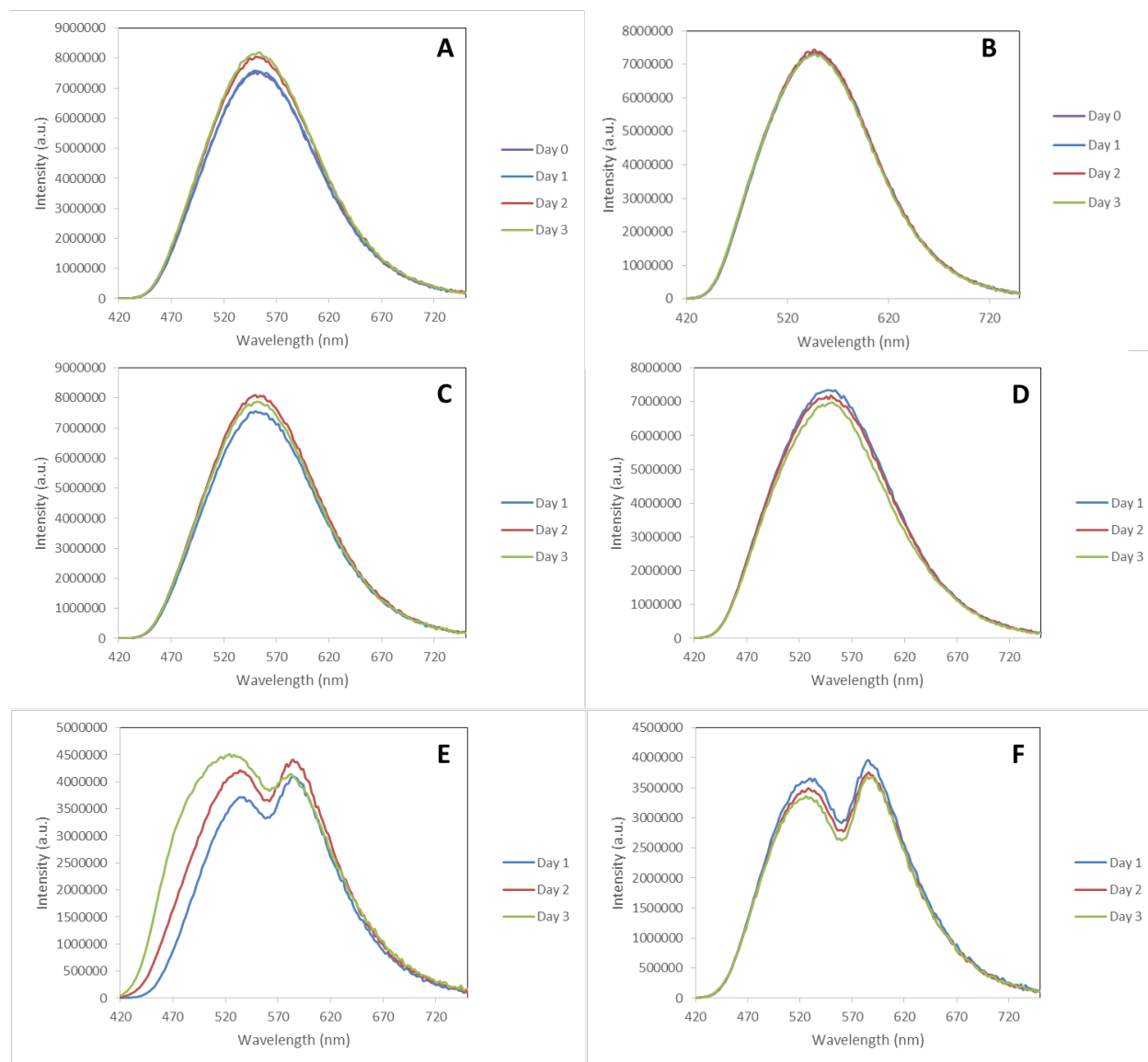


Figure S11. Total emission of nanoparticles over three days at room temperature. (A) **3NP** in DI water. (B) **3scNP** in DI water. (C) **3NP** in PBS. (D) **3scNP** in PBS. (E) **3NP** in DMEM. (F) **3scNP** in DMEM.

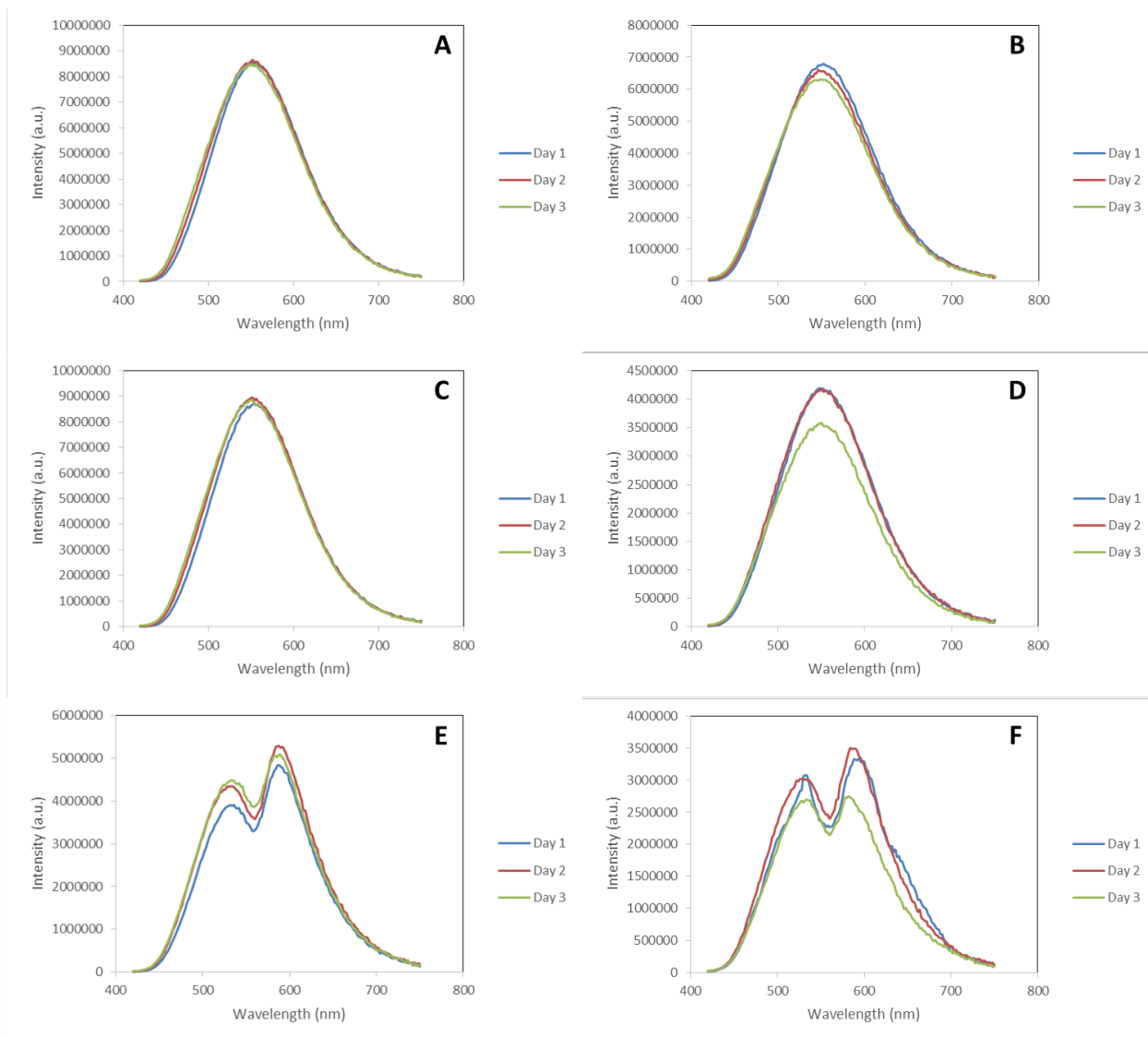


Figure S6.12. Total emission of NPs over three days at 37 °C. (A) **3NP** in DI water. (B) **3scNP** in DI water. (C) **3NP** in PBS. (D) **3scNP** in PBS. (E) **3NP** in DMEM. (F) **3-scPLA** in DMEM.

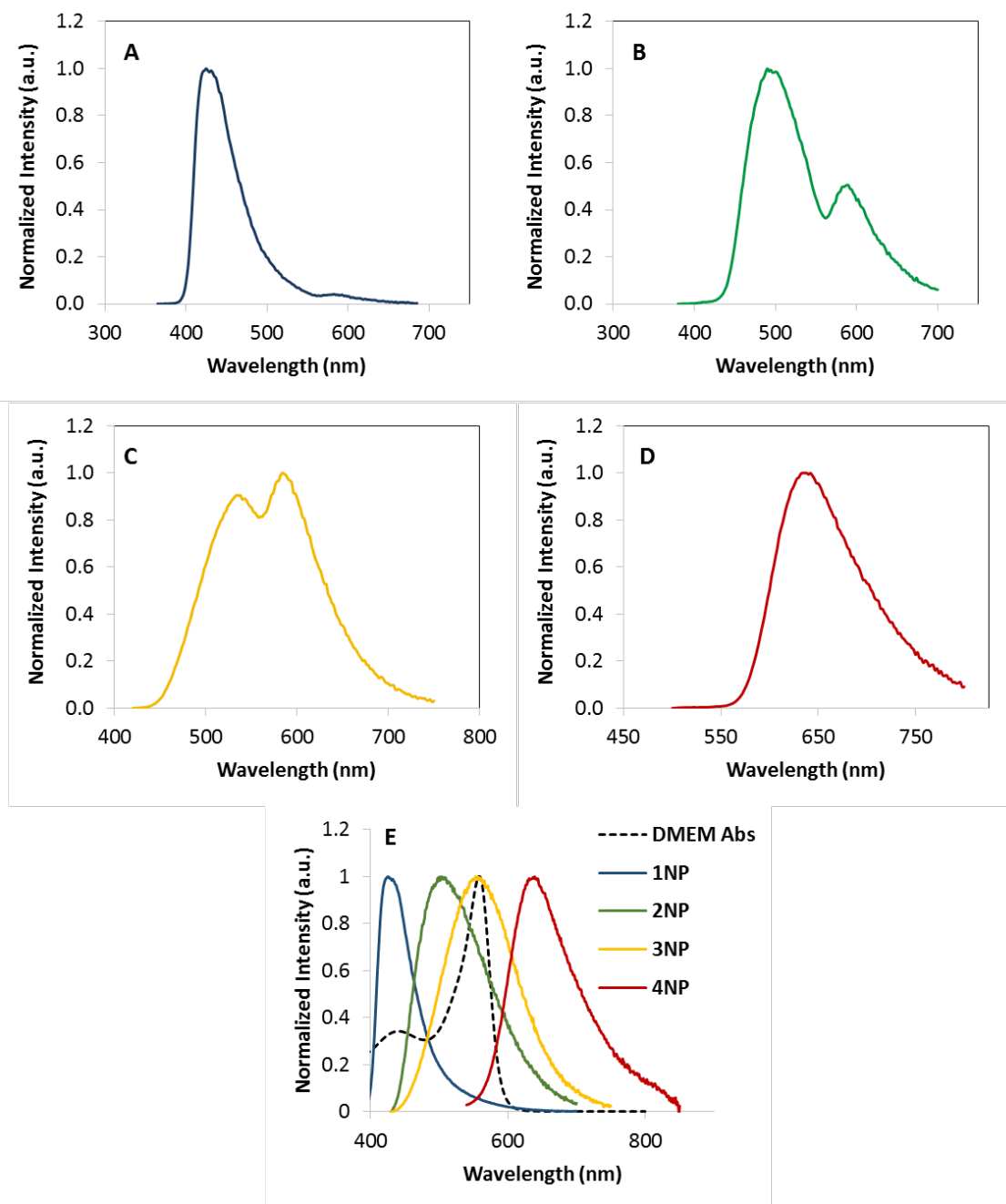


Figure S6.13. Sensitization of phenol red in emission spectra. Total emission of (A) **1NP** in DMEM in air. (B) **2NP**. (C) **3NP**. (D) **4NP**. (E) Total emission of **1-4NP** in DI water in air and absorbance spectrum of DMEM.

Appendix F:

Supporting Information to Chapter 7



Figure S7.1. Camera Imaging Equipment. (A) Laptop, (B) excitation source, (C) camera and (D) USB cables: camera power source and data collection.

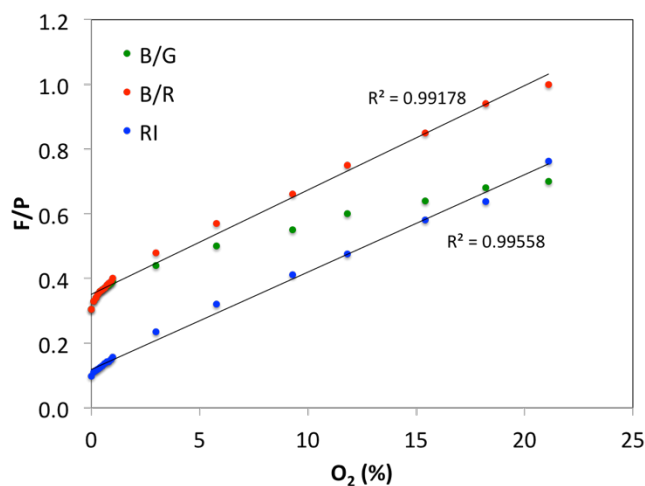


Figure S7.2. BF₂nbm(I)PLA Ratiometric Oxygen Calibration (0-21% O₂). Stern-Volmer (F/P) plot displayed as blue channel/green channel (B/G), blue channel/red channel (B/R), referenced intensity (RI; fluorescence and phosphorescence peaks from the total emission spectra).

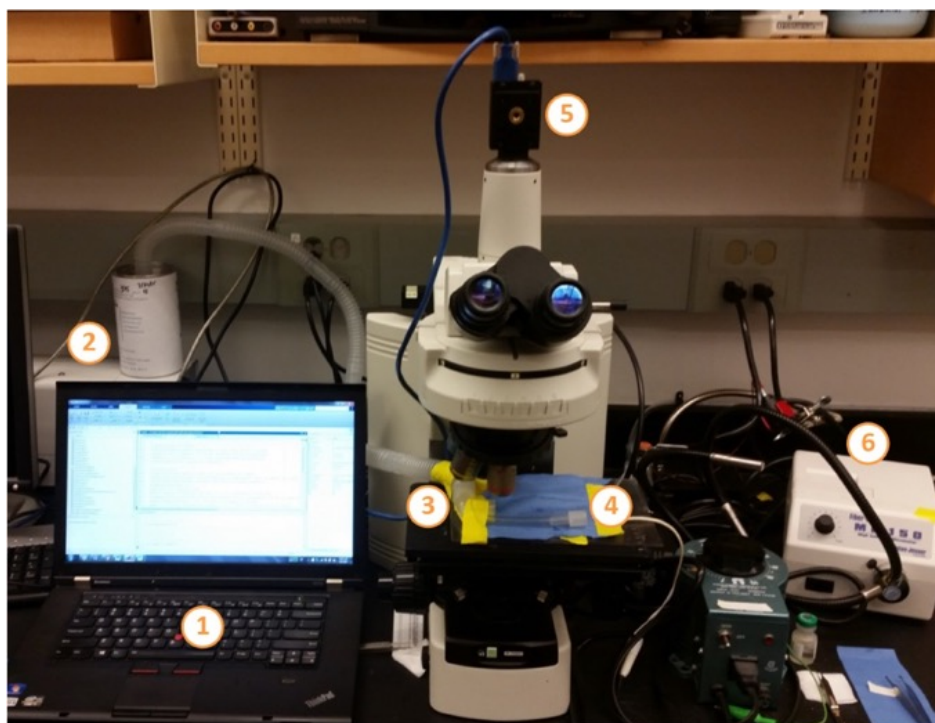


Figure S7.3. Wound Imaging Setup. (1) Computer used for acquiring images/analysis. (2) Fluorescent light lamp source. (3) Nose cone with inhalable anesthesia (2% isoflurane in oxygen). (4) 37 °C stage for imaging. (5) Camera mounted to Nikon Eclipse 80i Microscope. (6) White light lamp source.

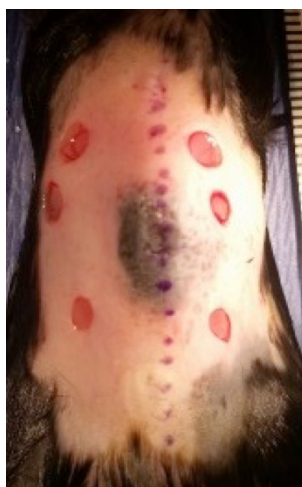


Figure S7.4. Sample Image of Mice Dorsal Wounds (3 mm diameter wounds)

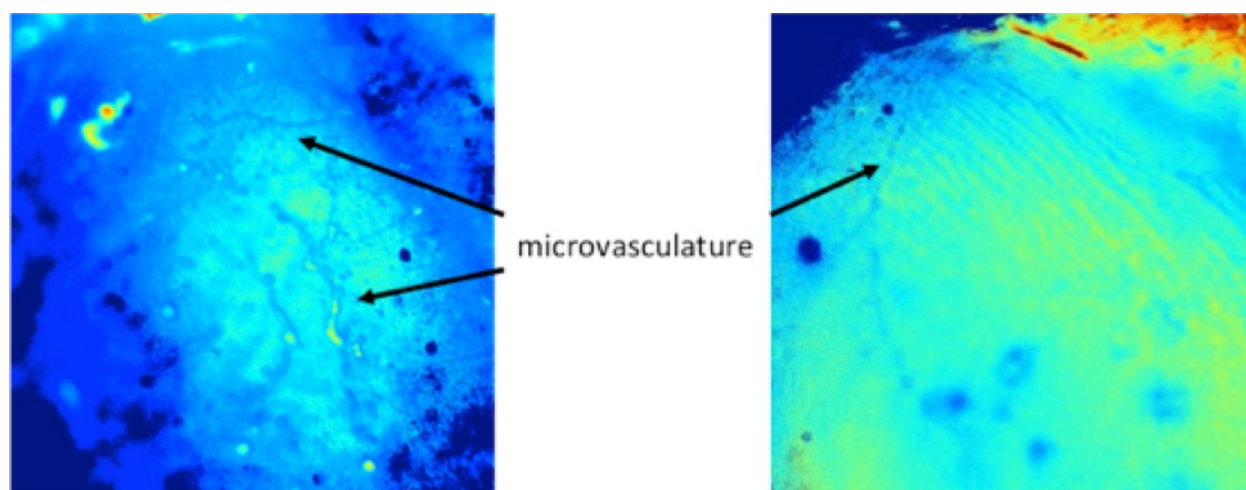


Figure S7.5. Ratiometric I-NP images revealing microvasculature.

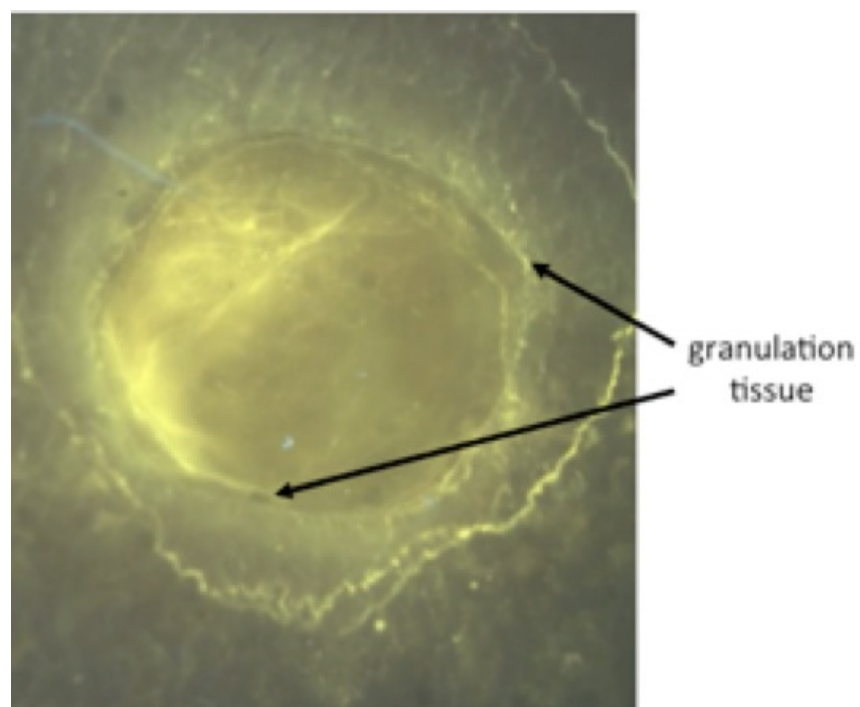


Figure S7.6. Image showing formation of granular tissue along the wound bed boundary revealed by I-NP with UV illumination.